



**HAL**  
open science

# Influence of filler /polymer interface on reinforcement, strain-induced crystallization and tear resistance in reinforced natural rubber

Arnaud Vieyres

► **To cite this version:**

Arnaud Vieyres. Influence of filler /polymer interface on reinforcement, strain-induced crystallization and tear resistance in reinforced natural rubber. Materials. Université Claude Bernard - Lyon I, 2013. English. NNT : 2013LYO10024 . tel-01170268

**HAL Id: tel-01170268**

**<https://theses.hal.science/tel-01170268>**

Submitted on 1 Jul 2015

**HAL** is a multi-disciplinary open access archive for the deposit and dissemination of scientific research documents, whether they are published or not. The documents may come from teaching and research institutions in France or abroad, or from public or private research centers.

L'archive ouverte pluridisciplinaire **HAL**, est destinée au dépôt et à la diffusion de documents scientifiques de niveau recherche, publiés ou non, émanant des établissements d'enseignement et de recherche français ou étrangers, des laboratoires publics ou privés.



N° d'ordre : 24-2013

Année 2013

THESE DE L'UNIVERSITE DE LYON

Délivrée par

L'UNIVERSITE CLAUDE BERNARD LYON 1

ECOLE DOCTORALE MATERIAUX

DIPLOME DE DOCTORAT

soutenue publiquement le 07/02/2013

par

M. Arnaud VIEYRES

## **Influence of Filler/Polymer Interface on Reinforcement, Strain-Induced Crystallization and Tear resistance in reinforced Natural Rubber.**

Directeur de thèse : M. Paul SOTTA

Encadrant Rhodia-Solvay : M. Oliver SANSEAU

### **JURY**

M. Bertrand HUNEAU  
M. Juan LÓPEZ VALENTÍN  
M. Srećko VALIĆ  
M. Laurent CHAZEAU  
M. Pierre-Antoine ALBOUY  
M. Loïc VANEL  
M. Paul SOTTA  
M. Olivier SANSEAU

Rapporteur  
Rapporteur  
Examineur  
Examineur  
Examineur  
Examineur  
Directeur de thèse  
Encadrant Rhodia-Solvay

---

---

## Remerciements !

Ces trois années (et un peu plus...) de thèse ont été pour moi d'une grande richesse à de nombreux points de vue et je souhaite remercier vivement ici toutes les personnes qui m'ont aidé et soutenu durant cette période.

Je tiens en premier lieu à remercier Ludovic Odoni et Didier Long, directeurs du LPMA de m'avoir chaleureusement accueilli dans leur unité de recherche et de m'avoir permis de réaliser ce travail dans de très bonnes conditions.

Je remercie Laurent Chazeau pour m'avoir fait l'honneur de présider le jury chargé d'évaluer mon travail. Merci beaucoup à Bertrand Huneau et muchas gracias à Juan López Valentín pour avoir accepté de rapporter ce manuscrit un peu indigeste! J'ai beaucoup apprécié la qualité et la pertinence de leurs rapports et j'espère que nous aurons encore de nombreuses occasions de discuter renforcement et cristallisation du NR entre autres! J'exprime ma reconnaissance à Srećko Valić pour avoir lui aussi activement pris part à mon jury de thèse.

J'ai également des remerciements appuyés à apporter à mes encadrants au LPMA. Les nombreux échanges que nous avons pu avoir ont toujours été très enrichissants pour moi. Je garde un excellent souvenir des longues et joyeuses réunions passées ensemble.

Ce travail doit beaucoup à l'apport scientifique de mon directeur de thèse Paul Sotta, je souhaite saluer ici ses qualités pédagogiques et sa capacité à saisir la complexité d'un problème et à la traduire en concepts et équations (relativement!) simples. Je le remercie aussi pour la confiance qu'il m'a accordée, pour son sens constructif du dialogue, pour ses conseils et pour s'être toujours montré disponible et à l'écoute. Merci enfin pour son méticuleux travail de relecture et de correction notamment pour le manuscrit !

J'ai également beaucoup appris au contact d'Olivier Sanseau qui a suivi ma thèse côté Rhodia. J'aimerais souligner l'implication et l'enthousiasme (parfois débordant) dont il a fait preuve lors du suivi de mon sujet et qui nous ont amené à redessiner au moins cent fois la courbe contrainte-déformation d'un caoutchouc chargé ! Je le remercie également pour ses nombreux conseils tout au long de la thèse et pour sa confiance (malgré ma notion un peu vague du timing !).

Merci à Loïc Vanel de s'être penché avec intérêt sur ma thèse et notamment sur la partie déchirure. Son avis et ses propositions lors des discussions sur mon travail étaient toujours les bienvenus.

J'exprime mes remerciements à Pierre-Antoine Albouy pour m'avoir accueilli chaleureusement au Laboratoire de Physique des Solides. J'ai pu profiter à la fois de ses grandes connaissances sur le sujet de la diffraction et de la formidable machine que lui et son équipe ont conçue pour l'étude des cinétiques de cristallisation et de fusion du caoutchouc. Je suis également reconnaissant envers Denis Petermann pour son aide précieuse dans la mise en œuvre des manips.

Je souhaite vivement remercier l'équipe Silice de Collonges-au-Mont-d'Or qui m'a permis de réaliser mes mélanges dans les meilleures conditions pendant ces trois ans.

Je remercie tout d'abord Laurent Guy pour son implication et l'intérêt qu'il a porté à mon sujet depuis le lancement, à la fois lors des discussions et de la préparation des campagnes de mélanges. Merci également à Aurélie Papon pour son aide précieuse et sa grande disponibilité. Une mention spéciale pour la fine équipe du labo caoutchouc : Jean-François Devis, Violaine Ducru, Amina Hebbache, Nicolas Godin, Alain Monton et Benoit Moreaux. Je garde un excellent souvenir des quelques morceaux de la vie au labo que j'ai eu la chance de partager. Merci beaucoup pour votre accueil, votre bonne humeur à toute épreuve et vos enseignements sur le caoutchouc et le reste ! Je dois un grand merci en particulier à Benoit, avec qui j'ai eu le plaisir de travailler directement. J'insiste sur l'apport déterminant de son travail dans ma thèse: je suis persuadé que sans son savoir-faire sur les mélanges et leur caractérisation, les points ne seraient pas si bien tombés sur une même droite dans un bon nombre de nos résultats (cf. chap VI !!).

---

Je n'oublie pas Frédéric Brun et Hélène Coste pour leur assistance et leurs conseils avisés au laboratoire de mécanique, mes essais mécas ne s'en portaient que bien mieux ! Merci également pour leur aide sur la partie acquisition d'image.

Je suis également reconnaissant envers les membres du laboratoire de microscopie notamment Magalie Fontana, Clémence Abadie et Rémi Sellier pour leur aide et leur sympathie.

Une bonne part de mes remerciements s'adresse aussi aux membres permanents comme non-permanents du LPMA, du LAIM et plus largement du CRTL. J'ai beaucoup apprécié l'ambiance de travail à la fois décontractée et stimulante qui y régnait. Les techniciens, ingénieurs, chercheurs, doctorants et postdocs que j'y ai croisés ont ainsi largement contribué à mon épanouissement sur mon lieu de travail et en dehors. Je remercie donc tous ceux qui ont enrichi mon passage à Rhodia par de nombreuses discussions et conseils plus ou moins scientifiques autour d'un café, d'une bière ou d'un bon vin.

Merci donc à Louise-Anne Fillot, Lise Trouillet-Fonti, Elodie Seignobos et Brice Gabrielle qui m'ont mis le pied à l'étrier respectivement en stage et en début de thèse, Sandrine Rossi pour son aide et son énergie communicative, Elian Masnada, Marie-Laure Milan, Erik Lange, Alain Dequidt toujours prêt à rendre service, Clio Cocquet et Alexandra Argoud qui m'ont donné de très nombreux coups de pouces, Luisa Muñoz et Zélie Mané avec qui j'ai partagé de fructueuses campagnes de mélanges, Simona Ceccia qui nous a initié au vrai tiramisù, Roberto Pérez-Aparicio pour sa contribution primordiale à ma thèse autant par nos échanges scientifiques intenses (et multilingues !) que par ses qualités humaines et ses conseils de « tonton ». Merci aussi à Agustin Rios de Anda et Naji Hussein mes deux compères de thèse dont j'admire la gentillesse et le parcours. J'étais fier de faire équipe avec eux (même si j'avais tendance à trouver que le premier buvait trop de bière et le second pas assez!). Merci à mes co-bureaux Pauline Grau (aux articulations élastiques), Caroline Fayolle et Chloé Epinat qui ont patiemment écouté mes problèmes et m'ont encouragé jusqu'au bout et aussi à Grégoire Julien qui supportait le volume sonore parfois élevé! Au fait j'espère que le nouveau bâtiment ne cachera pas la torchère! Merci à Aurélie Sandeau, Coraline Millot, Congyu Bao, Mathieu Tauban, Florentina Preda, Lucca Conca ainsi qu'à tous ceux passés par le labo à l'occasion d'un stage ou autre. Merci aussi à Guillaume Normand pour le travail conséquent qu'il a réalisé lors de son stage ingénieur, ce qui a considérablement enrichi ma thèse. Merci enfin à Didier Tupinier (et ses nombreuses idées), Olivier Gilbain, Pierre-Yves Lahary, Jean-Yves Delannoy (pas avare de conseils), Anthony Bocahut, Nick Suek, Léo Georges, Séverine Dauffer, Sylvie Ghiringhelli, Christiane Prébet, Caroll Vergelati, Sébastien Nébut, Cécile Corriol et Vincent Curtil. Je me rappelle avec nostalgie des gâteaux tous meilleurs les uns que les autres que l'on a partagés lors des pauses, sans oublier les sorties culturelles (ou non) et quelques séances de sport (de l'escalade à la trottinette en passant par la pétanque et le tournoi de foot où notre 4ème place me laisse un goût d'inachevé!).

Je terminerai par les remerciements pour les proches avec qui j'ai partagé mes inquiétudes, mes joies et mes projets. Merci donc à la bande des Toulousains (A7 & Co) toujours partants pour des retrouvailles fort animées aux quatre coins de la France, et merci aussi aux vieux amis de Tours et d'Angoulême!

Un remerciement spécial pour mes parents, ma grande sœur et mon petit frère qui m'apportent depuis si longtemps un soutien sans faille et bien plus encore. J'ai également une pensée pour toute ma famille.

Enfin je remercie tout particulièrement Cécile pour sa patience, ses mots et ses petits gestes qui m'ont toujours permis d'avancer.

---

# Table of contents

<b>General Introduction</b> .....	10
<b>I. Context and motivation of the project</b> .....	13
I.1. Historical aspects on rubber an tires .....	13
I.2. The complex structure of modern tires .....	13
I.3. Current issues in the tire industry.....	14
I.3.a. Precipitated Silica reinforcement benefits .....	14
I.3.b. Tire labeling .....	17
I.4. Research project motivations .....	18
<b>II. Literature survey: Structure and Properties of reinforced rubber materials</b> .....	21
II.1. Microstructure and physical properties .....	23
II.1.a. Polymers and Elastomers.....	23
II.1.b. Crosslinking of rubbers: vulcanization .....	24
II.1.c. Theory of Rubber elasticity .....	26
II.1.d. Rubber network characterization by equilibrium swelling.....	33
II.2. Reinforcement by nanometric fillers.....	34
II.2.a. Small Strain regime.....	34
II.2.b. Large Strain regime.....	46
II.3. Strain-induced Crystallization.....	51
II.3.a. Effect of crosslink density on a traction-retraction cycle .....	52
II.3.b. Effect of fillers on SIC:.....	55
II.3.c. Effect of temperature on SIC:.....	57
II.3.d. Strain-induced crystallization at crack tip.....	58
II.4. Resistance to crack propagation in Rubbers .....	60
II.4.a. Energy release rate and Tear energy .....	60
II.4.b. Crack propagation instabilities .....	63
II.4.c. Effect of material variables on crack propagation .....	67
II.5. Conclusion.....	67

---

<b>III. Materials, Compounding procedures and Characterization methods ...</b>	<b>69</b>
III.1. Components .....	71
III.1.a. Natural Rubber .....	71
III.1.b. Styrene-Butadiene Rubber .....	72
III.1.c. Reinforcing fillers .....	73
III.1.d. Interface agents. ....	78
III.1.e. Vulcanization system .....	81
III.2. Formulations, processing and standard rubber tests .....	81
III.2.a. Formulations.....	81
III.2.b. Mixing procedures.....	83
III.2.c. Rheology and other tests. ....	92
III.3. Characterization techniques.....	92
III.3.a. Dynamic Mechanical Analysis in small strains regime .....	92
III.3.b. Mechanical measurements in the large strain regime .....	94
III.3.c. Scanning Electron Microscope.....	100
III.3.d. DQ Proton NMR .....	101
III.3.e. Equilibrium swelling measurements .....	101
III.3.f. X-ray diffraction experiments .....	104
<b>IV. Overview of Mechanical Properties .....</b>	<b>115</b>
IV.1. Mechanical behavior in the linear regime .....	117
IV.1.a. Effect of filler volume fraction.....	117
IV.1.b. Effect of interface type.....	119
IV.1.c. Applications .....	121
IV.1.d. Discussion .....	122
IV.2. Mechanical behavior at small and medium strains: Payne Effect .....	123
IV.2.a. Effect of filler amount .....	123
IV.2.b. Effect of the filler specific surface .....	125
IV.2.c. Effect of interface type .....	126
IV.2.d. Discussion .....	128
IV.3. Mechanical behavior at large strains .....	129
IV.3.a. Unfilled Natural Rubber.....	129
IV.3.b. Effect of the Silica volume fraction .....	130

---

IV.3.c.	Effect of the crosslink density in filled samples .....	131
IV.3.d.	Effect of the Silica specific surface.....	132
IV.3.e.	Effect of interface agents.....	133
IV.4.	Conclusions .....	138
<b>V.</b>	<b>Strain-induced Crystallization</b> .....	<b>141</b>
V.1.	Introduction .....	142
V.2.	Unfilled Natural Rubber.....	143
V.2.a.	Description of a traction-retraction cycle. ....	143
V.2.b.	Tensile tests up to failure: Effect of the crosslink density.....	146
V.2.c.	Traction-retraction cycle: Effect of crosslink density.....	149
V.3.	Filled Natural Rubber.....	149
V.3.a.	Crystallized fraction.....	149
V.3.b.	Size and orientation of crystallites.....	152
V.3.c.	Effect of precycling on SIC. ....	154
V.4.	Crystallization and melting kinetics.....	156
V.4.a.	Measurements principle .....	156
V.4.b.	Interpretation of the results .....	159
V.4.c.	Results for Unfilled NR .....	161
V.4.d.	Results for Filled NR .....	166
V.5.	Conclusions .....	167
<b>VI.</b>	<b>Reinforcement</b> .....	<b>169</b>
VI.1.	Unfilled NR .....	170
VI.1.a.	Proton DQ-NMR experiments .....	170
VI.1.b.	Equilibrium swelling experiments .....	171
VI.1.c.	Mechanical modulus .....	171
VI.1.d.	Amorphous chain orientation.....	173
VI.1.e.	Correlation of mechanical, amorphous orientation, equilibrium swelling and NMR measurements.....	175
VI.2.	Filled NR .....	179
VI.2.a.	Proton DQ-NMR experiments .....	179
VI.2.b.	Equilibrium swelling experiments .....	180

---

VI.2.c.	Modulus in the large strain regime.....	181
VI.2.d.	Modulus in the small strain regime.....	182
VI.2.e.	Amorphous chain orientation.....	183
VI.3.	Correlations between the various measurements.....	187
VI.3.a.	Correlations between large amplitude mechanical behaviour, amorphous orientation, swelling and NMR measurements.....	188
VI.3.b.	Mechanical Reinforcement in the linear regime.....	192
VI.3.c.	Strain Amplification discussion.....	195
VI.4.	Conclusion.....	200
<b>VII.</b>	<b>Dissipation at large strain and Ultimate properties.....</b>	<b>203</b>
VII.1.	Dissipation at high strain.....	204
VII.1.a.	Mullins effect.....	204
VII.1.b.	Dissipation on « stabilized » samples.....	206
VII.1.c.	Dissipation on « non-stabilized » samples.....	209
VII.1.d.	Relationship between dissipation and tangent modulus.....	211
VII.2.	Cavitation.....	213
VII.2.a.	Introduction.....	213
VII.2.b.	Measurements principle.....	213
VII.2.c.	Effect of fillers and interface on cavities formation.....	215
VII.3.	Microscopic observations.....	217
VII.4.	Resistance to failure for un-notched sample.....	218
VII.5.	Conclusions.....	220
<b>VIII.</b>	<b>Tear Resistance in Reinforced Natural Rubber.....</b>	<b>223</b>
VIII.1.	Tear resistance in unfilled NR.....	224
VIII.1.a.	Stress-strain curves.....	224
VIII.1.b.	Evaluation of the tear energy in the pure shear geometry.....	226
VIII.1.c.	Effect of crosslink density on tear resistance.....	229
VIII.2.	Tear resistance in reinforced Rubbers.....	229
VIII.2.a.	Tear behavior for reinforced Synthetic and Natural Rubbers.....	229
VIII.2.b.	Effect of filler/rubber interface on tear resistance.....	232
VIII.2.c.	Effect of crosslink density on tear resistance.....	234

---

VIII.2.d. Effect of test speed .....	236
VIII.3. Study of the crack tip .....	236
VIII.3.a. State of the crack tip.....	237
VIII.3.b. Strain amplification at the crack tip .....	239
VIII.3.c. Local stress estimation at crack tip .....	243
VIII.3.d. Crystallized zone at crack tip .....	244
VIII.3.e. Crystallized fraction measurement at crack tip .....	245
VIII.4. Conclusion .....	248
<b>IX. General Conclusion .....</b>	<b>223</b>
<b>X. Bibliography .....</b>	<b>254</b>
<b>XI. Appendices .....</b>	<b>265</b>
X.1. Sample series recipes .....	265
X.1.a. Series 021-10 .....	265
X.1.b. Series 054-10 .....	265
X.1.c. Series 095-10 .....	266
X.1.d. Series 115-10 .....	266
X.1.e. Series 030-11 .....	267
X.1.f. Series 046-11 .....	267
X.1.g. Series 119-11 .....	268
X.1.h. Series 038-12 .....	268
X.1.i. Series 051-12 .....	269
X.2. Dispergrader .....	269
X.2.a. Measurements .....	269
X.2.b. Results for series 030-11.....	269
<b>XII. Résumé en français.....</b>	<b>271</b>

---

## General Introduction

In this manuscript, various aspects of the physics of reinforced Natural Rubber (NR) are studied. Reinforced elastomers are very complex materials, made of an elastomer matrix in which particles or aggregates of sub-micrometric sizes (denoted as fillers) are dispersed. A special emphasis has been put on the effect of filler/elastomer interface on the mechanical properties increase in filled samples (effect of reinforcement) and on the Strain-Induced Crystallization (SIC) phenomenon.

The applicative context is the following one. In order to improve the properties or compromise of properties of reinforced natural rubber materials, it is needed to identify the physical mechanisms responsible for the mechanical and ultimate properties. The reinforcement in the Payne effect regime in particular is of importance for the balance of properties such as the wet grip and the rolling resistance. As regards the wear properties, they may ultimately be related to crack propagation properties and for this reason the tear resistance was also studied. Identifying the mechanisms should then allow proposing some ways towards improved materials.

On the scientific point of view, this study fits in the frame of research works aiming at better understanding the physical origin of reinforcement of elastomers by nano-particles. The ultimate properties of reinforced rubber and the strain-induced crystallization phenomenon are also addressed in order to yield new insights on the outstanding wear properties of reinforced Natural Rubber.

The strategy that we adopted consisted in processing various rubber compounds using a standard mixing procedure and changing different materials variables such as filler fraction, filler specific surface, interface type and crosslink density one at the same time. Several Silica/Rubber interface agents were used and the obtained samples were compared to Carbon black filled NR to analyze the effect of the interface strength on the properties. Interface agents either consisted of a sulfurized coupling agent (TESPT), a non-sulfurized coupling agent (NSC) or a covering agent that, conversely to coupling agents, does not create covalent bonds with the rubber matrix (OCTEO).

The first chapter briefly presents the historical aspects about Natural Rubber and tires. Although tires have turned from simple goods to high-technology products over the past century, the current issues of greenhouse gas emissions, energy savings and road safety are continuously driving new tire designs and material developments. The introduction of the “green tire” by Michelin in the early 90’s has marked a technological breakthrough with a simultaneous improvement of rolling resistance and wet grip without deterioration of wear resistance. These improvements were made possible by substituting Carbon Black by precipitated Silica.

A literature review on rubber elasticity and reinforced rubbers properties is presented in chapter II. After reminding the basics of rubber elasticity, the effect of reinforcing fillers on the mechanical behavior in the different strain regimes is detailed together with the common physical interpretations for the observed behaviors. The Strain-Induced Crystallization (SIC) phenomenon which plays a key role in the outstanding mechanical properties in Natural Rubber

---

is introduced. Finally the specificity of Naturel Rubber in terms of crack propagation resistance is shown.

Chapter III introduces the different components and recipes that have been used to manufacture the Natural Rubber samples used in this work. The mixing procedures are then detailed in order to emphasize the key role of the processing steps on the final properties. The characterization techniques that have been used and developed are also presented in this chapter.

An overview of the mechanical properties in both the small strain regime and the large strain regime is given in chapter IV. The effects of the filler content, the filler specific surface and the filler/polymer interface type in the Payne effect regime are presented and the interpretations are discussed in the frame of a reduced mobility layers model. These various materials parameter and the matrix crosslink density effects on the reinforcement in the large deformation regime are also shown.

The study of the Strain-induced crystallization phenomenon is reported in chapter V. The evolution of the crystalline content, amorphous orientation parameter and crystallites orientation with strain for unfilled NR samples with several crosslink densities are presented first. The effect of the filler interface is highlighted.

The kinetics of Strain-Induced Crystallization has been studied thanks to a newly developed stroboscopic acquisition procedure during oscillations of various frequencies. Two unfilled NR samples of different crosslink densities are analyzed and the effect of the average applied strain on the kinetics of crystallization and melting is analyzed.

In chapter VI, one presents a comparative study of unfilled and filled NR samples with several characterization techniques all related with the local chain orientation. The true stress, amorphous orientation parameter and equilibrium swelling are correlated to the crosslink density measured by DQ-NMR experiments. Comparing the results for reinforced and neat NR samples, some new insights on the reinforcement mechanisms in small and large strain regimes are proposed.

The dissipation properties at large strains are presented in chapter VII. The increase of the dissipation above a given strain is related to the Strain-Induced Crystallization phenomenon for reinforced NR with various interface types. Finally a cavitation measurements based on X-ray absorption measurements is presented.

Chapter VIII is dedicated to the Tear resistance properties of unfilled and filled NR materials. In addition to pre-notched pure shear experiments to measure tear resistance, strain fields in the vicinity of the crack tip calculated by digital image correlation are presented. The role of the crystalline content at the crack tip is also highlighted by X-ray diffraction mapping at the crack tip in silica reinforced NR.

---

# I. Context and motivation of the project

## I.1. Historical aspects on rubber and tires

The native people of South and Central America were the first to use articles made of rubber. They extracted the latex by tapping the rubber tree (*hevea brasiliensis*) which they use to call “cahu-chu” meaning the crying tree. The introduction of the rubber material in Europe is generally attributed to the French explorer Charles-Marie de La Condamine in the sixteenth century. The name of “rubber” was given to this material in England after noticing that it was a very effective material for rubbing off pencil marks.

Nevertheless, the wide use of rubber did not start earlier than the nineteenth century when Charles Goodyear accidentally discovered in 1839 that heating a rubber piece in presence of sulfur dramatically increases its elasticity. The obtained material was no longer brittle at low temperatures and tacky at high temperatures opening a wide range of applications for rubber products such as impermeable cloths. The first solid tires simply made of a rubber sheet fixed to the wheel and covered with fabric were commercialized in the early times of the automotive industry. The air-inflated tire era began with the patent of John Boyd Dunlop who successfully manufactured the first pneumatic tires for bicycles in 1887. Four years later, André and Edouard Michelin developed a new bicycle tire that can be easily replaced and later adapted the pneumatic tire to automobiles. In order to increase the mechanical properties of rubber compounds such as abrasion resistance and tensile strength, carbon black was incorporated in tires in the early 1900s.

Among the numerous further evolutions in the tires technology, one could cite the diffusion of synthetic rubber which started after the strong improvements performed during World War II. The radial tire technology was developed by Michelin and released in the late 40's.

## I.2. The complex structure of modern tires

The structure and composition of the different parts of a tire reflects the role played by each part and the different properties that are required depending on the solicitation encountered.

The main constituent of a tire are represented in Figure 1 and shortly detailed below:

- The tread is the part in contact with the road where the wear resistance and traction properties are essential. The design of tread blocks and grooves is adapted to the each tire application and has an impact on the grip and the wear of the tire.
- The sidewall is the lateral part that needs to resist to ozone cracking and tear.

The carcass includes all non-tread and sidewall constituents: the body ply, belt and beads.

- The form of the tire is provided by the body ply made of calendered sheets of rubber-coated fabric (nylon, kevlar).
- The tread is supported by a one or more rubber-coated sheets of steel cords oriented radially called the belt. Reinforcing the body plies, the belt also holds the tread flat on the road.

- The beads consist of high strength steel wire encased in rubber that ensures an inflexible link between the wheel and the tire in particular to transfer the engine torque. The “bead filler” is a soft rubber profile playing the role of cushion between the bead and flexible parts fitted to the bead (inner liner and carcass)
- The internal layer (inner liner) must have very low air permeability and is often made of butyl rubber.

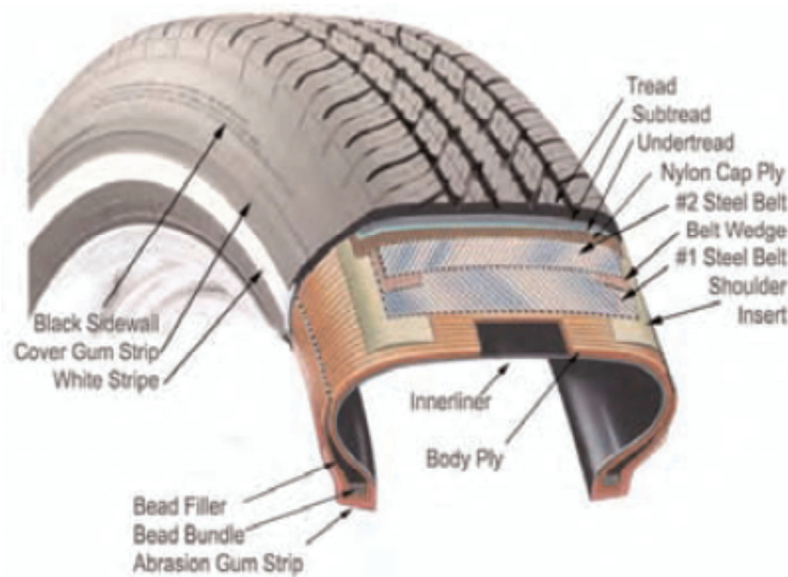


**Figure 1: Structure of a passenger car tire<sup>1</sup>**

### **I.3. Current issues in the tire industry**

The reduction of greenhouse gas emissions is a major concern in the automotive industry. In addition to climate change concerns, fuel consumption cuts are also of interest for customers facing the increase of energy costs. On the other hand, road safety is at the center of transportation politics in many countries. Those issues of fuel efficiency and safety are therefore the main drivers of innovations in tires nowadays.

The part of the passenger cars contribution in CO<sub>2</sub> emissions in the European Union was estimated around 12%. 20 to 30% of the fuel consumption can be attributed to energy losses in tires<sup>2</sup>. The rolling resistance i.e. the energy input required to overcome the viscosity of the rubber material is the main dissipation mechanism in tires. Concerning wet grip, this property is essential when it comes to reducing braking distances.

#### *1.3.a. Precipitated Silica reinforcement benefits*

Historically the reinforcement of rubber that is necessary to meet tire performance requirements was obtained by using Carbon Black fillers due to their reactivity towards rubber and relatively good dispersibility.

Nevertheless the 1990's have seen the introduction of low rolling resistance tires (Figure 2) based on recipes using highly dispersible precipitated silica as a substitute to carbon black. The decrease of rolling resistance was achieved without reducing wet grip and wear performance.

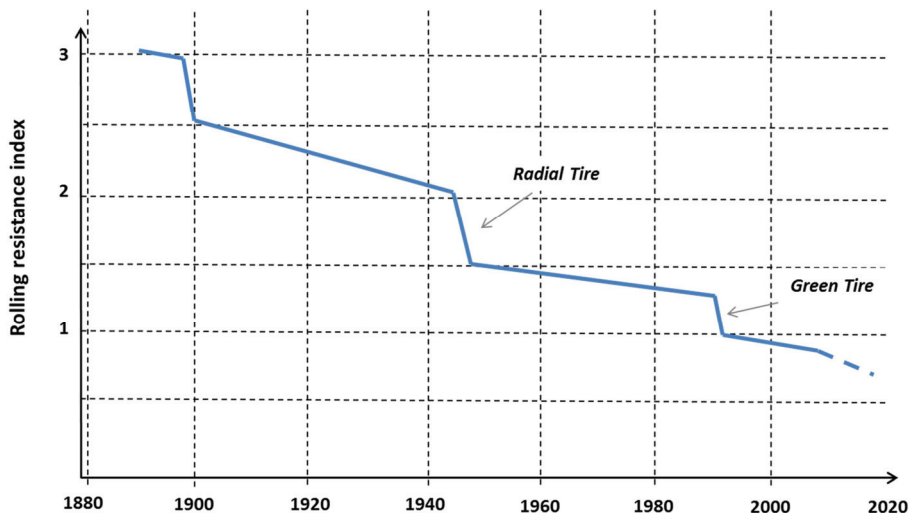


**Figure 2: Decrease of the Rolling resistance index for Michelin tires since the end of the nineteenth century<sup>3</sup>.**

This technologic breakthrough was the result of several advances: first the introduction of efficient coupling agents for silica such as the TESPT silane molecule by Degussa<sup>4</sup>, then a specific compounding procedure developed by Michelin<sup>5</sup> for high vinyl content SBR and finally new precipitated silica from Rhône-Poulenc as the reinforcing fillers.

It has been shown that the loss factor at low strains (ratio of loss modulus versus storage modulus, also called damping factor) can be used as a relevant indicator for wet grip and rolling resistance depending on the frequency range applied<sup>6</sup>. The wet grip can be determined by the behavior at the high frequencies involved in the friction mechanisms of the rubber on the road asperities whereas the rolling resistance is related with lower frequencies of tire-road contacts<sup>7,8</sup>. Because of accessible frequency limitations in standard laboratory equipment, the wet grip is associated to the dissipation at low temperature assuming a time-temperature superposition (high frequency corresponds to low temperature).

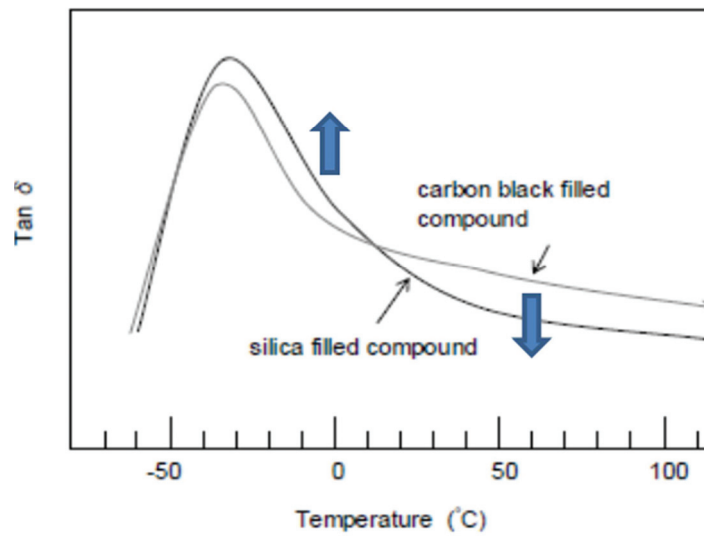


**Figure 3 : Loss factor as a function of temperature. The arrows indicate the direction to innovation: higher dissipation in the wet grip regime (0°C) and lower dissipation in the rolling resistance regime (60°C)<sup>9</sup>.**

The use of precipitated Silica especially in tire treads is now widely accepted as a key solution to better balance wet grip and rolling resistance. Figure 4 shows that precipitated Silica has enable some substantial improvement of rolling resistance and wet grip in the last two decades as compared to standard Carbon Black reinforcement.

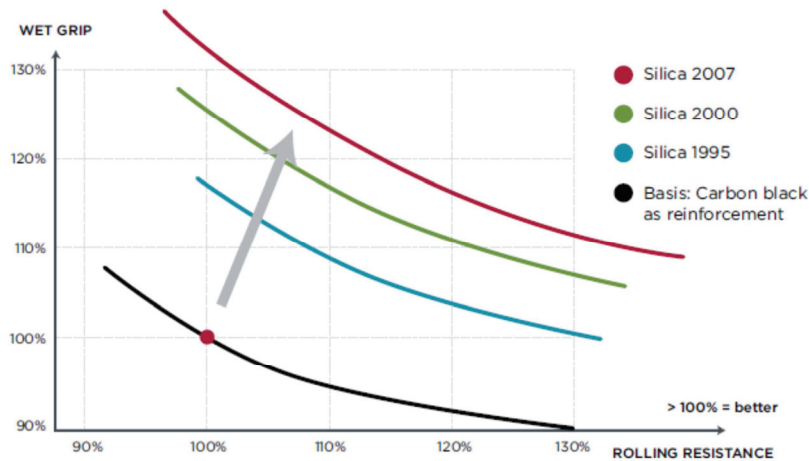


**Figure 4 : Improvement of Wet Grip and Rolling Resistance balance with the Silica technology as compared to Carbon Black<sup>2</sup>.**

### 1.3.b. Tire labeling

A first step towards tires efficiency improvement is the implementation of product ratings and labeling according to relevant and clear indicators. Japan for instance was the first country to adopt a tire labeling on a voluntary basis since 2010 and South Korea has done the same in 2011. It encourages costumers to select top efficient tires and manufacturers to propose improved products.

The introduction of standards for tires specifying minimum performance criteria is also effective in eliminating low performance tires from the market. Such a regulation has been put in place in the European Union in November 2012. This mandatory label concerns three classifications being rolling resistance, wet grip and noise. The conditions to obtain the lowest rating will progressively be more stringent in order to continuously promote tires efficiency.

Following the regulations in Europe, Japan and South Korea, similar labeling systems are expected in the USA, Brazil and China in the coming years.

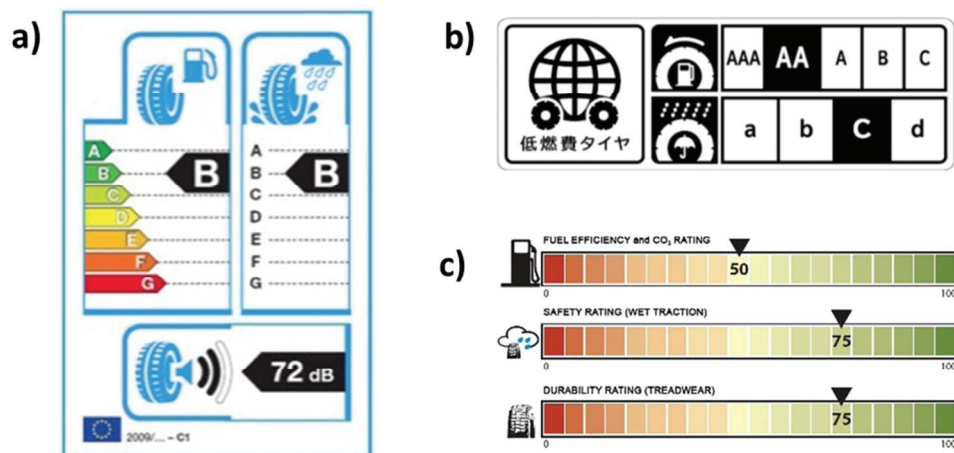


**Figure 5: Tire standards or labeling in a) the European Union, b) Japan and c) the United States<sup>10</sup>.**

The tire tread wear which should be taken into account in the American label can be considered as the third main issue tire manufacturers are trying to address. The reduction of tire wear is first motivated by health concerns since an important contribution to particles emissions by road traffic is due to the tire wear.

Moreover there is a need for improving durability of tires and therefore reduce tire tread wear. Following the continuous growth of the automotive market in Asia, the expanding demand for tires is expected to continue and may not be matched in the future. In the long run, the depletion of available land to cultivate rubber trees and the rising prices of synthetic rubber may lead to higher requirements in terms of durability of tires.

## I.4. Research project motivations

The successful replacement of Carbon Black by precipitated Silica in synthetic rubber was made possible by the advantageous balance of rolling resistance, wet grip and wear. Nevertheless as regards Natural Rubber matrix, the improvement of the properties compromise has not been clearly evidenced leading to a lower use of Silica in Natural Rubber based recipes. This is the case of truck and heavy vehicles tires that mainly use Natural Rubber blended with Butadiene Rubber as the polymer matrix.

The objectives for Rhodia as a silica manufacturer are to better understand the reinforcement mechanisms involved with Silica and come up with innovating solutions for its customers. Due to the limited use of Silica in truck tires, this application represents a key target for the precipitated silica manufactured by Rhodia.

This PhD fits in the frame of research works aiming at better understanding the physical origin of reinforcement of elastomers by nano-particles. The reinforcement in the low strain regime in particular is of importance for the balance of properties such as the wet grip and the rolling resistance.

The tear properties of reinforced rubber and the strain-induced crystallization phenomenon are also addressed since they may ultimately be related with wear resistance (Figure 6).



**Figure 6: Relationship between resistance to tear propagation and tire tread wear.**

The key research issues approached in this work can be summarized in the two following points:

- Which reinforcement mechanisms are predominant in the low and large strain regimes?
- What is the role played by Strain-Induced Crystallization on ultimate properties and tear propagation resistance in natural rubber?

---

---

## II. Literature survey: Structure and Properties of reinforced rubber materials

II.1. Microstructure and physical properties .....	23
II.1.a. Polymers and Elastomers .....	23
II.1.a.i. Polymeric materials .....	23
II.1.a.ii. Elastomers .....	23
II.1.b. Crosslinking of rubbers: vulcanization .....	24
II.1.c. Theory of Rubber elasticity .....	26
II.1.c.i. An isolated chain .....	26
II.1.c.ii. Elasticity of a rubber network .....	28
II.1.c.iii. Affine and Phantom molecular models .....	29
II.1.c.iv. Mooney-Rivlin model.....	31
II.1.c.i. Other models.....	32
II.1.d. Rubber network characterization by equilibrium swelling.....	33
II.2. Reinforcement by nanometric fillers.....	34
II.2.a. Small Strain regime.....	34
II.2.a.i. Effect on the modulus in the linear regime.....	34
II.2.a.ii. Nonlinear behaviour at small strains: Payne Effect.....	37
II.2.b. Large Strain regime.....	46
II.2.b.i. Stress softening at large deformations: Mullins Effect .....	46
II.2.b.ii. Reinforcement in the large strain regime .....	49
II.2.b.iii. Swelling restriction due to the interface .....	50
II.3. Strain-induced Crystallization.....	51
II.3.a. Effect of crosslink density on a traction-retraction cycle .....	52
II.3.b. Effect of fillers on SIC:.....	55
II.3.c. Effect of temperature on SIC: .....	57
II.3.d. Strain-induced crystallization at crack tip.....	58
II.4. Resistance to crack propagation in Rubbers .....	60
II.4.a. Energy release rate and Tear energy .....	60
II.4.b. Crack propagation instabilities .....	63

II.4.b.i. Tear bifurcations originate from anisotropy .....	64
II.4.b.ii. Energetic explanation for the improvement of crack resistance in the presence of rotations .....	66
II.4.c. Effect of material variables on crack propagation .....	67
II.5. Conclusion.....	67

## II.1. Microstructure and physical properties

### II.1.a. Polymers and Elastomers

#### II.1.a.i. Polymeric materials

Polymers consist of long macromolecular chains made of the repetition of elementary chemical structures called repeat units. Macromolecular chains are obtained by iterating chemical reactions (polymerization) starting from one or several monomer(s). Chains are entangled together and may form a tridimensional network either during polymerization or by addition of crosslinks.

The properties of the repeat unit and the polymerization scheme drive the structure and properties of the obtained polymers. The stereoregularity of the polymer chains also has an influence on the crystallization properties (see II.3).

The polymer has a rubber-like behavior above the glass transition temperature ( $T_g$ ). Upon cooling, the dynamics of the polymer chains is strongly slowed down. Below  $T_g$  the rubber is in a rigid, out-of-equilibrium and disordered state. As regards mechanical experiments, the concept of glass transition is associated with the principal relaxation temperature  $T_\alpha$ : the relaxation time of the polymer chains become larger than the observation time. In consequence, the modulus increases typically by 3 orders of magnitude as temperature decreases below  $T_g$ . The measured value of  $T_\alpha$  depends on the applied sollicitation frequency. Nevertheless the terms  $T_g$  (glass transition) and  $T_\alpha$  (principal relaxation) will indifferently be used in the following sections.

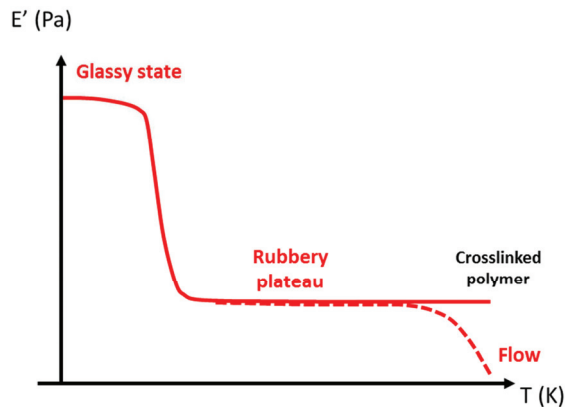


**Figure 7: Typical variation of the storage modulus versus Temperature for a polymer. At high temperature only crosslinked polymers present a permanent rubbery plateau whereas entangled linear polymers ultimately flow.**

#### II.1.a.ii. Elastomers

Elastomers are defined by their ability to sustain very high deformations (typically of several hundred percent) and recover their initial form almost completely. This definition involves two main criteria that distinguish elastomers:

- First, polymer chains have to be flexible in order to undergo very large deformation without failing. This means both a high statistical flexibility, related to a large number of accessible conformations, and a high dynamic flexibility, with the conformation changes being fast and involving low energy barriers. Thus the glass transition has to be low, usually several tenths of degrees below 0°C.
- The second condition is related to the recovery of the initial dimensions after a very large extension. The creation of a three dimensional network of polymer chains is necessary to achieve such an elastic recovery. This involves that polymer chains bear reactive functional groups for the creation of the network. In many cases this role is played by double bonds along the chain, and for this reason most elastomers are made on unsaturated polymer chains. In the case of copolymers, some unsaturated units are added in small quantity to perform the crosslinking. This is in particular the case of EPDM rubber.

A typical stress-strain elongation and recovery curve is presented in Figure 8, showing the high strains that can be reached (typically several hundred percent). The stress-strain curve also shows some characteristic features such as a stress softening for strains lower than 100% and then a stress hardening above 250%.

The recovery curve is never strictly superposed to the traction curve since elastomers are never purely elastic materials. Nevertheless, in the case of unfilled rubber, the hysteresis is quite low and stems from the friction of the chains during elongation: some energy is then dissipated in heat build-up. Similarly the strain at zero stress after a traction-recovery cycle is not strictly zero due to slippage and disentanglements of chains but the plastic set may sometimes be recovered completely or partially by waiting a long time or heating the material.

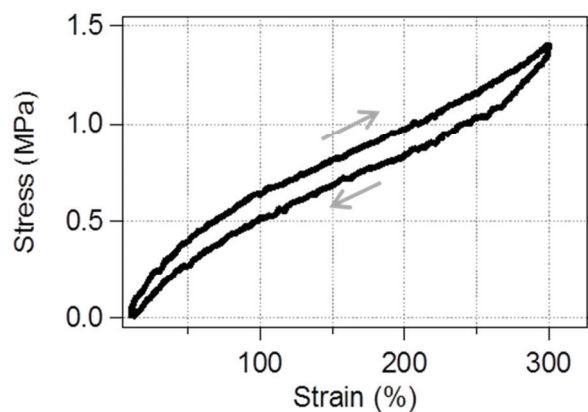


**Figure 8: Typical Stress-strain mechanical cycle (traction and recovery) for a vulcanized Natural Rubber sample.**

### *II.1.b. Crosslinking of rubbers: vulcanization*

The formation of a three dimensional network or vulcanization is an essential step of the rubber processing since many of the vulcanized rubber properties depend on the density of crosslinks.

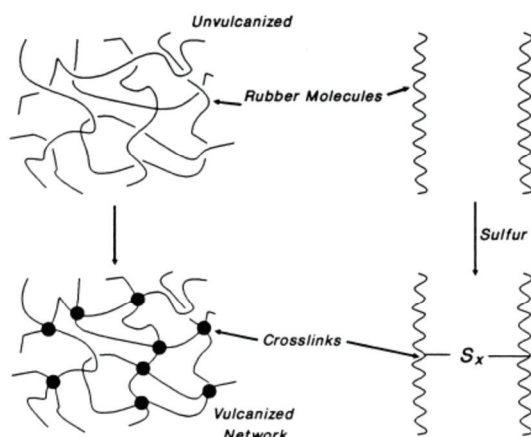


**Figure 9: Vulcanization of rubber chains by creation of sulfur bridges between the chains<sup>11</sup>.**

The models used to describe the behavior of the rubber network generally consider perfect networks. Nevertheless real rubber networks are quite heterogeneous by nature, firstly due to the heterogeneity of chain length between crosslinks and secondly due to some elastically inactive rubber chains such as loops, dangling chain ends and sol chains that are not linked to the chains of the network.

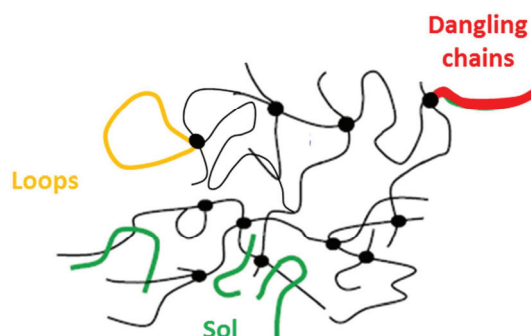


**Figure 10: Structure of the rubber network with dangling chains ends, loops and sol chains according to Saalwächter<sup>12</sup>.**

The structure of the network strongly depends on the type of crosslinking agent. Sulfur and peroxide are the most widely used molecules for the formation of bridges between rubber chains. It has been demonstrated by DQ low field proton NMR that the peroxide vulcanization of Natural Rubber is less homogeneous and that some highly reticulated and/or entangled clusters are formed (see Figure 11).

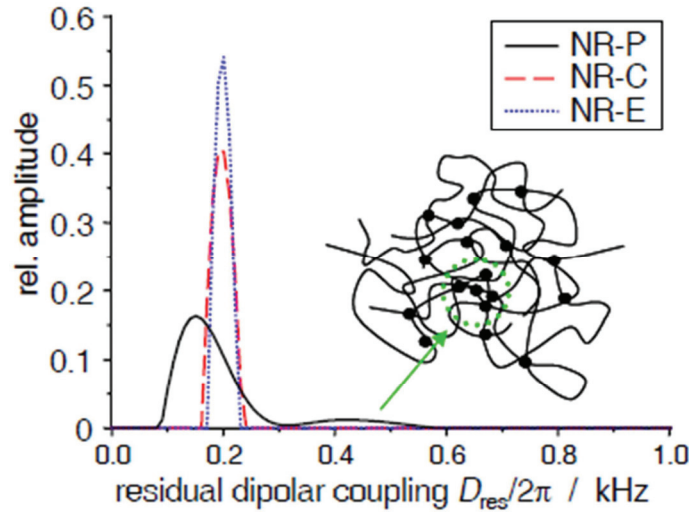


**Figure 11: Distribution of residual dipolar couplings directly related to chain length between crosslinks showing the heterogeneity of Natural Rubber networks crosslinked with Sulfur Conventional (C), Sulfur Efficient (E) and Peroxide (P) vulcanization packages. Reproduced from Saalwächter<sup>12</sup>.**

The effect of the initial chains length on the network characteristics has been investigated by Klüppel et al<sup>13</sup>. According to these authors, the fraction of entangled chains decreases and the fraction of dangling chains increases with shorter natural rubber chains.

### II.1.c. Theory of Rubber elasticity

The theory of rubber elasticity is briefly presented here as well as the models used to describe the network behavior under strain. It has to be reminded that these approaches are based on assumptions of perfect networks but they already yield fairly good descriptions of the thermal and mechanical behavior of elastomers.

#### II.1.c.i. An isolated chain

A polymer chain made of  $n$  monomer of average lengths  $l$  is described by its end to end vector  $\vec{R}$  being the sum of  $n$  vectors  $\vec{r}_i$ . For a long isotropic chain, the monomers do not have any preferential orientation and thus the average value of the end to end vector is zero ( $\langle \vec{R} \rangle = 0$ ). In order to easily describe the statistics of a chain without taking into account the correlation between neighboring monomers, an equivalent chain is considered: the Kuhn chain. Instead of looking at the monomers orientation, the chain is divided in  $N$  segments of length  $b$  defined such as the orientation of a segment is independent from the previous segment orientation (persistence length).

The root mean square of the end to end vector is proportional to the number of segments

$$\langle R^2 \rangle = nl^2 = Nb^2 \quad (1)$$

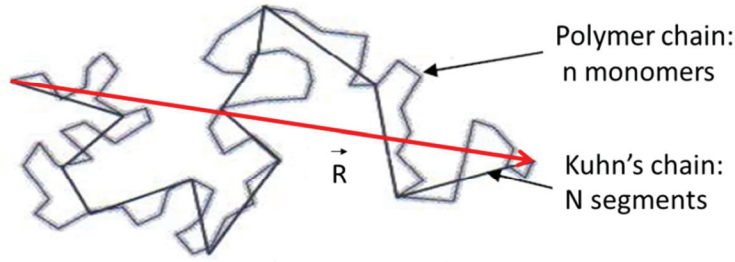


**Figure 12: Representation of an isolated polymer chain of end to end vector  $\vec{R}$  described by  $N$  Kuhn segments of length  $b$ . Scheme adapted from Halary et al<sup>14</sup>.**

Upon stretching the maximum chain length that can be reached is equal to  $Nb$  (all segments parallels to the stretching direction). The limited chains extensibility  $\xi$  can thus be defined as the ratio of the maximum chain length versus the quiescent average chain dimension:

$$\xi = \frac{Nb}{\sqrt{Nb^2}} = \sqrt{N} \quad (2)$$

Due to the thermal fluctuations, the chain may adopt a large number of conformations. The probability  $P(\vec{R})$  for the chain to adopt a conformation of end to end vector  $\vec{R}$  is given by a Gaussian law in the three dimensions:

$$P_N(\vec{R}) = \left(\frac{3}{2\pi Nb^2}\right)^{\frac{3}{2}} \exp\left(-\frac{3\vec{R}^2}{2Nb^2}\right) \quad (3)$$

With the distribution normalized to 1 such as  $\int P_N(\vec{R}) d^3R = 1$   
The entropy  $S$  of the chain can be written as:

$$S_N(\vec{R}) = k \ln \Omega_N(\vec{R}) \quad (4)$$

with  $\Omega_N(\vec{R})$  the number of accessible configurations corresponding to an end to end vector  $\vec{R}$ , which is proportional to the probability  $P(\vec{R})$ .

$$S_N(\vec{R}) = S(0) - \frac{3k\vec{R}^2}{2Nb^2} \quad (5)$$

The free energy of the system  $F$  contains internal energy  $U$  and the entropy  $S$ :

$$F_N(\vec{R}) = U_N(\vec{R}) - TS_N(\vec{R}) \quad (6)$$

The internal energy is zero since we consider that no interactions take place between the chains segments:

$$F_N(\vec{R}) = -TS_N(\vec{R}) = \frac{3kT\vec{R}^2}{2Nb^2} + F(0) \quad (7)$$

The retraction force necessary to maintain an end to end distance  $\langle \vec{R}^2 \rangle$  is directly obtained as the first derivative of the free energy:

$$\vec{f} = \left( \frac{\partial F}{\partial L} \right)_{T,V} = \frac{3kT}{Nb^2} \vec{R} \quad (8)$$

The elasticity thus has an entropic origin related to the Gaussian distribution of conformations. When a chain is extended close to its limited chain extensibility, the statistics of chain conformation are no longer Gaussian. An expression of the retraction force was proposed in this case<sup>15</sup>:

$$\vec{f} = \frac{kT}{N} \mathcal{L}^{-1} \left( \frac{r}{Nb} \right) \quad (9)$$

Where  $y = \mathcal{L}^{-1}(x)$  is the inverse Langevin function defined by  $x = \mathcal{L}(y) = \coth y - 1/y$ . This expression is a generalization of equation (8), which is recovered at low extension.

### II.1.c.ii. Elasticity of a rubber network

We consider an incompressible crosslinked rubber network and the following assumptions are made (perfect network):

- The parts of chains between two crosslinks can be described by Kuhn segments and their statistics is identical to the statistics of an isolated polymer chain.
- The knot of the network i.e. crosslinks do not interfere with the chains conformations and root mean square distance.

The force to apply to deform this network can be expressed as a combination of an energetic term and an entropic term:

$$f = \left( \frac{\partial F}{\partial L} \right)_{T,V} = \left( \frac{\partial U}{\partial L} \right)_{T,V} - T \left( \frac{\partial S}{\partial L} \right)_{T,V} = f_E + f_S \quad (10)$$

In the case of crystalline solids, the energetic contribution is dominant and increases as the strain increases due to the increase of inter-atomic distances. Nevertheless in the case of a rubber material, the energetic contribution is small and considered zero in perfect networks (no interactions of neighbouring chains). The elasticity is thus said to be of entropic nature in vulcanized rubbers and as a consequence the modulus increases with temperature conversely to other classes of materials.

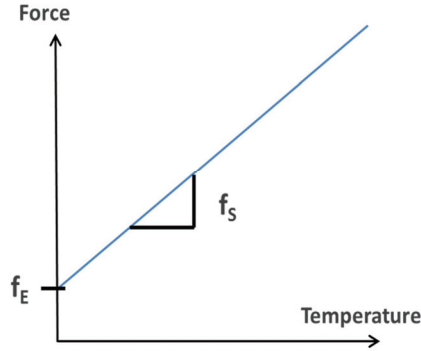


**Figure 13: Increase of the Force with Temperature due to the entropic contribution to the modulus. The energetic contribution  $f_E$  is considered very small in comparison to  $f_S$ .**

### II.1.c.iii. Affine and Phantom molecular models

Different molecular models have been proposed in the literature to describe the elasticity of crosslinked rubber networks<sup>16-22</sup>. We briefly present the principal ones that are the affine and phantom models since the others can be considered as sophistications of this basic models.

In the affine model proposed by Kuhn<sup>16</sup> and Flory<sup>17</sup> the deformation of the end to end vector distribution is the same as the macroscopic deformation (Figure 14).

The entropy variation in a uniaxial elongation (elongation ratio  $\lambda$  and (constant) volume of the sample normalized to 1) is:

$$\Delta S_{net}^{uniaxial} = -\frac{N_{ch}k}{2} \left( \lambda^2 + \frac{2}{\lambda} - 3 \right) \quad (11)$$

$N_{ch}$  is the number of chains per unit volume. If we neglect the enthalpic contribution, the nominal stress  $\sigma_N$  (force divided by the initial section  $s_0$  of sample perpendicular to the stretching direction) is

$$\sigma_N = \frac{d\Delta F_{net}}{d\lambda} = N_{ch}kT \left( \lambda - \frac{1}{\lambda^2} \right) \quad (12)$$

And the true stress is:

$$\sigma_T = N_{ch}kT \left( \lambda^2 - \frac{1}{\lambda} \right) \quad (13)$$

The term  $N_{ch}kT$  corresponds to the shear modulus  $G$  and can also be expressed with the molar mass between crosslinks  $M_C$  and the rubber density  $\rho$  by the relation:

$$G = N_{ch}kT = \frac{N_A \rho kT}{M_C} = \frac{\rho RT}{M_C} \quad (14)$$

$N_A$  the Avogadro's constant and  $R$  the ideal gas constant.

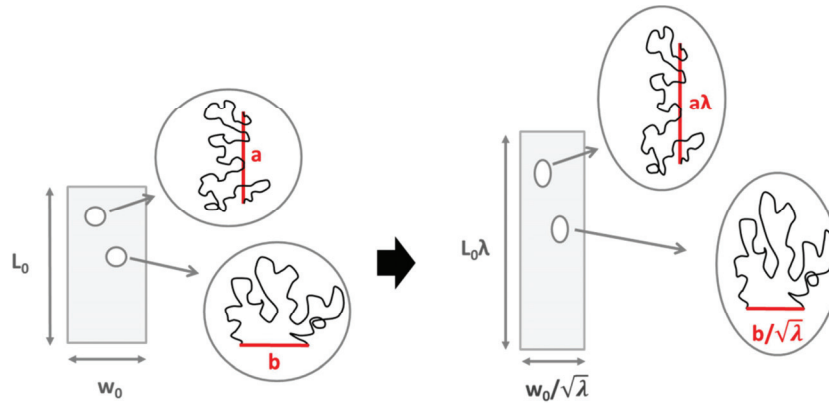


**Figure 14: Schematic representation of the affine model: unstretched state (left) and stretched state (right). The deformation of the rubber chains is identical to the applied strain on the sample.**

The phantom model introduced by James and Guth<sup>18</sup> takes into account the fact that crosslinks can fluctuate around average positions in space. Only the crosslinks located on the edge of the sample are fixed (see Figure 15).

The expression of the true stress is modified as:

$$\sigma_T = \frac{\rho RT}{M_C} \left(1 - \frac{2}{f_c}\right) \left(\lambda^2 - \frac{1}{\lambda}\right) \quad (15)$$

Where  $f_c$  is the functionality of crosslinks. Note that the higher the crosslink functionality, the lower the fluctuations. For a very large functionality, the factor  $(1-2/f_c)$  would tend to 1, crosslinks would be fixed and the affine model is recovered.

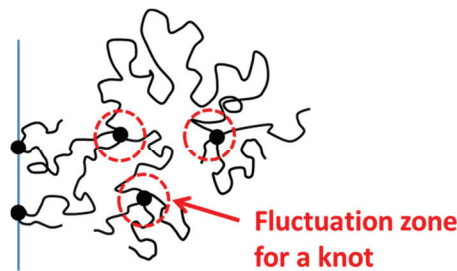


**Figure 15: Fluctuation zone for internal crosslinks in the phantom model. The knots located on the edge of the sample (straight line) cannot fluctuate.**

Both affine and phantom molecular models give a fairly good picture of the rubber elasticity. Nevertheless the comparison with experiments shows that the real behavior is somehow in between those two limits and several models were developed to account for the observed discrepancies between experiments and theory.

II.1.c.iv. Mooney-Rivlin model

The semi-empirical model developed by Mooney and Rivlin<sup>23</sup> is based on the relationship between the free energy (per unit volume) and strain invariants  $I_1$ ,  $I_2$ , and  $I_3$  defined from the right Cauchy-Green tensor:

$$\mathbf{F} = \mathbf{C}_0 + \mathbf{C}_1(I_1 - 3) + \mathbf{C}_2(I_2 - 3) + \mathbf{C}_3(I_3 - 1) \quad (16)$$

Assuming an incompressible network submitted to uniaxial extension, the stress invariants are easily computed as a function of  $\lambda$  and :

$$I_1 = \lambda_x^2 + \lambda_y^2 + \lambda_z^2 = \lambda^2 + \frac{2}{\lambda} \quad (17)$$

$$I_2 = \lambda_x^2 \lambda_y^2 + \lambda_y^2 \lambda_z^2 + \lambda_z^2 \lambda_x^2 = 2\lambda + \frac{1}{\lambda^2} \quad (18)$$

$$I_3 = \lambda_x^2 \lambda_y^2 \lambda_z^2 = 1 \quad (19)$$

The third invariant is the volume, which is supposed to remain constant. The true stress can be obtained from the free energy derivative with displacement:

$$\sigma_T = 2 \left( \mathbf{C}_1 + \frac{\mathbf{C}_2}{\lambda} \right) \left( \lambda^2 - \frac{1}{\lambda} \right) \quad (20)$$

This expression decomposes the modulus into a linear contribution  $C_1$  and a term  $C_2$  that accounts for the modulus decrease at small deformations. The physical meaning of this correction is still not clearly understood. Some authors<sup>24</sup> relate it to the effect of entanglements, as the ratio  $C_2/C_1$  decreases with increasing crosslink density and tends to zero for an almost non-entangled swollen sample.

It is of interest to represent the reduced stress ( $\sigma_R = \sigma_T / (\lambda^2 - 1/\lambda)$ ) as a function of the inverse of the elongation ratio (Figure 16) in order to highlight the differences of the above presented models. In the affine and phantom predictions a linear behavior is expected: the modulus  $G$  does not depend on the elongation ratio whereas the Mooney-Rivlin equation introduces a dependency on the elongation ratio that fits well the experimental data at low deformation in traction ( $1/\lambda < 1$ ). In the case of high extensions, the limited chain extensibility increases the reduced stress.

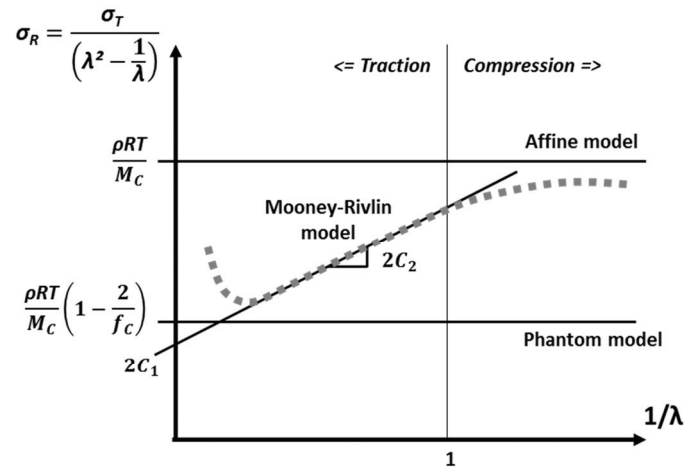


**Figure 16: Comparison of the experimental data trend represented by the dashed line with the Affine, Phantom and Mooney-Rivlin models predictions (after Erman et al<sup>25</sup> and Halary et al<sup>14</sup>)**

II.1.c.v. Other models

A number of more refined molecular models of rubber elasticity have been proposed, in particular to take into account the effect of topological interactions between network chains. In the constrained-junction model<sup>21</sup> an additional potential acting on the crosslinks is introduced. A more realistic picture is provided by the diffused-constraint<sup>26</sup> and tube<sup>19</sup> models that consider the effect of topological constraints affecting the fluctuations of all the chain segments and not only the crosslinks. The tube model describes the motion of the chains within the surrounding chains represented by a virtual constraining tube and provides some physical origin to the C2 term in the Mooney-Rivlin equation considering that topological constraints such as entanglements induce non-isotropic movements of crosslinks and chain segments.

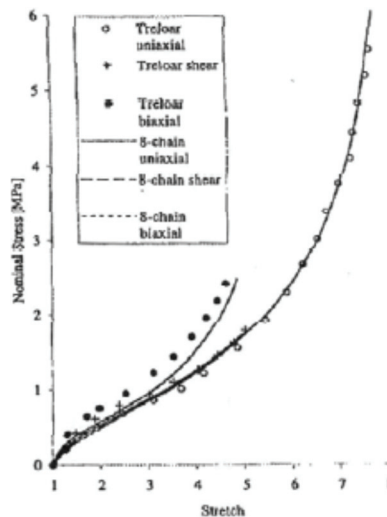


**Figure 17: Comparison of experimental data and fits by the Boyce-Arruda 8 chains model<sup>27</sup>.**

One should also mention the constitutive models that described the hyperelastic behavior (stress hardening at high deformations). These models are based on the description of a representative volume containing 3, 4 or 8 chains such as the Boyce-Arruda<sup>27</sup> model that fits very well the stress hardening (Figure 17).

#### II.1.d. Rubber network characterization by equilibrium swelling

Swelling experiments are widely used to characterize the network density of elastomers. The thermodynamics of the equilibrium swollen rubber systems may be described by The Flory-Rehner theory<sup>28</sup>. The first assumption is that elastic and mixing components of the free energy are separable and additive. The partial derivative of the free energy as respect to the number of moles yields to the equation in terms of chemical potential (21).

$$\frac{\Delta\mu_S^{total}}{RT} = \frac{\Delta\mu_S^{mixing}}{RT} + \frac{\Delta\mu_S^{elastic}}{RT} \quad (21)$$

In the equilibrium state, the total chemical potential is zero meaning that all the mixing free energy is balanced by the elastic energy stored by the extended network chains. The determination of the network density is based on this equality between the elastic term and the free energy of mixing which can be accessed through the rubber fraction in equilibrium with the solvent in the swollen state. The Flory-Huggins expression is used for this purpose: assuming an infinite molar volume for rubber macromolecules, it relates the rubber fraction and the solvent-polymer interaction parameter  $\chi$  to the free energy of mixing.

$$\frac{\Delta\mu_S^{mixing}}{RT} = \ln(1 - \phi_r) + \phi_r + \chi\phi_r^2 \quad (22)$$

The free energy associated to the elasticity of the chains can be related to the average molar mass of a chain segment between two crosslinks thanks to the theory of rubber elasticity<sup>20</sup>. The affine and phantom models of network deformation are mainly used to describe the behaviour of crosslinked rubbers. Using the affine model, we obtain the relationship between the rubber fraction  $\phi_r$ , the parameter  $\chi$ , the rubber density  $\rho_r$ , the volume of solvent in the sample  $V_S$ , the crosslinks functionality  $f$  and the molecular weight between crosslinks  $M_C$ .

$$\ln(1 - \phi_r) + \phi_r + \chi\phi_r^2 = -\frac{\rho_r}{M_C} V_S \left( \phi_r^{\frac{1}{3}} - \frac{2\phi_r}{f} \right) \quad (23)$$

The relationship in the case of the phantom model is the following one:

$$\ln(1 - \phi_r) + \phi_r + \chi\phi_r^2 = -\frac{\rho_r}{M_C} V_S \left( 1 - \frac{2}{f} \right) \phi_r^{\frac{1}{3}} \quad (24)$$

## II.2. Reinforcement by nanometric fillers

The concept of reinforcement of polymers describes the improvement of one or several mechanical properties by the addition of organic or inorganic fillers. In the present case of elastomers, the reinforcement is characterized by a simultaneous increase of the modulus and the ultimate properties, namely the energy at break (the stress at break increases and sometimes the strain at break as well). This simultaneous increase is a fundamental yet poorly understood feature of reinforced rubbers. This phenomenon is at the origin of the unique properties of reinforced elastomers and their wide use in very diversified areas of the industry. Being still not fully understood, it has also given rise to a large amount of research since the first use of reinforced natural rubber in the first part of the 20<sup>th</sup> century.

In all the manuscript, the term reinforcement is used to qualify an increase of the modulus whatever the strain range considered. The enhancement of the ultimate properties by fillers is not referred as reinforcement but rather as increased strength or increased resistance.

In the following sections, the influence of fillers on the mechanical properties is reviewed for the different strain regimes (small strains first, then large strains) as well as the models of microstructure modifications proposed in the literature.

### *II.2.a. Small Strain regime*

Although we present separately the reinforcement in the linear regime (modulus increase at very low strains compared to the pure matrix) and the Payne effect, it is important to understand that the latter is the direct consequence of the reinforcement. For the sake of clarity, the models developed to describe both properties will be detailed in the part dedicated to the Payne effect so that all the aspects of the reinforcement at small strains have been introduced first.

#### II.2.a.i. Effect on the modulus in the linear regime

The linear regime considered here is the strain range for which the modulus does not depend on strain. For unfilled rubbers we have seen that according to rubber elasticity theory this is true for quite large extension ratios but for reinforced rubbers due to non-linear effects, the modulus drops at low extension ratios and the linear regime is typically restricted to strains lower than 0.1%.

The storage modulus is increased by the addition of fillers in both the glassy and rubbery states as shown in Figure 18. Nevertheless the reinforcement is higher in the rubbery regime which is the one of interest for rubber materials applications. Several models have been proposed to account for this strengthening effect of nanosized fillers as well as the strain-induced softening called the Payne effect (see II.2.a.ii).

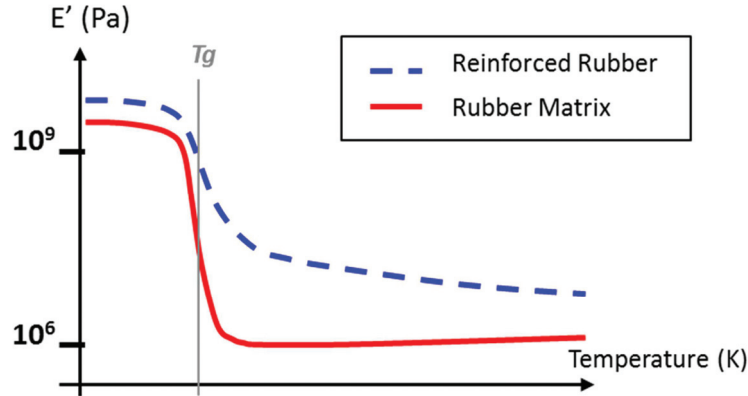


**Figure 18: Reinforcement effect on the storage modulus as a function of temperature.**

Based on the equation proposed by Einstein for the viscosity of a colloidal suspension of rigid spheres, Smallwood<sup>29</sup> proposed the following relationship (25) for the modulus of a reinforced elastomer  $E_R$  with a filler volume fraction  $\phi$  ( $E_0$  being the modulus of the unfilled matrix):

$$E_R = E_0(1 + 2.5\phi) \quad (25)$$

In the case of significant fractions of particles, filler-filler interactions are taken into account by the prediction of Guth and Gold<sup>30</sup> (26):

$$E_R = E_0(1 + 2.5\phi + 14.1\phi^2) \quad (26)$$

Guth has refined the equation for non-spherical objects by adding a form factor  $f$  equal to the ratio of an envelope ellipse major axis diameter over the minor axis diameter (27):

$$E_R = E_0(1 + 0.67f\phi + 1.62f^2\phi^2) \quad (27)$$

Finally in the case of highly structured fillers like Carbon black, Medalia<sup>31</sup> has proposed to express the modulus as a function of an effective volume fraction of fillers including the fraction of polymer that is trapped in the tortuosity of the fillers (28). Given the complex morphology of reinforcing aggregates and their distribution in space, some polymer chains do not participate in the deformation of the polymer network and can be considered as part of the hard reinforcing phase. This occluded rubber fraction may be located inside one aggregate (intra-aggregate Figure 19a) or between two adjacent aggregates (inter-aggregates Figure 19b)

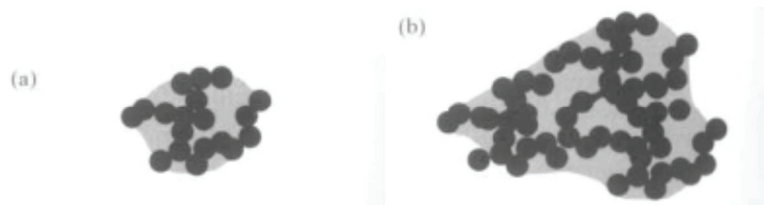


**Figure 19: Representation of a) intra and b) inter aggregates occluded rubber.**

An estimation of the effective volume fraction of fillers is given by oil adsorption measurements using the DBP (Dibutylphthalate) molecule.

$$E_R = E_0(1 + 2.5\phi_{eff} + 14.1\phi_{eff}^2) \quad (28)$$

$$\phi_{eff} = \frac{\phi}{2} * \left(1 + \frac{1 + 0.02139 * DBP}{1.46}\right) \quad (29)$$

The main drawback of this geometrical model is that it does not explain the decrease of the storage modulus over a wide temperature range, which is qualitatively different from the behavior of the pure matrix, (Figure 18), nor does it explain the very high value of the reinforcement (ratio of the modulus of the reinforced material to that of the matrix) in highly filled rubbers. As shown in Figure 20 this ratio can reach about 50 or more around  $T_g + 20$  typically.

For this reasons, other physical origins of the reinforcement at very low strains were proposed by several authors. This question was in most cases addressed simultaneously with the non-linearity of the modulus thus more details on the reinforcement mechanisms shall be found in the next paragraph which deals with the so-called Payne effect.

Nevertheless, to put it shortly we can mention three further steps that were taken towards a better understanding of the reinforcement at small strains. Firstly the reinforcement was described as the consequence of an over-reticulation of the system brought by the fillers acting as giant crosslinks<sup>32</sup>. Then it was proposed that both the approaches of the filler network and the filler-polymer interactions could be unified in a filler-polymer-filler network where rubber chains anchored at the fillers surface could transfer high stresses and participate in the percolating network<sup>33,34</sup>. Finally recent experimental and simulation results have supported the theory that fillers are surrounded by a layer of polymer chains remaining in the glassy state<sup>35</sup>. The percolating domains of reduced mobility form glassy bridges between fillers that account for the stiffening whereas the temperature increase results in thinner glassy layers explaining the observed decrease with temperature (Figure 20).

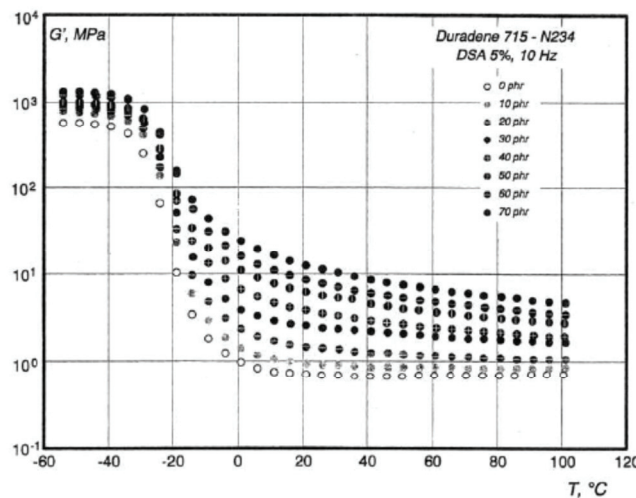


**Figure 20: Storage modulus as a function of temperature for several filler fraction of Carbon Black in rubber. Reproduced from Wang<sup>9</sup>.**

II.2.a.ii. Nonlinear behaviour at small strains: Payne Effect

For deformations ranging from 0.1 to 100%, filled elastomers exhibit a drop of the elastic modulus, this non-linear behavior is named after Payne who first proposed a general equation for describing it<sup>36</sup>. He explained the storage modulus decrease and loss modulus peak by the rupture and reformation of a filler network interconnecting the aggregates and bearing the load at low deformations.

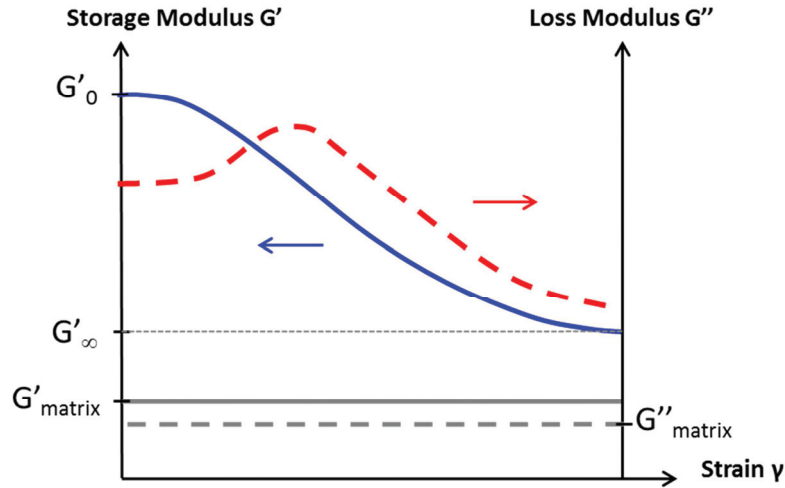


**Figure 21: Evolution of Storage modulus (continuous curves) and Loss modulus (dashed curves) during strain sweeps for a filled elastomer (coloured) and the pure matrix (grey).**

- **Filler-filler models**

Kraus<sup>37</sup> proposed a similar model adding Van der Waals retraction forces between carbon black aggregates and relating the decreasing number of direct contacts between fillers to the storage modulus evolution with strain. This author also introduced a critical strain for the beginning of the filler network breakdown  $\gamma_c$  that was used to fit the evolution of the modulus with the strain  $\gamma$ :

$$G'(\gamma) = G'_\infty + \frac{G'_0 - G'_\infty}{1 + \left(\frac{\gamma}{\gamma_c}\right)^{2m}} \quad (30)$$

$$G''(\gamma) = \frac{(G'_0 - G'_\infty) \left(\frac{\gamma}{\gamma_c}\right)^{2m}}{1 + \left(\frac{\gamma}{\gamma_c}\right)^{2m}} \quad (31)$$

The critical strain  $\gamma_c$  is related to the kinetics of filler agglomeration and breakdown and depends on the polymer type,  $m$  is the fitting parameter of the model.

Experimental evidences of a percolation threshold at a critical filler content were given by electrical conductivity measurements<sup>38,39</sup> and seemingly support the assumption of a filler network but Payne effect was also reported in system where the fillers do not percolate<sup>40</sup>.

Based on the occluded volume concept by Medalia<sup>31</sup>, Wang added to the filler network a contribution from the liberation of shielded rubber with strain, decreasing the effective fraction of fillers<sup>9</sup>. For Luginsland<sup>41</sup> however, an important part of the occluded polymer remains shielded from the strain due to high chemical bonding to the silica surface even when the filler network breaks. This immobilized part is referred as the in-rubber structure.

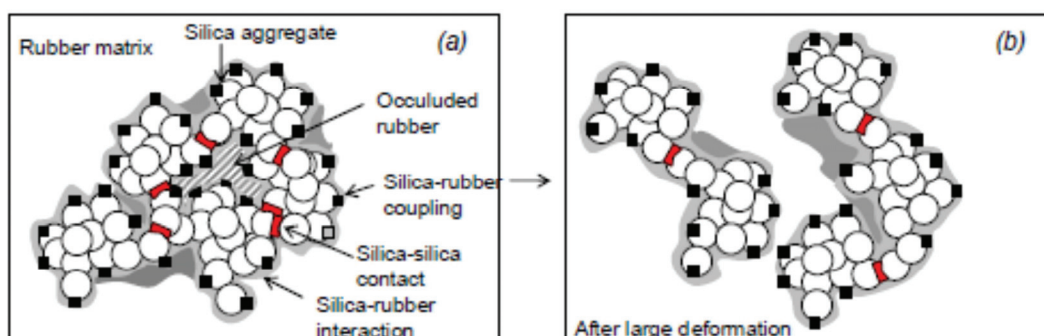


Figure 22: Filler-filler network and in-rubber structure as described by Luginsland<sup>41</sup>.

- *Filler-polymer models*

As a weakness of the filler-filler network theory is to neglect the influence of the polymer, it was proposed that the interface of fillers and rubber is playing a key role in the reinforcement and the strain softening. This effect of filler-polymer interactions is considered by Wagner<sup>42</sup> who points out the role of entanglements between the free rubber chains in the matrix and the rubber bound to the filler surface. O'Brien and coworkers<sup>43</sup> also distinguish two rubber phases and mention a glassy rubber shell covering the carbon black particles and therefore increasing the modulus. Funt<sup>40</sup> suggests that the reinforcement is due to filler-polymer interactions that reduce the mobility of the bound rubber. Entanglements of the bound rubber with the free rubber of the matrix create additional network points. The decrease of the storage modulus is viewed as the disentanglement of the two rubber phases.

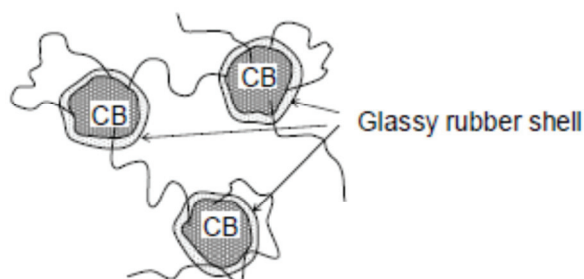
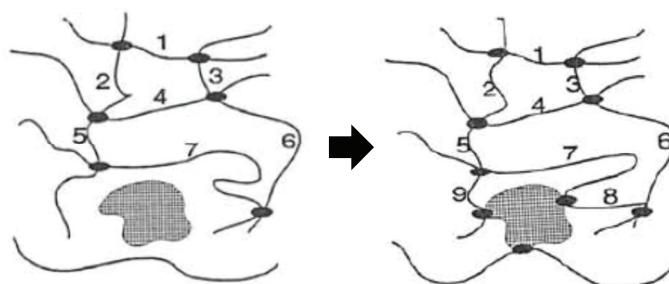


Figure 23: Polymer shell surrounding Carbon Black particles according to O'Brien<sup>43</sup>.

The lack of interpretation for the modulus decrease with temperature in the filler network theory led Maier and Göritz<sup>32</sup> to elaborate a predictive description relying on the adsorption and desorption of rubber chains at the interface. The fillers are thus pictured as giant multifunctional crosslinks with both stable and unstable links to the polymer. The reinforcement effect is understood as the crosslink density increase and the decay with temperature is explained by thermally activated desorption of chains. This model is also effective when it comes to explain the loss modulus increase with strain.



**Figure 24: Scheme representing the crosslinking effect of an active filler according to Maier and Göritz<sup>32</sup>.**

The difficulties in establishing a coherent model also arose from the seemingly different behavior of silica and carbon black particles. As a matter of fact, several authors suggested that the filler networking effect was predominantly explaining the behavior of silica filled compounds whereas adsorption of the polymer was prevailing in the case of carbon black<sup>44,45</sup>. Wolff and Wang<sup>46,47</sup> took a step further by proposing a joint network of carbon black and immobilized shell of polymer at the interface. This model was therefore combining a fraction of immobilized polymer to the filler network in the case of a strongly active interface while the filler network was considered sufficient to explain silica filled rubbers properties.

The non-linearity of the modulus has also been attributed to a decrease of entanglements with strain. Firstly it has been considered that the dissipation is the consequence of the disentanglements of the free rubber chains from the bound rubber chains and chains slippage at the surface<sup>48</sup>. Sternstein<sup>49</sup> suggests that the reinforcement in the linear regime is due to a higher entanglement density of the chains near the surface depending on the interactions between the surface and the polymer.

In order to reconcile the two different visions of the Payne effect based on filler networking and filler-polymer interactions, it was suggested that the non-linear behavior was a combination thereof: the formation of a strong network involving the reinforcing particles and a fraction of polymer strongly adsorbed on the filler surface. According to Leblanc<sup>50</sup>, a three-dimensional network consisting in fillers and a bound rubber layer of a few nanometers is obtained for high filler concentrations. The Bound Rubber represents the portion of the polymer that cannot be removed by immersion of the uncured compound in a good solvent. The chains are not necessarily chemically linked to the surface they can be physically adsorbed or entangled with other chains linked to the surface. Finally other works have based their interpretations on this so-called filler-polymer-filler network<sup>51,52</sup>.

$G'_0$  does not linearly depends on the total engaged surface of silica (Figure 25) showing the importance of the interconnecting network of fillers and strongly bound polymer<sup>53</sup>.

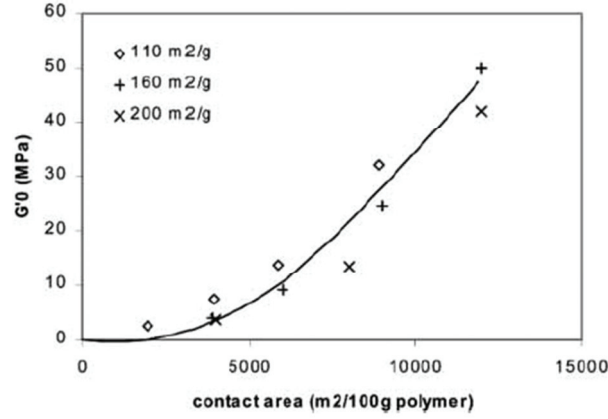


**Figure 25 : Effect of total contact area on the modulus in the linear regime for Silica filled SBR samples (reproduced from Guy et al.<sup>53</sup>).**

- ***Glassy layer percolation mechanisms:***

The latest development of importance in the understanding of the Payne effect has been brought by the works on the glass transition shifts in filled elastomers and the theory of glassy layers to account for the viscoelastic properties<sup>35,54,55</sup>.

Based on mechanical and NMR measurements Berriot and coworkers<sup>55,56</sup> have explained the mechanical behavior of filled elastomers by a long-range gradient of glass transition temperature of the polymer chains in the vicinity of the reinforcing particles. The glass transition temperature can thus be expressed as a function of the distance  $z$  from the filler surface:

$$T_g(z) = T_g^{bulk} \left( 1 + \left( \frac{\delta}{z} \right)^v \right) \quad (32)$$

The parameter  $v$  is close to 1 and  $\delta$  stands for an interaction parameter between the filler and the polymer: the higher this interaction, the larger the  $T_g$  shift at a fixed value of  $z$ . The thickness of the polymer layer in the glassy state is given by the following relationship:

$$e_g(T) = \delta \left( \frac{T_g^{bulk}}{T - T_g^{bulk}} \right) \quad (33)$$

The high reinforcement observed in reinforced elastomers with strong filler/matrix interactions or at low temperatures is understood in terms of percolation of the glassy layers. The stress is thus mainly borne by high modulus clusters made of fillers and glassy polymer (Figure 26). The model also predicts a significant increase of the modulus in the case where the glassy layers do not overlap.

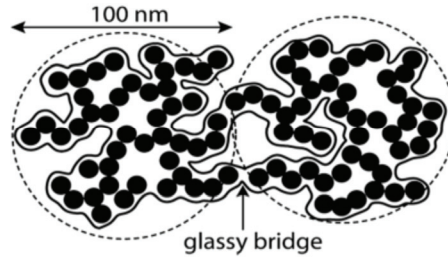


**Figure 26: Schematic representation of a glassy bridge connecting two aggregates of approximately 100nm of diameter.**

As regards the stress softening effect observed for increasing strain levels, the local stress lowers the local glass transition thus resulting in less glassy bridges. The dynamics of yield and rebirth of the glassy bridges was proposed to explain the Payne and Mullins effects<sup>35</sup>. A second term is added to equation (32) to take into account the yielding of the glassy bridges:

$$T_g(z) = T_g^{bulk} \left( 1 + \left( \frac{\delta}{z} \right)^v \right) - \frac{\sigma}{K} \quad (34)$$

Whether glassy layers subsist at temperatures far above  $T_g$  is under debate. In particular, the weak interactions present in some systems suggest that the glass transition shift is not sufficient to account for the high reinforcement at temperatures several tenths of degrees above the  $T_g$ . Gusev<sup>57</sup> has proposed a mechanical modeling based on glassy polymer strands connecting particles, thus only involving a low fraction of glassy polymer compared to higher critical fraction required to overlap glassy layers. This is of particular relevance when dealing with fractal aggregates having very short closest distances between fillers.

It can also be proposed that the dynamics being very heterogeneous on the nanometer scale<sup>58</sup>, some glassy connections referred as rare event can be established for a short period in between fillers and result in a strong increase of the modulus. In this frame, the concepts of the glass transition shift due to confinement and of heterogeneity of dynamics in Van der Waals liquids close to  $T_g$  have been combined by Dequidt et al<sup>59</sup> to model the mechanical properties of a non-polar polymer between two substrate. The glass transition is shifted and broadened by the percolation of very slow domains  $\xi$  of nanometric size that may connect the two surfaces leading to a high increase of the modulus.

The obtained results for the reinforcement ( $R(T, \phi)$  defined as the modulus of the polymer confined between two substrates and the free polymer) compare very well with the reinforcement observed in filled elastomers and also account for its evolution with temperature.

$$R(T, \phi) = \frac{G'(T, \phi)}{G'_{rubber}(T)} \quad (35)$$

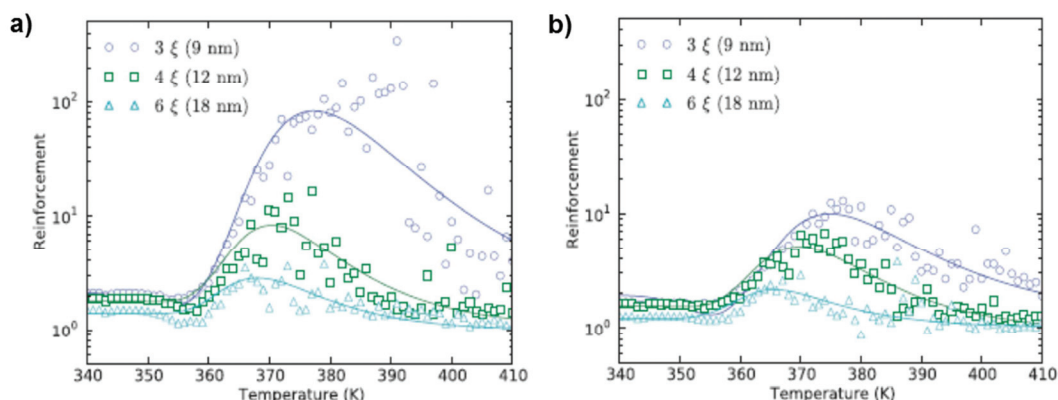


**Figure 27: Reinforcement (Modulus of the confined polymer versus modulus of the free polymer) versus Temperature for two values of interaction parameter a) strong interaction ( $0.5kT$  per monomer) and b) weak interactions ( $0.3kT$  per monomer).**

**It appears that the reinforcement in the linear regime and the Payne effect depend on two main parameters: the strength of the interactions at the interface and the distance between fillers, in particular the shortest distances between them.**

#### Existence of a critical filler fraction?

In a model of glassy layers, the distance between particles plays a critical role and one could think of a critical fraction above which the percolation of glassy layers occurs.

Mujtaba<sup>60</sup> et al have studied the effect of the filler fraction on the Payne effect and it is found that the modulus at large strain  $G'_{50}$  increases continuously with the filler fraction whereas the modulus in the linear regime  $G'_0$  shows a break in the slope with the filler fraction. Above a filler fraction of roughly 10%, the high increase of the modulus can be attributed to the percolation of glassy layers. Another interesting aspect of this work is that the modulus  $G'_0$  drops as temperature increases in the range of large filler fractions above the percolation threshold. This demonstrates the temperature dependent aspect of the reinforcement at high filler fractions.

#### Effect of the distances between particles:

As regards the latter parameter, Guy et al<sup>61</sup> have proposed a master curve relating the amplitude of the Payne effect with the estimated distance between fillers for several Silica types and volume fractions taking into account the morphology of the aggregates but the interface type was not modified in those materials.

The role of the distribution of reinforcing particles (thus the distance between them) on the Payne effect was evidenced by Montes and coworkers<sup>62</sup>. They studied two sets of spherical silica filled elastomers having an identical interface grafter and only differing by the distribution state of the silica as revealed by Small Angle Neutron Experiments. As shown in Figure 28 the modulus drop with strain is higher for the system with partially aggregated or connected fillers compared to well-dispersed silica.

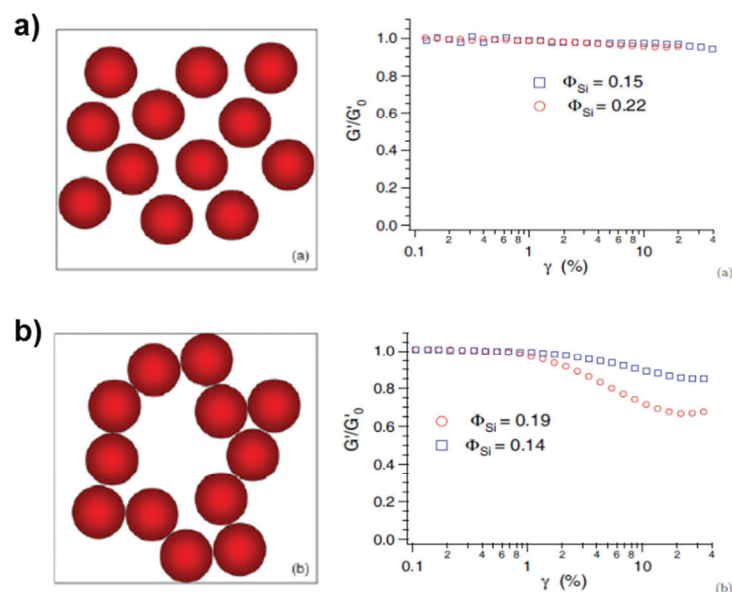


**Figure 28: Effect of silica particles distribution on the Payne effect (adapted from Montes et al<sup>62</sup>). The well-distributed silica (a) leads to a lower Payne effect than the equivalent system with a poor distribution.**

Finally a recently published study that is fully consistent with the decomposition of the Payne effect given by Dequidt et al may also be mentioned.

#### Effect of the mobility restriction and distances between particles:

The interpretation based on the number of glassy bridges was pushed further by Papon<sup>63</sup> from the same team with a larger set of samples with various filler contents and grafting agents. The authors were able to finely relate the Payne effect magnitude with the polymer mobility and the distribution state of spherical particles in model samples. SANS experiments coupled to reverse Monte Carlo simulations gave access to the average aggregation number of silica particles and then on closest distances between them. Then low-field proton NMR spectroscopy was used to quantify the reduction of polymer mobility imparted by the silica surface. Two zones of affected mobility were proposed: firstly a glassy layer where the polymer has a glass transition higher than the experimental temperature and secondly an intermediate mobility layer where the polymer is partially immobilized though not fully glassy (Figure 29).

Combining the results of these two techniques, the connections between glassy and immobilized polymer layers at the surface of particles are estimated. The decrease of the storage modulus in the Payne effect range was found to be correlated with the number of glassy and low mobility connecting bridges.

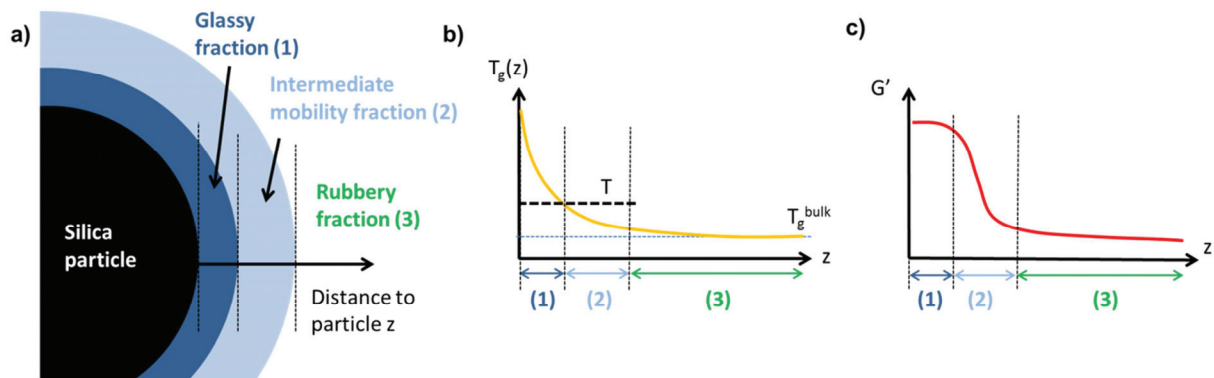


**Figure 29: Three layer model from Papon et al<sup>63</sup>: a) Representation of the different fractions of polymer, b) Glass transition and c) Storage Modulus  $G'$  versus distance to filler  $z$ . The polymer is in the glassy state (1) close to the filler, then an intermediate mobility layer (2) is in contact with the glassy layer, far from the filler the bulk polymer is rubbery (3).**

• **Conclusion**

To summarize, at a given temperature, the Payne effect depends on many parameters such as the filler amount, the filler morphology, the interactions between the filler and the polymer and the distribution state of the filler particles.

The various contributions the Payne effect are generally summarized as shown in Figure 30.

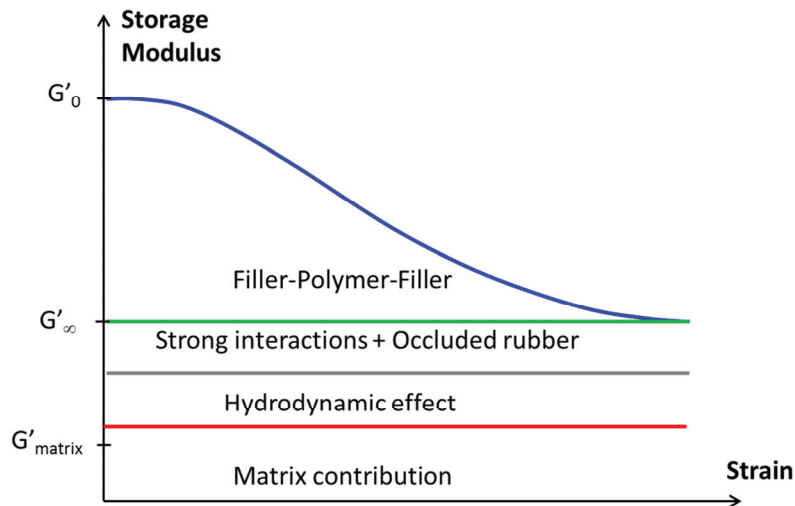


**Figure 30: Decomposition of the modulus drop with strain into four contributions, the filler-polymer network being the only one decreasing with strain<sup>64</sup>.**

The strain independent part of the storage modulus can be decomposed in the matrix modulus, the hydrodynamic effect of the fillers and a rubber-polymer contribution due to the occluded strongly bound rubber fraction. The strain dependent contribution to the modulus is attributed to

the strong network formed by the fillers and the immobilized polymer (glassy or intermediate mobility layers) that is broken under the effect of strain.

The four contributions can also be expressed as a function of the filler fraction (Figure 31) which highlights the presence of a percolation threshold for the glassy or intermediate mobility layers at a given filler fraction, as evidenced by Mujtaba et al<sup>60</sup>.

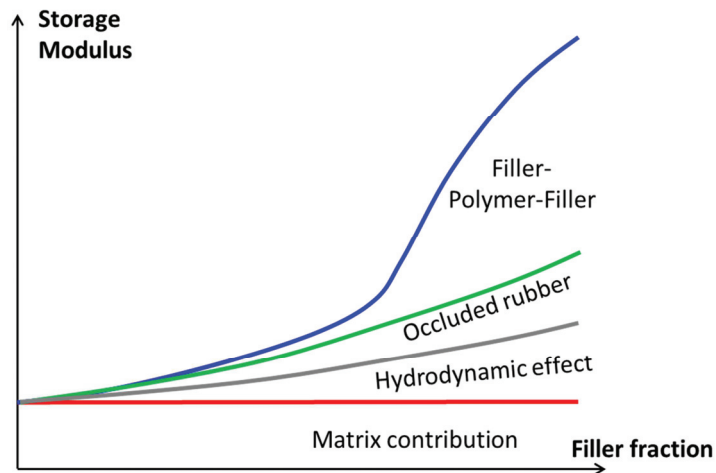


**Figure 31: Filler fraction effect on the different contributions of the Payne effect<sup>60</sup>.**

In the approach summarized here, the Payne effect is the result of the interplay between the strength of the interface and the distribution of particles in space. The first parameter controls the restriction of the polymer mobility in the vicinity of the fillers: the stronger the interactions with the rubber, the higher the  $T_g$  shift, i.e. the width of the glassy layer. The second parameter controls the distances between closest neighbors.

One major challenge in the description of the Payne effect in many systems is that the modification of the interface agent may act simultaneously on both parameters, since the distribution of fillers most probably depends to a large extent on the filler-polymer interactions and filler-filler interactions<sup>63</sup>.

The potential effect of the interface modification on the filler distribution may be at the origin of the Payne Effect decrease as the interactions at the interface increase. Indeed several authors have noticed the reduction of the Payne effect when adding coupling agents to the Silica<sup>64,65</sup> or conversely an increase of the Payne effect by using less active carbon black such as graphitized carbon blacks<sup>64</sup> (see Figure 32).

It has also been shown that the Payne effect decreases with increasing amounts of bound rubber (that could be considered as a measurement of the interface strength at a fixed dispersion of filler)<sup>65,66</sup>.

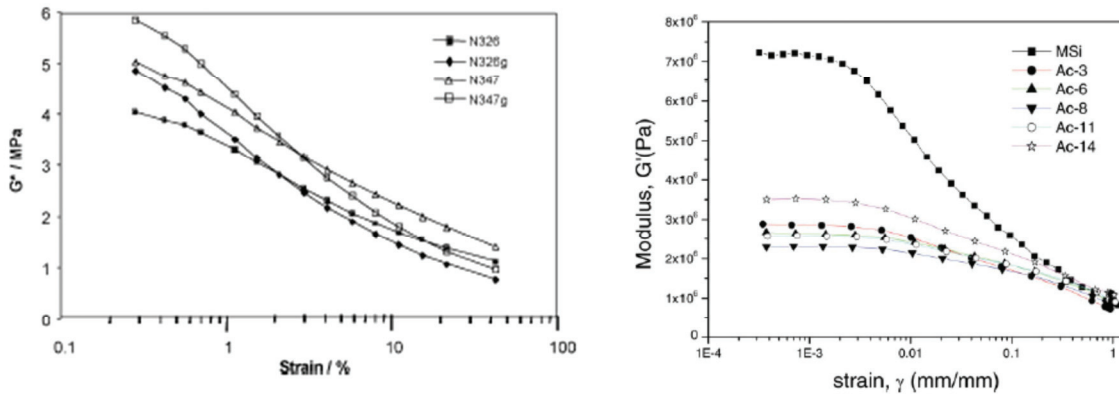


**Figure 32: Effect of the filler surface modification on the Payne effect: a) Graphitized Carbon Blacks (g) lead to a higher Payne effect<sup>64</sup>. b) Grafting increasing coupling agents amounts to the silica surface (series denoted Ac) decreases the Payne effect<sup>65</sup>.**

### II.2.b. Large Strain regime

#### II.2.b.i. Stress softening at large deformations: Mullins Effect

The primary effect of adding fillers on the large strain behavior is an important increase of the modulus. We first present the Mullins effect (decrease of the modulus with cycling) because the same mechanisms may account for this effect and the high modulus of a filled rubber during the first extension.

The Mullins effect is a stress-softening effect after application of large strain cycles, the stress necessary to extend the material to a given strain is lower during the second cycle than during the first (Figure 33).

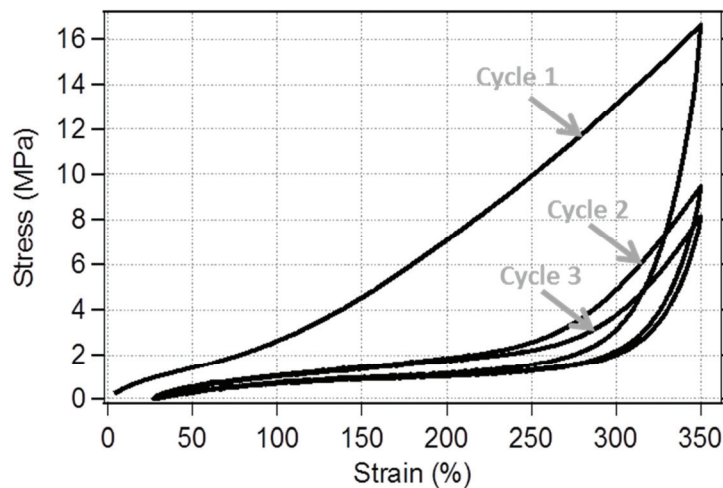


**Figure 33 : Three consecutive traction recovery cycles applied to an as-prepared reinforced Natural Rubber compound. An important stress-softening is observed after the first cycle and continues with the second cycle. Usually 3 or 4 cycles are sufficient to obtained “stabilized” samples.**

The decrease of the modulus continues at a lower extent after applying a second and third cycle. Three or four cycles are generally considered sufficient to observe only very little further softening. According to Mullins<sup>67</sup> who studied the phenomenon extensively, the Mullins effect is only observed in filled rubbers even if a slight stress-softening may also be noticed for unfilled rubbers.

The maximum cycling strain during the first cycle has a strong effect. After a first cycle of maximum strain  $\epsilon_{\max}$ , the stress-softening is indeed only observed for strains lower than  $\epsilon_{\max}$  (or more accurately  $\epsilon_{\max} + \Delta\epsilon$  the latter term related to the inhomogeneity of the network). This threshold strain for the recovery of the as-prepared sample modulus is represented in Figure 34.

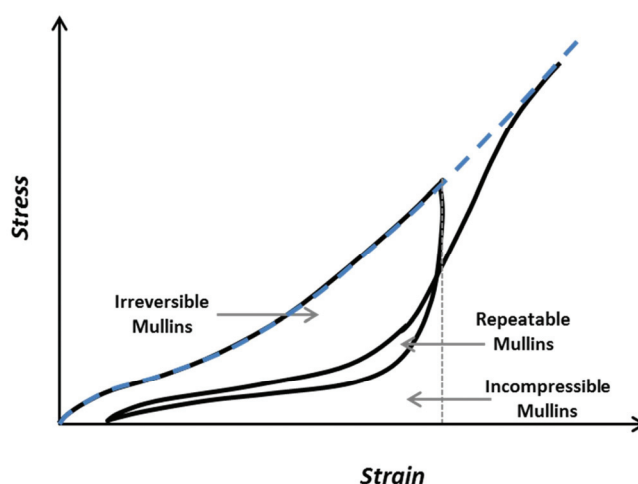


**Figure 34: Schematic comparison of the as-prepared tensile curve (blue dashed line) and the stress-softened curve due to the application of a cycle of maximum strain  $\epsilon_{\max}$ . The stress eventually becomes equivalent for the softened sample at strains higher than  $\epsilon_{\max}$ . The energy mechanically brought to the sample during the first cycle can be decomposed in three contributions: irreversible, repeatable and incompressible.**

The concept of strain amplification between fillers on the microscopic scale was proposed by Bueche<sup>68</sup> to account for the stress-softening after precycling at high strain. Strain amplification in the elastomer matrix is due to the presence of rigid particles that cannot deform. The remaining elastomeric phase is thus submitted to a higher local strain than the unfilled elastomer at a given macroscopic strain (Figure 35). Note that the stress transfer at the interface is considered perfect in this case but we will see that this may not systematically be true.

Based on this concept, Bueche explains the stress-softening by breakage of the shortest chains between fillers, which then do no longer contribute to the modulus in the following mechanical cycles. Using acoustic emission for studying the Mullins effect, Godin and coworkers<sup>69</sup> reported that the number and amplitude of acoustic events decreases with the number of cycles applied, in agreement with the lower stress-softening. Moreover the acoustic activity is drastically reduced when stretching a weakly filled rubber that shows a lower Mullins effect.

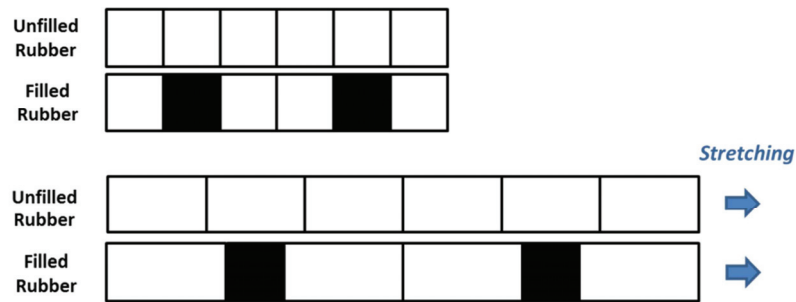


**Figure 35 : Strain amplification phenomenon schematization: the empty and filled squares represent respectively the rubber matrix and the rigid fillers. Upon applying a macroscopic strain  $\epsilon_1$ , the rubber matrix bears a higher local strain ( $\epsilon_2 > \epsilon_1$ ) due to the undeformable fillers.**

In order to address the partially reversible character of the Mullins effect Dannenberg<sup>70</sup> developed an interpretation based on slippage and re-adsorption of chains on the surface of carbon black fillers (see Figure 36). The shortest chains between two fillers are the first brought to their finite extensibility involving a high level of stress. These chains may then be desorbed from the filler surface enabling higher local strain levels (sketches b) and c) in Figure 36). This model also assumes that new interactions may be established between the chains and the filler after slippage. When the material is finally allowed to return to its initial length, the newly formed filler/chains interactions lead to a more homogeneous chain length between fillers. This reorganized structure accounts for the lower stress necessary during the second cycle to return to a fixed macroscopic strain.

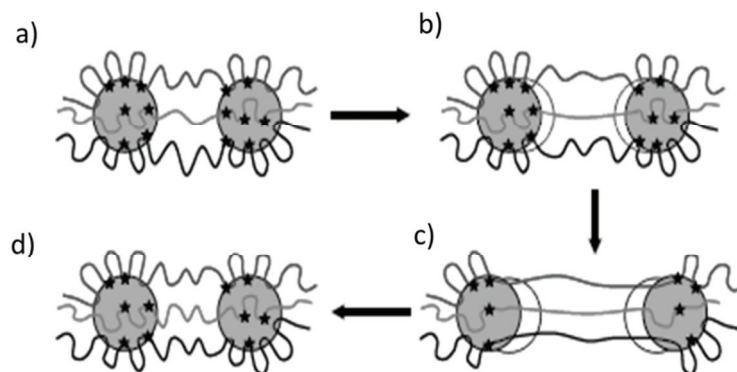


**Figure 36 : Chains adsorption and desorption mechanisms at the surface of Carbon black fillers: Unstretched state, b) the first desorptions occur under strain for the shortest chains. c) desorptions occur for other chains and d) back in the unstretched state the chain length between filler is more homogeneous.**

The fact that the stress softening is less pronounced above the maximum strain  $\epsilon_{\max}$  applied during the first cycle also confirms that the Mullins effect magnitude is related to a given maximum local strain and consequently a given macroscopic strain.

### II.2.b.ii. Reinforcement in the large strain regime

The presence of nanometric fillers strongly increases the modulus in the large strain regime. Accordingly, the filler fraction is a first order parameter that affects the stress-strain curves of reinforced rubber. The increase of crosslink density also plays a major role similar to what has been mentioned for unfilled rubber.

The reinforcement effect can be related to the same mechanisms that have been proposed to describe the Mullins effect. As a matter of fact, describing the Mullins effect requires understanding the rubber microstructure and changes induced in the microstructure by cycling at large strains.

In the case of unfilled Natural Rubber, the stress hardening phase at very large extension right before failure has been attributed to two effects, namely limited chains extensibility and strain-induced crystallization. This modification of the curve shape by introducing fillers may be explained by the strain amplification phenomenon which lowers the macroscopic deformation onset for the two hardening phenomena and therefore lead to an increase of elastic modulus. As regards strain induced crystallization, the strain onset indeed decreases significantly when adding carbon black<sup>71,72</sup> or silica<sup>73,74</sup>, due to strain amplification between fillers.

In addition to a local average strain amplification, Bueche also mentioned an heterogeneous strain field applied to the polymer matrix.

Gabrielle<sup>74</sup> has studied the crystallization behavior of filled samples before and after mechanical cycling and has shown that the SIC onset increases after mechanical cycling which indicates that the application of a large strain cycle lowers the strain amplification factor in highly strain amplified zone either by breakage or slippage of the shortest chains.

According to stress and molecular orientation measurements, Clément et al<sup>75</sup> have attributed the reinforcement to chains that reached their limit of extensibility and the stress-softening to slippage or detachment from the surface. These authors<sup>75,76</sup> also point out the heterogeneity of the strain amplification by observing that the reorganization under strain mainly takes place in the regions of high silica concentration in polydimethylsiloxane and styrene-butadiene rubber samples.

#### Effect of the filler/rubber interface:

The rubber matrix is submitted to a level of strain amplification that also greatly depends on the ability of the interface to transfer the stress to the matrix. In the case of a low filler/polymer interaction, the detachment of the rubber chains from the fillers completely changes the strain amplification scheme: the rubber matrix may slip on the fillers and the local strain amplification may only be due to some geometrical effects. This role of the interface strength on the modulus at large strains has been pointed out by several studies both with Carbon black<sup>77</sup> and Silica<sup>74,78</sup> as the reinforcing filler.

Mihara<sup>66</sup> has shown that the reinforcement index (defined as the stress at a strain of 300% divided by the stress at a strain of 100%) increases with the specific bound rubber (which can be related to the interface strength) showing that the higher the interface strength and the higher the modulus in the large strain regime.

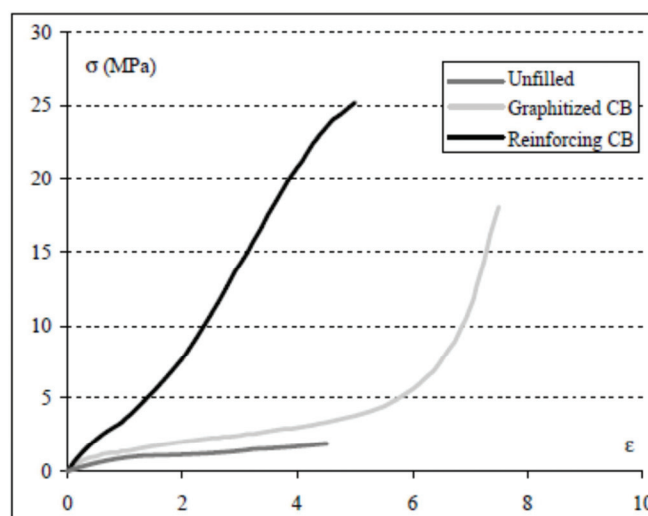


**Figure 37: Filler/Polymer interaction effect on the stress-strain curve in the large strains (reinforcing effect) : unfilled, Carbon black filled and Graphitized Carbon black filled rubber according to Medalia and Kraus<sup>77</sup>.**

Another important factor that may play a role on the modulus at high strains is the occurrence of cavitation in the rubber matrix and/or at the filler interface. The phenomenon has been recently evidenced in Carbon Black filled SBR by an increasing total Small Angle X-ray Scattering (SAXS) signal with strain<sup>79</sup>. Additional measurements by Digital Image correlation seem to be in good agreement with this observation<sup>80</sup>.

### II.2.b.iii. Swelling restriction due to the interface

In addition to being a precise technique for the measurement of the crosslink density of non-reinforced networks<sup>81,82</sup>, equilibrium swelling measurements can be carried out on reinforced rubbers to provide insights on the interface strength<sup>56,83-86</sup>. As a matter of fact, Valentín et al. have highlighted the restriction of swelling taking place in rubber networks reinforced by actively reinforcing particles. The mechanism responsible for this lower solvent intake is schematized in Figure 38. Chemical or physical bonds at the filler surface prevent the swelling of the surrounding rubber chains. On the contrary, in the case of a weak interface, some debonding may occur at the interface leading to an additional solvent absorption by the sample. In this case the rubber fraction in the swollen state is underestimated and so is the crosslink density.

The modification of the swelling behavior by adding fillers also depends on the filler fraction introduced. Considering a strong interaction between the filler and the polymer chains, the restriction of solvent intake is limited for small amounts of fillers as the only contribution is a small rubber fraction in the vicinity of the fillers. It has been shown that above a critical filler fraction the equilibrium swelling drops due to interconnecting domains of non-swollen rubber interphase<sup>84</sup> as schematically represented in the highly filled sample in Figure 39.

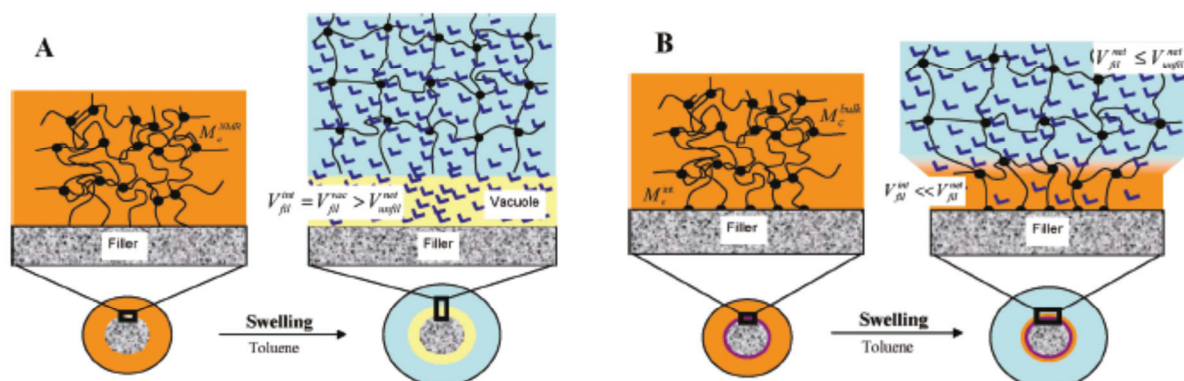


Figure 38: Schematic swelling behavior for a non-interacting filler (A) and a filler showing interactions with the matrix<sup>84</sup>. A: In the first case, debonding of the matrix occurs during swelling and additional solvent is absorbed in interfacial vacuoles. B: On the opposite, surface interactions with the polymer inhibit solvent intake in the vicinity of the fillers.

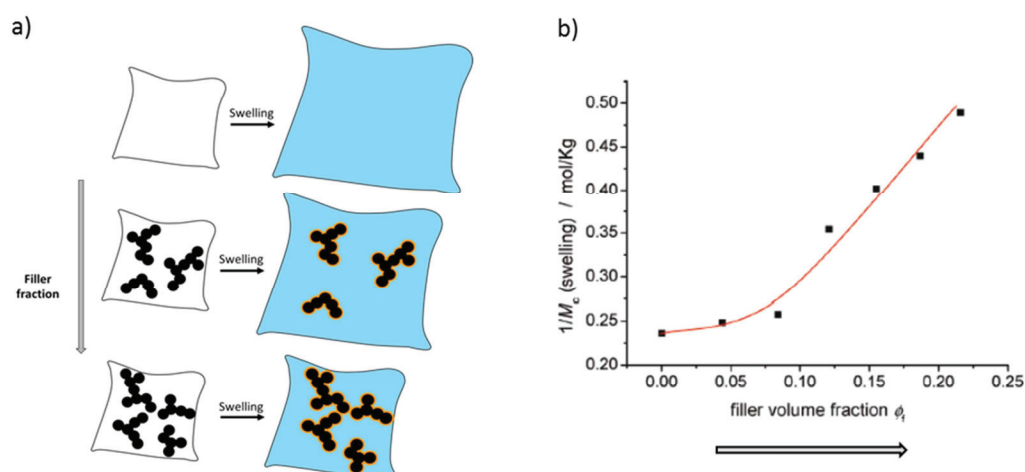


Figure 39: a) Schematization and b) Measurements (Valentín et al.<sup>84</sup>) of the equilibrium swelling restriction with strongly interacting fillers: above a given filler volume fraction, the non-swollen polymer zones (orange zones) at the interface overlap leading to a step increase of the swelling restriction.

### II.3. Strain-induced Crystallization

The phenomenon of crystallization under stretching in vulcanized natural rubber was first evidenced by X-ray diffraction by Katz<sup>87</sup> in 1925 and is still the object of many investigations since the formation of crystallites leads to a self-reinforcement effect that greatly enhances the ultimate strength of the semi-crystallized rubber<sup>88</sup>. During the last years, many progresses have been made in the characterization of the SIC phenomenon due to advances in detector's technologies and democratization of synchrotron radiation use for the study of soft matter. Direct measurements of the crystallinity during in-situ stretching experiments have been performed<sup>89,90</sup>

clarifying the influence of SIC on the stress strain behavior of NR and very rapid diffraction pattern acquisition are expected to enhance the understanding of crystallization kinetics in the near future.

A distinction has to be made between cold crystallization or thermally-induced crystallization (TIC) which occurs at very long time scales and low temperature (fastest crystallization kinetics occurs around  $-25^{\circ}\text{C}$  in the quiescent state) in unstretched rubbers<sup>91,92</sup> and strain-induced crystallization (SIC) which is due to alignment of chains under strain. This phenomenon occurs above a critical extension which depends on temperature and applied strain rate<sup>90,93</sup>. Strain-induced crystallization can be detected in polyisoprene (IR and NR), polyisobutylene (IIR) and polybutadiene rubbers (BR), nevertheless the effect is more pronounced in the case of polyisoprene rubbers<sup>94</sup>.

Synthetic polyisoprene rubber (PI) may also crystallize provided that the percentage of repetitive units in the cis configuration is high enough. The widely used Natsyn 2200 has 98.5% of isoprene units in the cis-configuration<sup>95</sup> which is still lower than the 99.5% reached in the case of Natural Rubber. Tanaka<sup>96</sup> has proposed that the presence of impurities (proteins, lipids, etc) in Natural Rubber (about 6% of non-rubber components) is also at the origin of the higher crystallization properties compared to synthetic polyisoprene due to a nucleating effect.

The organization of the crystallites has been studied in the relaxed state and stretched state<sup>97,98</sup>. The rubber films are stretched at room temperature at various stretching ratios and then cooled down at  $-25^{\circ}\text{C}$ . It was observed that the crystallites are organized in spherulites for unstretched NR and this structure is progressively replaced by a shish-kebab structure (see Figure 40) as the extension ratio was increased.

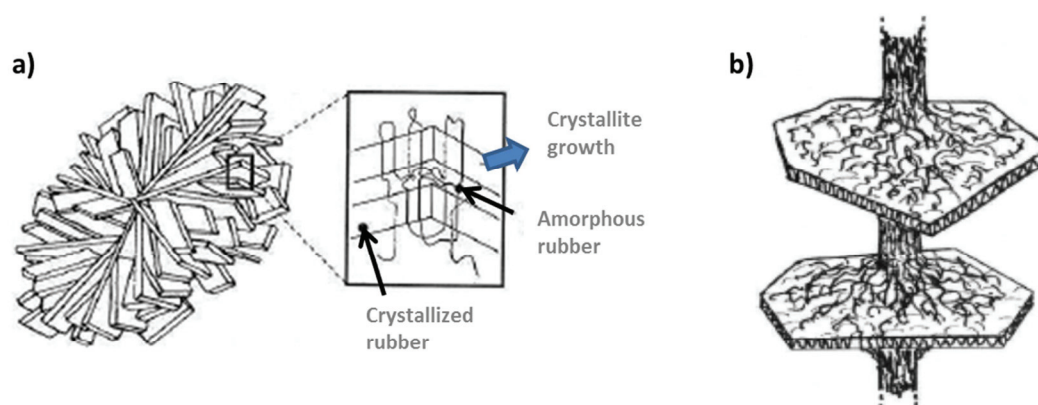


**Figure 40: a) Spherulitic and b) Shish-kebab arrangements of crystallites in Natural rubber<sup>99</sup>.**

Note also that vulcanization of Natural Rubber was not found to affect, or only very slightly, the crystalline morphology.

### *II.3.a. Effect of crosslink density on a traction-retraction cycle*

The evolutions of the stress and crystalline content as a function of strain in vulcanized Natural Rubber in a simple traction-retraction cycle at low strain rate are illustrated in Figure 41)<sup>90</sup>

The traction phase (OABC) can be decomposed in three successive parts:

- (OA) In the first part, the elastomer matrix is entirely amorphous.
- (AB) Above the critical crystallization extension ratio, the crystallites begin to form. The stress stabilizes in this regime as a result of the competition between the relaxation of the amorphous and the reinforcing effect of newly formed crystallites. This effect has been predicted by Flory<sup>100</sup>: the crystallization of a portion of a chain induces an increase in entropy for the rest of the chain which relaxes
- (BC) Above an extension ratio of 5, the hardening effect of crystallites becomes predominant over the relaxation of amorphous chains.

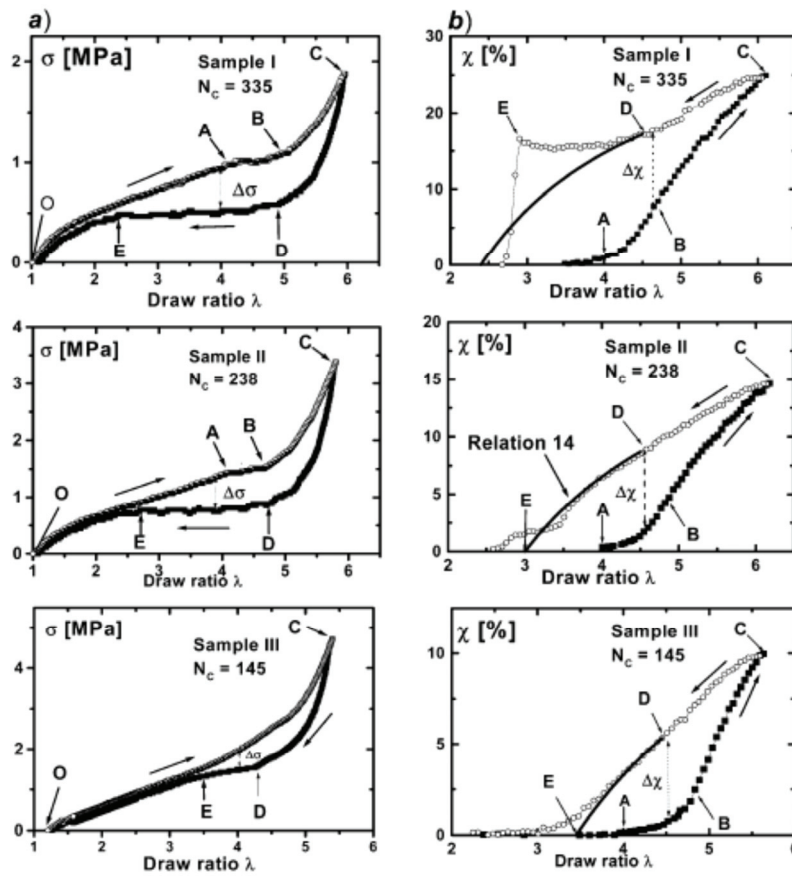


**Figure 41 : a) stress and b) crystallized fraction versus draw ratio  $\lambda$  during a mechanical cycles for three crosslink densities as reported by Trabelsi et al<sup>90</sup> (number of monomer between crosslinks  $N_c$ : 335; 238 and 145). The points OABCDE are discussed in the text. An inverse yielding phenomenon during the retraction impacts the crystallinity measurement thus the predicted behavior is marked by the thick line.**

The retraction phase (CDEO) is described as follows:

- (CD) The first retraction part consists in a decrease of the crystallized fraction and stress.
- (DE) When the strain becomes lower than a given extension ratio, the stress becomes constant due to a competition between the decrease of crystalline fraction and the

increase of the orientation of the chains as they melt (according to the effect proposed by Flory<sup>100</sup>).

- (EO) The last part of the retraction curve is exactly similar to the first part of the traction curve.

Another interesting observation from the data of Trabelsi and coworkers is that the strain onset for SIC is not modified with crosslink density, in contradiction with the prediction of the Flory theory<sup>15</sup>.

Ikeda et al<sup>101</sup> compared NR samples vulcanized with dicumyl peroxide (DCP) and Sulfur varying the amount of vulcanization agents: DCP in the first case, Sulfur and accelerator in the second. The results obtained show that the onset of crystallization does not depend on crosslink density for sulfur-crosslinked samples whereas the onset decreases with crosslink density in the case of DCP.

The same group then reported Small Angle Neutrons experiments showing that the peroxide-cured samples presented some highly crosslink clusters of different size<sup>102</sup>. This result was confirmed by DQ-NMR experiments<sup>103</sup> highlighting a broader distribution of residual dipolar couplings as compared with NR sulfur network and a highly crosslinked phase.

The coexistence of two network densities could explain the earlier strain crystallization onset when the crosslink density increases. It can either be assumed that these clusters will not deform as the rest of the matrix and play the role of small filler increasing the strain on the rest of the network. The other possible explanation is that the clusters act as a nucleating point for crystallites and this way promotes crystallization at lower strain as nucleation seems to be the limiting process, as a matter of fact it has been shown<sup>90</sup> that crystallites do not grow in size and crystallization proceeds by formation of new crystallites.

Tosaka and coworkers presented a SIC mechanisms where the heterogeneous nature of the rubber network is taken into account. The shortest chains which are the first to reach local extension ratios close to their limited extensibility play the role of nucleus for the formation of crystallites (Figure 42).

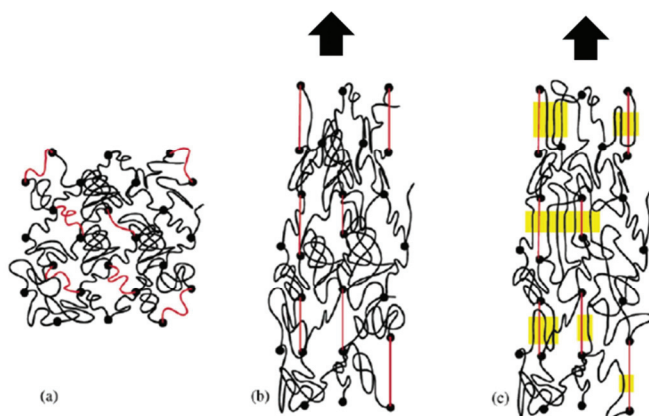


**Figure 42 : Strain-induced crystallization scheme according to Tosaka<sup>94</sup>. a) unstretched state, b) stretched right before SIC onset and c) right after SIC onset. The shortest chains (in red) act as nucleus for the crystallites (yellow rectangles).**

### II.3.b. Effect of fillers on SIC:

The incorporation of fillers in Natural rubber is known to strongly affect the SIC phenomenon. Several studies performed<sup>71,72,104,105</sup> have highlighted the reduction of the SIC onset when adding carbon black fillers.

The shift of SIC onset was evidenced by Trabelsi et al<sup>71</sup> (Figure 43) for a filler fraction of 50phr. Poompradub et al<sup>104</sup> also reported slight decrease of the SIC onset by incorporation of 20 and 40 phr of carbon black in NR, the higher the amount and the lower the SIC onset.

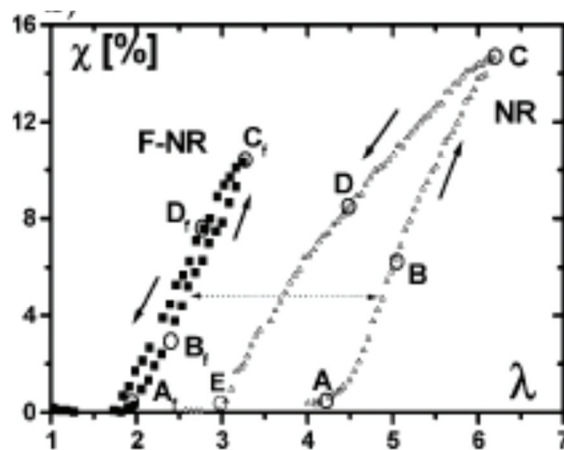


**Figure 43: Strain-induced crystallization onset shift due to carbon black fillers. Comparison of filled (F-NR) and unfilled NR crystallized fraction versus drawing ratio reported by Trabelsi et al<sup>71</sup>.**

In her thesis, Marchal<sup>99</sup> confirms that the onset is all the more lowered that the filler content is important with three volume fraction (see Figure 44).

Another observation should be mentioned: conversely to the crystallized fraction curves versus elongation obtained by Trabelsi (Figure 43), the reinforced NR curves have a lower slope meaning that the rate of crystallization with strain is lower that for unfilled samples. A similar result was obtained by Dupres et al<sup>72</sup> for several Carbon black morphologies and volume fraction.

Brüning and coworkers<sup>106</sup> have studied the SIC behavior of unfilled and filled with Carbon Black NR samples in order to calculate a strain amplification factor assuming that an given crystallized fraction in both types of samples meant an equivalent local strain. They also observe that the introduction of carbon black strongly lowers the strain onset (an amplification factor superior to 2 is found). Then the crystallized fraction increases slower with strain for a filled sample and for macroscopic strains of the order of 400%, the crystallized fraction is higher for the unfilled NR compared to the reinforced NR.

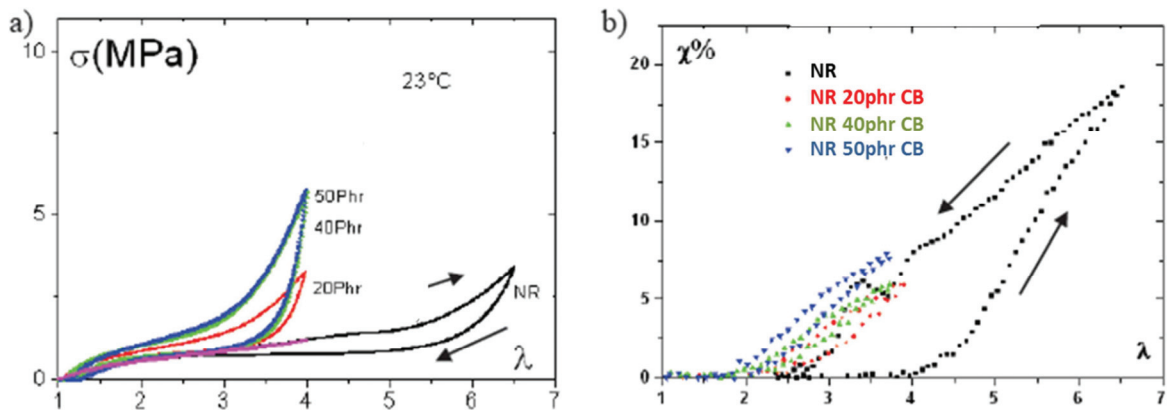


Figure 44 : a) Stress and b) Crystallized fraction versus Elongation ratio for three reinforced NR (filler fractions of 20, 40 and 50phr) and an unfilled NR<sup>99</sup>.

In addition to the crystallites formation characterization, the anisotropy of the X-ray scattering at wide angles can be followed up simultaneously, giving pieces of information on the orientation of the amorphous chains or part of chains<sup>107,108</sup>. Others techniques such as fluorescence polarization<sup>109</sup>, infrared dichroism<sup>110</sup> and quadrupolar NMR<sup>111</sup> are effective to measure the overall orientation of the rubber networks.

The comparisons of quadrupolar NMR results and X-ray diffraction results carried out by Rault<sup>105</sup> and Dupres<sup>72</sup> provide interesting insights on the relaxation of the amorphous chains imparted by the first strain-induced crystallites. Rault et al<sup>105</sup> have also shown by quadrupolar NMR that the orientation of NR chains increases with the fraction of introduced carbon black (Figure 45).

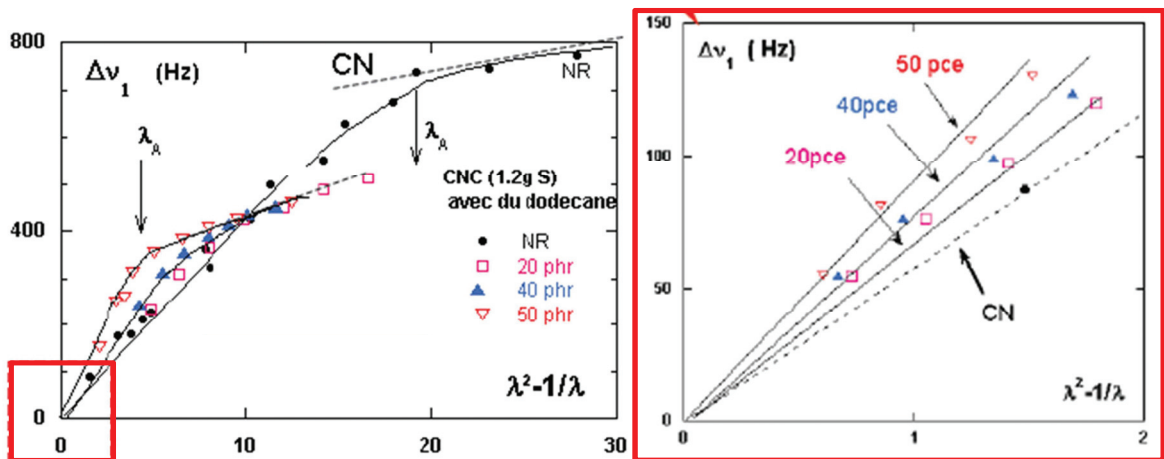


Figure 45 : Quadrupolar splitting in carbon black reinforced (20, 40 and 50phr) and non-reinforced samples of NR (labeled CN) as a function of rubber strain according to Marchal<sup>99</sup>.

Nevertheless this characterization of the orientation and X-ray diffraction cannot be carried out simultaneously and the solvent probe molecules may affect the dynamics and/or the orientation of the matrix.

The deconvolution of the scattered intensity anisotropy (anisotropic amorphous halo) in the X-ray patterns was thus used to estimate the “fraction of oriented amorphous”<sup>112</sup>. Nevertheless, this notion does not seem correct since there is no reason for some part of the amorphous rubber chains to go into an oriented intermediate state before crystallization while the rest of amorphous chains stay completely randomly oriented in an “unoriented amorphous fraction”.

### II.3.c. Effect of temperature on SIC:

Temperature increase reduces the crystallized fraction at a fixed extension ratio, as demonstrated by Albouy and coworkers<sup>90,105</sup>. Figure 46 shows the results of experiments where samples are pre-stretched to a given extension ratio and then quenched at  $-25^{\circ}\text{C}$  in order to fully crystallize. The crystallized fraction is then recorded upon heating for each extension ratio. The melting temperature  $T_m$  shift with the extension ratio is clearly evidenced here. The melting temperature found for an extension ratio of 3 is in good agreement with the melting point of a mechanical cycle (point E in Figure 43).

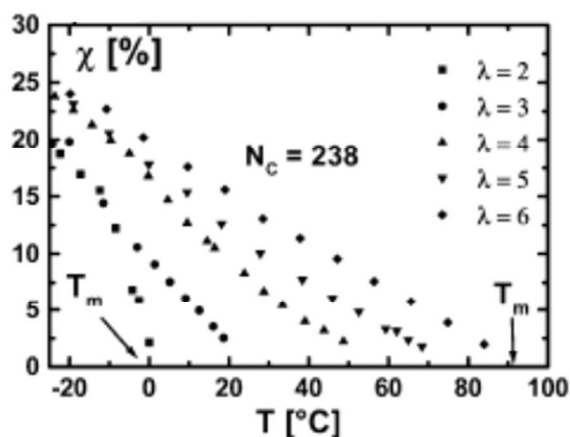


**Figure 46 : Crystallized fraction versus Temperature for several extension ratios<sup>90</sup>.**

As regards stress strain and crystallized fraction measurements during mechanical cycles at various temperature, the results of Marchal et al<sup>113</sup> show the decrease of crystallized fraction at a fixed extension ratio for increasing temperatures (Figure 47). The stress simultaneously decreases with temperature due to the lower amount of reinforcing crystallites.

These data also confirm the role of the crystallinity hysteresis on the mechanical hysteresis: increasing the temperature decreases simultaneously the crystallinity and mechanical hysteresis and an identical effect is observed when increasing the crosslink density (see Figure 41).

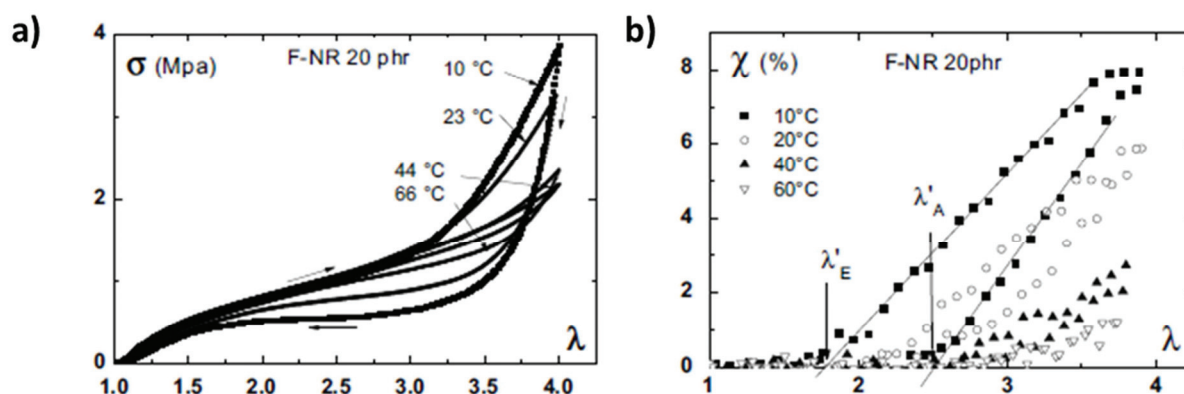


Figure 47: Effect of temperature on a) stress and b) crystallized fraction for a filled NR sample<sup>113</sup>.

#### II.3.d. Strain-induced crystallization at crack tip.

Lee and Donovan<sup>114</sup> have reported a study of the crystallized fraction at the crack tip by X-ray diffraction. With a resolution of 1mm, they plotted the crystallized fraction as a function of the distance to crack tip in the notch plane and showed that the introduction of Carbon black increases the local crystallized fraction which is in agreement with the SIC onset shift due to strain amplification when adding fillers as discussed earlier.

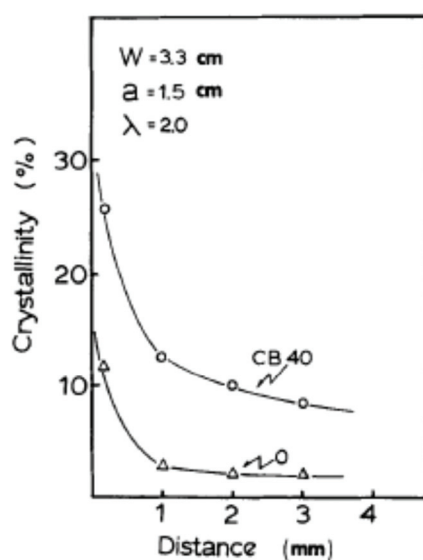
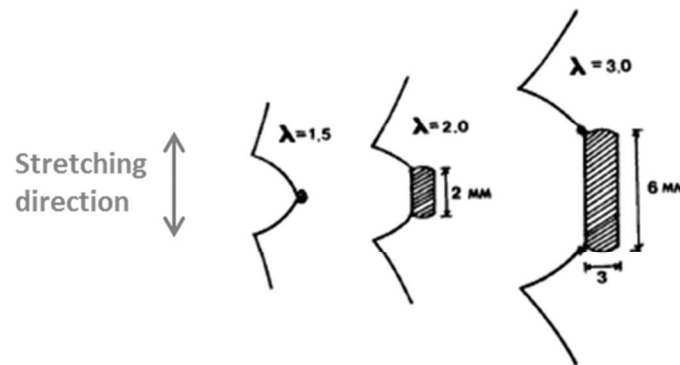


Figure 48: Crystallinity as a function of distance to crack tip in the notch plane for carbon black reinforced NR (CB40) and unfilled NR (0)<sup>114</sup>.

The size of the crystallized zone was also investigated by these authors as shown in Figure 49. The crystallized area is spreads more in the traction direction due to blunting of the crack tip.



**Figure 49: Increase of the crystallized zone (hatched area) as the applied macroscopic extension ratio  $\lambda$  increases according to Lee and Donovan<sup>114</sup>. The crystallized zone spreads in the stretching directions simultaneously to crack tip blunting.**

Trabelsi and coworkers<sup>115</sup> have been the first authors to perform a mapping of the crystallized fraction with a resolution (limited by the beam size) of  $50\mu\text{m}$  (Figure 50). The studied unfilled NR was found to crystallize at crack tip for low macroscopic extension ratio, depending on the notch length.

A constant crystallized fraction was also reported in the first hundreds of  $\mu\text{m}$  at the crack tip at a large enough macroscopic extension ratio.

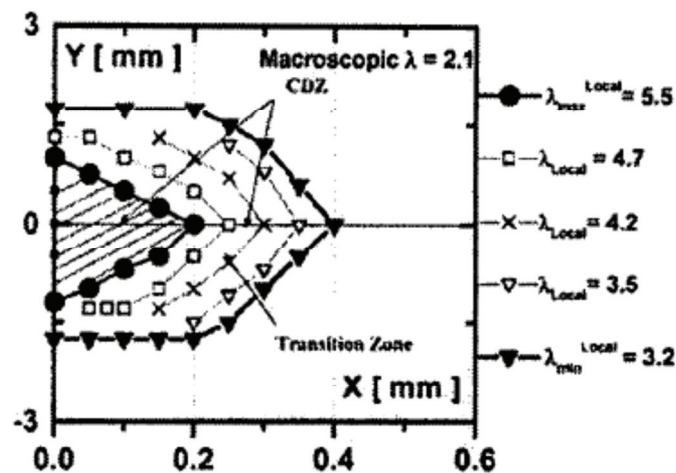


**Figure 50 : Crystallized fraction mapping around the crack tip of a pre-notched NR samples according to Trabelsi et al<sup>115</sup>. The X axis is dilated compared to Y axis.**

Huneau et al<sup>116</sup> have performed similar mapping of the degree of crystallinity at the crack tip by in-situ X-ray diffraction experiments during fatigue tests in order to relate the crystallized fraction to the endurance of the sample. They found that the crystallized fraction at the crack tip and size of the crystallized zone was increasing with increasing volume fractions of carbon black in agreement with the study by Lee and Donovan.

## II.4. Resistance to crack propagation in Rubbers

### II.4.a. Energy release rate and Tear energy

The study of tear or crack propagation resistance in fatigue of materials basically consists in estimating the amount of energy that is required to propagate a crack. The initiation of the crack (the creation of a defect) is not addressed in this approach assuming that micro cracks are systematically present in the studied systems and the propagation is the key phenomenon leading to failure.

First, it is important to distinguish the notions of tear energy and energy release rate:

- The tear energy  $T$  denotes the energy necessary to create two surfaces of interfacial energy  $\gamma$  of unit area, which implies breaking the chemical bonds in the newly created crack plane.

$$T = 2\gamma \quad (36)$$

- The energy release rate  $G$  is defined<sup>117</sup> as the amount of elastic energy  $W$  stored in the sample that is released during the propagation of a unit crack area  $A$ :
- 

$$G = - \left. \frac{\partial W}{\partial A} \right)_l \quad (37)$$

Subscript  $l$  denotes that the sample is held at constant displacement during the propagation ruling out any contribution of external forces.

The generalization of Griffith's theory<sup>118</sup> to elastomers assumes that the released elastic energy is completely converted into surface creation as the crack propagates. This hypothesis thus neglects the energy dissipation in the bulk of the material during crack propagation.

$$G \geq G_c = T \quad (38)$$

$$G_c = - \left. \frac{\partial W}{\partial A} \right)_l \quad (39)$$

This relationship states that the Tear energy  $T$  and the critical energy release rate  $G_c$  are equivalent, which leads to a confusion of the terms that are often interchanged although denoting different physical terms.

Elastomers can undergo very large strains before failure even in pre-notched geometries. Rivlin and Thomas<sup>119</sup> have proposed several testing geometries in which the energy release rate can be estimated in a simple way. They confirmed that the Tear energy is independent of the sample geometry and the solicitation mode but is a characteristic of the rubber material.

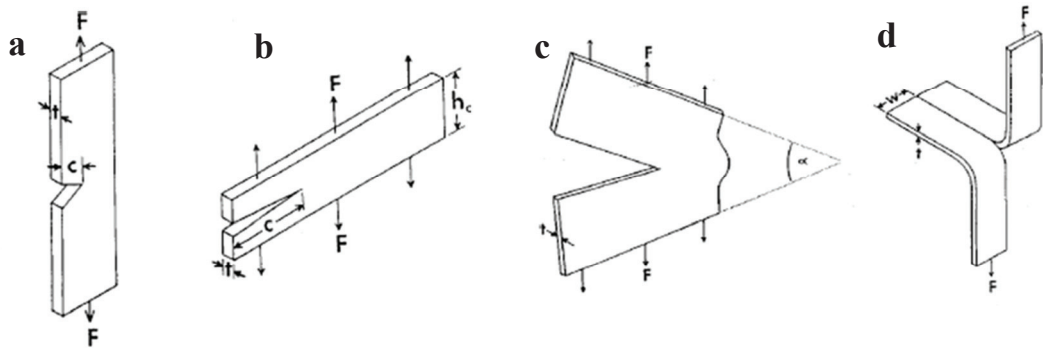


**Figure 51: Tests pieces commonly used for the calculation of the tear energy for rubber materials. Adapted from Tsunoda<sup>120</sup>. a: Single Edge Notched Stripe sample; b: pure shear; c: Y-shaped ; d: trouser.**

The Pure Shear geometry (b) is of particular interest due to the very simple relationship between the mechanical energy  $W$  brought to the sample and the critical energy release rate  $G_c$ :

$$G_c = Wh_0 \quad (40)$$

Where  $W$  is the density of elastic energy and  $h_0$  the height of the sample in the relaxed state. The crack propagation simply consists in transferring part of the material from the pure shear region B to the unstretched state region A (Figure 52).

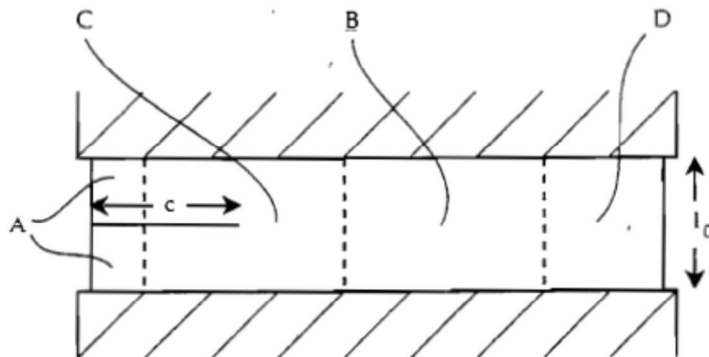


**Figure 52: Schematic strain regions in a pure shear test piece according to Thomas<sup>119</sup> : A unstrained region, C complex strain region around the crack tip, B : Pure Shear region and D : region with side effect.**

Thomas<sup>121</sup> has further proposed an empirical relationship relating the tear energy to the properties of the crack tip through the crack tip diameter  $d$  and a local energy density  $W_b$ :

$$G_c = W_b d \quad (41)$$

With the characteristic energy  $W_b$  that does not depend on the sample geometry.

Persson et al<sup>88</sup> have proposed that the energy per unit area to propagate the crack  $G$  is related to an energy required to break the bonds at the crack tip  $G_0$  and the viscoelastic dissipation in front of the crack tip crack tip  $f(v, T)$  depending on temperature and crack velocity.

$$G(v, T) = G_0(1 + f(v, T)) \quad (42)$$

This relationship is illustrated by the tear energies surfaces as reported by Thomas<sup>122</sup> for unfilled SBR (Figure 53a)). The energy required to propagate the crack (or tear energy according to Griffith criterion) increases with the increasing crack growth rate and decreasing temperature due to viscoelastic dissipation mechanisms at the crack tip.

As regards unfilled NR, the propagation was reported to be unstable with alternating phases of rapide crack advances and crack stop. Therefore the estimation of the crack propagation rate based on the imposed grip separation speed (trousers samples) did only enable to measure an average rate of tear. This explains why the tear energy seems not to depend much on temperature and propagation rate.

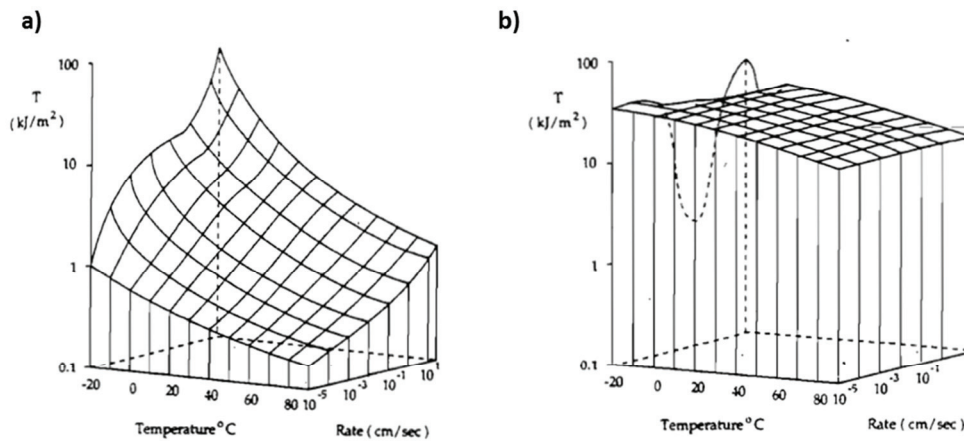


**Figure 53: Tear energy versus Temperature and crack growth rate (in trouser geometry) for a) unfilled SBR and b) unfilled NR<sup>122</sup>.**

A more appropriate dependency is proposed by Persson et al<sup>88</sup> for strain induced crystallizing elastomers (Figure 54). The tear energy is high at low crack propagation speed due to crack propagation instabilities but decreases as the SIC phenomenon is reduced for fast propagations. Above a critical propagation rate the crystallization at the crack tip does not have enough time to proceed and the tear energy increases again due to viscoelastic effect similarly to non-crystallizing rubbers such as SBR.

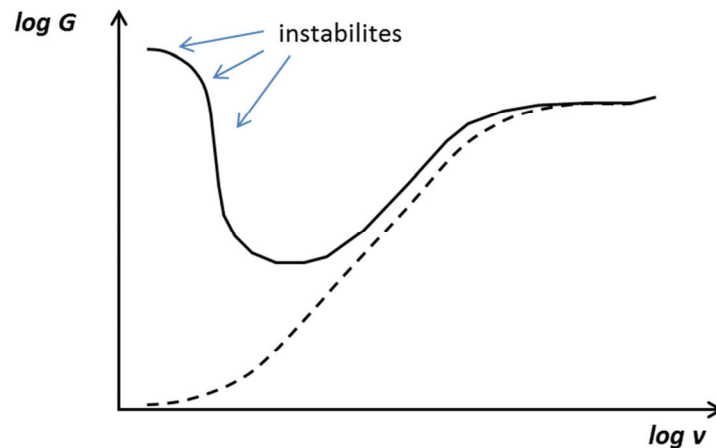


**Figure 54: Schematization of the dependence of crack propagation energy  $G$  on the crack velocity  $v$  for a non-crystallizing rubber (dashed curve) and a crystallizing rubber (continuous curve). Adapted from Persson et al.<sup>88</sup>.**

In recently reported works<sup>123</sup>, Sakulkaew and coworkers have shown the effect of strain rate on Tearing energy in various rubber formulations. Instead of trying to measure the crack velocity, they measured the strain energy release rate and the rate of change of the strain energy release rate i.e. the strain energy variation with time that can be associated with strain rate.

Their results indicate that in the case of non-crystallizing rubber (SBR), the critical strain energy release rate increases with the rate of change of the energy release rate (equivalent to the strain rate) as a result of visco-elastic strengthening. As far as Natural Rubber is concerned, a similar increase of the tear energy (i.e. critical strain energy release rate) is found for high solicitation rate but this regime follows a decrease of tear energy for lower rates. This decay was understood as the effect of SIC kinetics: the higher the strain rate and the lower the crystalline content at the crack tip. These authors also investigated the effect of temperature<sup>124</sup> and noticed that the transition between the two regimes is shifted to lower strain rate for increasing test temperature in agreement with the temperature effect on crystalline content (see II.3.c).

#### *II.4.b. Crack propagation instabilities*

The propagation instabilities mentioned by Persson et al. results in various propagation paths that are summarized in Figure 55. The stick-slip and knotty tearing have been observed in unfilled and filled NR<sup>125-127</sup>.

Note that stick-slip propagation can also be observed in filled SBR samples depending on the loading conditions as demonstrated by Greensmith<sup>128</sup>.

On the other hand, Hamed et al. and Gabrielle et al. have studied the tear rotation phenomenon<sup>127,129</sup> corresponding to a knotty tearing in reinforced Natural Rubber Single Edge Notched Tensile samples. In this geometry, the tear rotations have a length of typically several hundred micrometers in the relaxed state. The distance between consecutive rotations is of the order of 100  $\mu\text{m}$  as shown in Figure 56.

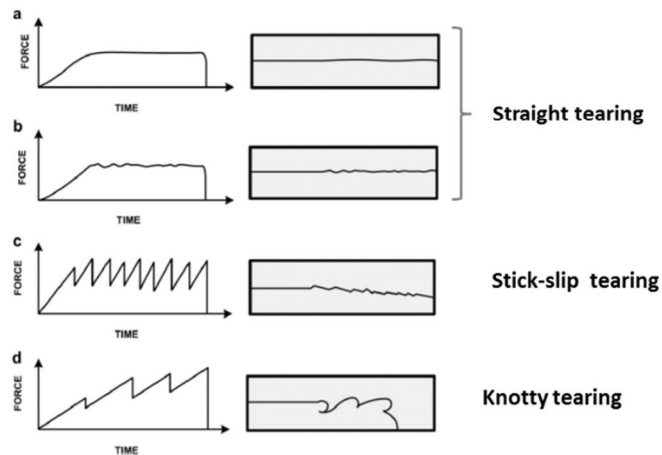


**Figure 55: Different Force versus time behavior associated with different propagation paths in trousers test samples made of Natural rubber according to Sakulkaew<sup>123</sup>.**

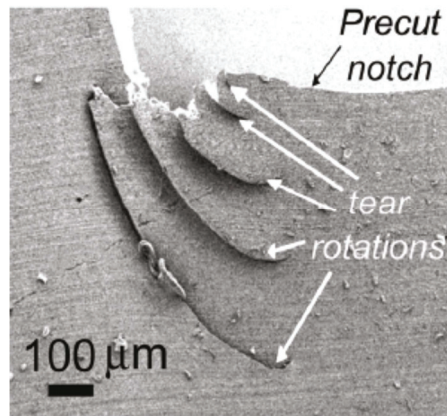


**Figure 56 : Tear rotations corresponding to crack propagation in the loading direction observed by SEM in the relaxed state. The typical rotation length by Gabrielle<sup>129</sup>.**

II.4.b.i. Tear bifurcations originate from anisotropy

Kendall<sup>130</sup> has manufactured specific test samples consisting of a thin sheet and a block of rubber put together. The thin sheet is cut with a razor blade and the propagation path is observed upon stretching: the crack can either propagate perpendicularly to the stretching direction in a cohesive way or deviate and follow the interfacial path (adhesive failure).

The effect of crack speed on crack deviation was analyzed showing that the cracks with high velocities propagate in a cohesive way and bifurcations were observed with low velocity cracks. The ratio of interface and cohesive fracture energies is found to be the main controlling parameter of the crack deviation process.

Gent et al<sup>131</sup> have also reported lower energy release rate for a crack propagation in the loading direction compared to a propagation in the notch plane based on a Finite Element Analysis.

One can expect that the occurrence of SIC at the crack tip increases the tear energy in the direction perpendicular to the stretching direction (i.e. the cohesive fracture in forward direction). In addition, the tear energy in the direction parallel to the stretching direction may be reduced due to the strong anisotropy and the gradient of crystallites content from the crack tip to the bulk.

The amount of anisotropy at the crack tip could thus be viewed as the driving factor of the cohesive and adhesive fracture energies ratio. The higher the anisotropy and the lower the adhesive fracture energy compared to the cohesive fracture energy. The anisotropy is increased in the case of Natural Rubber due to the crystallites at the crack tip. Another way to increase the anisotropy and thus the crack deviation potentialities is to add fillers to the rubber increasing the local strain amplification in the stretching direction.

The observations of Marano et al<sup>132</sup> on tear bifurcations in filled Natural rubber fit in this interpretation frame. These authors estimated the amount of mechanical energy release by the forward crack propagation and the one release by the sideways propagation in the case of uniaxial propagation by optical monitoring of the crack propagation. When increasing the carbon black content, the sideways energy decreases and the forward energy increases strongly promoting the crack bifurcation phenomenon.

They also studied the propagation path of the crack after drawing the sample in the direction of the crack thanks to a biaxial test (Figure 57). Their results show that above a given pre-drawing strain in the crack direction no sideways propagation occur due to the reduced anisotropy in the sample.

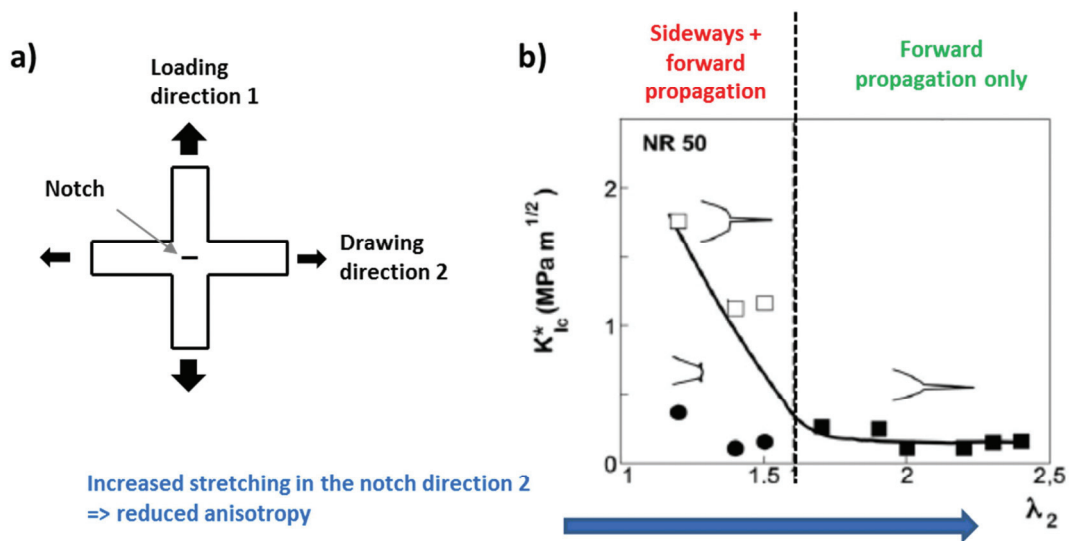


**Figure 57 : Biaxial experiments from Marano et al<sup>132</sup>: a) a notched sample is drawn up to a fixed extension ratio  $\lambda_2$  then loaded in direction 1. b) The stress intensity factor at failure  $K^*_{Ic}$  is computed from the stress at the onset of crack propagation and the notch initial length and reported as a function of  $\lambda_2$ : above a critical drawing ratio, no sideways propagations are observed.**

The effect of pre-cycling in the direction perpendicular to the loading direction on the crack bifurcations was also stressed by Gabrielle in his thesis<sup>74</sup>. The samples were first stretched in

direction 2 then a notched stripe of rubber is cut out of the initial rubber sheet and loaded in direction 1. The number and length of tear rotations was significantly reduced for samples precycled in direction 2 compared to as-prepared samples.

II.4.b.ii. Energetic explanation for the improvement of crack resistance in the presence of rotations

An interpretation to the high increase of energy density at failure imparted by the tear rotation phenomenon was proposed<sup>129</sup>. Tear rotation effectively corresponds to a large crack tip blunting: the longer the propagated crack in the direction of loading, the larger the effective tip radius (Figure 58).

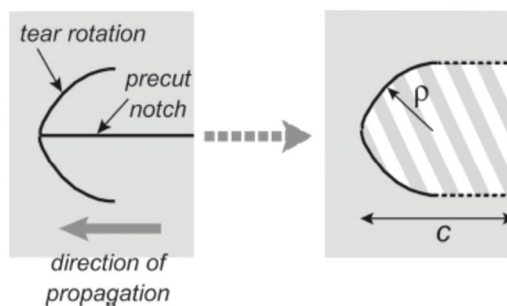


Figure 58: Schematization of the macroscopic crack tip radius creation by tear rotation (tip blunting)<sup>129</sup>

As a consequence, the energy density at break could be related to the sum of all rotation lengths measured in the relaxed state i.e. to the amount of crack tip blunting (Figure 59). The initial notch length was also taken into account to obtain a master curve for samples with various notch lengths.

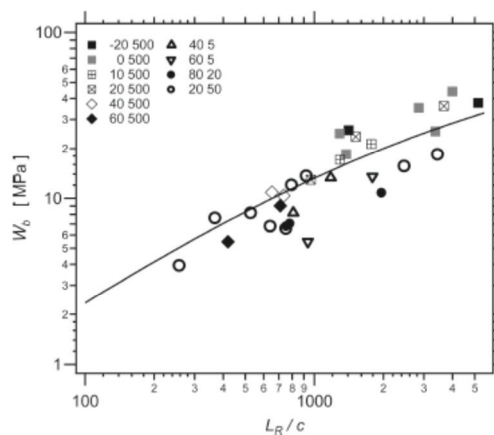


Figure 59: Energy density at break  $W_b$  as a function of the reduced total length of rotations (sum of rotation lengths  $L_R$  divided by initial cut length  $c$ ) for various temperature (first number of the legend in °C) and crosshead speeds (second number in mm/min). Reproduced from Gabrielle<sup>129</sup>.

### *II.4.c. Effect of material variables on crack propagation*

Hamed et al<sup>133</sup> have shown that an optimum of crosslink density existed in terms of crosslink densities for the resistance to crack propagation.

Gherib et al<sup>134</sup> have studied the failure behavior of unnotched and notched unfilled and filled SBR and NR samples. Their study highlights the effect of strain rate that lowers the energy at break in the case of notched samples. Higher energy at break in the case of silica-filled NR samples compared to carbon black when it comes to notched samples.

It was also proposed that the superior failure energy obtained with non-coupled silica SBR samples compared to covalently coupled and carbon black filled ones stems for higher dissipation properties through cavitation and crack deviation.

Gabrielle<sup>74</sup> has tested reinforced NR samples with two types of fillers namely precipitate Silica coupled to the rubber with TESPT and Carbon Black. The study of the crack propagation resistance and tear bifurcations phenomenon did not highlight any differences between those two kinds of samples having very similar mechanical properties.

## **II.5. Conclusion**

This literature review aimed at presenting the mechanical properties relevant for our work on reinforced Natural Rubber. The emphasis has been put on the supposed mechanisms and microstructural features at the origin of the observed macroscopic behaviors.

The following properties and phenomenon have been presented: the rubber elasticity, the Payne and Mullins effects relative to reinforced elastomers in respectively small and large strain regime, the Strain-Induced Crystallization and finally the crack propagation properties.

We have detailed the entropic origin of the modulus which originates in the flexibility of long chains connected by crosslinks.

The mechanisms controlling the Reinforcement at small strains and the Stress-softening effect (Payne effect) are still debated but a glassy and intermediate mobility layers percolation model was shown to account qualitatively for the observed properties even if the role of filler distribution is difficult to analyze in some systems. The modulus in the large strain regime has been attributed to the strain amplification phenomenon keeping in mind that the local chain stretching may be very heterogeneous.

The comparison of the Strain-induced crystallization in unfilled and filled Natural Rubber has confirmed the strain amplification effect. This phenomenon is also known to affect the tear behavior in particular due to a strain-induced crystallization phenomenon at the crack tip.

Finally the basics of crack propagation resistance studies have been presented. The effect of crack velocity on the critical energy release rate was shown and the propagation instabilities origin and effects have been detailed in Natural Rubber.

---

### III. Materials, Compounding procedures and Characterization methods

III.1. Components .....	71
III.1.a. Natural Rubber .....	71
III.1.b. Styrene-Butadiene Rubber .....	72
III.1.c. Reinforcing fillers .....	73
III.1.c.i. Carbon Black .....	75
III.1.c.ii. Precipitated Silica.....	76
III.1.d. Interface agents. ....	78
III.1.d.i. Coupling agents TESPT and NSC.....	79
III.1.d.i. Covering agent OCTEO .....	80
III.1.e. Vulcanization system .....	81
III.2. Formulations, processing and standard rubber tests .....	81
III.2.a. Formulations.....	81
III.2.b. Mixing procedures.....	83
III.2.b.i. Mixing in internal blender. ....	84
III.2.b.ii. Adding sulfur and accelerators. ....	89
III.2.b.iii. Determination of the vulcanization time by rheometry .....	90
III.2.b.iv. Vulcanization under press and storage.....	91
III.2.c. Rheology and other tests. ....	92
III.3. Characterization techniques.....	92
III.3.a. Dynamic Mechanical Analysis in small strains regime .....	92
III.3.a.i. Temperature sweep .....	93
III.3.a.ii. Strain sweep : Payne effect characterization.....	93
III.3.b. Mechanical measurements in the large strain regime .....	94
III.3.b.i. Tensile tests .....	94
III.3.b.ii. Dissipation at large deformations .....	95
III.3.b.iii. Tear tests .....	97
III.3.b.iv. Digital image correlation.....	98
III.3.c. Scanning Electron Microscope.....	100

III.3.d.	DQ Proton NMR .....	101
III.3.e.	Equilibrium swelling measurements .....	101
III.3.f.	X-ray diffraction experiments .....	104
III.3.f.i.	Description of the in-situ tensile device .....	104
III.3.f.ii.	Analysis of the X-ray Diffraction Patterns .....	106
III.3.f.iii.	Stroboscopic acquisitions during periodic cycling .....	113

In this chapter, the components, recipes and processing methodology used to elaborate the samples are presented.

The filled Natural Rubber recipes have been chosen close to industrial formulations of truck tire treads, at least in terms of filler fraction, vulcanization package and mixing parameters. However, the number of different components has been restricted here to the minimum in a view to simplify the formulations as much as possible. The compounding step is of particular importance for the properties of rubber composites. Indeed, properties depend to a large extent on mixing parameters such as temperature, rotor speed, mixing time and number of mixing steps. This confirms the important role played by the distribution of fillers on the final properties during such mixing procedure.

In a second part, the different characterization techniques that have been used as well as the analysis protocols are presented. Characterization techniques include standard rubber characterizations, mechanical tests, microstructure analysis tools and X-ray diffraction experiments.

### **III.1. Components**

A classical filled rubber recipe consists of the polymer matrix, a reinforcing system based on filler particles or aggregates and interface agents in the case of Silica, a vulcanization system based on sulfur and vulcanization agents (activators and accelerator) and an oxidation protector. A particular focus of this work was to study the impact of the interface agent on the properties in silica filled elastomers.

#### *III.1.a. Natural Rubber*

Natural Rubber manufacturing starts with the harvesting of the latex of the rubber tree (*hevea brasiliensis*) containing about 40% in weight of rubber. The obtained latex is diluted in water and coagulated to separate the rubber from the water, forming a solid matter called the coagulum. Different types of Natural Rubber can be produced depending on the coagulation method:

- Crepe rubber is obtained from a sodium hydrogen sulfite coagulation followed by washing and milling and air-drying steps. It yields high quality NR sheets with very low impurities amount.
- Ribbed Smoked Sheets (RSS) are produced from a formic acid or acetic acid coagulation of the latex. The milled coagulum is washed in a less intensive procedure compared to crepes therefore the sheets undergo a preservation process: they are “smoked” that is to say dried in smokehouse for one week. The sheets are visually graded according to their color, consistency and impurities.

Standard Rubber (or Technically Specified natural Rubber TSR) is the most widely used kind of Natural Rubber. This denomination does not refer to a specific processing method but is rather a grading scheme introduced to specify the rubber quality based on impurity contents. The limit contents for each grade limits are fixed by the producing country, which is why the origin of Standard Rubber must always be specified.

All Natural Rubber compounds were made of SMR 5L (L stands for light color) whose technical specifications are listed in

Table 1. In addition to the specified contents, the main impurities are lipids and proteins, polyisoprene itself representing 94% of the total mass.

Parameter	Maximum content
<b>Dirt Retained on 44<math>\mu</math>m aperture (wt %)</b>	0.05
<b>Volatile matter (wt %)</b>	0.80
<b>Nitrogen (wt %)</b>	0.60
<b>Ash Content (wt %)</b>	0.60

**Table 1 : Technical specifications for Standard Malaysian Rubber SMR 5.**

The stereoregularity of chains is very high for Natural Polyisoprene with 99.9% of monomers in cis conformation (Figure 60). As a comparison, synthetic polyisoprene shows a fraction of cis units of 98.5% at most. It is believed that this higher stereoregularity imparts unrivalled Strain induced crystallization properties even though some authors argue that the non-rubber components as proteins and lipids play the role of nucleating points enhancing the crystallization properties<sup>95</sup>.

Another important feature of Natural Polyisoprene is the huge molecular weight of the chains, which is often comprised between one or several millions of grams per mole ( $10^6$  g.mol<sup>-1</sup>).

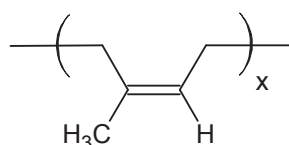


**Figure 60 : Molecular formula of cis-polyisoprene.**

### *III.1.b. Styrene-Butadiene Rubber*

Styrene-Butadiene Rubber (SBR) is a random synthetic copolymer obtained either by emulsion or in solution by anionic polymerization. The copolymer properties such as the glass transition temperature depend on the ratio of styrene (x), 1,4-butadiene (y; cis and trans) and 1,2-butadiene (z; vinyl) groups. According to the nomenclature, the SBR grade is denoted by the vinyl group (z) and styrene group (x) contents (see Figure 61).

All presented results on SBR samples were obtained using a non oil-extended solution SBR 2525 supplied by Lanxess.

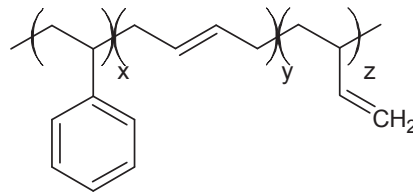


Figure 61 : Molecular formula of a SBR copolymer

### III.1.c. Reinforcing fillers

Reinforcing aggregates are characterized by their morphology and their surface activity, both depending on their synthesis process and chemical composition. The morphology can be described by several parameters describing the size, shape and organization of the multi-scale constituting entities of the filler:

- The **elementary particle size**, which is also referred as the fineness of the particles, drives the **specific surface** of aggregates, i.e. the surface of the aggregate per unit mass (Figure 62).

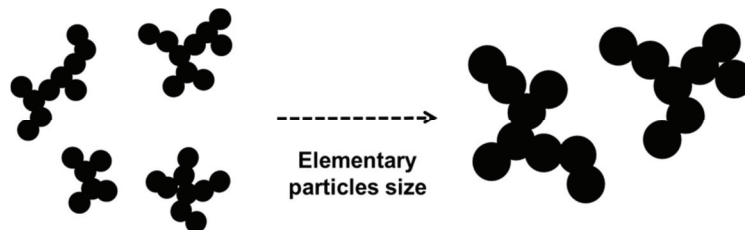


Figure 62: Elementary particle size effect on filler specific surface (at constant filler weight fraction)

The specific surface  $S$  (in  $\text{m}^2/\text{g}$ ) is related to the particle radius  $R$  by

$$S = \frac{3}{\rho R} \quad (43)$$

With  $R$  expressed in m and the density  $\rho$  in  $\text{g}/\text{m}^3$ .

Specific surface measurements are carried out by absorption of a probe molecule called CTAB (Cetyl Triethyl Ammonium Bromide) which is supposed to accurately represent the approach of a rubber chains on the filler surface.

- **Aggregate size and structure** are closely related parameters based on the number of elementary particles constituting an aggregate and the shape of the aggregate which can have a tenuous, fractal like or more compact configuration (see Figure 63). The compactness of the aggregate is an important parameter which impacts the distance to neighbors and the fraction of occluded rubber, for a given volume fraction. Occluded rubber is the fraction of chains trapped in the filler tortuosity, which are supposed to remain unaffected by constraints applied to the material. The more tenuous the aggregates, the larger their size at a given aggregate mass, and thus, the smaller the inter-aggregate distances at a given volume fraction.

At a given filler fraction, increasing the aggregate size tends to very slightly decrease the specific surface, for there are more contacts between elementary particles, and to increase quite significantly the intra-aggregate occluded rubber fraction.

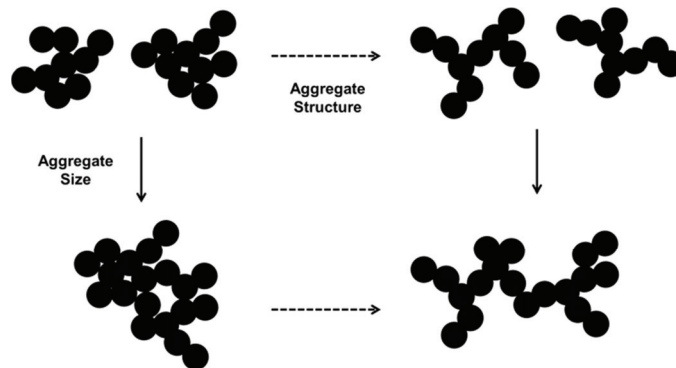


**Figure 63: Schematics of aggregate Size and Structure (at constant filler weight fraction)**

The structure of reinforcing aggregates is measured thanks to oil absorption experiments using Dibutylphtalate (DBP). It was proposed that the effective fraction of rubber that is not trapped within the filler structure can be directly deduced from measurement of the DBP index i.e. the absorbed milliliters of oil per hundred grams of filler (equation 5 in chapter 2).

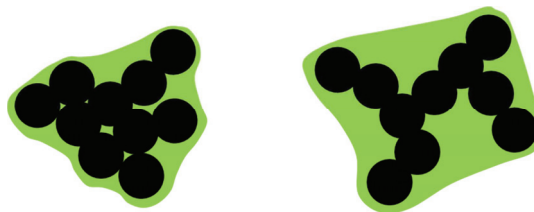


**Figure 64: Effect of filler structure on DBP absorption.**

- The **microporosity** of the filler surface can be estimated with the BET method relying on nitrogen adsorption. Contrary to CTAB molecules, micropores are accessible to nitrogen.

The microporosity, defined here as the difference between BET and CTAB measurements, is not relevant for the interactions between the polymer and the filler surface since micropores are not accessible to the large rubber macromolecules. Nevertheless it is important to control that the microporosity is low, because of the potential adsorption of active species such as vulcanization and coupling agents.

The notion of surface activity will be discussed in the next section dedicated to Carbon Black and Silica which are the most common kinds of reinforcing fillers compounded with rubber in the tire industry.

### III.1.c.i. Carbon Black

Carbon Black is produced by controlled pyrolysis of hydrocarbon products. A wide range of carbon black sizes and structures can be obtained depending on the process type. Carbon black grades are classified according to their reinforcing effect, i.e. specific surface and structure. The ASTM denomination (Table 2) consists of three numbers, the first one stands for the specific surface range and the two other ones are related to the structure of the aggregates. In general the more open the structure is and the lower the numbers (a N326 black has a higher structure than a N358) even though there is no direct proportionality rule between the numbers and a measured parameter. A prefix letter is also assigned to indicate if the carbon black filler imparts a normal or slow vulcanization time (N or S). Nowadays most grades belong to the first group (N), since channel blacks that affected crosslinking are almost no longer used.

In tire treads, in which highly reinforcing blacks are needed, high abrasive furnace blacks from the series N300 to N100 are used. Products from series N700 to N400 are designed for the tire carcass or flanks and low reinforcing thermal blacks are used for profiles such as hoses, pipes and seals.

Primary particle diameter (nm)	Specific surface (m <sup>2</sup> .g <sup>-1</sup> )	ASTM denomination	Previous nomenclature
201-500	0-10	900-999	Medium Thermal
101-200	11-20	800-899	Fine Thermal
61-100	21-32	700-799	Semi-Reinforcing Furnace
49-60	33-39	600-699	General Purpose Furnace
40-48	40-49	500-599	Fine Extrusion Furnace
31-39	50-69	400-499	Fine Furnace
26-30	70-99	300-399	High Abrasive Furnace
20-25	100-120	200-299	Intermediate Super Abrasive Furnace
11-19	121-150	100-199	Super Abrasive Furnace
1-10	>150	0-99	-

**Table 2 : Particles diameter, specific surface and denomination according to the ASTM Nomenclature.**

Microscopy observations<sup>135</sup> of the carbon black surface have revealed overlapping of graphitic sheets in an onion-like morphology (Figure 65). This results in high energy sites on the edge of graphitic sheets, whereas graphitic planes have lower interactions. High energy sites are believed

to be at the origin of the high reinforcement properties of Carbon Black. This is confirmed by poor reinforcement results obtained after graphitization of carbon blacks, a thermal treatment that reduces the number of edge sites by smoothing the surface of the particles.

The carbon black grade that we have used is N234, which has a mean aggregate diameter of 90 nm and a specific surface of  $120 \text{ m}^2 \cdot \text{g}^{-1}$ .

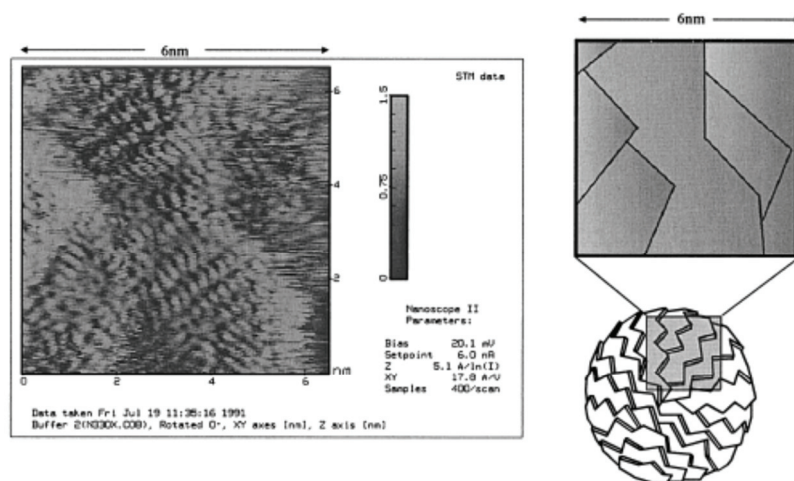


**Figure 65: Scanning Tunneling Microscope (STM) picture of the Carbon Black surface structure<sup>135</sup>.**

### III.1.c.ii. Precipitated Silica

Precipitated silica is obtained by the action of an acid on the sodium silicate originating from sand and sodium carbonate. The synthesis is carried out in aqueous phase and the targeted physico-chemical properties are tuned by controlling the key parameters temperature, pH and reaction time.

Four Rhodia Silica grades have been used (see Table 3), all of them denoted Z for Zeosil which corresponds to a precipitation process type. Thanks to a specific drying process, the silica particles are under the form of non pulverulent agglomerates of several micrometers (MP stands for micropearl) at the end of the synthesis, allowing easy handling.

Typical analysis value	Z1085 Gr	Z 1115 MP	Z 1165 MP	Z HRS 1200 MP
BET Surface area ( $\text{m}^2 \cdot \text{g}^{-1}$ )	85	115	165	205
CTAB Surface area ( $\text{m}^2 \cdot \text{g}^{-1}$ )	80	110	160	200
Mean Aggregates Diameter (nm)	100	70	50	40

**Table 3 : Typical specific surfaces and aggregate sizes for highly dispersible Rhodia Silicas**

The Silica manufactured by Rhodia under the Zeosil brand are called highly dispersible silica, for the agglomerates break down easily under the applied shear in the rubber mixer into nanometer size consolidated aggregates that finely disperse in the rubber matrix (Figure 66

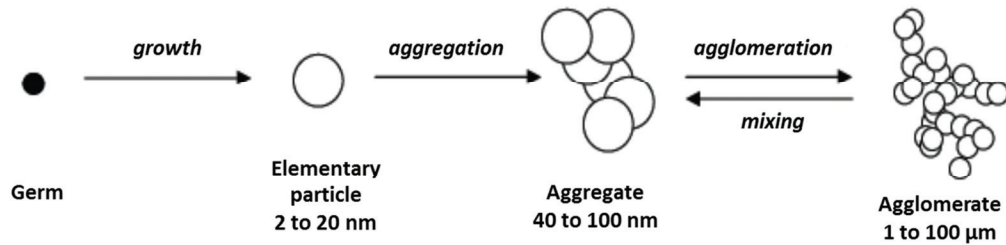


**Figure 66 : Multi-scale organization of silica particles during synthesis and mixing steps.**

Unless otherwise specified in the next chapter, the Silica that we have used is Z 1165 MP (specific surface of approximately  $160 \text{ m}^2.\text{g}^{-1}$ ), that we took as a reference for its very good reinforcement properties. The other three grades of silica in Table 3 have homothetic structures. Only the primary particle size changes, with no change in the number of primary particles per aggregate or in the aggregates shape (see Figure 63). This is illustrated in Figure 67: the aggregate mean diameter is directly related to the primary particle size.

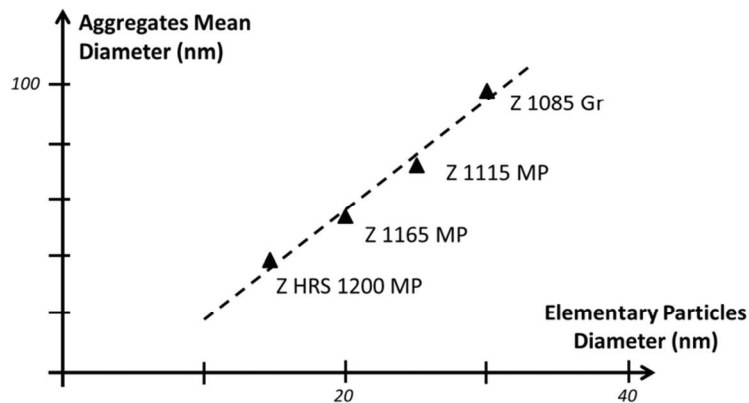


**Figure 67 : Direct correspondence between the elementary particle diameter and the aggregate mean diameter in a series of ‘homothetic’ (measured by X-ray Disc centrifugation)<sup>136</sup>**

At this point, it is also important to keep in mind the broad distribution of aggregate sizes for a given grade of silica as shown in Figure 68.

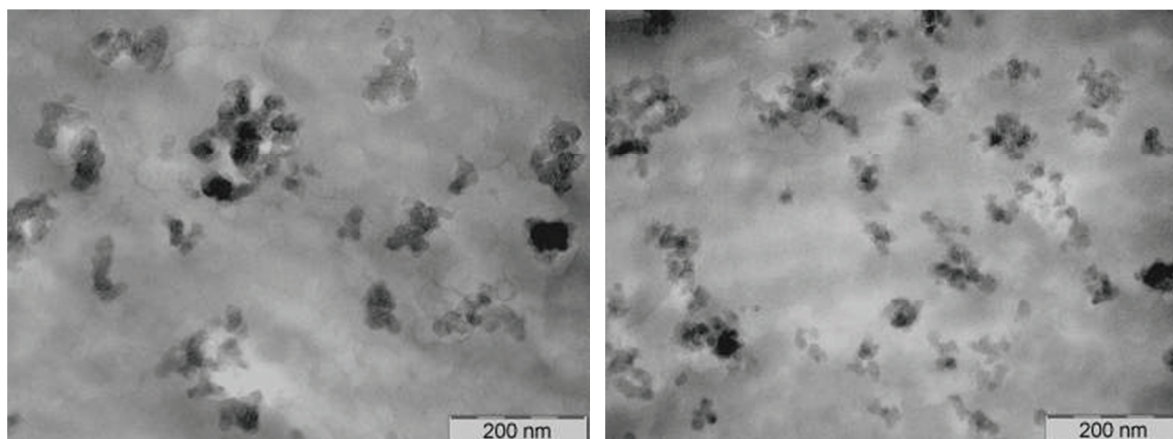


**Figure 68: TEM pictures (magnification x100000) performed by Rémi Sellier (Rhodia) of swollen NR samples filled with 50phr of: a) Silica Z1115MP (120m<sup>2</sup>/g) and b) Silica Z1165MP (160m<sup>2</sup>/g). The same interfacial agent TESPT was used in both cases (sample series 021-10).**

The physico-chemistry of the silica surface is of importance for the interactions with rubber and for the silica-silica interactions as well. The functional groups present at the surface are mostly made of polar groups such as silanols (Si-OH) along with some siloxane functions (Si-O-Si). Thus, conversely to the case of Carbon blacks, the silica surface is mostly hydrophilic and has a high surface tension with the rubber, which is hydrophobic. Therefore, the interactions taking place with the rubber macromolecules do not enable a high reinforcement at high strain.

The presence of Silanols induces hydrogen bonding interactions between adjacent particles, stronger than filler-rubber interactions, which are at the origin of strong filler-filler interactions. This characteristic feature of silica nanoparticles must be overcome in order to obtain a proper dispersion of silica within the rubber matrix, by using chemical interface agents that shield direct silica-silica interactions upon grafting on the silica surface. As a consequence, the compatibility, or wettability, of the silica fillers with the rubber matrix, and thus the dispersibility, is improved. Much better mechanical properties result.

In the case of fumed silica, the silanol density is of the order 2 silanol groups per square nanometer, whereas it may reach 6 or 10 silanols for precipitated silica.

The pH value and water content at the silica surface have to be finely controlled to ensure an efficient reaction with the coupling agent. In particular, if the water content is too low, the silanization reaction, which requires water molecules, will not be complete. Conversely, excessive water contents are expected to increase condensation of the coupling agent molecules. According to Mihara<sup>66</sup>, the control of the pH as well as of the silica drying process are key parameters to control the synthesis of a highly dispersible silica.

#### *III.1.d. Interface agents.*

Let us define the denominations ‘coupling agents’ and ‘covering agents’ that will be used throughout the manuscript: on the one hand (covering agent) the interfacial molecules only graft on the silica surface and provides shielding of direct interactions between silica particles, on the

other hand (coupling agent) the interfacial molecules graft on the silica surface, thus shielding silica-silica interactions, and also reacts with the rubber chains to create covalent bonds between the elastomeric matrix and the fillers.

### III.1.d.i. Coupling agents TESPT and NSC

Figure 69 gives the chemical formula of bis(triethoxysilylpropyl)tetrasulfane (TESPT). Actually, commercial Si69 silanes are a mixture of polysulfanes with a number of sulfur atoms ranging from 2 to 10 with an average sulfur length around 3.8<sup>137</sup>.

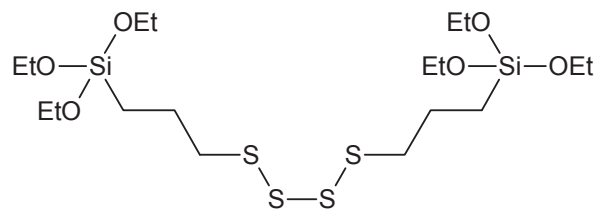
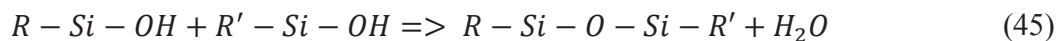
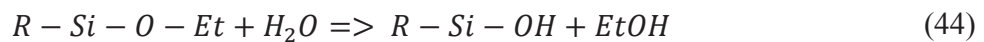


**Figure 69 : Chemical structure of the coupling agent TESPT**

It was proposed that the chemical grafting on the silica surface takes place in two steps<sup>138</sup> (Figure 70).

In the first step, a primary hydrolysis reaction occurs between one ethoxy group of the coupling agent and one silanol group of the silica surface yielding ethanol. It is then followed by the condensation of the coupling moiety (R) on the silica surface (denoted R' in equation (45)).



The second step consist of further condensation of the remaining ethoxy groups with neighboring TESPT ethoxy groups and OH groups on the silica surface.

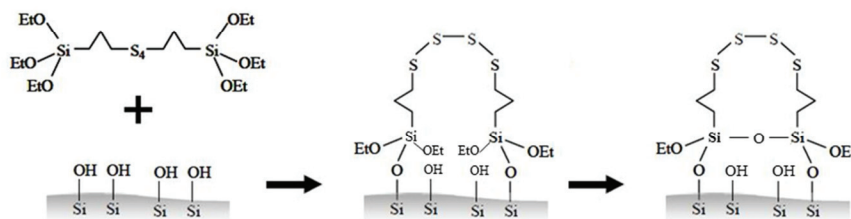


**Figure 70 : Silanization: TESPT grafting on the Silica surface in two steps during rubber mixing.**

One should emphasize the relatively small fraction of the available number of silanol groups actually occupied by the coupling or covering agent. It is thought to be of the order of 1 to 1.2

molecule of TESPT per square nanometer for a density of silanol groups between 6 and 10 silanol groups per square nanometer<sup>11,61</sup>. This means that a large fraction of the silanol and siloxane functions are still available to interact with the rubber chains.

The reaction of the TESPT polysulfidic moiety with the rubber chains is often represented as the breakage of the instable sulfur-sulfur bonds which react on the unsaturated rubber chains according to a mechanism that is supposed to be similar to the vulcanization one.

According to the work of Luginsland<sup>137</sup>, the efficiency of the TESPT reaction with squalene (which should behave in the same way as rubber chains) is greatly improved when introducing the vulcanization accelerator CBS to the mixture. We thus conclude that the rubber coupling may possibly occur during the mixing step to some limited extent but mainly takes place during the curing phase.

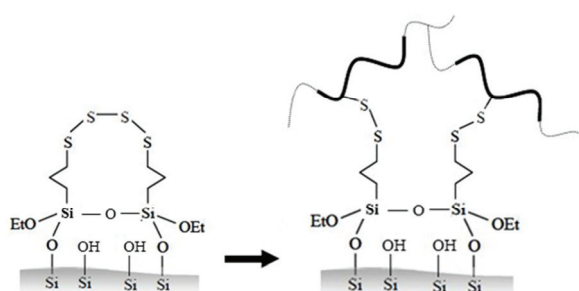
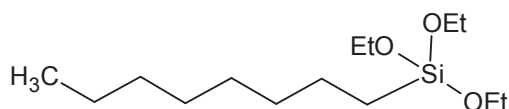


**Figure 71: TESPT coupling with rubber chains mainly during the vulcanization process**

A second coupling agent (which shall be denoted NSC for Non-Sulfurized Coupling) has been used in this study. It is composed of the same reactive moiety towards silica and a non-sulfurized functional group that is supposed to react with the rubber chains through a radicalar reaction during the mixing step. Note however that no significant increase in the viscosity of the compound during mixing (uncured compound) was detected.

#### III.1.d.ii. Covering agent OCTEO

The covering agent that was used is shown in Figure 72. The triethoxysilyl group is identical to that in the coupling agents, ensuring a comparable degree of grafting on the silica surface. The hydrocarbon chain has eight carbons, which is comparable to the length of the coupling agents. As a matter of fact, it has been demonstrated that the length of the covering agent strongly influences the mechanical response of the composite<sup>139</sup>.

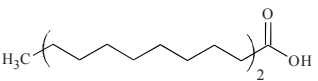
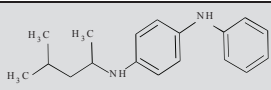
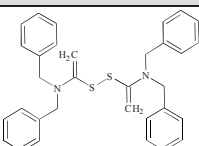
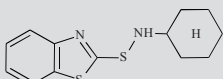


**Figure 72 : Chemical structure of the covering agent OCTEO**

### III.1.e. Vulcanization system

The vulcanization system consists of two activators, one vulcanization agent and two accelerators. In the case of sulfur, which we have used as vulcanization agent, several additives contribute to achieve a fast and efficient formation of the network, as required in the industrial manufacturing of tires. The ingredients of the vulcanization system are summarized in Table 4. Stearic acid will form a complex with Zinc Oxide, which is the starting point of the complex vulcanization reaction. This zinc oxide complex is progressively recovered as the reactions proceed. Activators are expected to delay the onset of sulfur bridge formation and to increase significantly the reaction rate. The final number of sulfur bridges is of course controlled by the sulfur amount, but also by the CBS amount. Indeed, the presence of this accelerator in larger amount reduces the average length of sulfur bridges<sup>103</sup>.

In addition to the vulcanization system, 6PPD was added as a protection against oxidation and ozonation. As ageing of the rubber network involves creation of radicals, the role of the protector is to react with those species to inhibit degradation processes.

Component	Chemical Structure	Function
Zinc Oxide	ZnO	Activator
Sulfur	S <sub>8</sub>	Vulcanization agent
Stearic Acid		Activator
6PPD		Protector
TBzTD		Secondary Accelerator
CBS		Primary Accelerator

**Table 4 : Chemical structures of the vulcanization system components and protecting (antioxidation) agent.**

## III.2. Formulations, processing and standard rubber tests

### III.2.a. Formulations

The recipes are always expressed in phr units (per hundred rubber), that is to say in grams of component per 100 grams of gum. Most of our compounds include a volume fraction of fillers of

about 18% which corresponds to 50phr of Silica and 45phr of Carbon Black the density of the two fillers being slightly different. All sample series that have been elaborated during the thesis are summarized in Table 5 . The samples have been processed in the Rhodia Silica application laboratory in collaboration with Benoit Moreaux (Rhodia Silica). All detailed recipes are available in the appendices. The possible variable parameters in a compounding campaign were the interface agents, the filler type (carbon black and different silica), the filler volume fraction and the crosslink density.

Sample series identification	Blender type	Number Of compounds	Variable parameter(s)	Remarks
021-10	Brabender 390cm <sup>3</sup>	9	Silica interface	
054-10	Banburry 1L	2	Silica/carbon black	
095-10	Banburry 1L	6	Silica type and interface	Mixing in one phase
115-10	Brabender 70cm <sup>3</sup>	9	Filler volume fraction and interface	
030-11	Banburry 1L	7	Interface and crosslink density	
046-11	Banburry 1L	6	Silica type and crosslink density	
119-11	Banburry 1L	15	Interface and Crosslink density	
038-12	Brabender 390cm <sup>3</sup>	12	Interface and Silica volume fraction	SBR matrix
051-12	Haake 300cm <sup>3</sup>	8	Interface and process	NR and Natsyn matrix

**Table 5 : List of all sample series with the reference of the used mixing tool (blender), the number of manufactured compounds and variable parameters. The detailed recipes can be found in appendices.**

The studies presented in the following chapters have been carried out on different samples series that will be specified each time. Most of the presented experiments concern samples from series 95-10, 30-11, 46-11 and 119-11. An example of recipes for the sample series 119-11 is given in Table 6.

Formulation	1	2	3	4	5	6	7	8	9	10	11	12	13	14	15
SMR 5L	100	100	100	100	100	100	100	100	100	100	100	100	100	100	100
Z 1165 MP	50	50	50	50	50	50	50	50	50						
N234													45	45	45
TESPT	4	4	4												
OCTEO				4,1	4,1	4,1									
NSC							4,5	4,5	4,5						
6PPD	1,9	1,9	1,9	1,9	1,9	1,9	1,9	1,9	1,9	1,9	1,9	1,9	1,9	1,9	1,9
Stearic Acid	2	2	2	2	2	2	2	2	2	2	2	2	2	2	2
ZnO	4	4	4	4	4	4	4	4	4	4	4	4	4	4	4
Sulfur	0,5	1,5	2,5	0,5	1,5	2,5	0,5	1,5	2,5	0,5	1,5	2,5	0,5	1,5	2,5
CBS	0,66	2	3,33	0,66	2	3,33	0,66	2	3,33	0,66	2	3,33	0,5	1,5	2,5
TbZTD	0,2	0,2	0,2	0,2	0,2	0,2	0,2	0,2	0,2	0,2	0,2	0,2	0,2	0,2	0,2

**Table 6 : Typical compounds formulation: sample series 119-11.**

The amount of coupling agent has been optimized in previous internal Rhodia studies, stating that for a Z1165 silica fraction of 50phr no further variation of the properties was observed above an optimum TESPT amount of 4phr. When using different silica volume fractions or silica grades with a different specific surface, the quantity of interface agent is adjusted in proportion to the total surface of filler in the material (the product of the quantity and the specific surface (denoted *SSA*) of the considered silica) according to the equation:

$$TESPT (phr) = 0.0005 \times Silica(phr) \times SSA(m^2.g^{-1}) \quad (46)$$

Taking into consideration the adsorption of part of the vulcanization accelerator CBS on the silica surface, the amount of this component should also be corrected in proportion to the total silica surface, based on adsorption isotherm corrections proposed by Bomo<sup>140</sup>. Nevertheless, it was chosen not to modify the CBS amount upon changing the silica specific surface or amount. The actual changes in crosslink density were measured by DQ-NMR. Only in samples filled with carbon black was the CBS amount comparatively reduced in order to obtain similar crosslink densities and thus comparable mechanical behavior in tear experiments as silica filled samples. When studying the influence of the crosslink density, the amounts of both sulfur and CBS were modified, but the ratio of the two quantities was kept constant (CBS/S=1.3) in order to obtain sulfur bridges of similar average lengths.

### III.2.b. Mixing procedures

Once the components proportions have been chosen, the amounts that will be blended are computed by taking into account the empty volume of the blender and the filling factor. Filling factors vary between 0.6 and 0.8. They are adjusted to the estimated viscosity of the compound in the blender, which depends primarily on the filler fraction. The mixing procedure mainly consists in three steps that are schematized on the temperature profile presented in Figure 73. The first step is the mixing itself in a closed blender, followed by the incorporation of the vulcanization system (sulfur and accelerators) in an open mill. An intermediate characterization of the vulcanization time is carried out on a rheometer before launching the vulcanization process under press, which takes place at 150°C in the case of Natural Rubber.

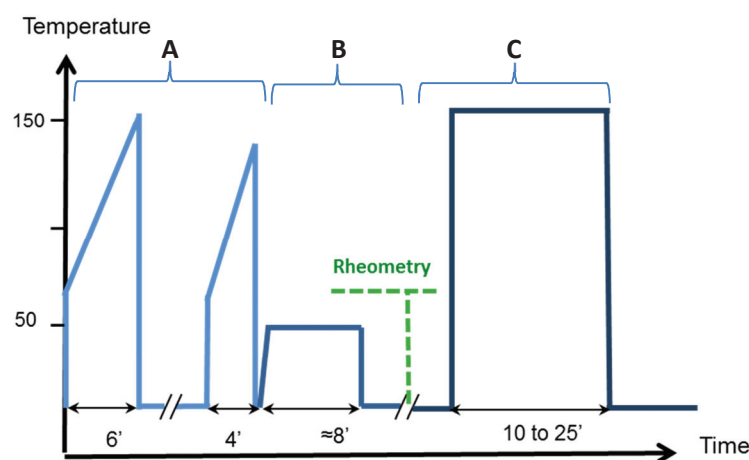


**Figure 73 : Temperature profile for the compounding steps in the case of Natural Rubber: mixing (A), incorporation of vulcanization system (B) and vulcanization (C).**

Note that in sample series 030-11 and 119-11, one single formulation (one recipe) obtained after internal mixing was split into 3 different formulations before adding vulcanization ingredients on the roll mill, in order to get samples with different crosslink densities out of the same initial batch. In this way, the variability usually observed from one batch to another was minimized, ensuring that only the vulcanization was modified, leaving other parameters (precise composition of the rubber matrix batch, dispersion of fillers) unaffected.

For instance, a batch of 1 kilogram of NR Silica TESPT was split into 3 sub-batches of 330g and each was added with a different vulcanization package, i.e. with different sulfur and CBS amounts.

Incorporation of silica in a rubber matrix in the blender is a complex process which involves several mechanisms. The impact of the processing parameters on the properties of the final composite is very important. In this regard the rubber blender can be viewed as a chemical reactor in which a combination of simultaneous and stepwise reactions take place, among which the principal ones are the plasticization of rubber, the breakdown and re-agglomeration of filler agglomerates, the wetting of the filler surface by rubber chains and the silanization reaction.

### III.2.b.i. Mixing in internal blender.

- ***Mixing procedure***

The first mixing steps were usually performed in a Banburry or a Brabender internal mixer of respective empty volumes of 1L and 390cm<sup>3</sup> (other blenders have been used occasionally). The tangential rotor technology (Figure 74) is used in both mixers. The advantage of the Brabender mixer was the possibility to record the evolution of temperature and torque during the mixing

process, which was impossible in the case of the Banbury mixer. In order to obtain a proper grafting of the interface agents on the silica surface, the target for the mixing phase is to maintain for about 1 minute a temperature of 150°C in the blender at the end of the first mixing phase.

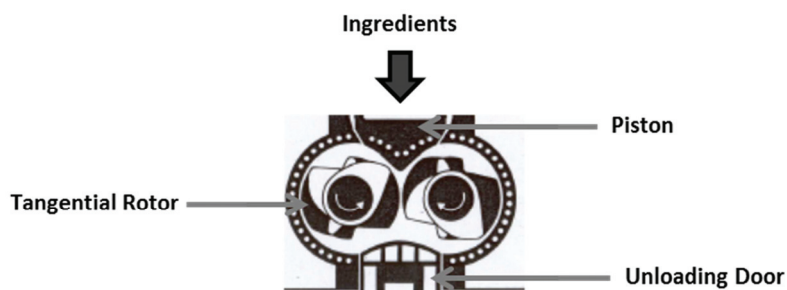


**Figure 74: Schematics of a tangential rotor mixer<sup>141</sup>. The mixed ingredients are added through the loading door by removing the piston.**

The mixing sequence always starts with the introduction of the rubber taken as the initial time. The filler is then added in two steps (first 2/3, then 1/3 of the final filler amount, respectively) in order to guarantee a better incorporation and dispersion of the particles. This same procedure was used for both carbon black and silica. The whole amount of coupling or covering agent was added to the first 2/3 of silica and zinc oxide was introduced with the second filler part. At the temperatures reached in the mixer, the stearic acid crystals melt and play the role of lubricant of the filled rubber mix, thus decreasing the torque and heat build-up. The introduction time of stearic acid was thus adjusted in order to obtain the desired plateau at 150°C for 1 minute. The blender opening time was also adjusted in order to control the time spent at high temperature.

Component added	Introduction Time
Rubber	0'
2/3 Silica + Coupling agent	1'30
½ Silica + ZnO	3'30
Stearic Acid	5' to 5'30
Unloading door opening	6' to 7'

**Table 7 : Introduction sequence for Silica filled NR.**

- *Torque and temperature profile*

The evolutions of temperature and torque are given in Figure 75 for a standard NR Silica TESPT recipe. The initial temperature was fixed here at 75°C and the rotor speed at 60 rpm (rotation per

minute), these parameters were adjusted in other sample series depending on the mixer type, the fill factor and the filler fraction. It should be noted that the temperature gauge was not accurate at the end of the mixing phase and the temperature was instead measured on the compound right after opening the mixer with a thermocouple. The final temperature measured was then close to 145°C which is in agreement with the requested final plateau at approximately 150°C.

The incorporation of a component corresponds to a drop of the torque during the introduction time where no ram pressure is applied to the mix. Apart from this, the torque increases significantly each time filler is added and then lowers. The temperature increases up to 150°C but stabilizes once the stearic acid is introduced for lubricating the mixture. The torque is reduced as well.

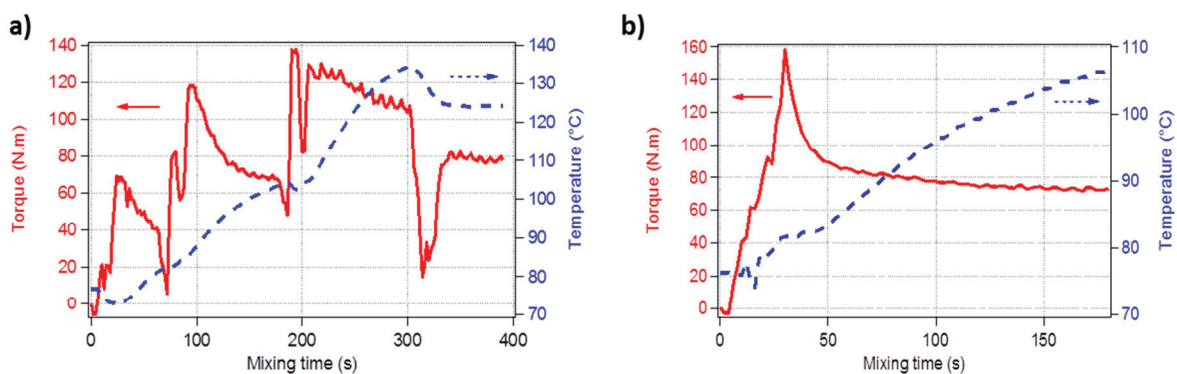


**Figure 75: a) First and b) second mixing phases: Torque and Temperature profiles.**

The decrease of the torque after introducing each component highlights the combined effect of the rubber mastication/plasticization and the dispersion of the filler in the rubber:

- As far as mastication is concerned, it can be evidenced by the important drop of the Mooney viscosity when mixing Natural Rubber without adding any filler. It was found that during a 6 minute mixing step at maximum temperature close to 140°C, the Mooney viscosity falls from 90 to roughly 40 whereas a 10 minutes mastication of the same rubber on a rolling mill yields a Mooney viscosity of approximately 60.
- The second process is related with the breakdown of agglomerates and the distribution of aggregates that lowers the composite viscosity.

It is important to make the distinction between the dispersion and distribution concepts (in the same way as in the mixing of immiscible polymers), even though both processes are likely to occur simultaneously and to be closely interrelated during the mixing of fillers with rubber.

**Distribution** can be defined as the process that creates a spatially more or less random, thus more homogeneous, repartition of particles, without considering changes on their size.

**Dispersion** corresponds to the reduction of the agglomerate sizes down to their final aggregate size. An example of partially broken agglomerate is shown in Figure 76, showing the resulting highly filled zone where numerous aggregates do not interact with the rubber matrix.

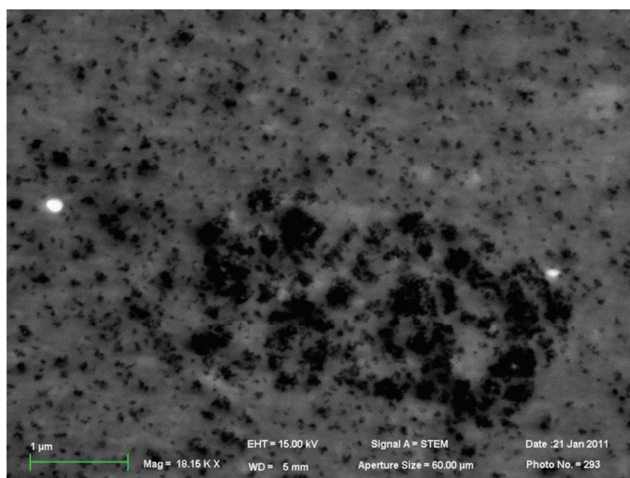


**Figure 76: Highly filled zone due to incomplete breakage of a Silica agglomerate (STEM picture, NR Silica swollen in styrene).**

Wang<sup>142</sup> proposed that the incorporation of the Carbon Black agglomerates to the rubber phase was followed by first the distribution and then the dispersion phase, in which the agglomerates are progressively destroyed into unbreakable aggregates according to an onion peeling like or erosion process (see Figure 77). On the other hand, it may also be considered that dispersion starts prior to agglomerate distribution. Nevertheless, the most plausible scenario is that both phenomena are concomitant. They probably depend in a crucial way on the input energy brought to the sample. In this respect it might be interesting to carry out a full study of the effect of different interface agents in terms of mixing energy.

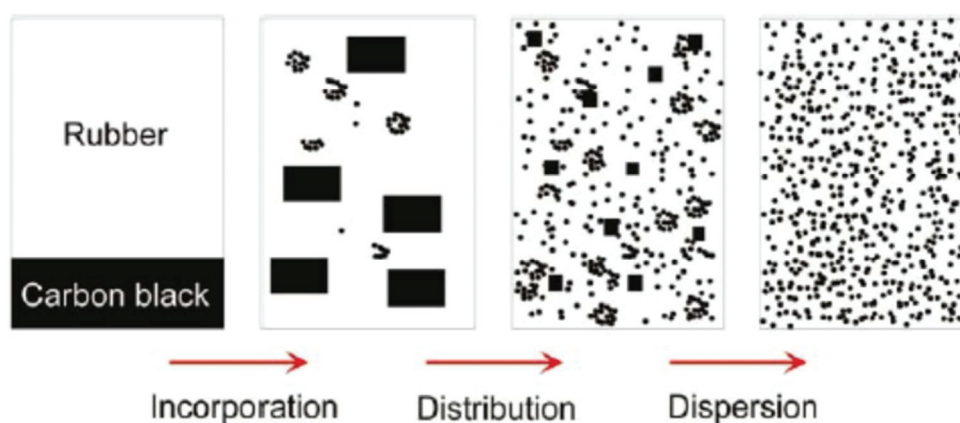


**Figure 77 : Incorporation in the rubber in the case of Carbon Black. Distribution and Dispersion processes according to Wang<sup>142</sup>.**

The surface energy plays a key role on the dispersion and distribution of the fillers in the rubber matrix. It has been observed that increasing the polymer surface energy closer to the filler surface energy enhances the dispersion of the aggregates. This concept is applied by the group of Le and Ilisch<sup>143</sup> in order to predict filler localization in rubber blends.

- *Effect of the number of mixing stages*

From the point of view of industrial tire production, one seeks an optimum balance between a fast mixing procedure that minimizes the energy input and good properties of the final product. As a matter of fact the distribution and dispersion of fillers may be improved by mixing rubber during longer times or several mixing steps<sup>141,144</sup>. This effect may explain some differences we have observed on the Payne effects of filled samples mixed in 1 of 2 phases (see chapter IV).

- *Effect of dump temperature*

A minimum temperature of about 130°C is necessary to achieve an efficient silanization, as reported in the literature<sup>137,138,144</sup>. On the other hand, mixing at a temperature higher than 150°C may induce some further reaction of the coupling agent with the rubber chains leading to an increase of viscosity during the first step (so-called scorch phenomenon). This corresponds to an excessive increase of the uncured (so-called 'green') compound viscosity that deters the processing performance as extrusion for instance.

Nevertheless, it is of interest to understand the influence of the temperature reached at the end of the mixing process, which is called dump temperature. It has been shown that the amplitude of the Payne effect lowers as the dump temperature increases in both SBR/BR and NR silica filled rubbers<sup>144,145</sup>. The modulus in the large strain regime is also enhanced when mixing is performed at a higher temperature<sup>144</sup>.

An interesting study on this topic has been reported by Mihara<sup>66</sup>, who compares the impact of the mixing dump temperatures on the specific bound rubber (i.e. the bound rubber normalized by the silica specific surface) with various silica grades (Figure 78). The specific bound rubber increases as dump temperature increases, suggesting an increased degree of chemical bonding between rubber and silica. Finally, considering the bound rubber as representative of the efficiency of the mixing phase (including both the efficiency of the coupling reaction and of the silica dispersion), it is observed that the efficiency depends on the silica type, the Z1115MP providing the highest bound rubber per unit surface

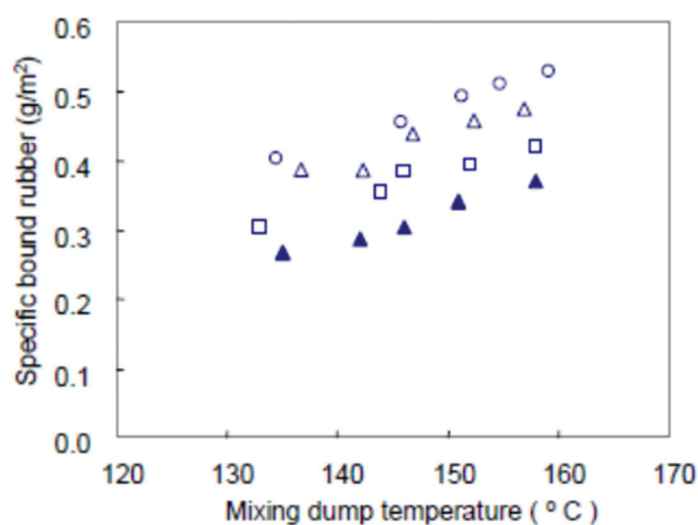


**Figure 78 : Effect of increasing mixing dump temperature on the specific bound rubber (ratio of bound rubber versus silica specific surface) for different precipitated silica (○: Z1115MP ; △: Z1165MP ; □: 7005 ; ▲:VN3). Reproduced from Mihara<sup>66</sup>.**

### III.2.b.ii. Adding sulfur and accelerators.

The incorporation of sulfur and both CBS and TBzTD accelerators was performed on an open mill. A total of 16 cuts were made, this operation consisting in cutting the green rubber film and folding it before it goes into the mixing area between the rolls. The time necessary for this operation was about 8 minutes. The rotation speed is higher for one of the rolls in order to promote mixing, the ratio of speed chosen here was 1:1.1. A second parameter that could be adjusted was the inter-roll gap used at the final pass, it was chosen close to 2 mm for most compounds and it was smaller when it was intended to prepare thin vulcanized samples under press. The temperature of the rolls is controlled by an oil bath at 50°C.

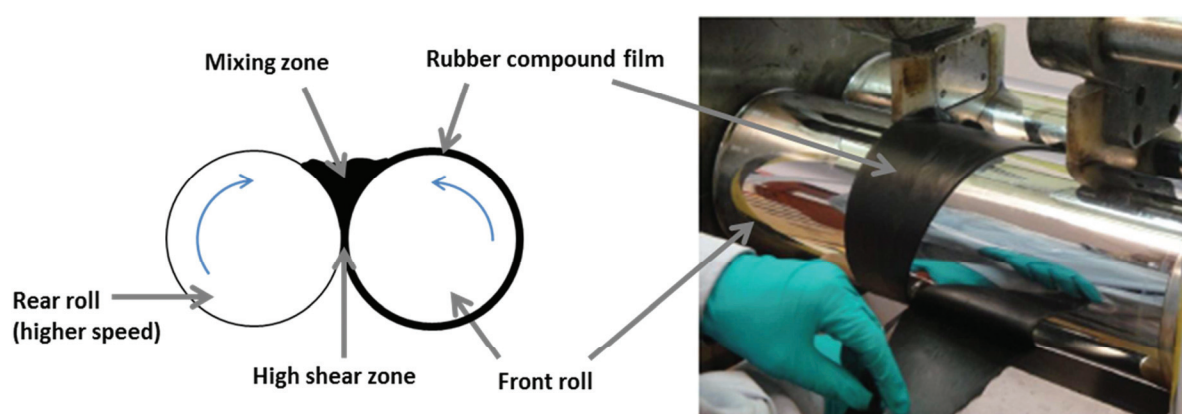


**Figure 79 : a) Side and b) Front view of the two-roll mill used for incorporation of vulcanization agents (Sulfur and accelerators). The picture taken from Muñoz<sup>146</sup> (b) shows how a cut is made: the rubber film is partly cut from one side to the other and then folded on itself to increase the mixing process between the rolls.**

III.2.b.iii. Determination of the vulcanization time by rheometry

The vulcanization time is measured with a Monsanto R100S Oscillating Die Rheometer (ODR). A fixed volume of uncured ('green') compound (corresponding to 6 to 8 grams) is introduced into the apparatus chamber preheated at a temperature of 150°C in the case of Natural Rubber. The temperature is maintained constant and an oscillating shear strain is applied by the rotor in plane-plane geometry. A typical torque versus time curve obtained for filled Natural rubber is shown in Figure 80. The torque (i.e. the viscosity) first decreases slightly due to rubber heating and reaches a plateau of minimum torque noted  $C_{min}$ . After some delay at roughly constant viscosity, the torque increases strongly under the effect of the network formation and a second plateau is observed once the sulfur bridge formation reaction is complete.

A decrease of the torque may be observed at longer time due to further reactions known as reversion. The time for reaching 98% of the maximum torque difference value ( $C_{max} - C_{min}$ ) is taken as the vulcanization time ( $t_{98}$ ).

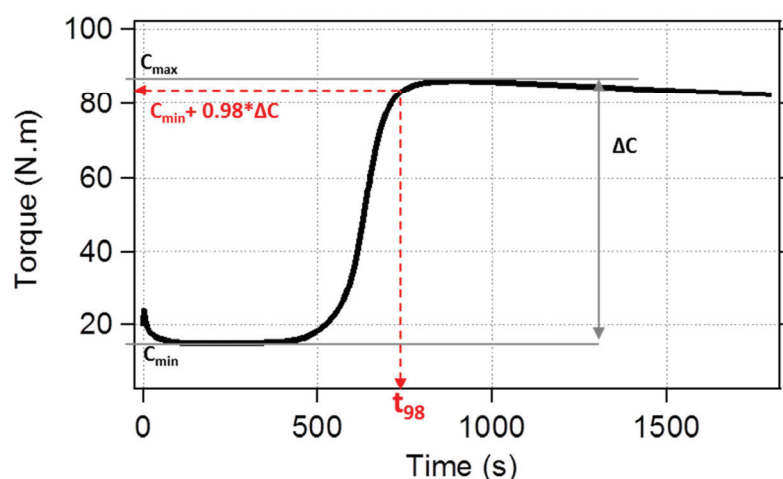


**Figure 80: Torque versus time curve for a filled natural rubber compound at 150°C. Determination of the vulcanization time  $t_{98}$  (the time to reach 98% of the total torque increase  $\Delta C = C_{max} - C_{min}$ ).**

Torque versus time curves for three unfilled compounds of different sulfur and CBS amounts are shown in Figure 81. The values of  $C_{min}$  cannot be distinguished since the mixing procedure was identical for the three compounds. However, the maximum torque  $C_{max}$  significantly increases as the sulfur and CBS amounts increase, and it can be shown that the torque increase ( $C_{max} - C_{min}$ ) is directly related to crosslink density in unfilled materials.

Using Carbon black as the reinforcing filler generally results in lower vulcanization time whereas Silica does not strongly modify it compared to unfilled rubber (Figure 82).

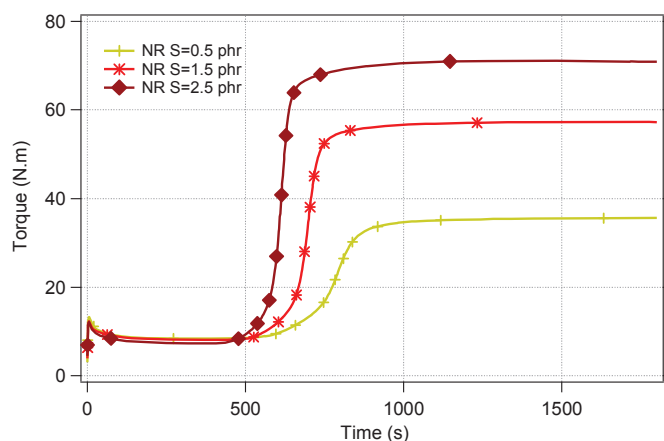


**Figure 81: Effect of Sulfur and CBS amounts on the vulcanization curves of unfilled NR.**

Vulcanization curves of unfilled and Silica TESPT reinforced NR samples at three sulfur contents (0.5; 1.5 and 2.5) are compared in Figure 82 b). The torque increase is larger and the direct proportionality of the crosslink density to the torque increase is no longer true in the case of filled compounds, since the contribution of fillers to the viscosity is higher in the vulcanized state.

Note that for the silica filled compound with the lower sulfur content, the vulcanization reaction is rather slow compared to the unfilled counterpart. This may correspond to an adsorption of the vulcanization accelerators on the silica surface.

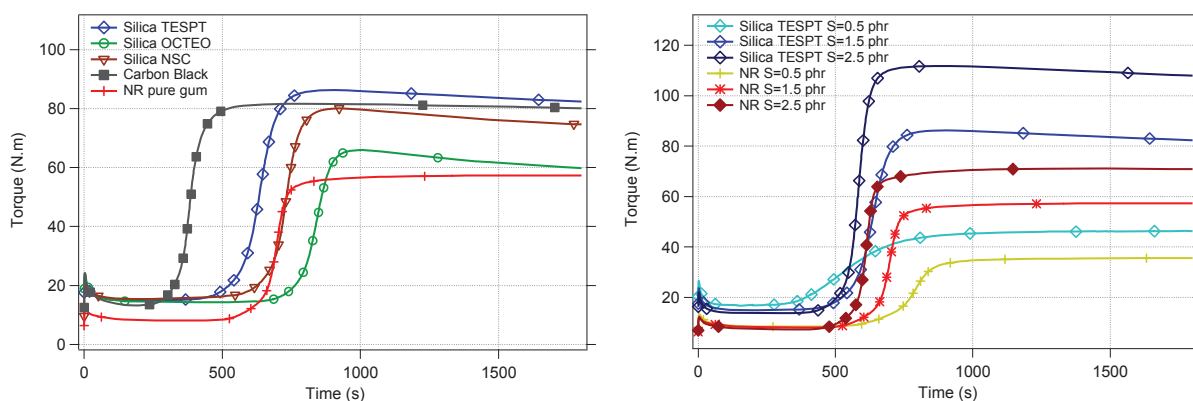


**Figure 82 : Vulcanization curves for a) different filler and interface types and b) Silica TESPT at three sulfur contents compared to unfilled NR.**

#### III.2.b.iv. Vulcanization under press and storage

All green compounds vulcanizations were performed in a hot press. Depending on the desired test sample geometry, molds for plates or for pure shear test samples were used. The plate molds

being designed for 2mm thick plates, blocks of 1 or 0.5mm were introduced to obtain thinner rubber plates of 1 or 0.5mm. As regards Pure Shear samples, two molds were available, one yielding samples with a useful height between cylindrical parts of 20mm and the other offering two possible heights: 10 and 15mm.

Three presses have been used, a vapor press model Blère and two electrical presses models Thiebault and Agila, the latter having an automatic degassing procedure and a time controller.

<b>Vulcanization Press Parameters</b>	<b>NR</b>	<b>SBR</b>
<b>Pressure applied</b>	200 bars	200 bars
<b>Temperature</b>	150°C	160°C
<b>Time</b>	t <sub>98</sub>	t <sub>98</sub>
<b>Number of degassing</b>	3	3

**Table 8 : Parameters applied in hot press for the vulcanization of Natural Rubber and Styrene-Butadiene compounds.**

Once the whole processing of the samples was completed, samples were kept away from light at a temperature of 22°C in order to avoid accelerated ageing effects. Mechanical experiments and microstructure characterizations were generally carried out within a few months after processing, although in some cases some tests were performed more than six months after completing the compounding. Nevertheless, all tensile repeatability tests and NMR crosslink density measurements performed in order to check a possible degradation effect over several months indicated that there were only small modifications of the material properties.

### *III.2.c. Rheology and other tests.*

The viscosity of the non-vulcanized compounds was estimated thanks to a Mooney rheometer following the ASTM standard<sup>147</sup>, a rotor of large type was used and the Mooney viscosity index was recorded at 100°C after 1 minute of temperature stabilization and 4 minutes of rotor shearing.

The compounded materials were also submitted to other tests, such as abrasion resistance, standardized tearing strength and hardness measurements. The principles and some results can be found in the PhD thesis of Brice Gabrielle.

The rheological properties could also be estimated with a Dynamic Mechanical Die rheometer (DMDR) enabling dynamic strain sweeps in the small and large displacement regimes.

## **III.3. Characterization techniques**

### *III.3.a. Dynamic Mechanical Analysis in small strains regime*

The Dynamical Mechanical Analysis (DMA) experiments were performed by Benoit Moreaux (Rhodia Silica) at the Silica application laboratory in Collonges-au-Mont-d'or. Both temperature and strain sweeps have been carried out on a Metravib VA3000 Dynamic Analyser.

III.3.a.i. Temperature sweep.

The mechanical response is measured in the linear regime as a function of temperature. This experiment is used to characterize the mechanical glass transition and to obtain reinforcement curves, by comparing the modulus of a reinforced sample to that of the corresponding pure rubber matrix.

Oscillating uniaxial elongation is applied to the samples up to a maximum strain of  $1.25 \times 10^{-3}$  (or 0.125%) at a frequency of 10Hz. The range of temperature selected here is  $-80^{\circ}\text{C}$  to  $80^{\circ}\text{C}$ , which is well suited to NR having a glass transition temperature ( $T_g$ ) close to  $-70^{\circ}\text{C}$ . The apparatus records the evolution of the stress which can be expressed the sum of in-phase and out of phase contributions.

$$\varepsilon^* = \varepsilon_0 \exp(i\omega t) \quad (47)$$

$$\sigma^* = \sigma_0 \exp(i(\omega t + \delta)) \quad (48)$$

The corresponding storage modulus  $E'$  and loss modulus  $E''$  are then computed according to  $E^* = \sigma^*/\varepsilon^* = E' + iE''$  with:

$$E' = \frac{\sigma_0}{\varepsilon_0} \cos \delta \quad \text{and} \quad E'' = \frac{\sigma_0}{\varepsilon_0} \sin \delta \quad (49)$$

Note that the values of the modulus in temperature sweep are carried out on as-prepared samples and thus depend on the processing history.

III.3.a.ii. Strain sweep : Payne effect characterization

The mechanical response is measured as a function of the strain amplitude at a given temperature. In this experiment, the Payne effect (decrease of the storage modulus and maximum of the loss modulus as the amplitude increases) is characterized. A plane shear geometry is used for the strain sweep measurements (Figure 83). Oscillating shear is applied at a frequency of 10 Hz and shear amplitudes ranging from 0.1% to 50%. The temperature of the experiment is usually  $60^{\circ}\text{C}$ , unless otherwise specified.

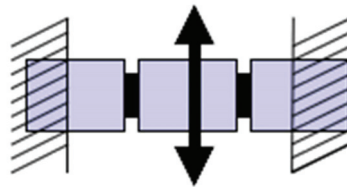


**Figure 83 : Schematics of the set-up used for the strain sweep experiments: two test pieces (in black) are glued between fixed cylinders and the moving central cylinder.**

The complete procedure consists in first increasing the strain cycle amplitude up to 50% and then decreasing back the amplitude down to 0.1%. Due to some accommodation of the material, the storage modulus is smaller during the return sweep compared to the first, increasing sweep (Figure 84). As the modulus measurement is also more reproducible at the return sweep, only the data points of this second sweep were taken into account.

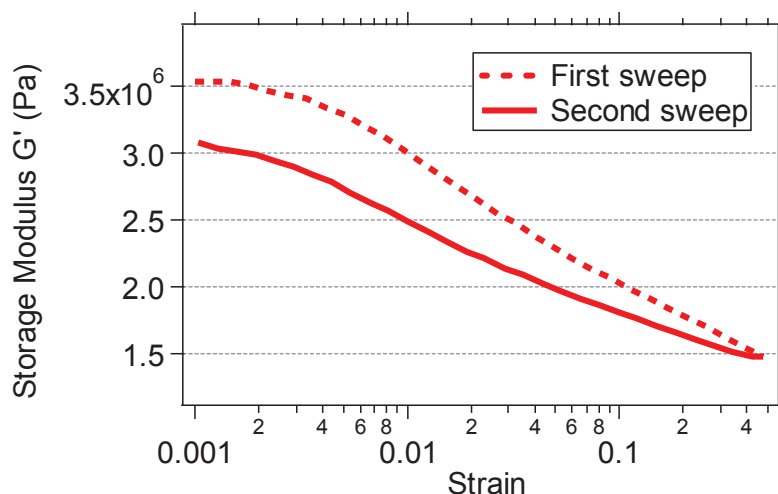


**Figure 84:** Comparison of first, increasing (dashed line) and second, decreasing (continuous line) strain sweep in Dynamical Mechanical Experiments on filled NR.

### III.3.b. Mechanical measurements in the large strain regime

#### III.3.b.i. Tensile tests

Tensile tests were performed on die-cut standard H2 dumbbell samples. The sample geometry is described in Figure 85. The sample thickness is approximately 2mm, originating from the vulcanized sheets. The actual thickness was systematically measured and taken into account for all test samples.

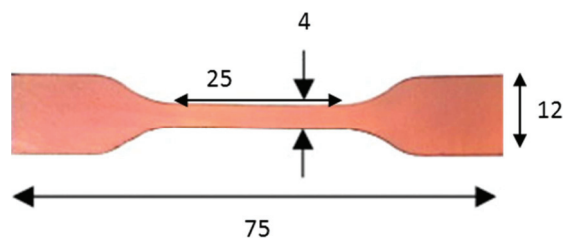


**Figure 85:** Dumbbell shape samples H2 geometry.

Parts of the presented tensile measurements were performed by Benoit Moreaux at the Collonges Application Laboratory on an Instron machine at a traction speed of  $500\text{mm}\cdot\text{min}^{-1}$ . Other tensile

tests were done with a constant crosshead speed ranging from 1 to 1000 mm.min<sup>-1</sup> which is the maximum admitted value of the MTS machine model 1/Me.

Strains were measured thanks to an EX44 contact extensometer. The initial length between displacement gages is fixed to 13mm and the maximum course reaches 600mm with a precision of 0.01mm. To measure the stress, two different load sensors of 500N and 5kN maximum applicable loads were used, with an error of 0.5% of the measurement value.

### III.3.b.ii. Dissipation at large deformations

The dissipative behavior has been measured as a function of strain by applying uniaxial traction cycles of increasing amplitude. Two procedures have been implemented: in the first one (stabilized samples), the samples are cycled up to 400% strain amplitude to remove the Mullins effect, then, in a second step, cycles of increasing amplitudes are applied on the previously stabilized samples. In the second one (as-prepared samples), no preliminary stabilization (removal of the Mullins effect) is done. The samples are cycled three times at each maximum deformation, only the third cycle is analyzed.

- ***Stabilized samples***

The samples were first submitted to 3 cycles of large strain amplitude (400%) to stabilize the stress-strain curve (removal of the Mullins effect). Cycles of increasing maximum strain amplitude from 60 to 400% were then applied by steps of 20% (see Figure 86). The applied crosshead speed was 100mm.min<sup>-1</sup> (and -100mm.min<sup>-1</sup> on the return parts of the cycles) which corresponds to an elongation rate  $\dot{\lambda} = 2.8 \times 10^{-2} \text{ s}^{-1}$ . The initial length of the sample before removal of the Mullins effect was used as reference, undeformed length to compute the strain during all the experiment. Thus, due to permanent set, the minimum deformation obtained when unloading the sample down to zero stress is of the order of 40%.

For each cycle, the total mechanical energy input to the sample and the dissipated energy were calculated respectively as the area under the traction curve and the hysteresis cycle area (the difference between traction and retraction curves) as shown in Figure 86 b).

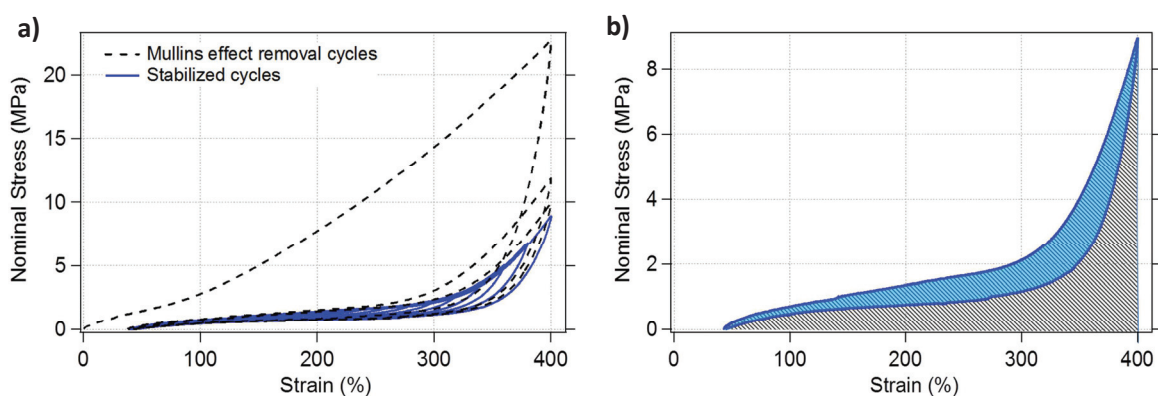


**Figure 86 : Measurement of the dissipation at high strain on stabilized samples: a) 3 cycles of high strain amplitude are first applied to remove the Mullins effect (dashed curves) then cycles of increasing maximum strain are performed (full curves. b) The relative dissipation is computed as the ratio of dissipated energy (blue area) on the total mechanical energy input in the traction phase (hatched area).**

- *As-prepared samples*

In this case, no large amplitude cycles are applied prior to the cycles of increasing amplitude. The cycles of increasing strain amplitude (from 20 to 400% by steps of 20%) are directly carried out on as-prepared samples. For each amplitude, 3 cycles are performed and the total input and dissipated energies are calculated for the third cycle only in order to obtain progressively “demullinized” samples (Figure 87). In all cases, energies densities are obtained by dividing by the volume of the deformed test sample.

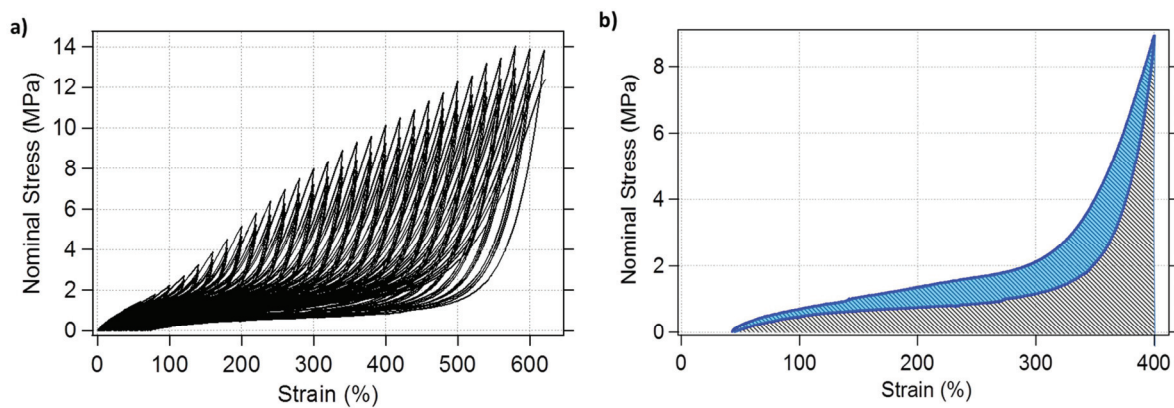


**Figure 87 :** Measurement of the dissipation at high strain on as-prepared samples: a) Cycles of increasing maximum strain are applied. 3 cycles are applied for each value of the maximum strain. b) The relative dissipation is computed as the ratio of dissipated energy (blue area) on the total mechanical energy input in the traction phase (hatched area).

The residual set at the end of the third cycle of each strain amplitude could also be recorded in this test as shown in Figure 88.

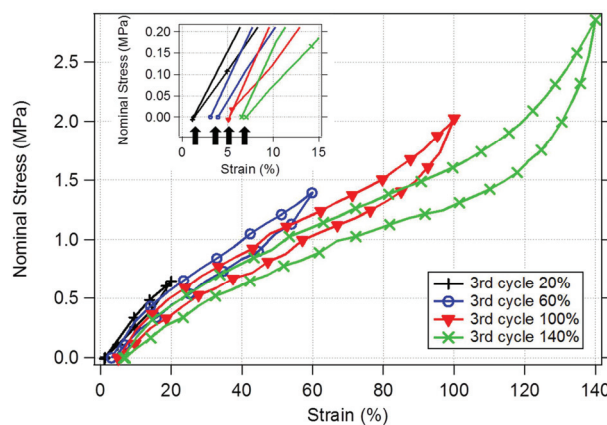


**Figure 88 :** Examples of 4 mechanical cycles of increasing amplitudes. Only the third cycle of each strain amplitude is shown here. The residual set as indicated by arrows in the insert was measured for each third cycle.

Figure 89 gives examples of total input and dissipated energy densities calculated for two NR Silica TESPT samples as a function of the maximum strain amplitude, showing the reproducibility of the measurements. The relative dissipated energy is then computed as the ratio of these two quantities for each maximum strain amplitude. The results presented in the next chapter are obtained as the mean value of 2 or 3 samples for each studied system.

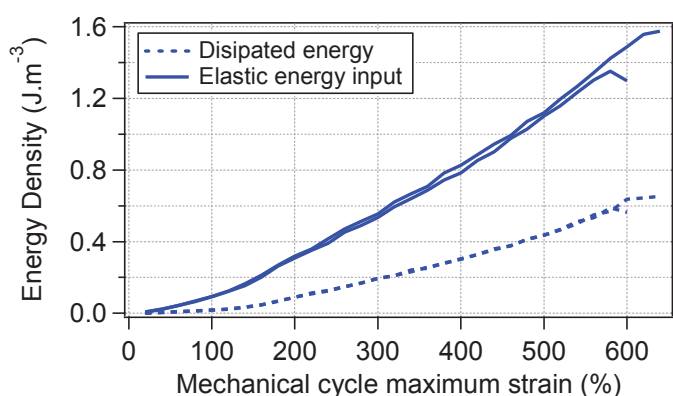


**Figure 89 : Plots of dissipated and input energy densities during cycles of increasing strain amplitude, for two samples of the same formulation. The relative dissipated energy is computed as the ratio of these two energy densities.**

### III.3.b.iii. Tear tests

Tear tests were either performed on single edge notched strip samples or on Pure Shear samples. The former were obtained from rubber film with a hollow puncher and Pure Shear samples were obtained by vulcanization in a specific mold (as described in I.2.b.i).

The Pure Shear geometry was preferred in order to limit the influence of the tear bifurcations (tear rotation) that induce a high dispersion of the results<sup>74,129</sup>. In order to be able to test a sufficient number of samples, the 215mm long molded stripes were cut in two pieces, the obtained half stripes still having a low enough height/length ratio (Figure 90). Moreover it was checked on one material that the tear tests give the same results when using full length (215mm) or half-length (107.5mm) samples.

A 20mm notch was created using a razor blade covered with soap. After creating the notch, the remaining useful length was measured in order to compute the nominal stress. Five thickness measurements were performed to calculate the mean thickness of the sample. As a matter of fact, it was noticed that, even though the mold were designed to have a constant thickness of 1.4mm, incomplete flowing of the green compounds under press tend to induce a thickness somewhat larger in the middle than on the edges of the useful stripe.

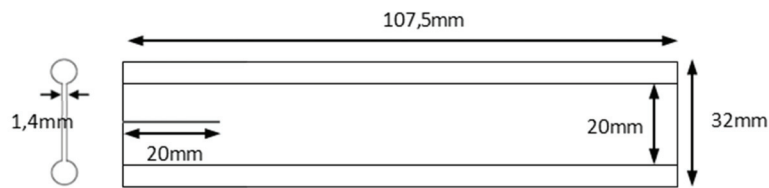


**Figure 90 : Pure Shear sample geometry. The notch length is systematically measured and the thickness of the samples is taken as the mean values of 5 measurements from the notch tip to the opposite edge.**

Specifically designed holding jaws were used to perform the tear tests. The crosshead speed was fixed at 1, 100 or 1000mm/min, which in terms of macroscopic strain rate corresponded to  $\dot{\lambda} = 8.33 \times 10^{-4}$ ,  $8.33 \times 10^{-2}$  and  $0.833 \text{ s}^{-1}$ .

In the case of Pure Shear samples, the calculation of the Energy release rate at break taken as the Tear energy is made simple due to the assumed constant width (in practice some minor width reduction due to edge effects is observed). The Tear energy is thus directly given by the mechanical work  $W$  multiplied by the initial height of the sample  $h_0$ :

$$G = Wh_0 \quad (50)$$

The work  $W$  is the integral of the stress-strain curve up to failure as illustrated in Figure 91. In some case of long tear bifurcation, the Tear energy is more difficult to define precisely, this point will be further discussed in chapter VIII.

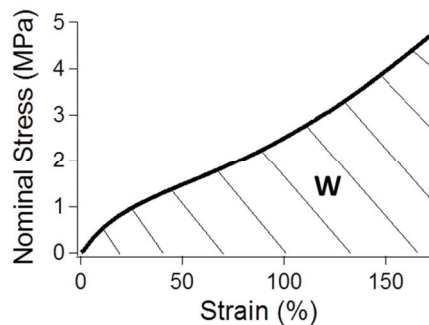


**Figure 91 : Example of stress-strain integration yielding the total brought energy up to tear propagation for a filled NR sample.**

### III.3.b.iv. Digital image correlation

Digital image correlation analyses have been carried out on images recorded during tear tests. The purpose was to measure the strain field in the vicinity of the tear tip at a local scale (typically a few hundredths of microns). This is done by comparing the displacements of

computer-defined analyze areas (called facets) during the experiment with respect to the initial, untrained state. Identification of the facets relies on grey leveled patterns either naturally present on the sample or created by spraying paint dots.

In our case there is no sufficient contrast on the sample surface. Specimen surfaces are dark grey in the case of silica reinforcement and black when using carbon black. A white aerosol paint (MR70 Developer normally used for part inspections by penetrant testing) was sprayed to create a pattern on the sample surface.

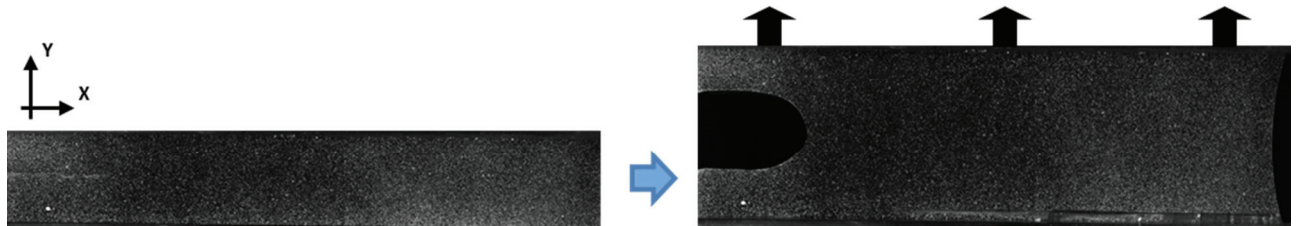


**Figure 92 : Pure Shear filled NR sample a) Unstretched and b) stretched close to the onset of tear propagation.**

Digital Image Correlation was carried out with the commercially available software ARAMIS from the GOM company. A reference picture of the sample in the initial, unstretched state and several pictures under deformation are recorded during the test and then uploaded in the software.

The discrete surface mesh is defined in the reference (undeformed) image. The size of the analyzed zones (facets) is adjusted to the typical size of the created pattern, in order to be easily identified by the recognition algorithm. The facets can also overlap in order to increase the precision and accuracy of the local strain calculation but this results in longer calculation times.

In the deformed pictures, ARAMIS recognizes the initial patterns from the distribution of greys in the facets. The new coordinates of each facet are used to compute the strain field.

In rubbers, local deformations can reach several hundredths of percent. This induces contrast changes and fragmentation of initial patterns which finally lead to the loss of correlation for the analyzed facets, thus limiting somehow the range of analyzed local strain.

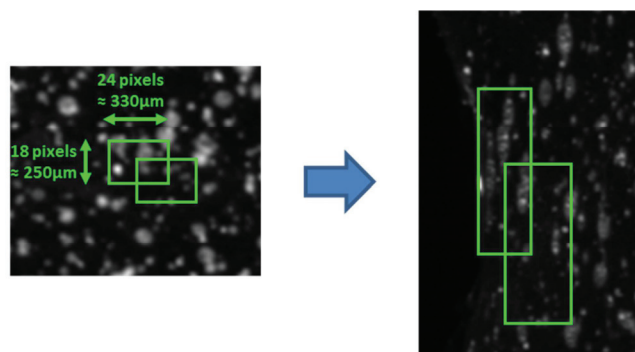


**Figure 93 : Schematic representation of pattern recognition from the reference image (left) to a deformed image (right). The fragmentation of the pattern at high local strain levels responsible for loss of contrast is clearly visible in the picture on the right.**

### III.3.c. Scanning Electron Microscope

Electron microscopy relies on the interactions between electrons and matter in order to characterize materials on very small scales.

A resolution of the order of the nanometer can be obtained at the lower wavelength of the electronic beam. In the case of Scanning Electron Microscopy (SEM), the pictures are obtained from scanning a focalized beam on the sample surface. Polymers having a low conductivity, it is necessary to coat a thin film of platinum or gold onto the surface by vapor deposition prior to put the sample in the microscope. For the same reason, it is also recommended to work at low electronic tensions (typically between 1 and 10kV) and low intensities to avoid charging the surface or altering the samples.

Among the various signals that can be collected, two types of electrons have been used to image the surface of the observed samples:

- Secondary Electrons stem from inelastic interactions with the material. As they have a low energy, only secondary electrons from the surface are detected, giving a topographic contrast.
- Back Scattered Electrons (BSE) are due to elastic interactions with the atoms in the material. The higher the atomic mass, the higher the collected current, which provides chemical contrast.

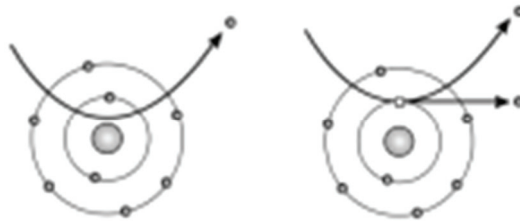


**Figure 94 : Schematic representation of atom/electron interactions resulting in a) Back-scattered (left) and b) Secondary (right) electrons.**

Scanning Electron Microscopy (SEM) observations were performed on unstretched and in-situ stretched samples. The latter were prepared in a small device adapted to the microscope chamber maintaining a pre-imposed deformation. The strains were calculated through silver pen marks made on the sample in the unstretched state.

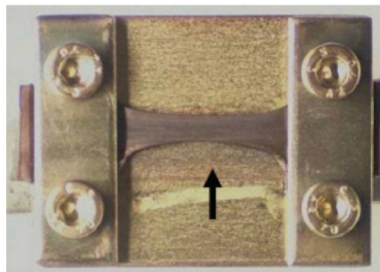


**Figure 95: Straining device adapted to the SEM chamber for the observation of notched and un-notched stretched rubber samples.**

### III.3.d. DQ Proton NMR

NMR experiments were carried out by Roberto Pérez-Aparicio (LPMA) on a proton low-field and low-resolution spectrometer “Brucker minispec mq20” using multiple-quantum experiments. This technique gives access to partially averaged residual dipolar couplings ( $D_{\text{res}}$ ) resulting from the time-average orientation of chains segments due to crosslinks and entanglements. The residual dipolar coupling  $D_{\text{res}}$  can then be related to the absolute molecular weight between crosslinks  $M_c$  thanks to a normalization applicable to Natural Rubber given by Valentín et al<sup>81</sup>. In addition to the average value of the molecular weight between crosslinks  $M_c$ , the analysis procedure used to analyze the shape of the NMR signal provides the distribution of  $M_c$ , thus allowing to characterize the inhomogeneity of the rubber network. In the following, only results on the average crosslink density in unfilled and filled systems will be presented. Detailed pieces of information on the technique and its versatility in the field of polymers and elastomers have been reported by Saalwächter and coworkers<sup>82,148,149</sup>.

### III.3.e. Equilibrium swelling measurements

Swelling experiments are widely used to characterize network crosslink densities in elastomer networks. The thermodynamics of a rubber material swollen at equilibrium in a good solvent may be described by the Flory-Rehner theory<sup>28</sup>. The first assumption is that elastic and mixing components of the free energy are separable and additive. The partial derivative of the free energy with respect to the number of moles yields to the equation in terms of chemical potential:

$$\frac{\Delta\mu_S^{\text{total}}}{RT} = \frac{\Delta\mu_S^{\text{mixing}}}{RT} + \frac{\Delta\mu_S^{\text{elastic}}}{RT} \quad (51)$$

In the equilibrium state, the total chemical potential is zero meaning that all the mixing free energy is balanced by the elastic energy stored by the extended network chains. The determination of the network density is based on this equality between the elastic term and the free energy of mixing which can be accessed through the rubber fraction in equilibrium with the solvent in the swollen state. The Flory-Huggins expression is used for this purpose: assuming an infinite molar volume for rubber macromolecules, it relates the rubber fraction and the solvent-polymer interaction parameter  $\chi$  to the free energy of mixing:

$$\frac{\Delta\mu_S^{\text{mixing}}}{RT} = \ln(1 - \phi_r) + \phi_r + \chi\phi_r^2 \quad (52)$$

The free energy associated to the elasticity of the chains can be related to the average molar mass of a chain segment between two crosslinks thanks to the theory of rubber elasticity<sup>20</sup>. The affine and phantom models of network deformation are mainly used to describe the behaviour of

crosslinked rubbers (see chapter 2). Based on the affine model and the assumption that the crosslinks functionality is 4, we obtain the relationship between the rubber fraction  $\phi_r$ , the parameter  $\chi$ , the rubber density  $\rho_r$ , the volume of solvent in the sample  $V_S$  and the molecular weight between crosslinks  $M_C$ :

$$\ln(1 - \phi_r) + \phi_r + \chi\phi_r^2 = -\frac{\rho_r}{M_C}V_S\left(\phi_r^{\frac{1}{3}} - \frac{\phi_r}{2}\right) \quad (53)$$

On the practical point of view, the experiments started by weighing dry samples of about 100mg on a precision balance. Three samples of each formulation were selected in order check the reproducibility. They were then immersed in toluene in a close vessel protected for the light to avoid degradation activation by UV rays. The toluene was renewed every 24h and samples were weighed to follow the solvent intake which was found to be nearly constant after 24h in all cases. After 72h the samples were removed from the toluene, weighed again and dried under vacuum for 24h. The final mass was also recorded since it enables to remove all extractable species from the calculations of the rubber fraction in the swollen state. Extractables are composed of sol chains i.e. chains that are not crosslinked to the overall network and other non-rubber components as vulcanisation accelerators.

The mass increase relative to initial mass of rubber specimens immersed in toluene is reported as a function of time in Figure 96 for all unfilled Natural Rubber formulations (with various sulfur and CBS amounts, with constant sulfur/CBS ratio). The swollen mass after 24 hours of immersion is already very close to the equilibrium solvent intake. A very slight decrease of the mass is even detected for some samples, maybe due to the removal of low molecular weight, extractable components. As expected, the swelling (solvent intake) drops on increasing the sulfur content especially for small sulfur contents.

The fraction of rubber is calculated as the ratio of volume of rubber divided by the total volume (rubber + solvent):

$$\phi_r = \frac{V_r}{V_r + V_S^{rubber}} \quad (54)$$

The estimation of the rubber volume takes into account the dried weight minus the weight of insoluble particles (ZnO and fillers if concerned) defined as the initial weight multiplied by their known fraction ( $f_{ins}$ ). The volume of solvent is defined as

$$\phi_r = \frac{\frac{w_d - f_{ins}w_i}{\rho_r}}{\frac{w_d - f_{ins}w_i}{\rho_r} + \frac{w_{sw} - w_d}{\rho_{toluene}}} \quad (55)$$

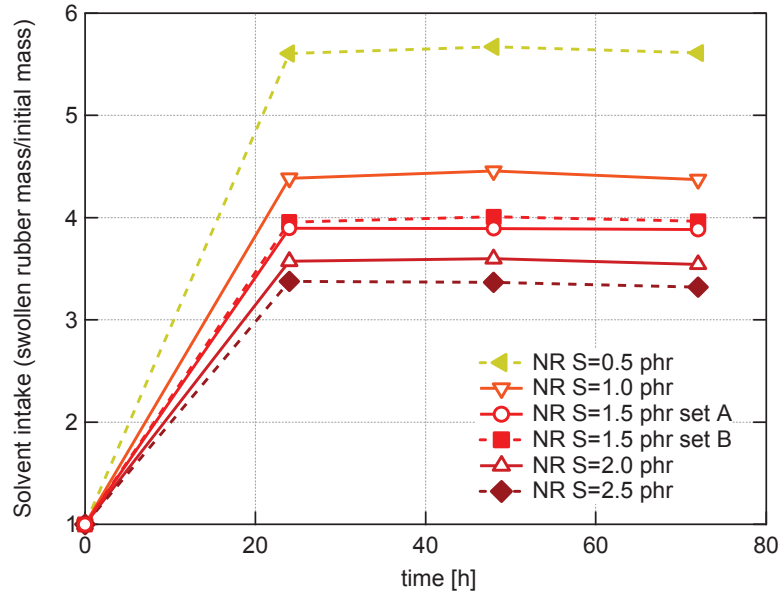


**Figure 96 : Solvent intake (ratio of swollen/dry rubber mass) for unfilled NR samples from series 046-11 (set A) and 119-11 (set B). The equilibrium swelling is attained after only 24 hours. Samples have various sulfur and CBS amounts as indicated, with constant sulfur/CBS ratio**

With  $w_i$ ,  $w_{sw}$  and  $w_d$  the mass in respectively initial, swollen and dried state.

In the case of a non-interacting filler, rubber chains can be detached from the interface during swelling and vacuoles containing solvent are created. The expression of the rubber fraction is thus not valid since a third term corresponding to the solvent in the vacuoles is at stake:

$$\phi_r = \frac{V_r}{V_r + V_S^{rubber} + V_S^{vacuoles}} \quad (56)$$

The solvent contained in this vacuoles can be estimated thanks to the method proposed by Valentín et al.<sup>81</sup> The volume of solvent in the vacuoles is directly related to the volume of insoluble particles (ZnO and fillers if concerned) and the fraction of rubber: the higher the fraction of rubber and the lower the vacuoles volume.

$$V_S^{vacuoles} = V_{ins} \left( \frac{1}{\phi_r^{corrected}} - 1 \right) \quad (57)$$

After combining equation (56) and (57), the expression of  $\phi_r^{corrected}$  is obtained:

$$\phi_r^{corrected} = \frac{V_r}{V_r + V_S^{rubber}} = \frac{1 + \frac{(f_{ins}w_i)/\rho_{ins}}{(w_d - (f_{ins}w_i))/\rho_r}}{\phi_r + \frac{(f_{ins}w_i)/\rho_{ins}}{(w_d - (f_{ins}w_i))/\rho_r}} \quad (58)$$

$$\phi_r^{corrected} = \frac{1 + \frac{(f_{ins}w_i)/\rho_{ins}}{(w_d - (f_{ins}w_i))/\rho_r}}{\frac{\frac{w_d - f_{ins}w_i}{\rho_r} + \frac{w_{sw} - w_d}{\rho_{toluene}}}{\frac{w_d - f_{ins}w_i}{\rho_r}} + \frac{(f_{ins}w_i)/\rho_{ins}}{(w_d - (f_{ins}w_i))/\rho_r}} \quad (59)$$

Once the molecular mass between crosslinks  $M_C$  is obtained, the density of crosslinks per mole  $\nu_c$  is equal to the inverse of 2 times  $M_C$ .

### III.3.f. X-ray diffraction experiments

X-ray diffraction experiments were used to characterize strain-induced crystallization (SIC) in samples based on Natural Rubber matrices. The onset of SIC, the absolute value of the crystallinity, the crystallite orientation and amorphous phase orientation were measured in in-situ stretching experiments.

All Wide angle X-ray Diffraction (WAXD) experiments were carried out in the Laboratoire de Physique des Solides (LPS) in collaboration with Pierre-Antoine Albouy and Denis Petermann. Two kinds of experiments were conducted: ‘quasi-static’ in-situ tensile tests and dynamic oscillating tests with stroboscopic detection. For dynamic experiments, the device configuration and experimental procedure are detailed in chapter 5. Both experimental set-up control and monitoring and pattern analysis are carried out with a home-made software “Traction” developed by Denis Petermann in a C++ environment.

#### III.3.f.i. Description of the in-situ tensile device

The apparatus is mounted on a copper rotating anode X-ray generator (focus size:  $0.2 \times 0.2 \text{ mm}^2$ ; 40 kV, 40 mA). The doubly curved graphite monochromator selects the copper  $K_\alpha$  radiation of wavelength 0.1542 nm. The sample is located at the focalization point close to the collimator exit to obtain a maximum diffracted intensity.

The device for simple in-situ X-ray diffraction measurements during a tensile test up to failure is schematized in Figure 97. The sample is symmetrically stretched, ensuring that the beam probes the same region of the sample throughout the stretching experiment.

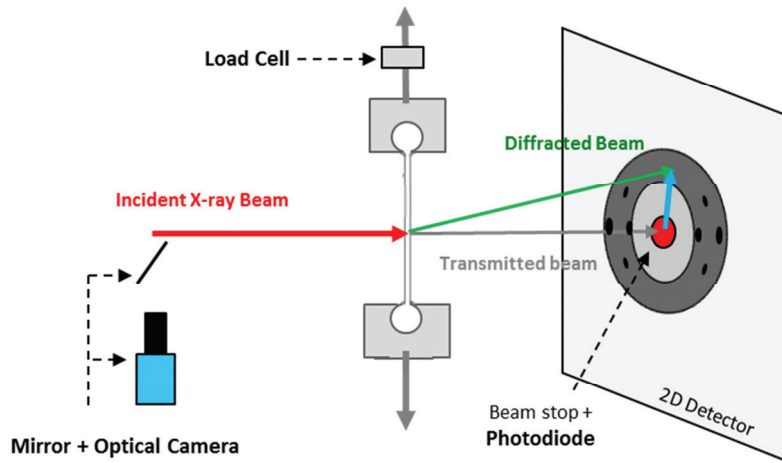


**Figure 97: In-situ X-ray tensile device. Both sample clamps are moved in opposite directions at the same speed. The optical camera records the sample thickness. A photodiode placed in the beam stop records the directly transmitted beam intensity.**

WAXD patterns were recorded with a Princeton CCD camera. Detected scattering angles  $\theta$  range from about  $3^\circ$  to about  $28^\circ$ , which correspond roughly to scattering angles between  $2 \text{ nm}^{-1}$  and  $20 \text{ nm}^{-1}$ . The exposure time was fixed at 10s and the data transfer from the CCD camera was about 6s, which ensures a reasonable number of measurement points during a tensile test to failure. A photodiode placed in front of the camera measured the directly transmitted beam and thus the absorption of the sample.

An optical camera was used to measure the sample thickness. Considering uniaxial extension and a Poisson's ratio of 0.5, the elongation ratio  $\lambda$  was calculated using equation (60) where  $e_0$  is the initial width and  $e$  the width of the sample recorded during stretching.

$$\lambda = \frac{e_0^2}{e^2} \quad (60)$$

As regards crystallization measurements done on samples from the series 30-11 and 46-11, the optical follow-up of the thickness was not yet implemented on the device, therefore the elongation ratio  $\lambda$  was taken as the displacement of the holding jaws divided by the initial length. Nevertheless, the upper and lower cylindrical parts of the samples were found to progressively slip in the holding jaw under the effect of the applied stress and some of the softest samples were completely pulled out of the holding jaw at high deformations. This effect is clearly demonstrated by comparing the strain values deduced from the thickness reduction with the applied displacement (see Figure 98).

In order to compare the results obtained on the different sets of samples, the strain applied to samples from the series 030-11 was re-computed taking into account the relationship found between displacement and strain for samples of series 119-11 (fit function represented by the red continuous line in Figure 98).

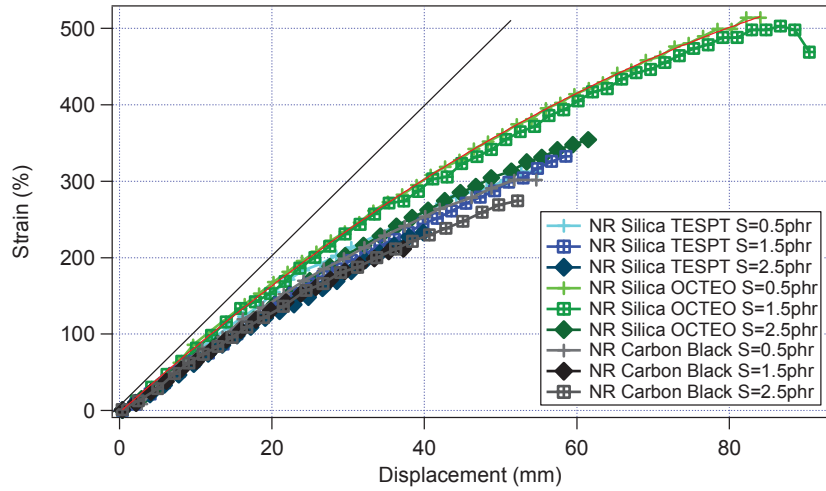


**Figure 98: Deviation from the linear relationship between displacement and strain computed from thickness reduction for several filled NR of the sample series 119-11. The red line represents the fit for a Silica OCTEO sample with a sulfur content of 0.5phr.**

The load  $F$  applied to the samples was measured with a 300N load sensor fixed on the upper sample holder. The true stress  $\sigma_T$  was calculated with the load and extension ratio according to equation (61) ( $S_0$  is the initial section of the sample):

$$\sigma_T = \frac{F}{S_0} \times \lambda = \sigma_N \times \lambda \quad (61)$$

### III.3.f.ii. Analysis of the X-ray Diffraction Patterns

- *Patterns corrections and analysis*

Typical patterns obtained in the case of unfilled and filled NR samples are shown in Figure 99. Note that the measured intensity is lower in the case of the silica filled samples since silicon atoms induce more absorption of the X-ray beam. In the unstretched state, only the amorphous halo due to isotropic scattering of the chains (more precisely, to monomer/monomer liquid-like correlations) is detected. The amorphous halo has its maximum intensity at a diffraction angle  $\theta = 19.05^\circ$ , which corresponds to a scattering vector  $q = 4\pi\sin(\theta/2)/\lambda = 13.5 \text{ nm}^{-1}$  (with  $\lambda = 0.1542 \text{ nm}$  the wave length of the X ray beam). Once the SIC onset is reached, the diffraction peaks associated with the crystalline planes  $\{200\}$ ,  $\{120\}$  and  $\{201\}$  are detected on the 2D detector (Figure 99, right). The  $\{002\}$  reflection would only be detected by tilting the sample with respect to the incident beam<sup>150</sup>. For the sake of simplicity, it was decided to keep the sample perpendicular to the incident beam and the error made on the crystalline content by measuring only the three reflections ( $\{200\}$ ,  $\{120\}$  and  $\{201\}$ ) was considered to be reasonably low.

Prior to pattern analysis, the recorded images were corrected for several defects:

- Defective columns of the camera were corrected by assigning the average value of neighboring columns (blemish).
- Geometric defects inherent to the camera and stemming from the optical fibers were corrected.
- The background of the camera i.e. the signal obtained for a fixed acquisition time in the absence of X-ray beam was subtracted.
- Impacts of cosmic rays are erased by correcting pixels which have a difference with their neighbors larger than the statistical interval.

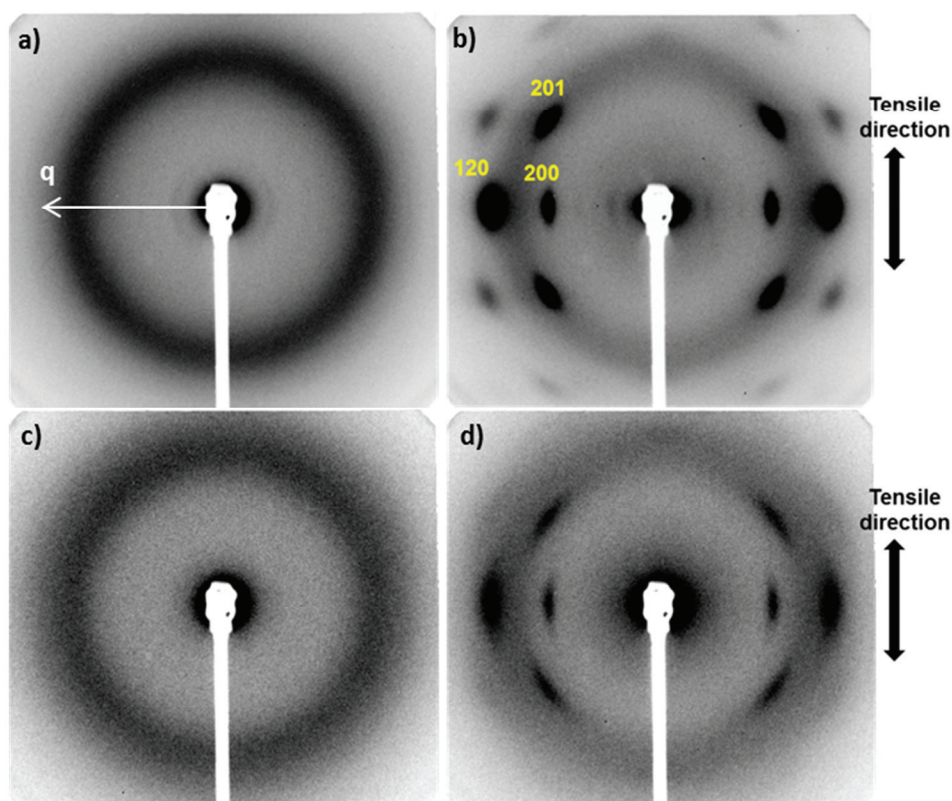


**Figure 99 : Typical diffraction patterns for an unfilled sample: a) unstretched and b) stretched close to failure. For a filled sample: c) unstretched and d) stretched close to failure. The indexation of the crystalline reflections and representation of the scattering vector  $q$  are shown.**

To analyze the scattering pattern, first the intensities for pixels in between a fixed scattering vector range (between roughly  $7 \text{ nm}^{-1}$  and  $16.5 \text{ nm}^{-1}$ ) represented by the circles in Figure 100 a) and c) are summed. The advantage of this procedure is the possibility to collect most of the intensity due to amorphous chain scattering (amorphous halo). Since most of the intensity diffracted by crystallized parts of chains (except the  $\{002\}$  reflection) is also included in this area, the crystalline fraction was computed as the direct ratio of crystalline over total intensity without using the unstretched diffraction pattern as reference, which would require some sample thickness corrections.

The summed intensity is plotted as a function of the azimuthal angle  $\varphi$  for the left hand side of the pattern (some modifications of the program now enable an addition of the right and left hand sides). Examples obtained in unfilled and silica-filled NR samples stretched close to failure are shown in Figure 100 b) and d).

As the detector (the CCD camera) response is higher at the top and decreases with line index (i.e. when going down), a correction slope was applied to the collected intensity to eliminate this defect.

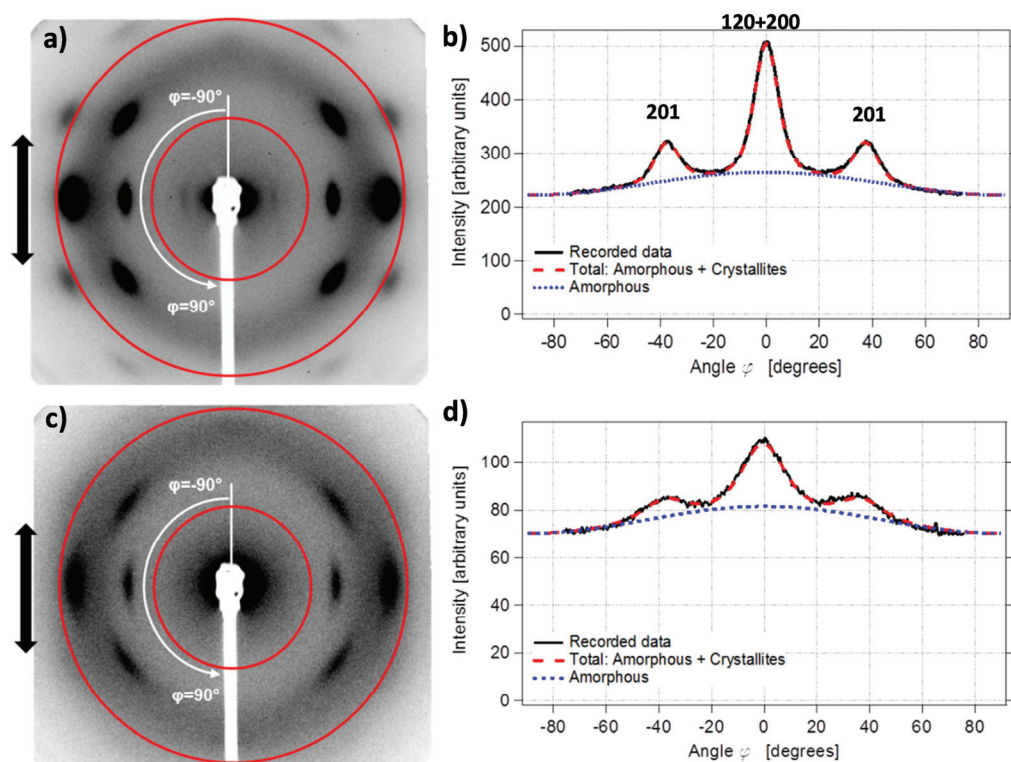


**Figure 100: Azimuthal integration of the intensity collected between the red circles on the diffraction pattern obtained in a) unfilled and c) silica filled NR samples stretched close to failure. The azimuthal scan were performed on the left side of the pattern from  $\varphi=0^\circ$  to  $180^\circ$ . The integrated intensities are plotted versus the azimuthal angle  $\varphi$  for b) the unfilled and d) the silica filled NR in continuous black line. The fits of total and amorphous contributions are respectively given in dashed red and dotted blue lines.**

The function used to fit the intensity versus azimuthal angle curves combines a constant background, a square cosine and a set of Pearson VII functions (62).

$$I(\varphi) = A + B \cos^2 \varphi + \frac{C}{\left(1 + \left(\frac{\varphi - \Delta\varphi}{\tau}\right)^2\right)^{3.1063}} + \frac{E}{\left(1 + \left(\frac{\varphi - \varphi_0 - \Delta\varphi}{\tau}\right)^2\right)^{3.1063}} \quad (62)$$

$$+ \frac{E}{\left(1 + \left(\frac{\varphi + \varphi_0 - \Delta\varphi}{\tau}\right)^2\right)^{3.1063}}$$

The parameters A and B are used to fit the anisotropic scattering of the amorphous phase, the higher the ratio B/A, the more oriented are the amorphous chains. Parameters C and E correspond to the height of the central and side peaks and  $\tau$  is the width at half maximum of the peaks.  $\varphi_0$  is fixed (to a value of  $37.5^\circ$ ) since it corresponds to the angular distance from the reflection {201} to reflections {120} and {200}.  $\Delta\varphi$  accounts for deviations of the pattern orientation with respect to the tensile direction i.e. when the crystallites are on the average tilted from the stretching axis. Unless the stretching device and the X-ray camera would for some reason be tilted from one another, such a configuration is not expected in our samples that are parallel to the stretching axis ruling out any local average disorientation of the crystallites. It was indeed observed that the  $\Delta\varphi$  parameter was remaining close to zero in all tensile tests.

Once all the fitting parameters are obtained, the isotropic scattering due to air and the fillers are subtracted from parameter A to finally access the natural rubber matrix contribution only:

- The (isotropic) X-ray intensity scattered by air between the sample and the detector is removed (Figure 101). For this purpose a pattern of fixed acquisition time is recorded in the absence of sample. After azimuthal integration of the intensity on this air scattering pattern, one obtains the fit parameter  $A_{\text{scatteringMAX}}$ , proportional to the direct beam intensity  $I_{\text{MAX}}$  recorded by the photodiode:

$$A_{\text{scatteringMAX}} = kI_{\text{MAX}} \quad (63)$$

The same proportionality coefficient  $k$  applies with rubber samples which absorb the beam depending on their thickness  $e$  (64). It is assumed that all the absorption is due to the sample. The corrected parameter  $A_{\text{corr}}(e)$  is obtained after removing the air scattering contribution (65):

$$A_{\text{scattering}}(e) = kI(e) \quad (64)$$

$$A_{\text{corr}}(e) = A - A_{\text{scatteringMAX}} \frac{I(e)}{I_{\text{MAX}}} \quad (65)$$

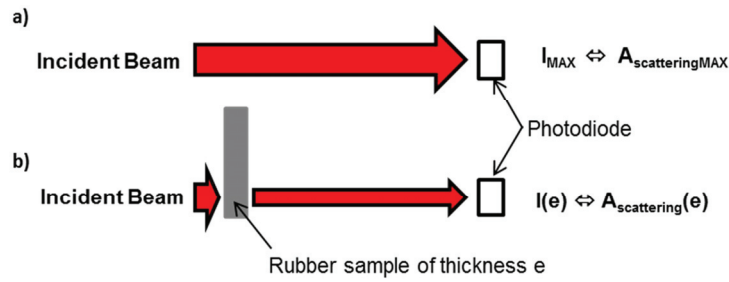


**Figure 101 : Air scattering correction: a) the photodiode records the maximum intensity  $I_{MAX}$  without any sample associated to the intensity collected on the 2D detector  $A_{scatteringMAX}$ . b) The intensity  $I(e)$  measured during the sample diffraction experiment allows to estimate the intensity collected on the 2D detector that comes from the air scattering.**

- The last correction concerned filled rubber samples, in which the scattering signal of the fillers has been measured directly using pure fillers in the form of powder and checked by comparing unstretched filled and unfilled samples. In the investigated  $q$  range the relative contribution of 50phr of Silica and 45phr of Carbon Black represents respectively 26% and 18% of the parameter  $A$ .

- **Crystalline content**

The crystalline fraction is defined as the ratio of the crystallite peak areas and the total area in the intensity versus azimuthal angle plot in Figure 100 using the value of the parameter  $A$  corrected for air and filler scattering (denoted  $A_{corr}$ ). The contribution from the crystalline phase is taken as the area between the total intensity (dashed red) and amorphous intensity curves (dotted blue).

$$\chi(\varepsilon) = \frac{\text{Crystallite Area}(\varepsilon)}{\text{Total Area}(\varepsilon)} \quad (66)$$

- **Amorphous Phase Orientation**

When stretching NR rubber samples, the amorphous scattering halo becomes anisotropic with a higher intensity in the direction perpendicular to the stretching axis (Figure 102) due to a preferential orientation of the chain segments in the loading direction.

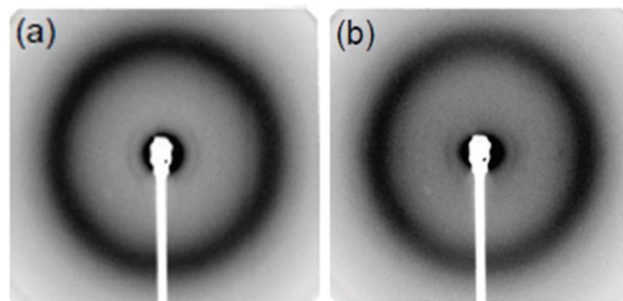


**Figure 102: Scattering pattern in the a) unstretched and b) stretched state close to SIC onset.**

The orientation of chain segments with respect to the force direction  $\vec{F}$  is described by the angle  $\beta$  (Figure 103). The symmetry is uniaxial around  $\vec{F}$ . The average degree of orientation of chain segments is described by the orientation order parameter (second order Legendre polynomial)<sup>107</sup>:

$$\langle P_2(\beta) \rangle = \left\langle \frac{3\cos^2\beta - 1}{2} \right\rangle \quad (67)$$

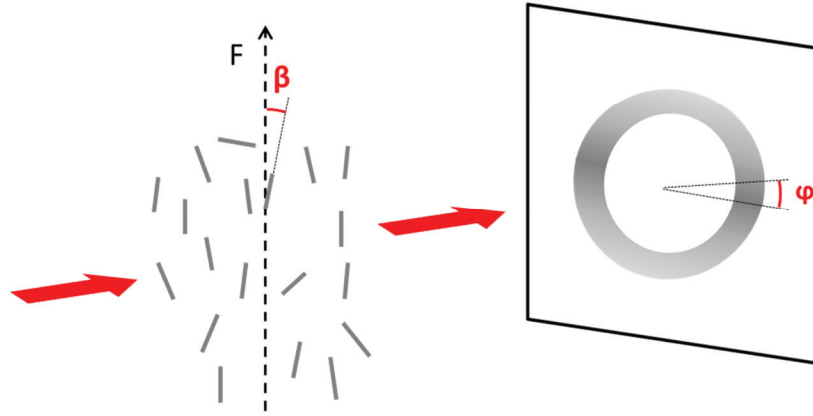


**Figure 103 : Schematization of X-ray scattered intensity for a system with a preferential orientation with respect to the direction of the force  $F$ . Chain segments are represented by the small rods. Note that the scattered intensity is maximal in the equatorial region.**

For an isotropic system:  $\langle P_2(\beta) \rangle = 0$

For a fully oriented system:  $\langle P_2(\beta) \rangle = 1$

The orientation order parameter is calculated as:

$$\langle P_2(\beta) \rangle = \frac{\int_0^\pi P_2(\beta) I(\beta) \sin\beta d\beta}{\int_0^\pi I(\beta) \sin\beta d\beta} \quad (68)$$

The X-ray scattering is maximum in the direction perpendicular to the preferential orientation of chain segments. As mentioned previously, The intensity of the amorphous halo as a function of the azimuthal angle can be fitted by a function  $I(\varphi) = A_{corr} + B \cos^2 \varphi$ .

Angles  $\beta$  and  $\varphi$  are related through:  $\beta = \pi/2 - \varphi$ .

$I(\varphi)$  can thus be rewritten equivalently:  $I(\beta) = A_{corr} + B - B \cos^2 \beta$ .

$$\langle P_2(\beta) \rangle = \frac{\int_0^\pi (A_{corr} + B - B \cos^2 \beta) \left( \frac{3\cos^2\beta - 1}{2} \right) \sin\beta d\beta}{\int_0^\pi (A_{corr} + B - B \cos^2 \beta) \sin\beta d\beta} \quad (69)$$

After integration, equation (69) gives:

$$\langle P_2 \rangle = \frac{-2B}{15A_{corr} + 10B} \quad (70)$$

It is negative, which is simply related to the fact that the intensity is maximum in the direction perpendicular to the stretching direction.

- **Crystallites disorientation**

The azimuthal width of the crystalline diffraction peaks is related to the degree of disorientation of the crystallites. In the case of a perfectly isotropic orientation of crystallites, the diffraction spots would turn into rings. Conversely, the azimuthal extension of diffraction peaks is relatively small (of the order  $10^\circ$ ), which means that the crystallites are well oriented along the tensile direction. Then, contrary to what has been proposed for the amorphous chains, it is not relevant here to compute a crystallite orientation parameter  $\langle P_2 \rangle$  since higher order terms of the Legendre polynomial expansion are not negligible.

As a consequence, the disorientation is described by the width at half maximum of the central peak in the azimuthal scan corresponding to crystalline planes  $\{120\}$  and  $\{200\}$  (Figure 104). In this way, the orientation distribution of an axis perpendicular to the tensile direction is monitored. The peak width at half maximum is related to the parameter  $\tau$  in the fitting equation (15).

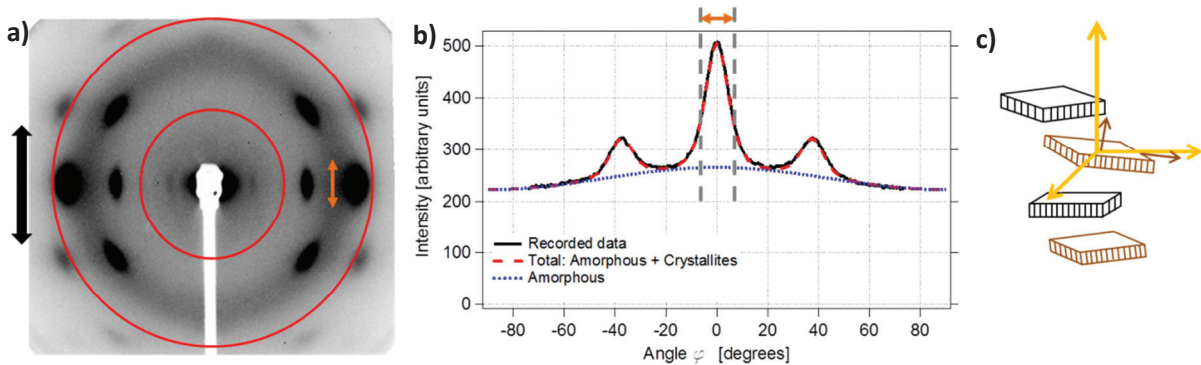


**Figure 104: Definition of the angular width (full width at half maximum of the central peak) related to the fit parameter  $\tau$ , which describes crystallite disorientation.**

- **Estimation of the crystallites size**

Comparisons of the crystalline peak width along the scattering angle were performed by doing a radial integration of the  $\{120\}$  and  $\{200\}$  peaks. The obtained spectrum as shown in Figure 105 is composed of the  $\{120\}$  and  $\{200\}$  reflection peaks as well as a bump due to the amorphous halo. The widths of the peaks were not calculated using complicated deconvolution techniques but simply compared between the different samples to provide pieces of information on the

relative crystallite sizes. The crystallite size in directions perpendicular to the chain axis is inversely proportional to the crystalline peak widths.

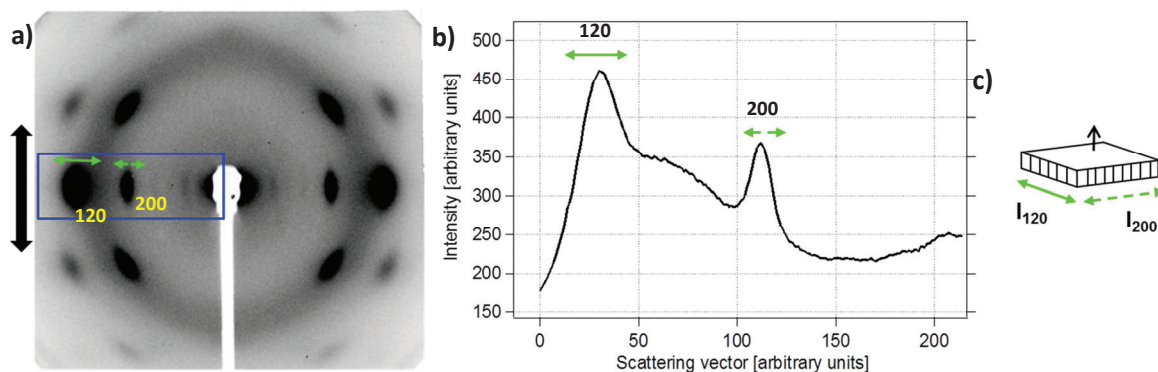


**Figure 105: Estimation of the crystallite size in the transverse direction by radial integration of the diffraction pattern (a). The intensity is reported as a function of the scattering vector (b) and the width of the {120} and {200} reflections qualitatively accounts for the crystallite dimensions perpendicular to chain axis (c).**

### III.3.f.iii. Stroboscopic acquisitions during periodic cycling

The development of a new in-situ stroboscopic high frequency testing machine was carried out at LPS. The principle and practical aspects of the periodic oscillations and the stroboscopic acquisition are detailed in a specific section of chapter V dedicated to Strain-induced crystallization kinetics since part of my work was to help in the development of the pattern analysis procedure and to perform measurements with the newly build device.



## IV. Overview of Mechanical Properties

IV.1.	Mechanical behavior in the linear regime .....	117
IV.1.a.	Effect of filler volume fraction.....	117
IV.1.b.	Effect of interface type.....	119
IV.1.c.	Applications .....	121
IV.1.d.	Discussion .....	122
IV.2.	Mechanical behavior at small and medium strains: Payne Effect.....	123
IV.2.a.	Effect of filler amount.....	123
IV.2.b.	Effect of the filler specific surface .....	125
IV.2.c.	Effect of interface type.....	126
IV.2.d.	Discussion .....	128
IV.3.	Mechanical behavior at large strains .....	129
IV.3.a.	Unfilled Natural Rubber.....	129
IV.3.b.	Effect of the Silica volume fraction .....	130
IV.3.c.	Effect of the crosslink density in filled samples .....	131
IV.3.d.	Effect of the Silica specific surface.....	132
IV.3.e.	Effect of interface agents.....	133
IV.3.e.i.	Nominal Stress.....	133
IV.3.e.ii.	True Stress .....	135
IV.4.	Conclusions .....	138

In this chapter, the mechanical properties in the small and large strain regimes are studied in pure and filled (reinforced) Natural Rubber materials, in relation to the microstructure. One objective is to better understand the key parameters affecting reinforcement. Also, the effect of large amplitude solicitation on the microstructural state of the filled rubbers will be discussed.

Concerning mechanical characterization, based on the observed mechanical behavior, several strain regimes may be distinguished for unfilled and filled NR samples (Figure 106). In unfilled NR, according to well-known rubber elasticity, the linear (or quasi-linear) regime extends up to very large strain amplitude (about 400% in uniaxial elongation typically). The regime at very large strain amplitude becomes non-linear for two reasons. First, finite chain extensibility may start to play a role and induce an upturn of the stress curve. Second, strain-induced crystallization (SIC) induces self-reinforcement, i.e. a strong upturn of the stress curve as well (stress hardening). Roughly speaking, these two regimes are sufficient to describe the properties of unfilled NR.

The behavior is much more complex and qualitatively different in filled NR materials. The linear regime is restricted to very small strain (smaller than 0.1% typically). In the range of strain amplitudes between roughly 0.1% and 50%, the behavior is strongly non-linear, with a drop of elastic modulus and maximum of loss modulus. This is the Payne effect regime (medium strain regime). The large strain regime (beyond 50% strain typically) may itself be divided into two regimes: first, a stress hardening regime is observed up to strain amplitudes of 100 to 200%, finally, in the very large strain regime (beyond 100 to 200% amplitude), a nearly constant modulus is observed.

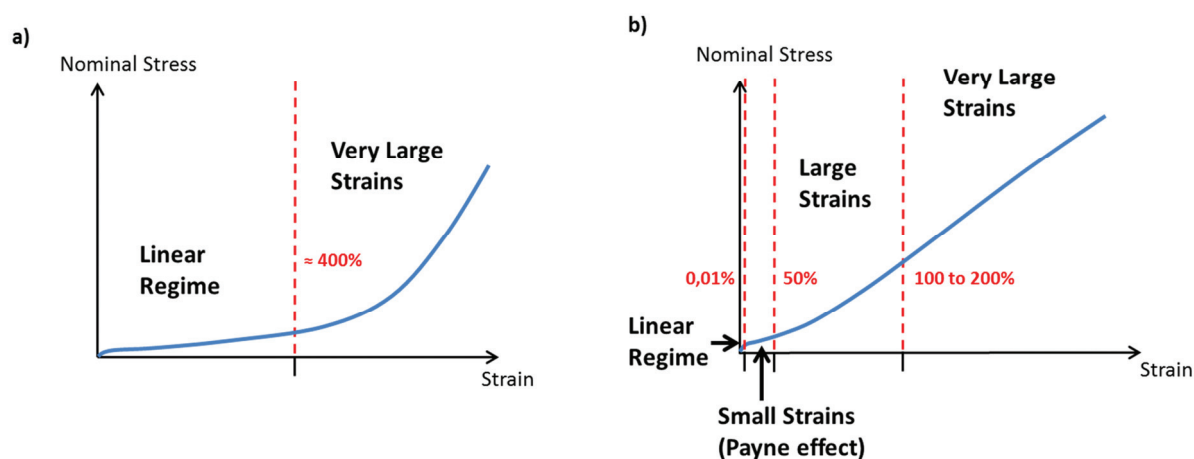


**Figure 106: Schematics of the different strain regimes in terms of mechanical properties for a) unfilled and b) filled NR samples.**

The mechanical behavior in the small and medium strain regimes (i.e. up to approximately 50% strain amplitude, corresponding to the end of the Payne effect regime) has been studied by Dynamical Mechanical Analysis (DMA). Both temperature and strain sweeps have been performed in various materials in order to identify the main mechanisms which drive the increase of modulus and dissipation in the presence of fillers.

As regards the large strain regime, the results obtained in reinforced materials are discussed and compared to the corresponding unfilled natural rubber properties. It was chosen to first study tensile properties on as prepared samples. Indeed, crack propagation mechanisms involve the solicitation and failure of the material in a very large deformations range without any previous mechanical cycling in this range. It is thus essential to characterize reinforcement at large strain amplitudes during the first traction.

The effect of cycling on the stress-strain curves in terms of reinforcement and dissipation was then analyzed separately in chapter VII.

Filled samples are denoted with the type of filler and interface agent (in the case of silica). For example, silica-TESPT-filled NR denotes a NR material filled with silica treated by TESPT as a coupling agent.

## IV.1. Mechanical behavior in the linear regime

The analysis of the modulus at very small strains in the linear regime over a wide range of temperatures highlights a very important feature of filled elastomers: the modification of the glass-transition behavior as revealed by the slow decay of the storage modulus with temperature in the rubbery regime.  $\tan \delta$  as the ratio of the loss modulus upon the storage modulus gives an indication on the ability of the materials to dissipate energy for a given elastic modulus. This quantity is consequently widely used since it enables a direct evaluation of both storage and loss modulus. We first discuss the effect of varying the filler volume fraction, then the effect of varying the filler/matrix type of interactions.

### *IV.1.a. Effect of filler volume fraction*

The storage modulus, the loss modulus and the ratio of the two of them ( $\tan \delta$ ) are presented in Figure 107 as a function of temperature, in NR samples reinforced with various volume fractions of silica.

Let us first consider the behavior of the pure Natural Rubber: The measurement of the modulus gives a signature of the principal relaxation (glass transition) of the polymer matrix. The decrease of the storage modulus  $E'$  from the glassy state to the rubbery state extends over a large range of temperature (from  $-60^\circ\text{C}$  to almost  $-20^\circ\text{C}$ ). At high temperature, beyond the glass-transition regime, the storage modulus increases linearly with temperature according to the entropic nature of rubber elasticity (see chapter 2). On the scale of the graph in Figure 6a), the slope would be small however, with a theoretical modulus of the order  $1.3 \times 10^6$  Pa at  $0^\circ\text{C}$  to  $1.7 \times 10^6$  Pa at  $80^\circ\text{C}$  (taking a crosslink density of the order  $2 \times 10^{-4}$  mol/g). On the other hand, the glass transition of the rubber matrix corresponds to a maximum of the loss modulus  $E''$ . The glass transition temperature  $T_g$  is currently defined as corresponding to the  $E''$  maximum or to the maximum in  $\tan \delta = E''/E'$ .

Introducing reinforcing particles such as Silica strongly modifies the behavior in the linear regime: Firstly the modulus in the glassy regime is enhanced due to the contribution of hard aggregates (which have a modulus even higher than that of the glassy polymer matrix). Then the decrease of the modulus as temperature increases is much broader than in the pure matrix. It covers a very broad range of temperature. The modulus continues to decrease slowly in the whole investigated temperature range, which covers temperatures up to  $T_g + 130^\circ\text{C}$ . Also, as regards the loss modulus  $E''$ , the material is much more dissipative in the rubbery regime.

Accordingly, the position of the maximum of the loss factor  $\tan \delta$  is not substantially modified by the addition of fillers but the transition region is spread up to higher temperatures, this effect being more pronounced as the filler content rises.

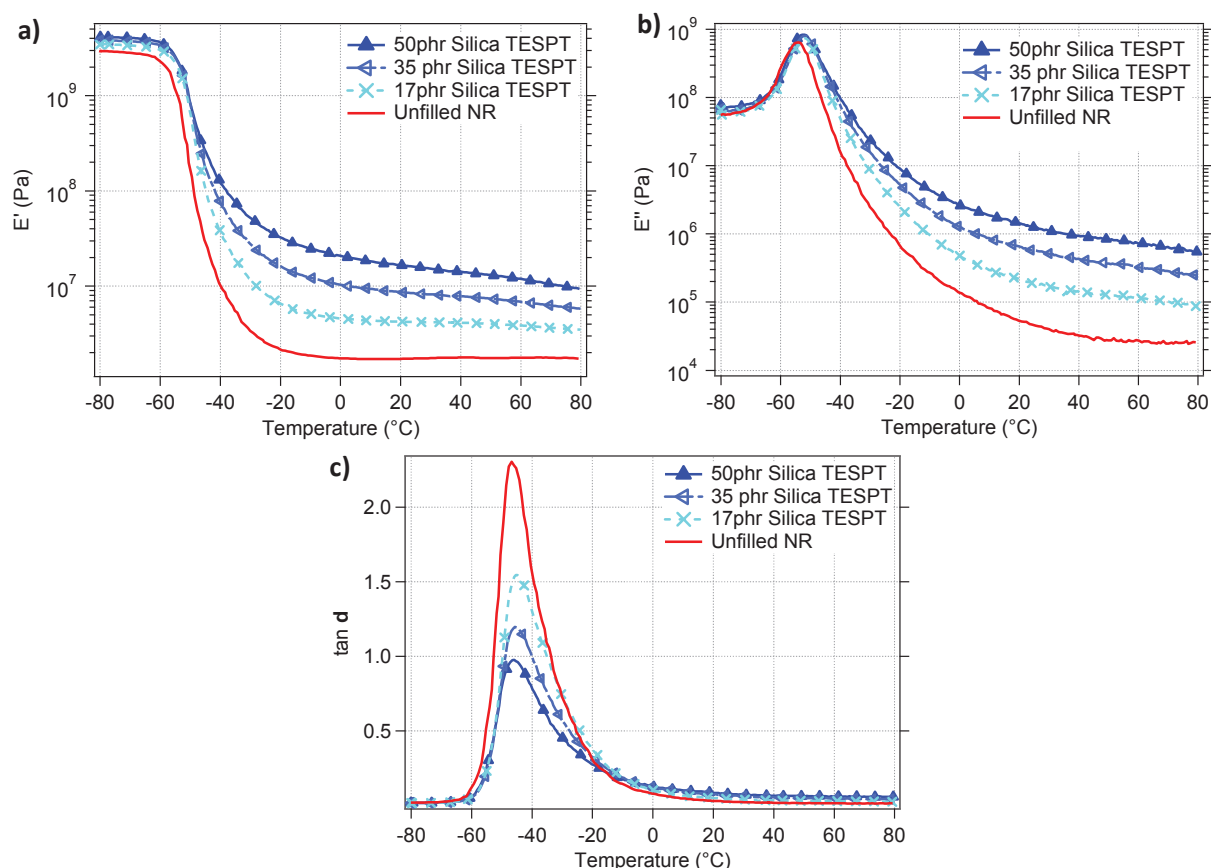


**Figure 107: Storage Modulus, Loss Modulus and tangent delta for unfilled and silica- TESPT-filled NR at three different volume fractions of silica (sample series 115-10). All samples have the same sulfur content (1.5 phr).**

In order to better figure out the reinforcement effect, the storage modulus of reinforced samples  $E'$  can be normalized by the storage modulus  $E'_0$  of the corresponding unfilled NR matrix. We can assume that the unfilled and filled NR systems compared here have roughly the same crosslink densities. It is indeed found that the effect of additional crosslinks is very weak as compared to the dramatic rise of modulus provided by fillers.

The obtained ratio  $R = E'/E'_0$  (Figure 108) is simply referred as *reinforcement* since it indicates the stiffness increase brought by the fillers. The maximum of reinforcement appears at approximately -20°C (that is roughly  $T_g + 30^\circ\text{C}$ ) and sharply increases with the filler fraction up to values far higher than the prediction of the Guth and Gold theory<sup>30</sup>, which is represented in the figure by dashed lines for the three concerned filler fractions. It is clear that geometrical reinforcement does not fit the data, both as regards the temperature variation of the reinforcement curves and the high reinforcement values which are obtained on a large temperature range.

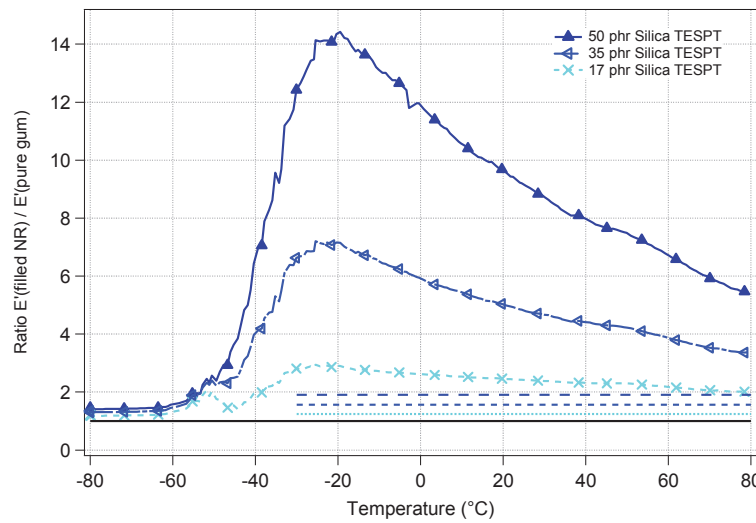
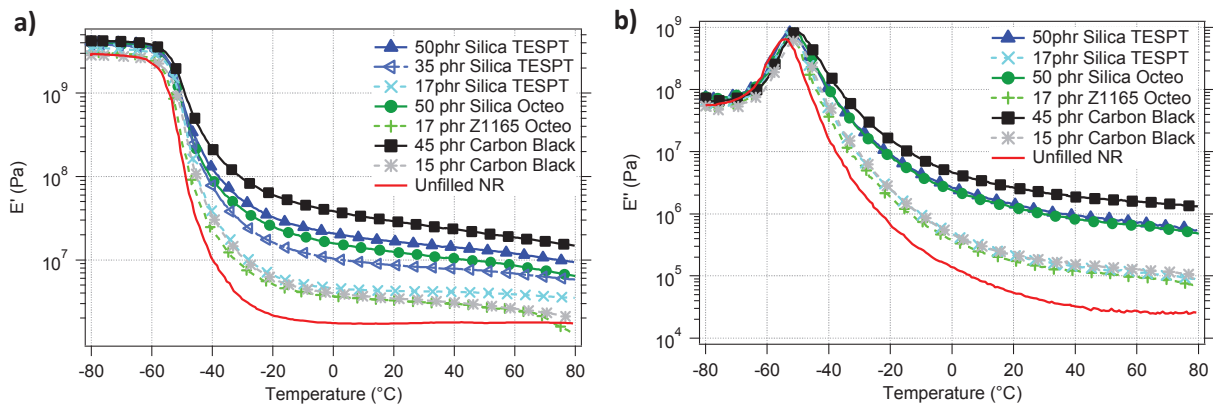


**Figure 108: Reinforcement curves of Silica-filled NR for 3 different volume fractions (from the data in Figure 107). The dashed lines indicate the Guth and Gold prediction (see chap. II) for the 3 considered volume fractions (sample series 115-10).**

#### IV.1.b. Effect of interface type

In addition to the strong dependence on the filler volume fraction, the modulus in the linear regime also depends on the type of interface with the rubber matrix. The storage modulus, the loss modulus and the loss factor  $\tan\delta$  are shown in Figure 109 as a function of temperature, in NR samples reinforced with carbon black and silica using either covalent (coupling) or non-covalent (covering) interface agents. Note that the density of carbon black is a little bit smaller than that of silica fillers, so that 45 phr Carbon Black corresponds to the same volume fraction as 50 phr silica.

Our measurements stress out a higher storage and dissipation modulus for Carbon black than Silica. Concerning the surface treatment of the silica, no influence is recorded on the loss modulus but the elastic modulus shows a slight enhancement for the covalent (coupling) agent.



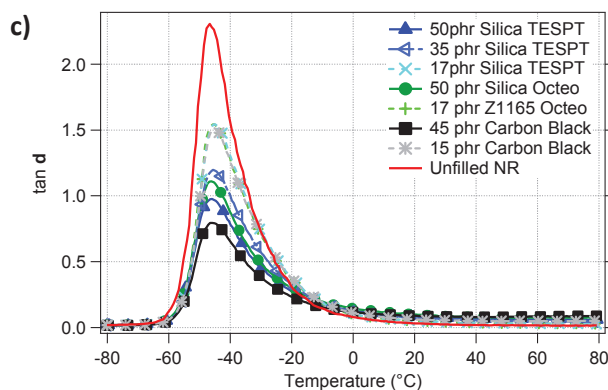


**Figure 109: Storage Modulus, Loss Modulus and tangent delta for pure NR and NR materials filled with Carbon black or silica with 2 different types of interface, at two different volume fractions (sample series 115-10).**

The corresponding reinforcement ratios  $R = E'/E'_0$  are shown in Figure 110.

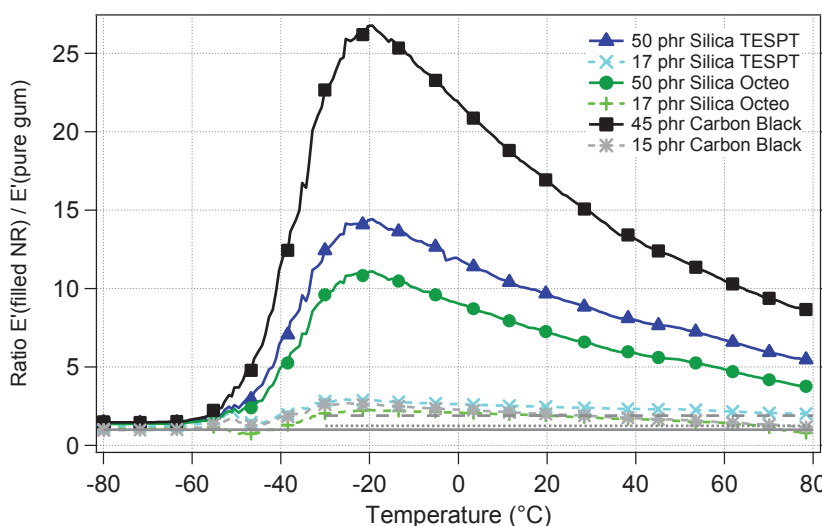


**Figure 110: Reinforcement curves obtained from the data in Figure 109 (for 3 different interface types and 2 different volume fractions) (sample series 115-10).**

The values of the maximum of the reinforcement curves are shown as a function of the filler volume fraction in Figure 111. **Figure 111 shows the high maximum reinforcement values (up to about 30) obtained in the most reinforced sample at large filler volume fraction.** Figure 111 also illustrates that at low filler fractions (roughly below 0.10), the maximum values of the reinforcement are similar whatever the interface type. Conversely at larger filler volume fractions, the maximum reinforcement value is higher for Carbon black compared to Silica.

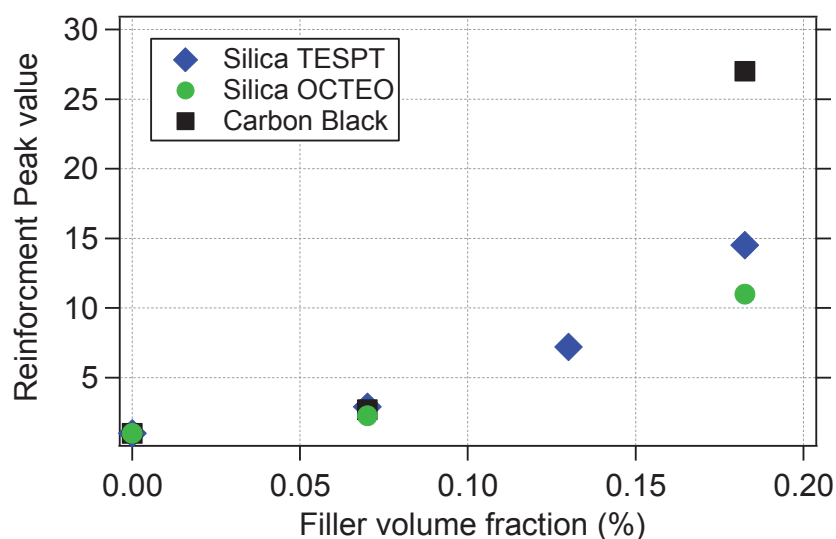


**Figure 111 : Values at the maximum of the reinforcement curves for 3 interface types at several volume fractions (sample series 115-10)**

#### *IV.1.c. Applications*

The loss factor  $\tan \delta$  indicates the ability of a material to dissipate energy for a given elastic modulus. This quantity is consequently widely used since it enables a direct evaluation of the compromise between high elastic modulus and low loss modulus.

For tire manufacturers there are two temperatures labeled as laboratory indicators of performance which are 60°C and 0°C. The first parameter at 60°C (temperature of a tire during rolling) for frequencies of 10Hz is related with the rolling resistance since the frequency of tire-road contact is of this order of magnitude. The lower the dissipation at this temperature, the lower the rolling resistance is and therefore the lower the fuel consumption is.

Assuming a correct time-temperature superposition, the second parameter corresponds to the modulus at 60°C for the very high frequencies involved in the friction mechanisms of the gum on the road asperities responsible for the wet grip performance. In this case the higher the dissipation the better the wet grip.

It is interesting to note here the difference between Silica in combination with a good coupling agent and Carbon Black. As demonstrated for our samples in Figure 112, the dissipation factor  $\tan \delta$  is higher for Silica at 0°C and lower at 60°C as compared to Carbon black ensuring a better compromise of properties for the Silica filler. This result is at the basis of the progressive replacement of Carbon black by silica in order to lower rolling resistance in tires.

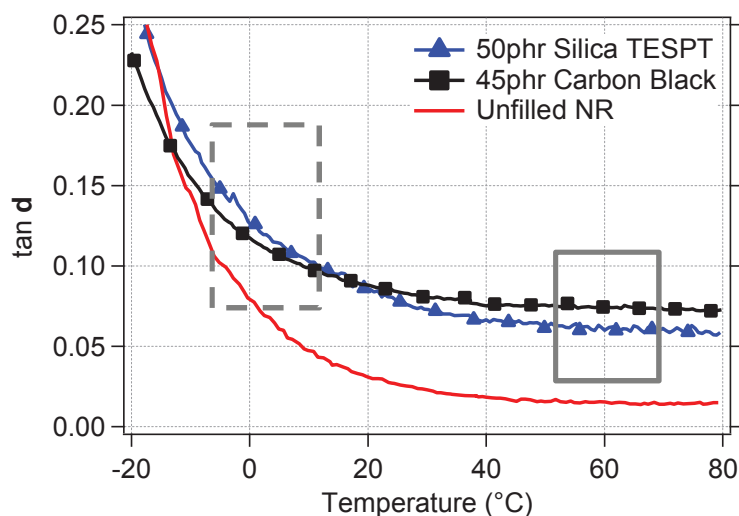


**Figure 112: Tangent  $\delta$  versus temperature for reinforced and pure NR (sample series 115-10). The Silica-TESPT compound presents a better balance of high dissipation at low temperature (higher Wet Grip: dashed rectangle regime) and low dissipation at high temperature (lower Rolling Resistance: continuous rectangle regime).**

#### *IV.1.d. Discussion*

An important conclusion drawn from these results is that the impact of the interface is only clearly visible at high enough filler fractions. It is impossible to distinguish reproducible differences in the reinforcement  $R$  for samples with filler fractions 7% in volume (17phr of Silica or 15phr of Carbon Black), whereas the modulus increase is about twice larger for Carbon black than for Silica at volume fractions of 18.5%. The percolation threshold above which the fillers are interconnected in a continuous network is of the order of 0.10 in volume for reinforcing aggregates of this size range<sup>74,84</sup>. This supports the idea that the weakly filled samples do not present a high reinforcement for only a few domains have a reduced mobility. A strong reinforcement is thus related to a filler networking effect in which the slow-motioned polymer chains participate.

The large difference between Silica and carbon black indicates that reinforcement provided by carbon black is generally significantly stronger than for silica at the same volume fraction, even though the surface area developed by carbon black is smaller than for silica for a same volume fraction. This suggests that the activity of the Carbon surface is much stronger and actively participates in reducing the mobility of NR chains.

We have seen how the filler volume and filler surface treatment affect the mechanical behavior close and far from the glass-transition temperature. This effect can be understood considering some restrictions of the polymer mobility or even glassy layers at the fillers interface extending the temperature domain for the subsistence of glassy bridges between fillers.

This can be understood in terms of heterogeneities in the local relaxation times of the rubber chains i.e. some of them are in a glassy state or have a low mobility at temperature above the pure polymer Tg. Increasing the filler fraction creates more restriction on the mobility for a large part of the polymer is in the vicinity of the fillers (a percolation phenomenon may also be

invoked but not necessary here). The percolation of a low mobility phase of rubber has to be taken into account to explain the increase of the modulus and its evolution with temperature.

This suggests that the activity of the Carbon surface is much stronger and actively participates in reducing the mobility of NR chains. On the other hand, this could be the result of a worst state of local distribution of carbon black fillers leading to numerous short distances between them. On the opposite well-distributed fillers yield less overlapping of mobility-restricted polymer phase between adjacent particles.

In the next section, to complement the measurements of the reinforcement in the linear regime, the effect of the amplitude of the applied strain in the so-called Payne effect regime is discussed.

## **IV.2. Mechanical behavior at small and medium strains: Payne Effect**

Oscillatory shear sweeps of strain amplitudes from 0.1 to 50% at a temperature of 60°C (as described in chapter III) were used to characterize the Payne effect in all elaborated systems. It is to be reminded that Payne effect characterization by dynamical measurement of the modulus is quite sensitive to the mixing process and mechanical history of the compounds. Despite the cautious repetition of the mixing procedure, some significant differences were observed from one sample series to another. Therefore, we have chosen never to compare samples from different series. This is why samples with similar formulations but from different series discussed in this section may have different moduli from one set of samples to the other.

Only the most relevant results are presented here to illustrate the effect of the different control parameters of the formulations: the filler amount, the specific surface of silica and the silica surface agent, also compared to carbon black.

### *IV.2.a. Effect of filler amount*

The storage moduli are plotted in Figure 113 as a function of the oscillatory strain amplitude for a series of NR samples filled with various silica volume fractions and using the same coupling agent. The drop of the storage modulus depends strongly on the silica fraction. Although the lowest volume fraction used here is considered below the percolation threshold for this type of fillers (around 0.10), a slight decrease of the modulus is visible meaning that the percolation is not necessary to observe a non-linearity effect.

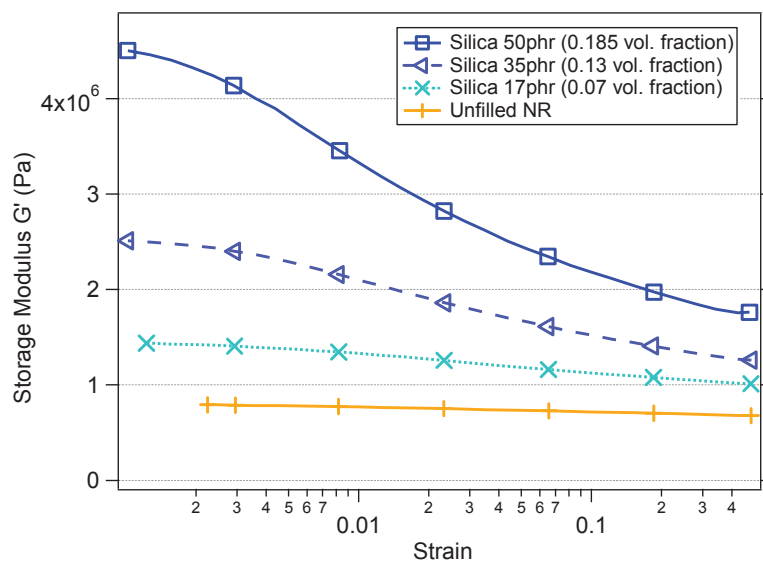


**Figure 113: Influence of filler volume fraction on the Storage modulus. The interface agent used is TESPT which quantity is adjusted to the total silica surface (sample series 115-10).**

Unlike the evolution of  $G'_{\infty}$  which is quite linear with the filler content,  $G'_0$  increases strongly with high volume fraction of silica (Figure 114). This non-linear dependence of the strain softening (or amplitude of the Payne effect)  $\Delta G' = G'_0 - G'_{\infty}$  on the filler amount indicates that it cannot be only described by contributions proportional to the total surface area of fillers.

It should be noticed that the temperature at which the experiments were carried out is far from the glass transition (more than 100°C of difference) which may indicate that no glassy layers percolation mechanism can be invoked for the modulus level at low strains. Nevertheless the effect of the fillers on the mobility of the rubber chains can account for the formation of constrained polymer bridges between fillers. Figure 114 highlights this contribution of the filler-polymer network since the modulus at low strain increases rapidly above filler fraction of the order of 0.10.

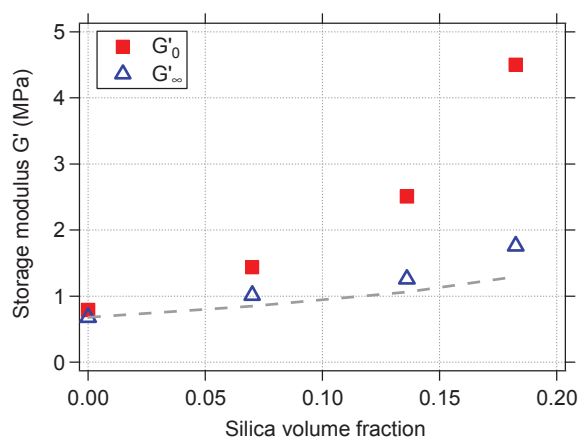


**Figure 114: Silica volume fraction effect on storage modulus at 0.1% ( $G'_0$ ) and 50% ( $G'_{\infty}$ ) of strain. The dashed line represents the Guth and Gold prediction<sup>30</sup>.**

Nevertheless, the Payne effect observed at low filler fraction is an indication that other mechanisms which are not related to a percolated filler-polymer-filler network may play a role. Similarly to what has been proposed in carbon black<sup>32</sup>, one could stress the effect of adsorption and desorption of the chains on the silica surface on the dissipation and elastic modulus drop.

#### IV.2.b. Effect of the filler specific surface

In Figure 115 the storage moduli are plotted as a function of the strain amplitude for NR samples filled with silica of different specific surfaces, keeping the same silica volume fraction and coupling agent. Increasing the silica specific surface increases the Payne effect amplitude.

Interestingly  $G'_{\infty}$  increases with the specific surface of silica although the hydrodynamic effect should be very similar for this series of samples since the filler fraction is identical. The matrix contribution can be considered to be roughly constant as well. Note that, as we have seen before, a higher specific surface should even induce more CBS adsorption, which should result in a lower crosslink density, and thus in a lower modulus, opposite to the observed trend.

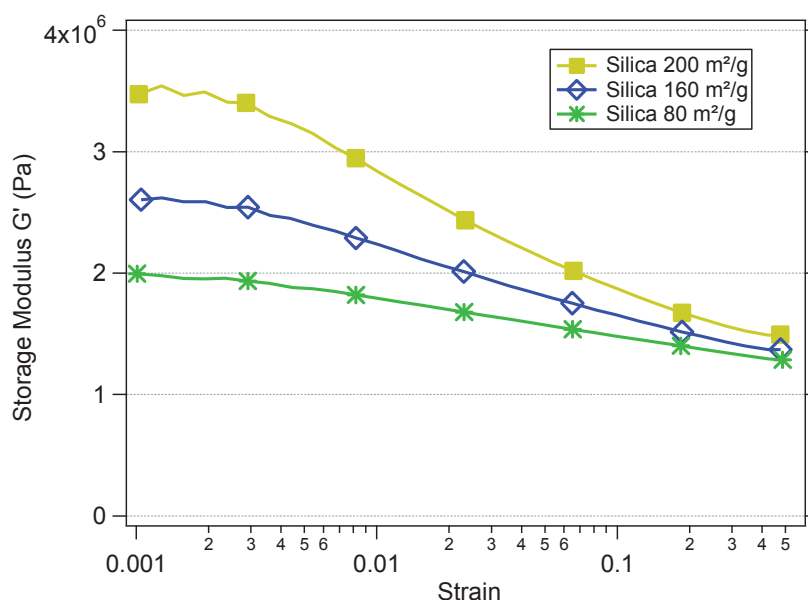


**Figure 115: Silica specific surface influence on storage modulus. The interface agent used is TESPT which quantity is adjusted to the total silica surface (sample series 046-11)**

This can be understood as the effect of a higher mobility restriction since more silica surface is accessible. It has also been shown that for those silica<sup>61</sup>, the distance between aggregates for a given filler fraction increases when the specific surface decreases which would explain part of the strain softening evolution with specific surface (in the glassy layer interpretation, longer distances between aggregates means less glassy bridges formation and thus a lower Payne effect).

Therefore the differences of  $G'_{\infty}$  are due to increased occluded and strongly bound rubber in the case of high specific surface silica. It may be reminded that the morphology of the 3 kind of silica presented here is identical ruling out a possible effect of this parameter on bound rubber.

As shown by Guy and coworkers<sup>53</sup>,  $G'_0$  does not linearly depend on the total engaged surface of silica (see chapter 2) showing the importance of the interconnecting network of fillers and strongly bound polymer.

#### IV.2.c. Effect of interface type

In Figure 116 the storage moduli are plotted as a function of the strain amplitude for NR samples filled with carbon black and silica with different interface agents, keeping the same filler volume fraction. First the quantities  $G'_0$  and  $\Delta G'$  are higher for Carbon black filled NR as compared to silica filled samples.

Figure 116 clearly shows the influence of the silica interface agent on the Payne effect, NSC exhibits a smaller decrease  $\Delta G'$  of the modulus as compared to TESPT.

It is important to note that several works within Rhodia have proved that Silica-TESPT compounds mixed at higher temperatures do have lower Payne effect amplitudes  $\Delta G'$ , close to the one recorded for NSC samples. It is also to be reminded that mixing temperatures were systematically higher for NSC in our sets of samples in order to ensure that the silane-rubber coupling was taking place in the mixer. The differences between the coupling agents measured here may thus be mainly related to the differences in the sample processing rather than to intrinsic effects of the coupling agents. Moreover, previous studies have put forward the effect of the dump temperature on the Payne effect for silica filled SBR and NR compounds<sup>141,145</sup>, confirming the importance of properly monitoring the mixing temperature.

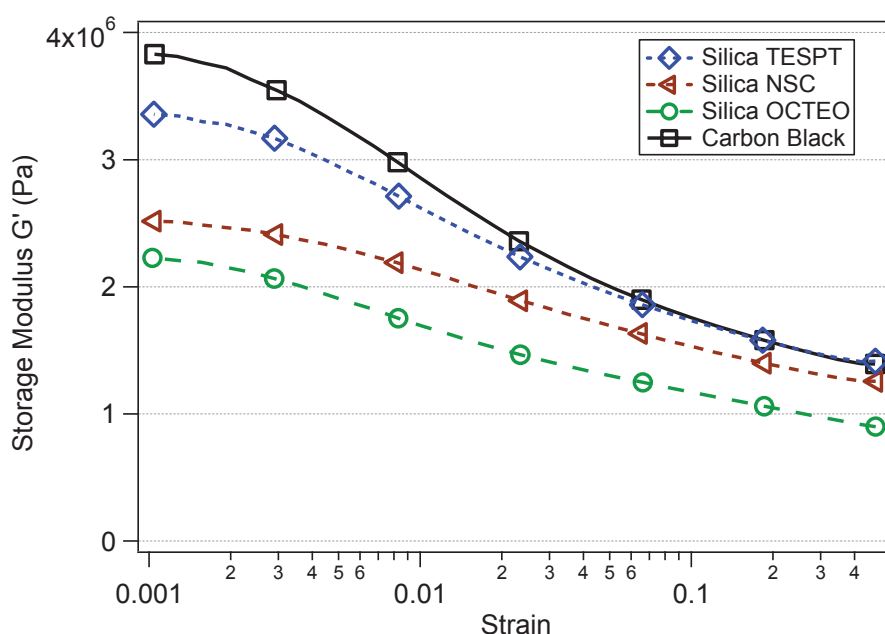


**Figure 116: Influence of rubber-filler interface on the storage modulus at constant filler volume fraction (sample series 119-11).**

As regards the effect of the covering agent, Ramier and coworkers<sup>65</sup> have found a clear increase of the Payne effect amplitude when the covering agent OCTEO is used in an SBR matrix

compared to the coupling agent TESPT. Our measurements do not show strong differences between Silica-TESPT and Silica-OCTEO in terms of modulus decrease.

Other processing parameters which have a strong influence are the mixing time<sup>141</sup> and the number of mixing steps, as evidenced in Figure 117. The non-linearity or Payne effect amplitude  $\Delta G'$  is significantly reduced when processing in two mixing steps, probably due to an improved distribution of the aggregates. This effect is particularly important in the case of hydrophilic silica, whose wetting by the rubber matrix during the process is more difficult to achieve than when using carbon black.

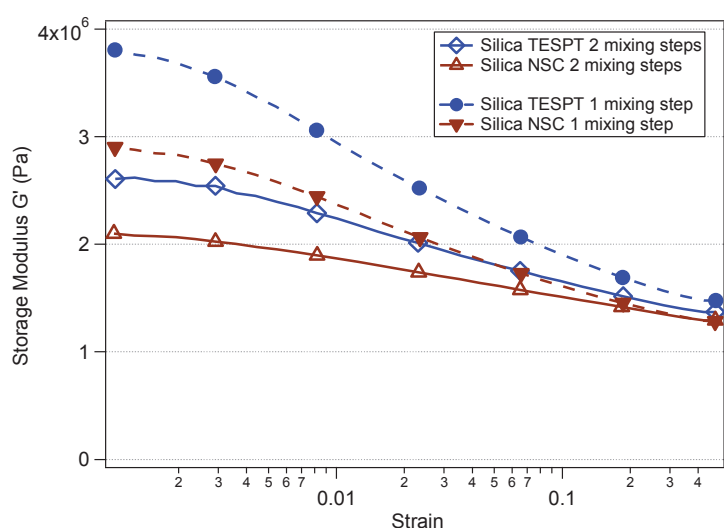


**Figure 117: Influence of the number of mixing steps on the Payne effect for Silica TESPT and Silica NSC (sample series 095-10: 1 mixing step and 030-11: 2 mixing steps)**

Figure 118 shows the loss moduli as a function of strain amplitude for the four kinds of polymer/filler interfaces, normalized by the loss modulus values  $G''_0$  at the lowest strain. The position of the maximum loss modulus curve corresponds fairly well to the inflexion point of the storage modulus curve. However, plotting the loss modulus gives much better defined values of the maximum.

It appears that the maximum of dissipation occurs for significantly different and reproducible strain amplitudes, depending on the interfacial agent used for silica. The peak occurs earlier for Silica OCTEO and later for Silica-NSC than Carbon black and Silica-TESPT. This result is discussed in the following paragraph.

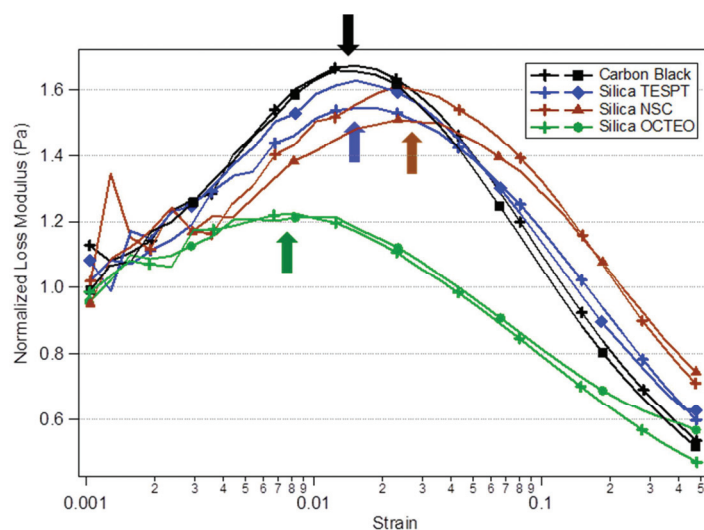


**Figure 118: Influence of NR/filler interface on the position of the maximum loss modulus. Arrows indicate the strain at which the dissipation is the highest (sample series 095-10 and 119-11)**

#### *IV.2.d. Discussion*

At the tested temperature of 60°C, higher  $G'_0$  and  $\Delta G'$  for Carbon black filled NR as compared to a silanized highly dispersible Silica is a well-established result. It is attributed to the supposed better distribution of the silica and/or the numerous physical interactions at stake at the carbon black interface that enhance the immobilization of rubber chains and induces adsorption/desorption phenomena that dissipate energy.

As previously mentioned, the NSC silane is supposed to increase chemical bonding to the matrix which should lead to more restriction of polymer mobility and consequently a higher  $G'_0$  value. As it is not the case, one may suggest that the average distance between particles is larger in the case of NSC compared to TESPT. It would thus be interesting to be able to measure the distribution of silica particles.

Another possible explanation would be that the dispersion of aggregates (breakdown of agglomerates) is lower in the case of NSC compared to TESPT. This would lead to the observed reduction of  $G'_\infty$  and  $\Delta G'$  (but has not been confirmed by the dispergrader measurements, see Appendices).

As shown by Montes<sup>62</sup> and Papon<sup>63</sup> on model samples, the distances between closest particles is of high importance for the percolation of glassy and/or intermediate mobility layers. Papon et al<sup>63</sup> show that for an identical silica fraction, the minimal distances between neighboring particles is higher when a covalent coupling agent is used. In other words, the distribution of distances is more homogeneous and silica particles are closer to a random close packing arrangement with the coupling agent. This suggests that the chemical coupling improves the silica distribution by enhancing the compatibility with the polymer. It is not straightforward that this argument can be applied to our systems consisting of a different polymer and different particles. Unfortunately diffusion measurements coupled with simulations cannot enable us to access the distribution of aggregates in our case for the fractal aspect of precipitated silica leads

to very complicated scattering signals. It is thus not possible to verify our assumption on the distribution of fillers as a function of the interface.

According to the classical decomposition of the Payne effect (see chapter II), the level of  $G'_{\infty}$  should depend on the so-called in-rubber structure consisting in occluded rubber and tightly bound rubber not participating to the deformation. In the case of the covering agent OCTEO, this fraction of elastically inactive polymer is low since no chemical bonds link the rubber chains to the filler.  $G'_{\infty}$  is higher in the case of TESPT compared to NSC which can be a further indication of a good distribution state of silica aggregates with the latter coupling agent leading to fewer inter-aggregates occluded rubber. Another more reliable explanation for this difference is the ability of the TESPT to release sulfur during the mixing process and in consequence increase the matrix crosslink density as demonstrated by DQ-NMR. Finally the structure of carbon black particles being different, it can be assumed that it results in more occluded rubber.

In the frame of the glassy bridges interpretation of the Payne effect, one understands the maximum loss modulus strain as the point where the yielding of glassy bridges is the highest<sup>35</sup>. Yielding of glassy bridges depends on the local stress amplification due to distances between fillers: the closer the particles and the higher the local stress for a specified strain amplitude. It would mean that when the silica fillers are closer, the strain amplification leads to the maximum yielding of glassy domains at a lower extension. Applying this frame of interpretation to our results would indicate that the distances between particles are lower for Silica OCTEO and higher for Silica NSC compared to Silica TESPT. Distances between Carbon Black aggregates and Silica-TESPT aggregates would be equivalent which would suggest a poorer distribution of Carbon Black aggregates since they are bigger than standard Silica Z1165MP aggregates.

### IV.3. Mechanical behavior at large strains

The results of simple uniaxial tensile tests on **as-prepared (not precycled)** unfilled and filled samples are discussed in this section. The effects of the filler content, filler specific surface and interface type on the stress-strain behavior in the large strain range are discussed. Two distinct regimes are distinguished for the sake of clarity: the large strain regime (from about 100 up to about 200% or 300% depending on the filler, coupling agent and crosslink density) and the very large strain regime, from about 200% or 300% up to failure.

#### *IV.3.a. Unfilled Natural Rubber*

The stress-strain behavior of the two sets of unfilled NR samples with various sulfur and accelerator amounts (sample series 046-11 and 119-11) is reported in Figure 119. The sulfur and accelerator amounts have a strong effect on the modulus. The effect on the modulus is in good qualitative agreement with the rubber elasticity theory that predicts a direct proportionality between the crosslink density and the modulus. This point will be further discussed in the next chapter.

The stress upturn observed at very large extension ratios is usually attributed to the limited chain extensibility phenomenon: the Gaussian like behavior is no longer applicable and the stress input required to pursue the deformation of a chain rises. The higher the crosslink density the lower the

maximum chain extensibility. This explains that the deviation from the classical rubber elasticity occurs at lower extension ratios for highly cross-linked samples. Actually, instead, the stress upturn rather seems to occur at a given, constant stress level for all samples. In addition, strain-induced crystallization (SIC) also strongly contributes to the stress upturn at high extensions. As regards the ultimate properties, a maximum true stress at break is reached around a sulfur amount of 1.0 phr:

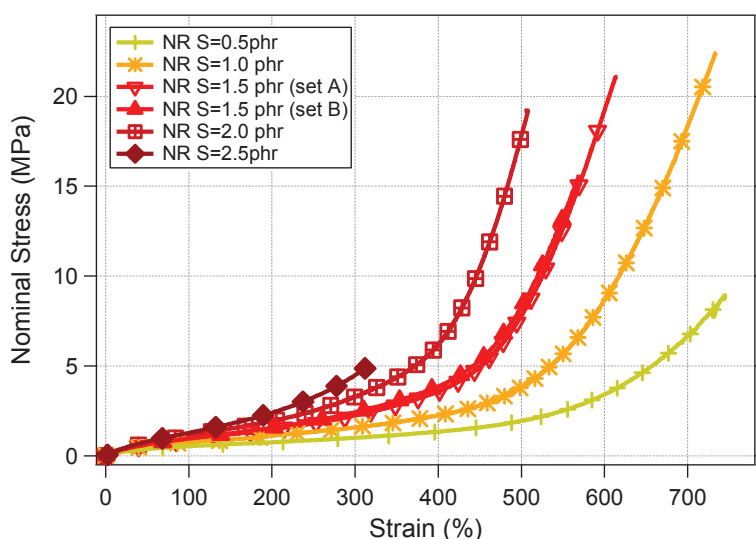


**Figure 119: Stress-strain curves for unfilled samples of samples series 046-11 (set A) and 119-11 (set B).**

#### *IV.3.b. Effect of the Silica volume fraction*

Uniaxial traction curves up to failure are shown in Figure 120, for a series of NR samples filled with various silica volume fractions and using the same coupling agent. The effect of the filler volume fraction on the stress-strain behavior is complex. In the large strain regime (up to about 300%), the stress (i.e. the reinforcement) is larger as the filler volume fraction is larger.

Then, the slope observed in the very high strain regime decreases as the filler fraction increases. It is even observed that the stress measured in the sample filled at 18.5 vol% becomes smaller than in the sample filled at 13 vol%.

The ultimate properties are improved as well when introducing silica aggregates. The strain at break is slightly lowered but the stress at break is higher. Together with the enhancement of the modulus, this leads to an increase of the energy at break (area under the stress-strain curves). The energy input required to break the sample increases quite strongly with small filler fractions and then rises more slowly for high fillers fraction.

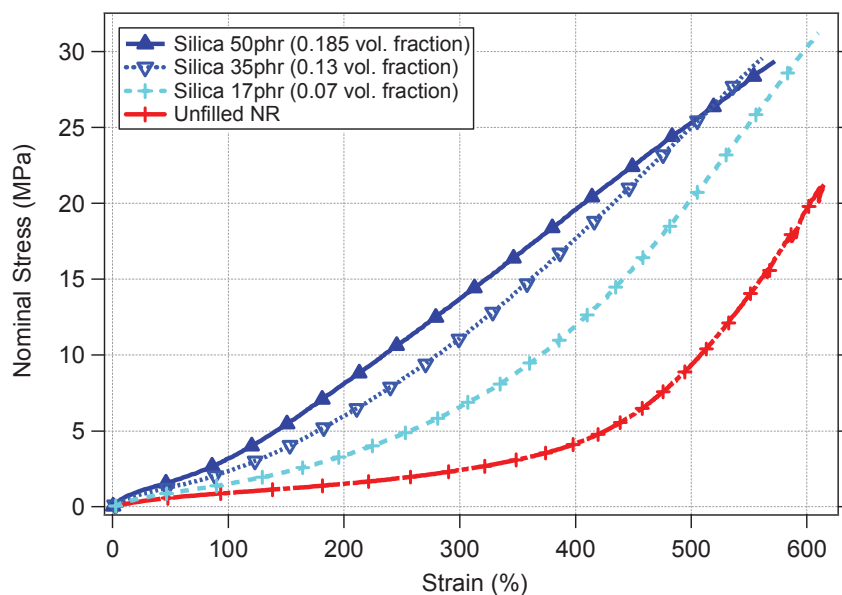


**Figure 120: Effect of the filler fraction on the stress-strain curves up to failure. Reinforced samples are silica-*TESPT* filled NR. The quantity of *TESPT* is adjusted according to the total silica surface (sample series 115-10) (reinforced samples not precycled).**

### Discussion

In the case of unfilled Natural Rubber, the stress hardening regime at very large extension right before failure has been attributed to two effects: limited chain extensibility and strain-induced crystallization.

The introduction of nanometric fillers is expected to increase the modulus due to the hydrodynamic reinforcement effect described earlier (chapter II). Nevertheless we have seen that this contribution is not sufficient to explain the modulus level in the low strain regime. The high values and the large increase of the modulus in the large strain regime are not predicted either.

This modification of the curve shape by introducing fillers may be explained by the strain amplification phenomenon<sup>68</sup> which lowers the macroscopic deformation onset for both limited chain extensibility and strain-induced crystallization. Indeed, it is known that the strain at SIC onset decreases significantly when adding carbon black<sup>71,72</sup> or silica<sup>73,74</sup> (see also chapter V). This leads to an increase of elastic modulus at a given strain value.

The fact that the stress upturn is not as steep in highly filled NR samples as in pure NR could be due to heterogeneous strain amplification. In this picture, regions with higher local amplification induce earlier increase of stress (macroscopic strain around 100%), less amplified regions induce an increase of stress at larger macroscopic strain values. As a consequence, the overall stress increase is more progressive.

### *IV.3.c. Effect of the crosslink density in filled samples*

Uniaxial traction curves up to very large strain values are shown in Figure 121 for a series of NR samples with various crosslink densities, filled with the same reinforcing system (same silica

volume fraction, same coupling agent). Crosslink density plays an important role on the mechanical properties at high extensions. First the modulus seems to depend quite linearly on the sulfur content through the rubber network crosslink density. The five tested samples display a failure envelope with an optimum network density that is situated around 1.5phr of sulfur in this series of samples.

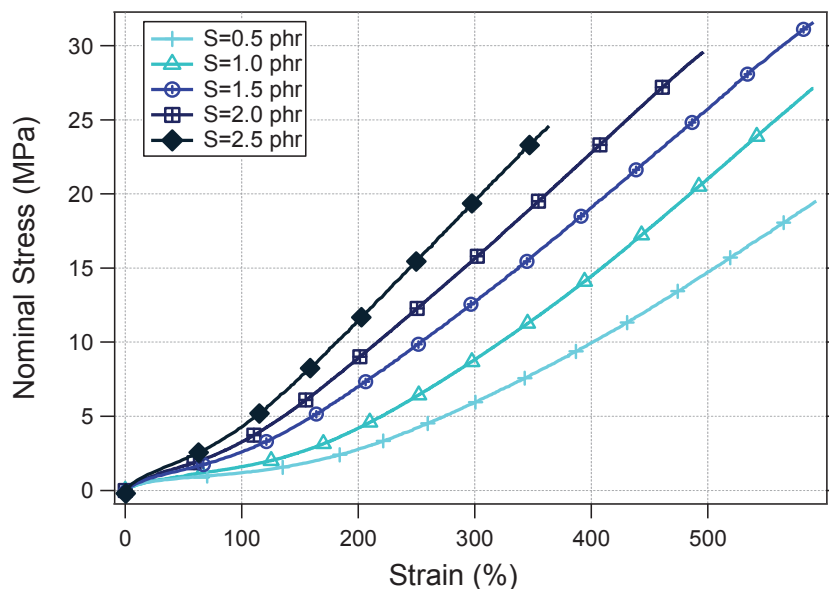


**Figure 121: Effect of the Sulfur amount effect on the stress-strain curves of reinforced NR. All samples have the same silica-TESPT amount (sample series 030-11 and 119-11) (samples not precycled).**

#### *IV.3.d. Effect of the Silica specific surface*

Uniaxial traction curves up to very large strain values are shown in Figure 24 for NR samples filled with silica of different specific surfaces, keeping the same silica volume fraction and coupling agent.

Increasing the specific surface of the silica aggregates (increasing fineness) does only have a slight effect on the reinforcement in the large deformations regime. This result is quite surprising since changing this parameter in carbon black compounds give large differences in the modulus<sup>72</sup>.

The differences between the systems would be a little more important if they were compared at equivalent crosslink densities. Recent studies<sup>60</sup> have put forward the adsorption of vulcanization accelerators as an explanation for decreasing crosslink densities with silica fraction. Moreover NMR measurements performed on our samples have shown that the crosslink density was decreasing with the specific surface.

A simple correlation was established between the modulus at large strain (arbitrary chosen at 300% strain) and the crosslink density measured by NMR for the five 160m<sup>2</sup>/g Silica-TESPT samples presented in Figure 121. Assuming an identical effect of the crosslink density on the stress-strain curve for the 80m<sup>2</sup>/g Silica-TESPT, the stress-strain curve could be corrected for

this sample knowing its crosslink density. The obtained curve is plotted in Figure 122b). Note that the 200m<sup>2</sup>/g Silica-TESPT curve is not corrected because the crosslink density is very similar to the 160m<sup>2</sup>/g Silica-TESPT samples.

Despite this necessary correction, the reinforcement still poorly depends on the silica specific surface. This observation can be compared to the effect of filler content which somehow also consists in tuning the total interface area in the material: one concludes that the geometrical constraints brought by the filler content are of the first order compared to the effective surface of silica at equivalent total surface area (a compound with 50phr of 80m<sup>2</sup>/g silica compared to a compound of 25phr of 160m<sup>2</sup>/g silica would present a higher modulus).

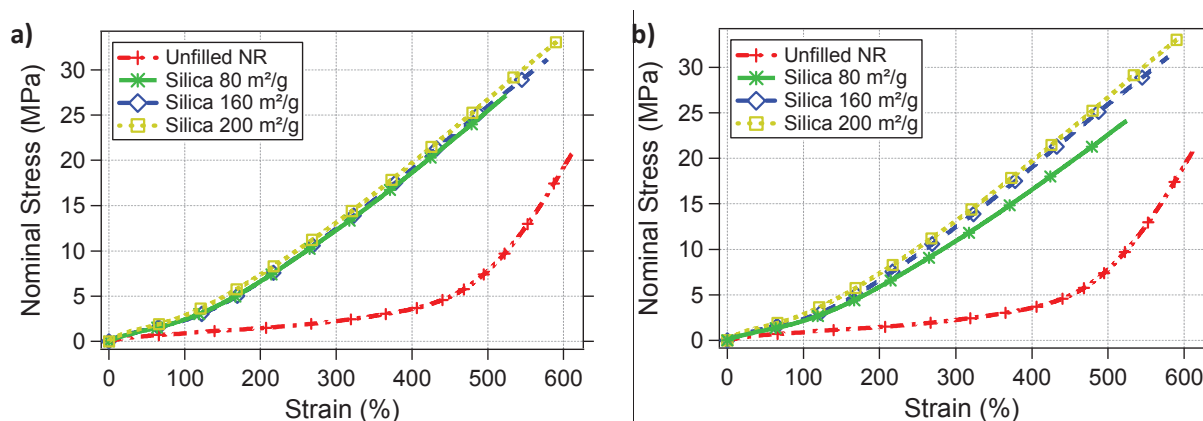


**Figure 122: Effect of the silica specific surface on stress-strain curves: a) without crosslink density correction and b) with crosslink density corrections for the 80m<sup>2</sup>/g sample. The interface agent used is TESPT which quantity is adjusted to the total silica surface (sample series 046-11).**

### IV.3.e. Effect of interface agents

#### IV.3.e.i. Nominal Stress

Uniaxial traction curves up to very large strain values are shown in Figure 123, for NR samples filled with carbon black and silica with different interface agents, keeping the same filler volume fraction.

Firstly the use of a coupling agent does not enable to reach the reinforcement level of the carbon black reference used here in spite of the lower specific surface developed by the carbon black compared to the Z1165 Silica.

NSC and TESPT present comparable modulus levels but the shape of the curve is slightly different with a lower modulus in large extensions and a more pronounced hardening in very large deformations. We have shown that this effect in large strain regime cannot be attributed to a higher Strain-induced crystallization (see chapter V), the crystalline content being equivalent for the two type of coupling agents at a fixed strain level.

The use of the covering agent OCTEO induces a low reinforcement compared to TESPT but the increase in the modulus versus the unfilled matrix is quite important. This is particularly

important when it comes to compare Natural Rubber and Styrene Butadiene Rubber where the use of OCTEO results in a very poor reinforcement at large strain.

The non-treated silica sample shows a very close mechanical behavior to that of Silica OCTEO although the crosslink density determined by NMR is much lower. It implies that the interface strength is stronger in the case of the non-treated silica. It is likely that the absence of covering agent leaving more available interaction sites on the silica surface is at the origin of this somehow more active interface.

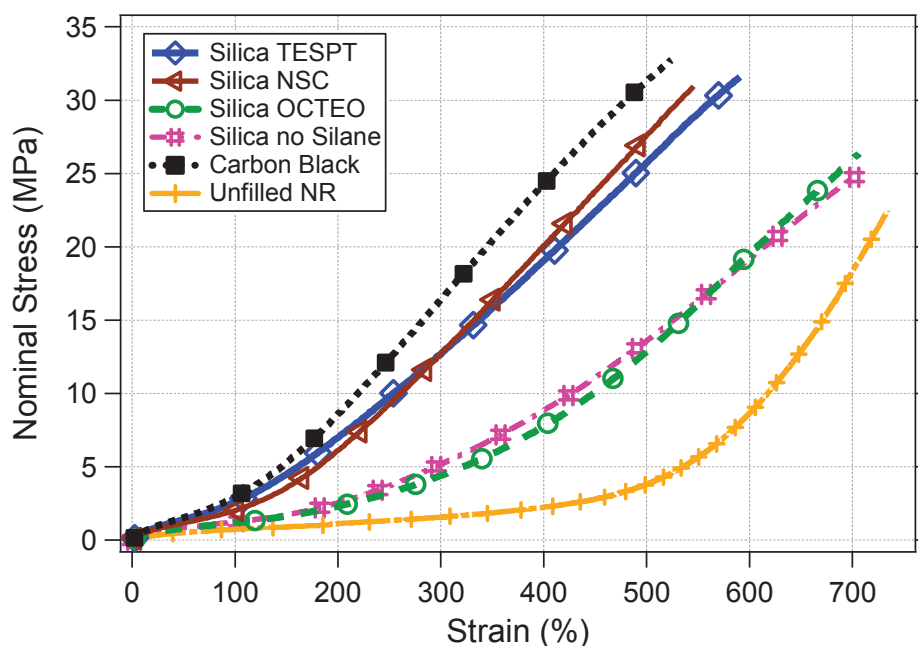


**Figure 123: Stress-strain curves for pure NR (series 046-11) and materials reinforced with carbon black or silica with different surface treatments: coupling agents TESPT and NSC, covering agent OCTEO, No silane treatment (sample series 030-11 and 119-11). Reinforced samples have 1.5 phr Sulfur, the pure NR has 1phr sulfur, which corresponds to the same crosslink density (except for the no-silane sample, which has a significantly lower crosslink density due to strong CBS adsorption), according to NMR measurements (experiments by R. Perez-Aparicio, see chapter VI).**

#### Discussion:

Monitoring the interaction at the interface in Silica filled rubber is of utmost importance since the polar functional groups (silanol, siloxanes) at the silica surface develop poor bonding with the rubber phase and lead the aggregates to re-agglomerate.

The strength of the Carbon Black-rubber interface is stronger and induces more restriction on the reorganization of the chains in the network under strain (higher strain amplification).

IV.3.e.ii. True Stress

Plotting the curves of true stress versus strain is also of interest to compare the reinforcement at high strain (Figure 124). The shape of the curves are very similar whatever the interface type, the true stress increasing steeper in the range of 100 to 300% of strain for Carbon Black and Silica-TESPT compared to Silica-OCTEO.

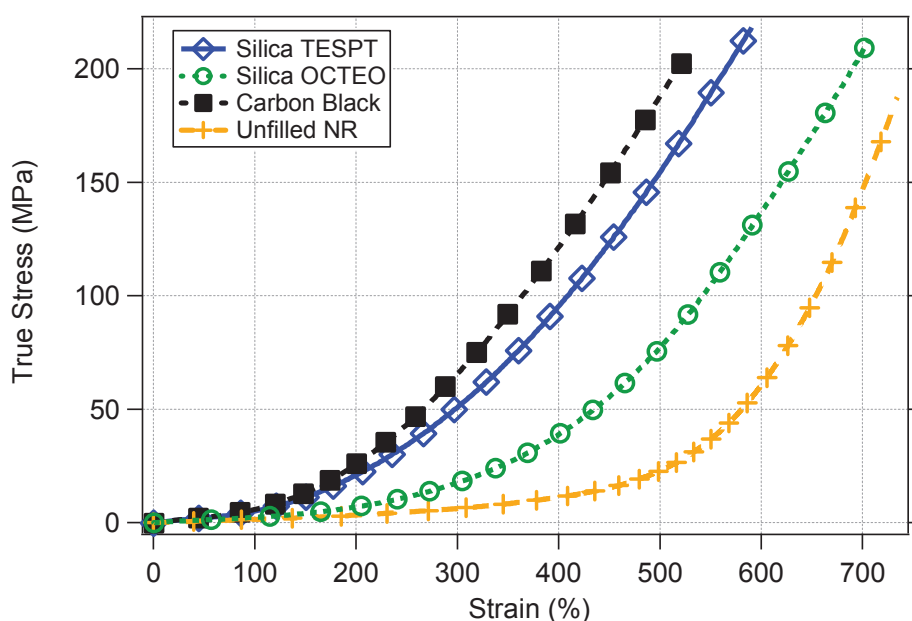


**Figure 124: True Stress-strain curves for pure NR (series 046-11) and materials reinforced with Carbon Black or Silica with different surface treatments: coupling agents TESPT, covering agent OCTEO (sample series 030-11 and 119-11). Reinforced samples have 1.5 phr Sulfur, the pure NR has 1phr sulfur, which corresponds to the same crosslink density (experiments by R. Perez-Aparicio, see chapter VI).**

In order to compare the behavior of the filled NR compounds at large strain in a more illustrative way, tangent moduli (defined as the derivative of the true stress with respect to strain) has been computed (Figure 125). Three different behaviors are observed. The pure NR matrix exhibits a constant tangent modulus up to a stress hardening due to strain-induced crystallization (onset marked by an arrow in Figure 125) and limited chains extensibility. All reinforced samples show a significant decrease of the tangent modulus at small strain values corresponding to the Payne effect. Then the tangent modulus increases with the strain for all types of interface. The increase is steeper for Carbon Black and Silica-TESPT filled NR samples compared to Silica-OCTEO and Silica with no silane treatment systems. Finally close to failure, the increase of the tangent modulus seems to be less pronounced.

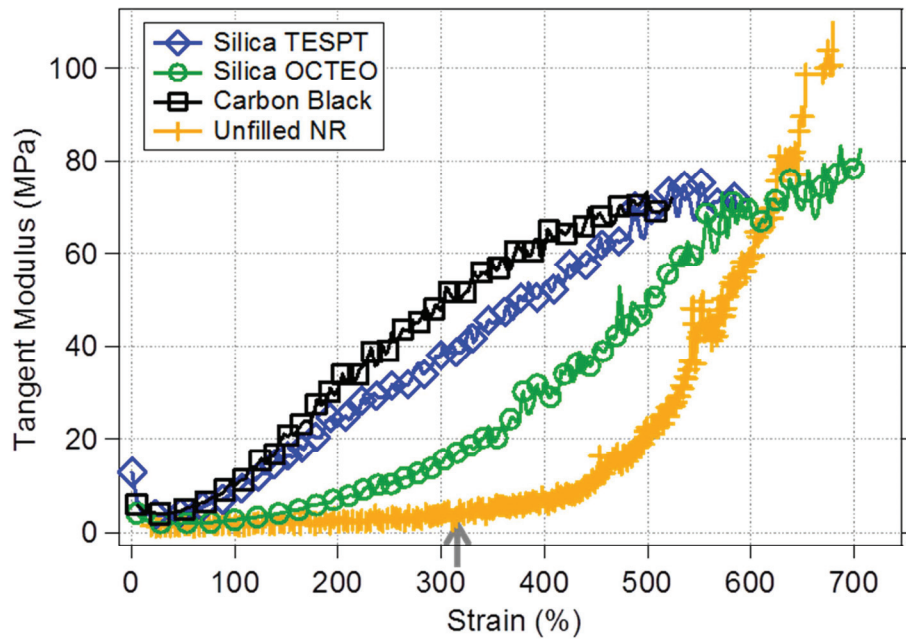


**Figure 125: Tangent modulus versus strain for unfilled and filled NR with different interfaces type (from the data in Figure 124) (sample series 046-11 and 119-11).**

The effect of crosslink density on the tangent modulus versus deformation is reported for TESPT and OCTEO in Figure 126. For both interface agents, the slope in the reinforcement regime increases with sulfur amount.

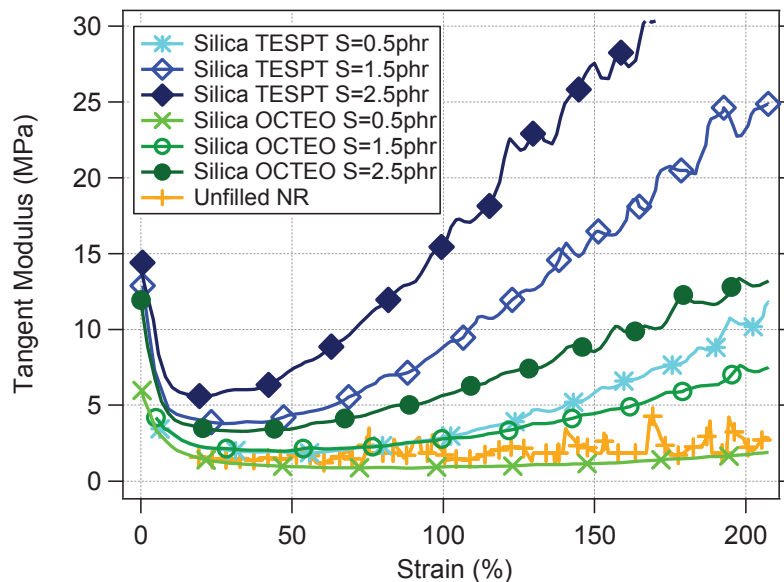


**Figure 126: Tangent modulus versus strain for pure NR (series 046-11), and filled NR Silica-TESPT and Silica-OCTEO at three different crosslink densities (sulfur amounts 0.5; 1.5 and 2.5 phr) (sample series 119-11).**

Some authors<sup>139,151</sup> have proposed that the inflexion point of the tensile curve would correspond to the shortest chain extension limit (we choose to use the true stress instead of the nominal stress to carry out this analysis). An amplification factor was thus proposed as the ratio of the strain values at the minimum of the tangent modulus in the filled and unfilled rubbers respectively. It is important to note that in this approach, unfilled and filled materials **with the same crosslink densities** must be compared. Indeed, Figure 126 shows that comparing silica reinforced NR with different sulfur amounts to an identical unfilled NR would lead to different amplification factors.

Therefore, in Figure 123 and Figure 125, care was taken to compare samples with the same crosslinks densities (except for the no-silane sample, which has a significantly lower crosslink density due to strong CBS adsorption on the untreated silica).

Figure 127 shows an enlargement of the tangent modulus for unfilled and filled NR samples Figure 125. The arrows indicate the minimum values of the tangent modulus.

The amplification factors determined for Carbon Black, Silica-TESPT and Silica-OCTEO samples are of 2.8, 2.6 and 1.7 respectively. These numbers might be used to quantify some ‘interface efficiency’. Note that this “interface efficiency” could be seen as the convolution of the total engaged surface area and the strength of interface per unit area. In this picture, the strength per unit area for Carbon Black samples is high compared to Silica-TESPT since the Carbon Black aggregates have a specific surface of 120m<sup>2</sup>/g compared to 160m<sup>2</sup>/g for the used Silica.

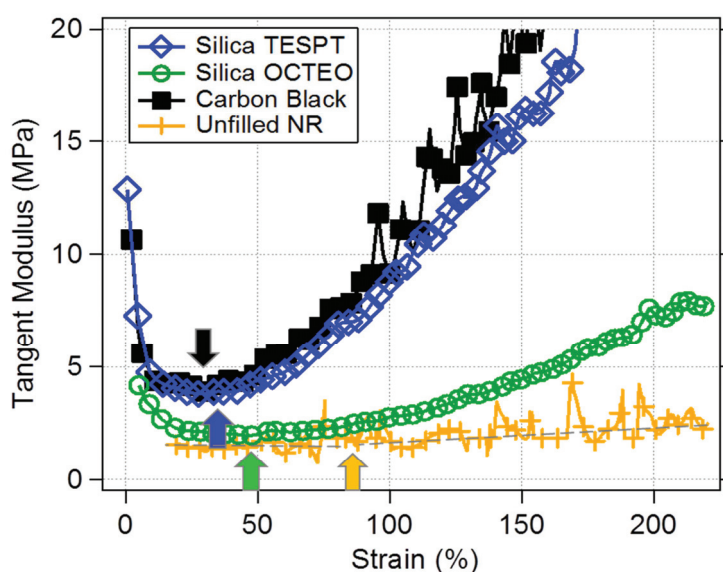


**Figure 127: Tangent modulus versus strain for pure and filled NR with different interfaces type (from the data in Figure 124) (sample series 046-11 and 119-11). The arrows indicate the minimum value of the tangent modulus.**

The tangent modulus for unfilled and filled SBR samples (series 038-12) is compared to NR samples in Figure 128.

In spite of the lower sulfur content, the Silica-TESPT SBR sample has a tangent modulus equivalent to the NR counterpart. When using OCTEO, the modulus of the silica-filled SBR

sample is close to the unfilled SBR sample. This results is in agreement with the data of Ramier et al.<sup>78</sup>, these authors indeed have adopted a similar analysis of the tensile properties using the tangent modulus computed from the nominal stress.

As regards Natural Rubber, the Silica-OCTEO sample shows a significant increase of the modulus compared to the pure NR. This may be due to the Strain-induced Crystallization or to a more cohesive interface in the case of the NR matrix.

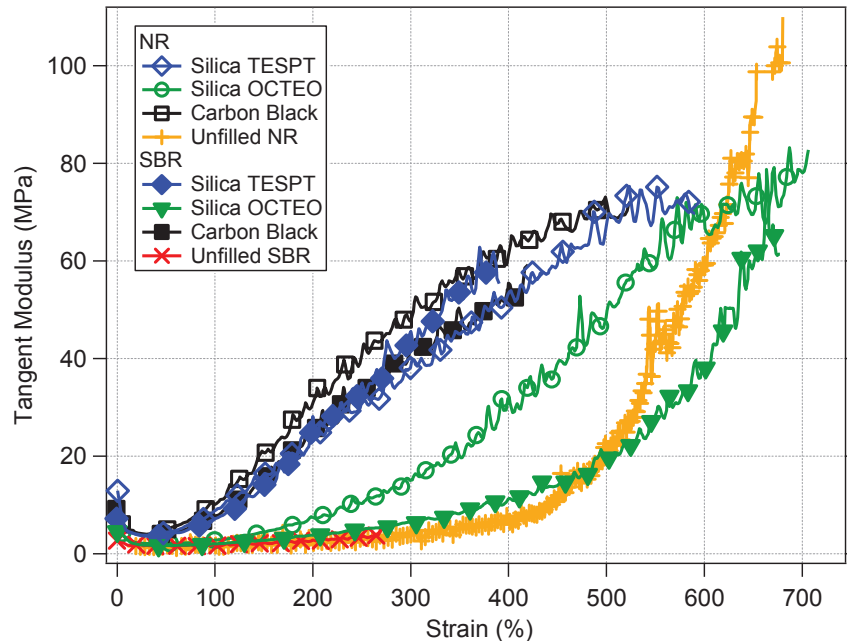


**Figure 128: Comparison of tangent modulus of unfilled and filled SBR and NR samples (sample series 038-12, 046-11 and 119-11). Reinforced NR samples have 1.5 phr sulfur, the pure NR has 1phr sulfur and all SBR samples have 1.2 phr sulfur.**

#### IV.4. Conclusions

The Reinforcement as a function of temperature in the linear regime and the Payne effect at 60°C have been studied for the series of elaborated samples.

We have emphasized the importance of the filler fraction and specific surface in the linear and small strain regime. At temperatures close to the glass transition temperature, high maximum reinforcement values are found for highly filled NR samples (50phr). The effect of the interface on the Reinforcement and Payne effect was also investigated. The stress-softening effect was found to be lower with Silica compared to Carbon Black particles and decrease with the use of a strong coupling agent such as NSC.

We consider that the main microstructure feature responsible for the Payne effect could be the formation of glassy bridges or low mobility polymer layers in the vicinity of the particles. The interconnection of those layers creates a high modulus filler/polymer/filler network that breaks

and reforms under the effect of deformation, the yielding of this interphase accounting for the dissipation maximum.

As the amplitude of the Payne effect is not directly correlated to the interface strength in our samples, we proposed that the distribution of aggregates was affected by the interface agent used. Reproducible shifts of the dissipation peak strain were found to be in agreement with this hypothesis. The amplitude of the Payne effect does not linearly depend on the filler fraction suggesting also a contribution of the fillers and glassy bridges network.

Uniaxial tensile experiments were performed on as-prepared (non-precycled) pure and filled NR samples to analyze the reinforcement effect in the large strains regime. The increase of the modulus at high strain as the crosslink density increases was shown in pure and filled NR. The introduction of silica strongly improves the modulus at high strains. The Silica surface treatment was found to have an important impact on the modulus at large deformations. In particular using a covering agent (with no covalent interactions with the rubber matrix) leads to a lower but still significant reinforcement effect in Natural Rubber.

The shape of the stress-strain curves in reinforced NR, compared to that in the pure NR, was discussed in terms of a heterogeneous strain amplification scenario, which will be further discussed in chapter VI.



## V. Strain-induced Crystallization

V.1. Introduction.....	142
V.2. Unfilled Natural Rubber.....	143
V.2.a. Description of a traction-retraction cycle.....	143
V.2.b. Tensile tests up to failure: Effect of the crosslink density.....	146
V.2.b.i. Crystallized fraction.....	146
V.2.b.ii. Crystallites size and orientation.....	147
V.2.a. Traction-retraction cycle: Effect of crosslink density.....	149
V.3. Filled Natural Rubber.....	149
V.3.a. Crystallized fraction.....	149
V.3.b. Size and orientation of crystallites.....	152
V.3.c. Precycling effect on SIC.....	154
V.4. Crystallization and melting kinetics.....	156
V.4.a. Measurements principle.....	156
V.4.b. Interpretation of the results.....	159
V.4.c. Results for Unfilled NR.....	161
V.4.c.i. Effect of average deformation.....	161
V.4.c.ii. Effect of oscillations frequency.....	164
V.4.d. Results for Filled NR.....	166
V.5. Conclusions.....	167

This chapter deals with the characterization of the Strain-Induced Crystallization phenomenon by means of X-ray diffraction experiments carried out in-situ during the elongation of the samples. It is divided in two parts:

- The first part presents **quasi-static X-ray diffraction and scattering experiments meant to better understand the evolution of the microstructure under strain**. The SIC mechanism in unfilled Natural Rubber is clarified and the effect of fillers/polymer interface in filled NR on the microstructure under strain is discussed thanks to crystallized fraction, crystallites size and orientation measurements. Part of the data collected during these experiments will be analyzed in the following chapters: amorphous orientation measurements in filled samples are discussed in the next chapter dedicated to the reinforcement mechanisms and X-ray absorption measurements have been used to estimate the cavitation phenomenon in chapter VII.
- The second part describes the **evaluation of the kinetics of the strain-induced crystallization and melting kinetics** by means of a novel device allowing **stroboscopic acquisition of X-ray patterns during cyclic solicitation of NR samples**.

## V.1. Introduction

Many progress has been made in the characterization of the SIC phenomenon due to advances in X-ray detector's technologies and use of synchrotron radiation for the study of soft matter. Direct measurements of the crystallized fraction during in-situ stretching experiments have been performed<sup>89,90</sup> clarifying the influence of SIC on the stress strain behavior of NR and very rapid diffraction pattern acquisition are expected to enhance the understanding of crystallization kinetics in the near future. The stress and crystalline content evolution in vulcanized Natural Rubber with strain in a simple traction-retraction cycle at a low strain rate has been given by Trabelsi et al<sup>90</sup>.

In addition to the crystallites formation characterization, the anisotropy of the X-ray scattering at wide angles can be followed up simultaneously, giving pieces of information on the orientation of the amorphous chains or part of chains<sup>107,108</sup>. Others techniques such as fluorescence polarization<sup>109</sup>, infrared dichroism<sup>110</sup> and quadrupolar NMR<sup>111</sup> are effective to measure the overall orientation of the rubber networks. The comparisons of quadrupolar NMR results and X-ray diffraction results carried out by Rault<sup>105</sup> and Dupres<sup>72</sup> provide interesting insights on the relaxation of the amorphous chains imparted by the first strain-induced crystallites. Nevertheless this characterization of the orientation and X-ray diffraction cannot be carried out simultaneously and the solvent probe molecules may affect the dynamics and/or the orientation of the matrix.

We carried out in-situ tensile experiments that combine strain and stress measurements, the classical measurement of the diffraction peaks area and the measurement of the anisotropy of the amorphous halo in the diffraction pattern. This deconvolution of the diffraction (crystalline) and scattering (amorphous) data is a very powerful tool to analyze the evolution of the microstructure under stretching and better understand the stress strain behavior of NR without and with fillers.

We will see in this chapter that the comparison of the amorphous orientation, crystalline content and true stress leads to a clearer understanding of the SIC mechanism.

## V.2. Unfilled Natural Rubber

### V.2.a. Description of a traction-retraction cycle.

The description of the device as well as the diffraction patterns analysis procedure has been given in chapter III. The measurement of the amorphous orientation provides us with a more precise picture of the crystallization and melting processes<sup>108</sup>. The plots of the crystallized fraction, nominal stress and amorphous orientation parameter  $\langle P_2 \rangle$  as a function of strain are shown in Figure 129. The traction phase can be decomposed in three successive parts:

- (I) In the first part, the elastomer matrix is entirely amorphous and its orientation follows the prediction of the rubber elasticity theory<sup>20</sup> (see paragraph II.1).
- (II) Above the critical crystallization strain  $\epsilon_c$ , the crystallites begin to form and the amorphous orientation stabilizes and even slightly decreases. This effect has been predicted by Flory<sup>100</sup>: the crystallization of a portion of a chain induces an increase in entropy for the rest of the chain which relaxes. This explains why the stress stabilizes in this regime (provided the strain rate is low enough) as a result of the competition between the relaxation of the amorphous phase and the reinforcing effect of newly formed crystallites<sup>90</sup>. A decrease in the slope of the amorphous orientation versus strain has been reported by Rault et al<sup>105</sup> but their data do not show a real plateau (or even a small decrease) in the orientation.
- (III) Above a strain  $\epsilon_h$  around 400%, the hardening effect of crystallites becomes predominant over the relaxation of amorphous chains as proved by the fact that the orientation (the local state of extension in the amorphous phase) starts to increase again above  $\epsilon_{\text{hardening}}$ . It can be noted that the crystallization process in this regime tend to slow down as if the relaxation of amorphous chains was the limiting phenomenon, inhibiting the crystallization.

The retraction phase is divided in three parts as well:

- (IV) The first retraction part consists in a decrease of the crystallized fraction, orientation of amorphous phase and stress. The higher crystallized fraction at a given strain as compared to the traction phase highlights the supercooling effect which states that crystallization and melting strains are different due to a kinetic retardation at the crystallization onset.
- (V) When the strain becomes lower than an equilibrium strain  $\epsilon_{\text{eq}}$ , the local strain in the amorphous phase reaches the melting strain  $\epsilon_f$  as shown by the plateau in the orientation of the amorphous phase from  $\epsilon_{\text{eq}}$  to  $\epsilon_f$ . The stress becomes constant as well due to a competition between the decrease of crystalline fraction and the increase of the orientation of the chains as they melt (according to the effect proposed by Flory<sup>100</sup>). This part is equivalent to the second regime of the traction phase and stresses out the regulation of the deformation of the amorphous phase by the strain-induced crystallization kinetics.
- (VI) The last part of the retraction curve is exactly similar to the first part of the traction curve, all chains have melted and the strain is directly related to loose orientation.

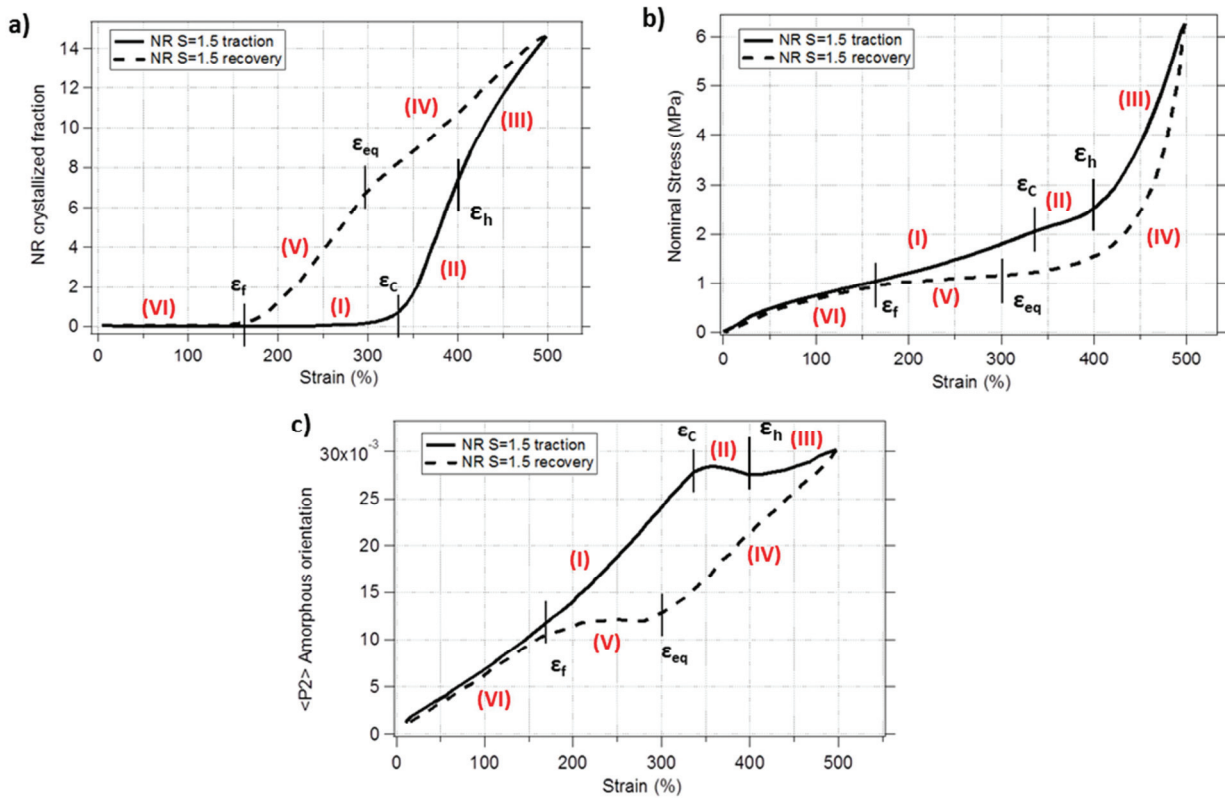


**Figure 129: Plots of a) crystalline content, b) Nominal Stress and c) Orientation parameter  $\langle P_2 \rangle$  as a function of strain (samples series 119-11). Elongation speed of 4mm/min ( $3.33 \cdot 10^{-3} \text{ s}^{-1}$ ). The different parts of the traction and retraction cycle are described in the text.**

The inverse striction observed in loose crosslinked NR at low strain rate illustrates the equilibrium of semi-crystalline and amorphous phases during the second regime of the retraction phase<sup>152</sup>.

This feature arises when the equilibrium strain  $\epsilon_{eq}$  is reached during the retraction, a zone of lower deformation appears, most frequently in the vicinity of the holding jaw, while the deformation is constant in the rest of the sample (see Figure 130). It has been shown<sup>90</sup> that the evolution of the mean crystallized fraction of the two phases follows the same relationship in the more crosslinked samples where no inverse yielding is observed. This result is a first proof that once  $\epsilon_{eq}$  has been reached on the retraction there is an equilibrium of melted and semi-crystalline phases and the inverse striction is a macroscopic evidence of this behavior whatever the crosslink density. If the elongation is maintained constant in this regime there is no further evolution of crystalline content in the thinner phase<sup>90</sup> which indicates a true 1<sup>st</sup> order phase equilibrium.

Figure 130 b) and c) illustrate the transition from the semi-crystalline phase of deformation  $\epsilon_{eq}$  and crystalline content  $\chi(\epsilon_{eq})$  to the melted phase of deformation  $\epsilon_f$ . The crystalline content measured as long as the X-ray beam goes through the crystalline phase is almost constant, the displacement applied to the sample decreases but the measurement of the thickness in the semi-crystalline region is constant as evidenced by the bunch of points at  $\epsilon_{eq}$ . Then the deformation drops abruptly when the striction neck reaches the thickness measurement zone. Finally the X-ray measurement zone enters the amorphous part which explains the crystalline content drop.

Our measurements of a constant orientation of amorphous phase are further evidences that the local deformation of the amorphous phase is equal to  $\epsilon_f$  even when no inverse striction is observed. However it is still unclear why the macroscopic equilibrium is only observed for weakly crosslinked samples. One explanation we can put forward is that the melting process is faster for weakly crosslinked samples as compared to higher crosslinked samples. We will discuss this point later in paragraph V.4 but a hypothesis that can be made here is that the orientation of the amorphous phase surrounding crystallites is lower at a given macroscopic strain when crosslink density is lower and that this tends to promote crystallite melting.

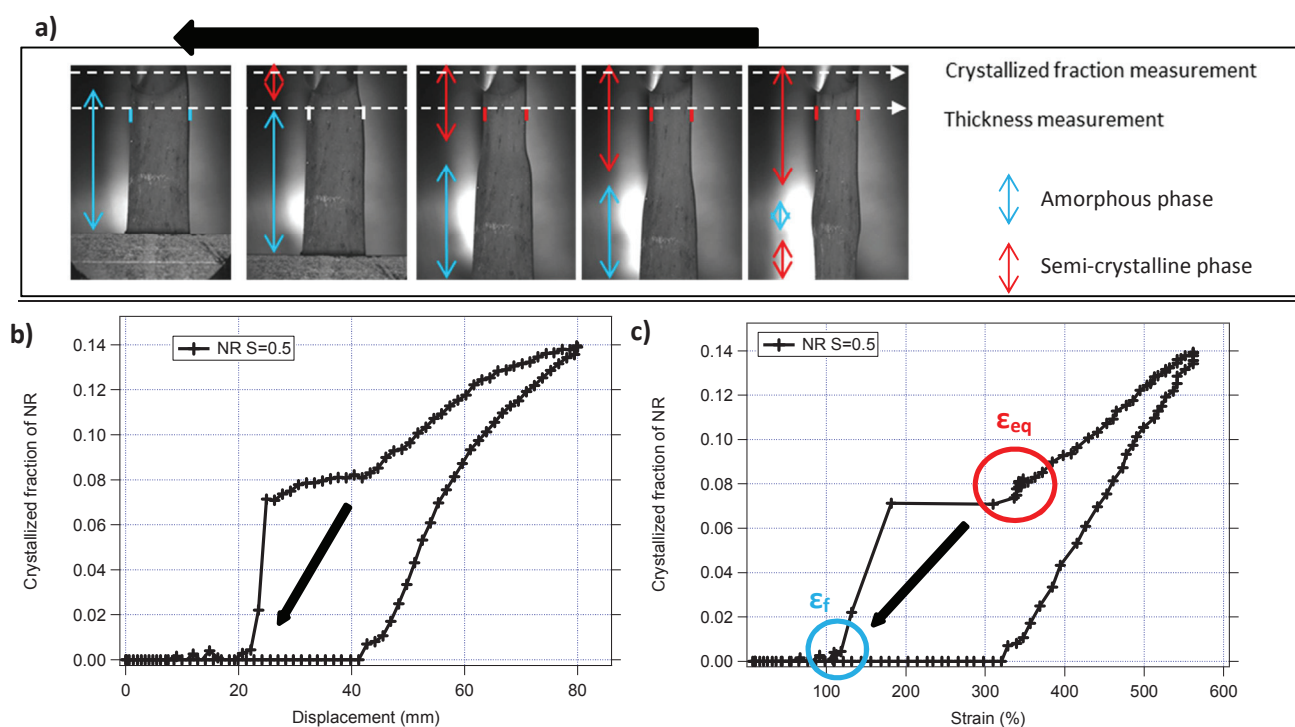


**Figure 130: Inverse striction phenomenon in weakly crosslinked NR (sample with 0.5phr of sulfur, series 119-11): a) Amorphous and Semi-crystallized phases for decreasing macroscopic strains (thick arrow); b) Macroscopic displacement and c) Strain deduced from the thickness measurement as shown in a). Elongation speed 5mm/min (or  $8.33 \cdot 10^{-3} \text{ s}^{-1}$ )**

The necessity to have a low strain rate to observe the necking of the sample suggests that the reorganization on the macroscopic scale requires a large difference between the melting rate and the applied strain rate, strengthening our previous hypothesis on crosslink density effect on melting kinetics.

It is to be noted that the strain rate is a key parameter controlling the crystallization curve. A first example has been given here for inverse striction and it is known that the onset of crystallization is shifted towards higher strains for higher strain rate<sup>90</sup>.

Many stress-strain curves presented in this chapter do not show a plateau in the stress at the onset of crystallization because of the rather high extension speeds used and the SIC onset may be shifted when using different strain rates. This effect will be emphasized in the next chapter dedicated to the study of SIC kinetics.

### V.2.b. Tensile tests up to failure: Effect of the crosslink density

#### V.2.b.i. Crystallized fraction.

The evolution of crystalline content and amorphous orientation as a function of strain in quasi-static experiments has been described paragraph V.1. In the results presented in the following, the samples are stretched up to failure at a slightly higher extension rate ( $\dot{\lambda}=1.6 \times 10^{-2} \text{ s}^{-1}$ ). The crystallized fraction, true stress and parameter  $\langle P_2 \rangle$  are plotted versus the deformation function  $\Lambda = \lambda^2 - \lambda^{-1}$  (or rubber strain) in Figure 131a), b) and c) respectively. The behaviour of the six samples of various crosslinked densities can be described in the following way:

- (I) From unstretched state to strain-induced crystallization strain onset, the amorphous orientation parameter  $\langle P_2 \rangle$  linearly increases as predicted by the rubber elasticity theory (equation 5). The agreement with theory is excellent up to deformation function ( $\lambda^2 - \lambda^{-1}$ ) of approximately 10 for the most crosslinked sample and 12 for all other samples which corresponds to strain induced crystallization onsets. The common SIC onset (green continuous line) has already been reported in samples of similar crosslink densities<sup>90,94,153</sup>. As the samples are thermodynamically out of equilibrium during the traction phase, the Flory theory<sup>100</sup> cannot be applied to predict the influence of crosslink density on the strain crystallization onset nor on the crystallinity-strain slope. This strain onset is a kinetic parameter and does depend on strain rate and temperature; conversely the melting strain at the end of the recovery phase is closer to a thermodynamic parameter. The shift of SIC onset for the highly crosslinked sample may correspond to a critical density of the network above which the kinetic of crystallization is significantly increased. To our knowledge, this earlier crystallization has only been reported by J. Marchal<sup>99</sup>. One should finally mention that the very first recorded values of the orientation parameter are somehow higher than 0 indicating that there may be a slight residual anisotropy resulting from the processing of the rubber sheets.
- (II) The amorphous orientation parameter reaches a plateau at the onset of crystallization<sup>108</sup> when any increment of strain increases amorphous orientation but also transfers part of the chains from the amorphous to the crystallized phase, resulting in a relaxation of the amorphous part of chains and a relaxation of the local stress (not clearly visible here because of a higher extension rate). The crystallization slope depends on crosslink densities suggesting again accelerated crystallization kinetics for highly crosslinked samples.
- (III) The strain onset  $\epsilon_h$  of the stress hardening (blue dashed line) appears less clearly here than in Figure 129 (presumably due to strain rate). The effect of crosslink density on the hardening strain is evidenced. This can be understood in terms of limited chains extensibility or considering the reinforcing effect of crystallites (predominant over relaxation of the amorphous). Rault et al<sup>105</sup> claim that the latter phenomenon is the only contribution to the hardening since a similar tensile test at 80°C where no crystallization proceeds display almost no hardening effect. Considering this approach, the critical extension for the predominance of the reinforcing effect of crystallites over the amorphous relaxation decreases with crosslink density since the constraints on the chains are higher and relaxation of amorphous is inhibited.

In our sample geometry, early failure often occurs at the holding part of the test samples. As a result, the crystalline fraction at break is often lower than in other studies<sup>71,72,105</sup>. Nevertheless, this early failure seems in fair agreement with measurements of chapter IV and it can be noted that the crystalline fraction at break decreases with the crosslink density of the network.

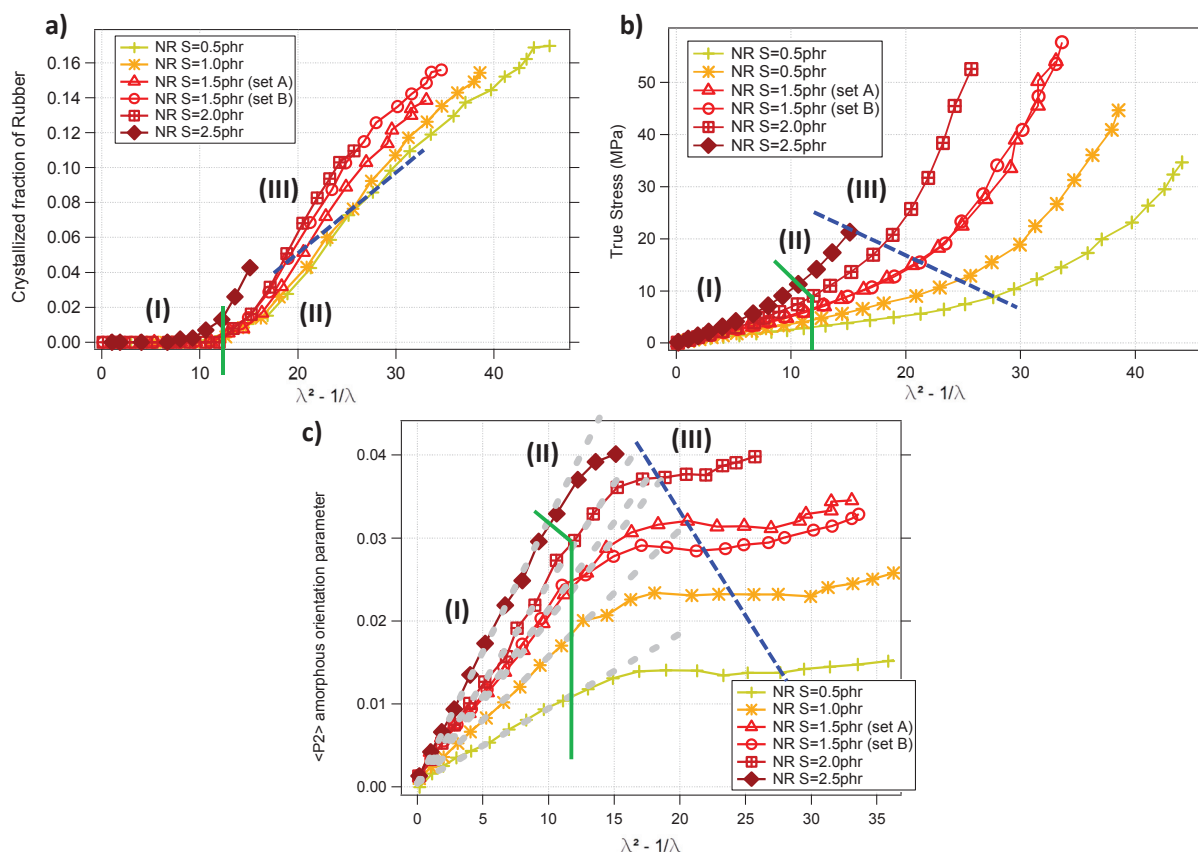


**Figure 131: In-situ tensile test up to failure: a) Crystallized fraction b) True stress and c) Amorphous orientation parameter versus rubber strain for unfilled NR of sample series 46-11 (set A) and 119-11 (set B). Solid green lines indicate the SIC onset and dashed blue lines indicate the onset of the strain hardening ( $\epsilon_h$  in Figure 129).**

### V.2.b.ii. Crystallite size and orientation.

In addition to the crystalline content, the orientation of the crystallites as a function of strain has been recorded systematically (Figure 132a)). Since the crystalline content has a small dependence on the sulfur amount at a given strain, the crystallite orientation is plotted against crystalline fraction to compare the alignment of crystallites along tensile direction for an equivalent amount of rubber chains in the crystallized state (Figure 132b)). We found that the orientation of crystallites is similar for all systems at the crystallization onset and then increases faster with strain for higher crosslink densities. Although the change in orientation with network density is quite small, the trend is clearly established by our set of data.

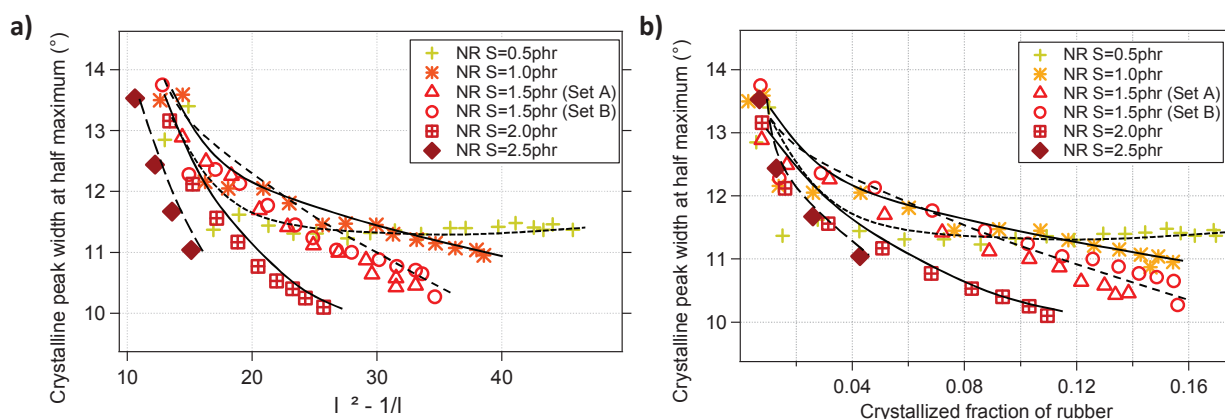


**Figure 132: Width of diffraction peak at half maximum (inversely proportionnal to crystallites orientation) as a function of a) strain and b) Crystallized fraction for sample series 046-11 (set A) and 119-11 (Set B). Curves as guides for the eyes.**

Radial scans were performed in order to compare the radial peak widths of reflections  $\{200\}$  and  $\{120\}$  for a given crystallites fraction of 0.10 (see chapter III). No significant differences were observed on the  $\{200\}$  peak but as regards the  $\{120\}$ , the spot clearly broadens as the crosslink density increases, which indicates that the size of the crystallites decreases in this direction associated with the  $\{120\}$  planes (Figure 133). This is in agreement with results published in the literature. Some authors have measured the actual crystallite size in several directions and reported a significant decrease with the crosslinks density<sup>90,94</sup>. Observing that the crystallite orientation also decreases with the network density, Tosaka and co-workers<sup>94</sup> here conclude that larger crystallites bend yielding higher fluctuations in orientations. We suggest that the higher orientation of crystallites can be attributed to the higher degree of orientation of the amorphous chains in the highly crosslinked samples inducing a higher orientation of the crystallites<sup>108</sup>.

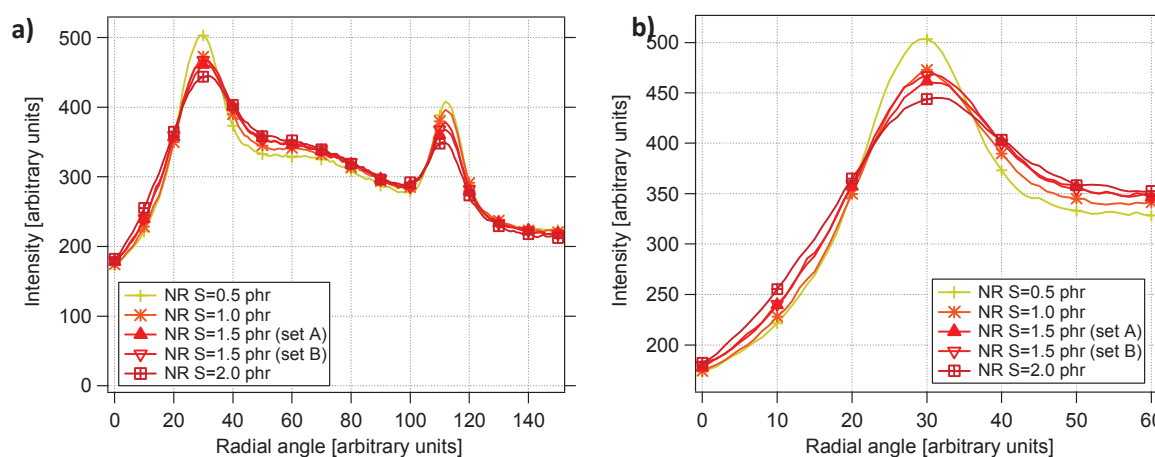


**Figure 133 : Comparison of pattern radial scans (along scattering vector) for unfilled NR samples from samples series 046-11 (set A) and 119-11 (set B). Each scan has been done for a crystalline content of 10%. b) the enlargement shows the width increase of peak  $\{120\}$  for increasing crosslink density.**

### V.2.c. Traction-retraction cycle: Effect of crosslink density

Traction-retraction cycles were compared for two crosslink densities in order to highlight the effect on the retraction phase and in particular on the amorphous orientation plateau (part V in Figure 129). Conversely to the SIC onset strain that was found to be similar for all crosslink densities, the melting strain  $\varepsilon_f$  increases with crosslink density. The value of the amorphous orientation parameter at the plateau (part V) increases as well with crosslink density. One finally remarks that the equilibrium strain  $\varepsilon_{eq}$  seems to depend on the crosslink density.

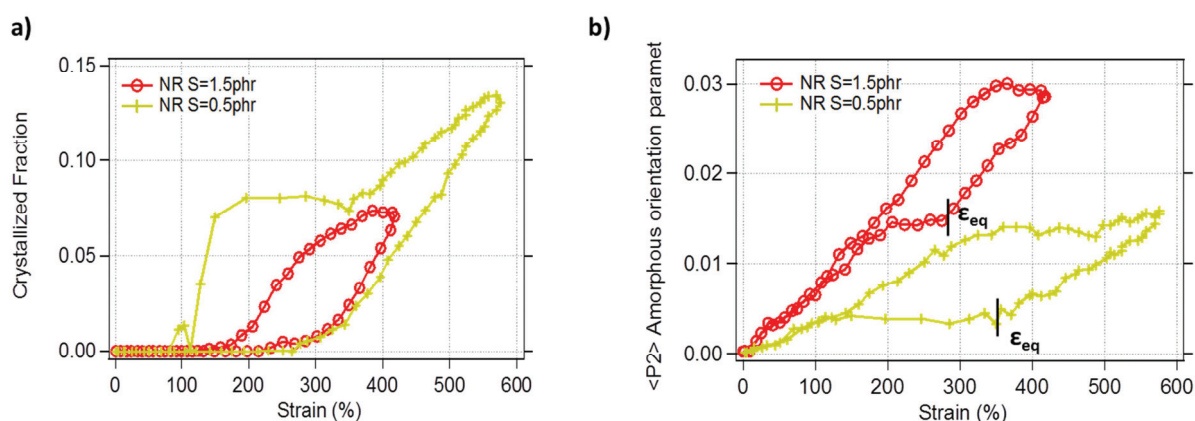


**Figure 134: In-situ traction-retraction cycles: a) Crystallized fraction and b) Amorphous orientation parameter versus strain for unfilled NR of sample series and 119-11.**

## V.3. Filled Natural Rubber

### V.3.a. Crystallized fraction.

In filled NR, strain-induced crystallization (SIC) occurs at lower strain than in pure NR samples (Figure 135). The shift of the onset depends on the rubber/filler interface. Indeed, the onset for Silica-OCTEO-filled NR is intermediate between Silica-TESPT-filled NR and pure NR. The onset for CB-filled NR is slightly lower than for silica-TESPT-filled NR. The Silica-OCTEO-filled NR shows a lower (but non-zero) shift of the onset.

As regards the Silica covalent coupling agents, it was found that the crystalline content versus deformation is identical for TESPT and NSC (Figure 136).

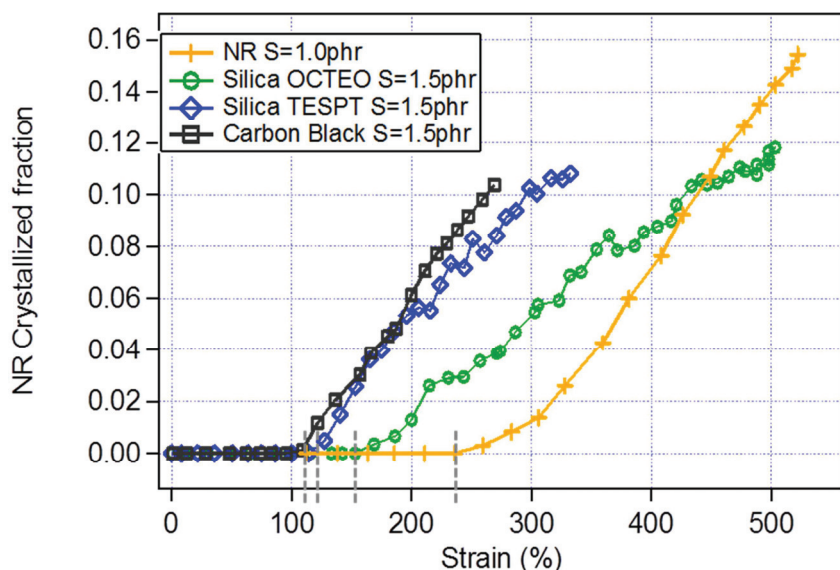


**Figure 135: Crystallization behavior for unfilled (series 046-11) and filled samples at equivalent crosslink densities (sample series 119-11). The crystallization onsets are indicated by dashed grey lines. (precycled samples)**

The filler volume fraction and morphology are known to affect the value of the strain at SIC onset<sup>72,105</sup>. This effect has been attributed to local strain amplification<sup>71,104</sup>. This interpretation is based on the assumption that the kinetics of crystallization is not strongly modified by the fillers and the interface type. In other words, although the SIC onset is a kinetic parameter, it is considered that, for a given strain rate, it only depends on the local strain whatever the formulation. This allows estimating a local strain amplification factor (as compared to unfilled NR of similar crosslink density) in each reinforced sample.

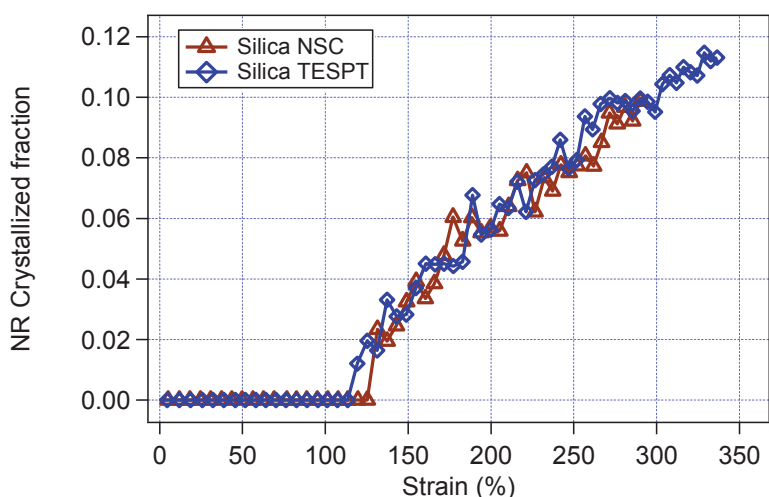


**Figure 136: Crystallization behavior for silica samples with the covalent coupling agents TESPT and NSC (series 030-11).**

The slope of the crystallization versus strain curves is also affected by the introduction of fillers: In all reinforced NR samples, it is lower than for pure NR, and the effect seems to be more pronounced for the Silica-OCTEO-filled NR. At large deformations, it is even observed that the crystallized fraction in unfilled NR becomes larger than in the Silica-OCTEO-filled sample.

This observation indicates that the crystallization curves of the filled samples are not similar to that of the pure matrix, simply shifted to account for strain amplification. Two explanations might explain this difference:

- The crystallization curves of the reinforced samples are convolutions of the curve of the pure matrix (in which the local strain is supposed to be homogeneous, equal to the macroscopic strain) with a distribution of local strains. It may even be possible that the local strain is lower than the macroscopic strain in some part of the material, thus leading to the behaviour observed for the Silica-OCTEO-filled NR.
- There are some restrictions to crystallite formation and growth induced by the fillers. Specifically, this may be the case at the rather high filler volume fraction considered here (18.5 vol%). Indeed, the mean distance between fillers is believed to be of the order of 5 nm, which is comparable to the dimensions of the crystallites (approximately 10 nm in the transverse direction according to Trabelsi et al<sup>71</sup>).

Indeed, Scanning Electron Microscopy observations (see chapter VII) have shown that the strain seems very heterogeneous on the microscopic scale. A significant part of the rubber seems to be close to the relaxed state, although the macroscopic applied strain is large. This may support the first hypothesis (without ruling out the second one).

The influence of the crosslink density on the crystallization curves is shown in Figure 137. There seems to be an increase of the slope of these curves as the crosslink density increases, which is qualitatively similar to what is observed in unfilled NR (see Paragraph V.2.b). For each interface type, the strain at SIC onset is higher for the less crosslinked sample, especially for Silica-reinforced NR samples.

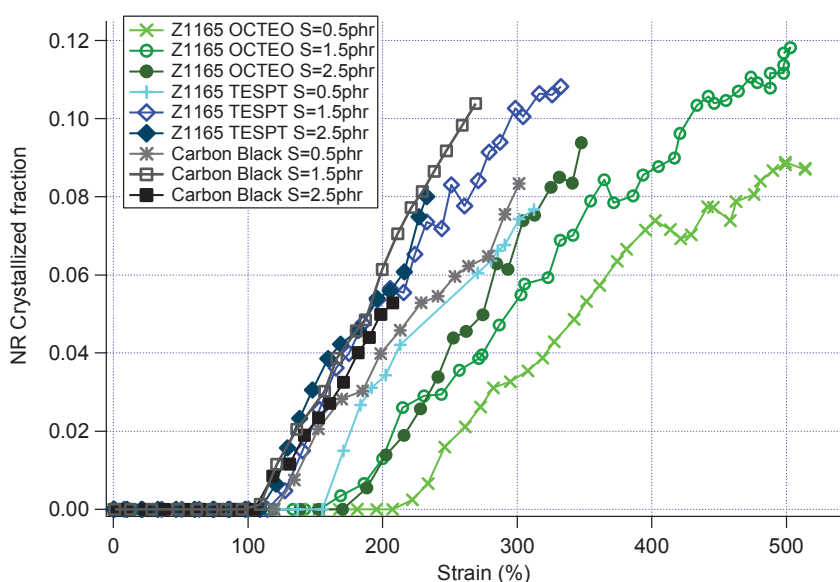


**Figure 137: Effect of crosslink density on crystallized fraction/strain curves for CB, Silica TESPT and Silica OCTEO (series 119-11)**

The crystallized fraction has also been determined for reinforced samples of series 030-11 and the results are reported as a function of strain for Silica-TESPT NR samples. The agreement between the different series of samples is fairly good and shows that the increase in the SIC onset only occurs for a sulfur amount of 0.5phr since all other samples display an identical critical deformation (Figure 138).

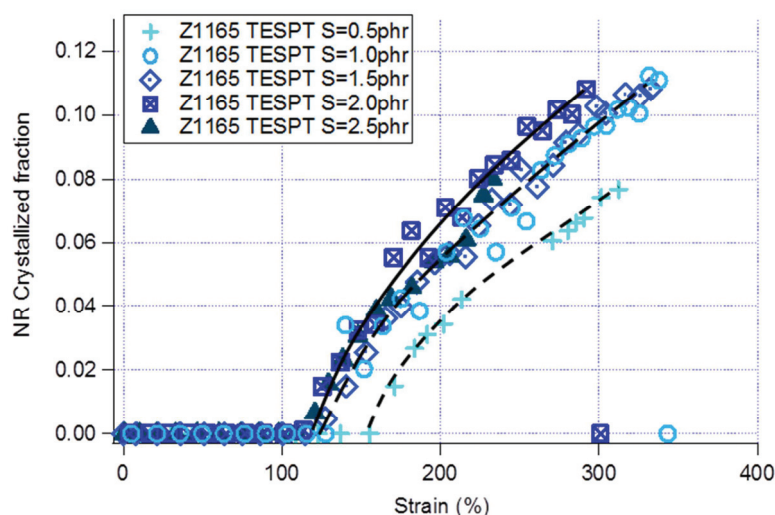


**Figure 138: Crystallized fraction for NR-Silica-TESPT as a function of strain for 5 sulfur amounts (series 030-11 and 119-11).**

Crystallite development in NR depends on two mechanisms, namely nucleation and growth<sup>87</sup>. Nucleation would be enhanced by numerous sulfur bridges in the network. Conversely, crystallite growth would be favoured by long chain length between crosslink points, i.e. by a low density of sulfur bridges, since it is observed that the crystallite size decreases as the crosslink density increases<sup>90,94,153</sup>. The competition between these two mechanisms would then be responsible for the rather difficult interpretation of the effect of crosslink density on crystallization.

Within this interpretation, nucleation of crystallites may be reduced in the silica reinforced samples with a sulfur amount of 0.5phr (which has a low crosslink density), due to insufficient orientation of the chains acting as crystallite nuclei.

Considering the results of both unfilled and filled samples, we have seen that, for the strain rates applied in our study, the SIC onset does not depend on crosslink density within a given range. The onset seems to be shifted towards lower strains if the crosslink density exceeds  $2.8 \times 10^{-4} \text{ mol.g}^{-1}$  in unfilled samples and towards higher strains if it is lower than  $1.1 \times 10^{-4} \text{ mol.g}^{-1}$  in reinforced samples (see crosslink density measurements by NMR in chapter VI).

### *V.3.b. Size and orientation of crystallites.*

The radial widths of the {120} reflection in filled NR samples at a crystalline content of 10% were compared to that in the unfilled NR sample of similar crosslink density (Figure 139). A large increase of the peak width is observed for reinforced samples as compared to the unfilled

sample, which indicates a decrease of the crystallite size in the presence of fillers. This is in agreement with previous studies<sup>71,104</sup>.

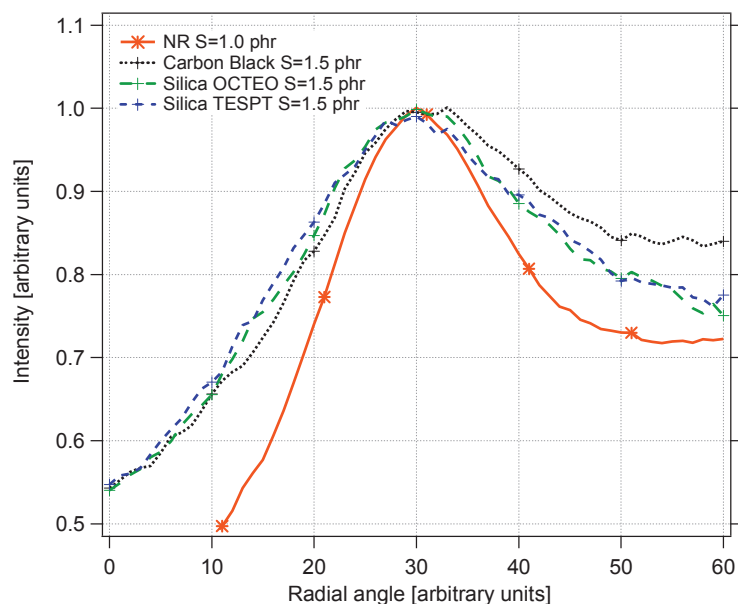


**Figure 139 : Effect of fillers on the {120} radial peak width as obtained by radial scans of the patterns (samples series 119-11). All scans have been done at the same crystalline content of 10%.**

The orientation of the crystallites provides additional pieces of information on the influence of reinforcing aggregates on SIC. The azimuthal width of the crystalline peak is plotted as a function of the deformation or as a function of the crystallized fraction (which increases with deformation) in Figure 140. Similarly to unfilled samples, the peak width decreases, i.e. the crystallite orientation increases slightly with deformation.

The important result here is that the orientation of crystallites is far lower for reinforced NR than pure NR. Along with the crystallite size reduction, this corroborates the hypothesis that the fillers inhibit the crystallization phenomenon at comparable local strain state.

One can also note in Figure 140a) that for a given strain the orientation depends on the type of filler but when plotted against the crystallized fraction (Figure 140b), the disorientation of crystallites is equivalent for the three filled systems. This means that there is no specific disorientation effect associated to a given type of interface.

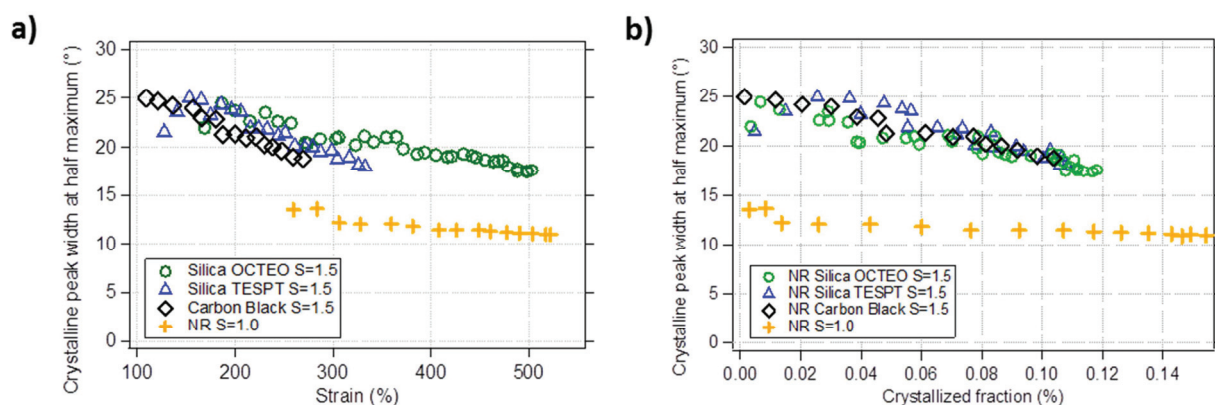


**Figure 140: Crystalline azimuthal peak width as a function of a) strain and b) crystallized fraction for unfilled (series 046-11) and filled samples at equivalent crosslink densities (series 119-11).**

We conclude that crystallite formation is strongly affected by the presence of fillers and the interface plays a determinant role in the strain amplification that lowers the SIC onset. It was also found that the slope of the crystallization curve as a function of strain is reduced as compared to unfilled NR, we attributed this effect to a possible perturbation of the crystallites formation and a strong heterogeneity in the local strain intensification. The analysis of the amorphous phase orientation given in the following chapter is in full agreement with those two points.

### *V.3.c. Effect of precycling on SIC.*

The effect of precycling was investigated by comparing the crystallization behavior of a non precycled sample to a sample previously submitted to three cycles of extension-retraction up to approximately 400% of strain. The time elapsed between the precycling and the in-situ tensile test under the X-ray beam was of the order of one week so some recovery of the Mullins effect could be observed. It was found that the non-precycled samples exhibit a lower SIC onset and a lower slope of the crystallinity vs strain curve (Figure 141). We understand this as the modification of local strain distribution due to the Mullins effect: chains breakage and slippage occurs in the regions of high strain amplification. This explanation is in agreement with Atomic Force Microscopy observation made by Lapra et al<sup>76</sup> on silica filled PDMS networks. These authors conclude that Mullins effect occurs in regions with a high concentration of silica, which we can picture as the highly strained regions. Altogether, the material becomes more homogeneous after precycling in terms of local strain distribution.

The accommodation of the rubber network lowers the maximal strain amplification and thus increases the SIC onset which can be understood as the macroscopic strain necessary to bring the extremity of the strain distribution up to the SIC onset for a perfectly homogeneous network.

When plotted as a function of the strain referred to the same initial length of the sample, (curves with crosses and diamonds in Figure 141), both crystallization curves (as-prepared and precycled samples) seem to merge at large extensions. This is consistent with the observation that, above

the maximum precycling strain, the stress becomes equal in the as-prepared and precycled samples. In our case, early failure of the non-precycled sample does not allow to reach the precycling strain of 400%, but the extrapolation of the curve is in agreement with previous observations by Gabrielle in his thesis on similar silica reinforced NR<sup>74</sup>. Above the precycling strain amplitude, the network has not been affected by precycling and both samples display both identical crystallized fractions and stresses.

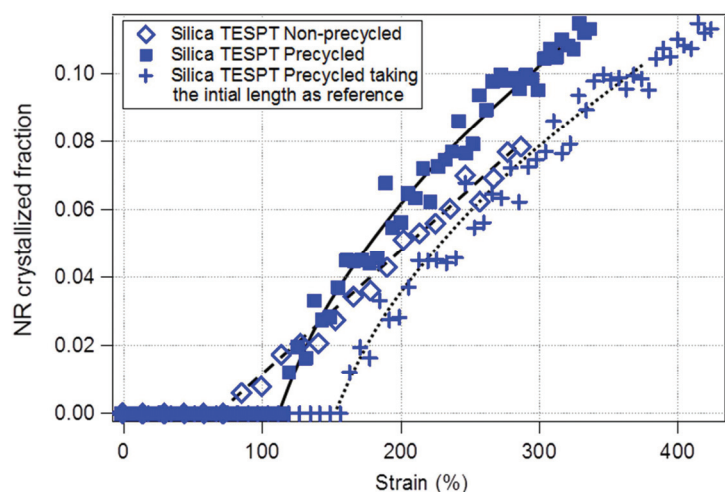


**Figure 141 : Influence of precycling on crystallized fraction for a Silica TESPT system (030-11). Precycled sample strain is either calculated from the sample length after precycling (filled squares) or before precycling (crosses). Lines are guides for the eyes.**

The effect of large strain amplitude cycles was also investigated for unfilled NR. A slight increase of SIC onset was recorded at high enough precycling maximum strain (typically above 90% of the strain at break).

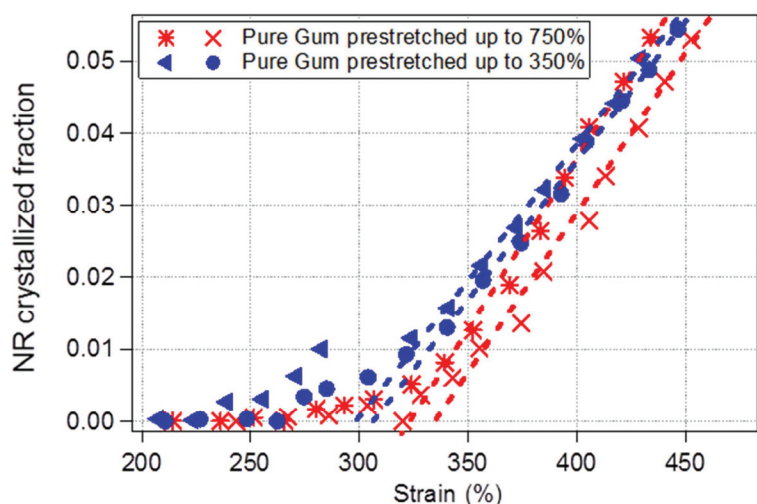


**Figure 142 : Effect of precycling maximum strain on the SIC onset in an unfilled NR sample (sulfur content 0.5phr; series 119-11). The strain at break is about 800% for this sample.**

## V.4. Crystallization and melting kinetics.

### V.4.a. Measurements principle

The influence of crosslink densities and filler-matrix interface on the crystallization behavior has been studied in quasi-static configuration. It provides interesting insights on the evolution of the microstructure with strain and the relevant parameters playing a role on SIC.

Nevertheless the characteristic sollicitation time is known to have an influence on the Strain-Induced Crystallization behavior<sup>93,99</sup>. Therefore if one wants to draw relationships between SIC and crack propagation in tear or fatigue experiments and even further with wear mechanisms, the knowledge of the SIC kinetics is necessary. As a matter of fact, these failure mechanisms are dynamic processes where the crack propagation speed plays a central role and the ability of the NR to crystallize in small characteristic times is supposed to be driving its excellent resistance. The question we have to address could be summarized in this way: Is there enough time for the polyisoprene chains to strain crystallize during a given mechanical sollicitation?

It is of utmost importance to better understand and measure the crystallization and fusion kinetics as a function of elongation ratio and temperature since fatigue resistance depends on strain levels and temperature<sup>146,154</sup>.

For those reasons many research groups have been trying to study SIC kinetics through different strategies<sup>155-159</sup>. Two main experimental set-ups have been designed for the study of SIC kinetics by X-ray diffraction:

- The first type of devices is meant to apply a very rapid stepwise sollicitation and record the crystallinity evolution as a function of time once the very fast elongation step is stopped. This implies very short X-ray diffraction pattern acquisition times and consequently very intense X-ray synchrotron sources. The characteristic time of elongation is of the order of a few milliseconds to a few tens of milliseconds<sup>156,159</sup> which in Tosaka and coworkers' experiments turns out to be a bit long as compared to the characteristic times of crystallization of approximately 20ms found by these authors.
- The device we used in our study relies on stroboscopic pattern acquisition during periodic cycling experiments at various frequencies. As firstly described by Kawai<sup>160</sup>, the crystallization kinetics can be estimated by measuring the difference between the crystalline content at the minimum and maximum deformation on a mechanical cycle. In the device we have used, a beam chopper consisting in a pierced disk with two opposite holes rotates in a synchronic way with the elongation device letting the X-ray beam reach the sample at the maximum and minimum elongations. Behind the sample is another beam chopper disk with a specific design that enables the illumination of one half of the detector at the maximum and the other half at the minimum. Due to the application of repetitive cycles, the intensity can be collected on several cycles making a laboratory X-ray source sufficient for these experiments and leading to a good accuracy of the results. The typical time for the acquisition of a diffraction pattern was 1 minute.

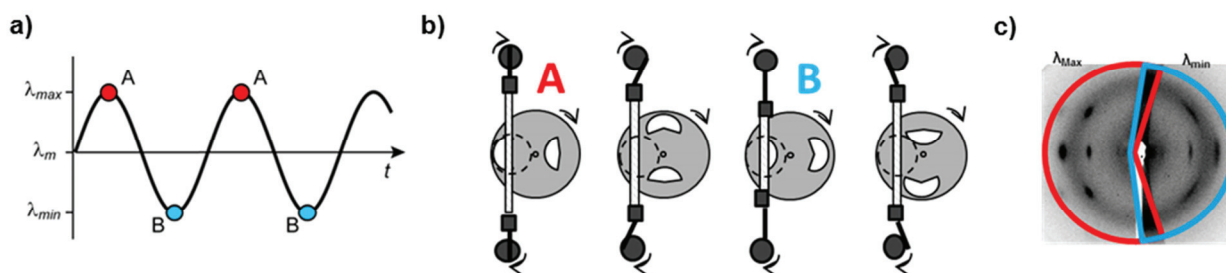


**Figure 143: Schematic principle of the stroboscopic acquisition: a) Applied oscillating extension ratio b) Beam chopper positioned behind the sample in order to illuminate alternatively one half and the other half of the detector c) Obtained diffraction pattern with each side corresponding to a given mechanical state.**

In order to investigate the crystallization and fusion kinetics, the time available for the crystallites to form or melt is monitored by changing the frequency of the mechanical cycling in a range of typically 0.1 to 10Hz.

Another important characteristic of the machine is the possibility to carry out experiments at different average deformations allowing studying the influence of this parameter on the kinetics.

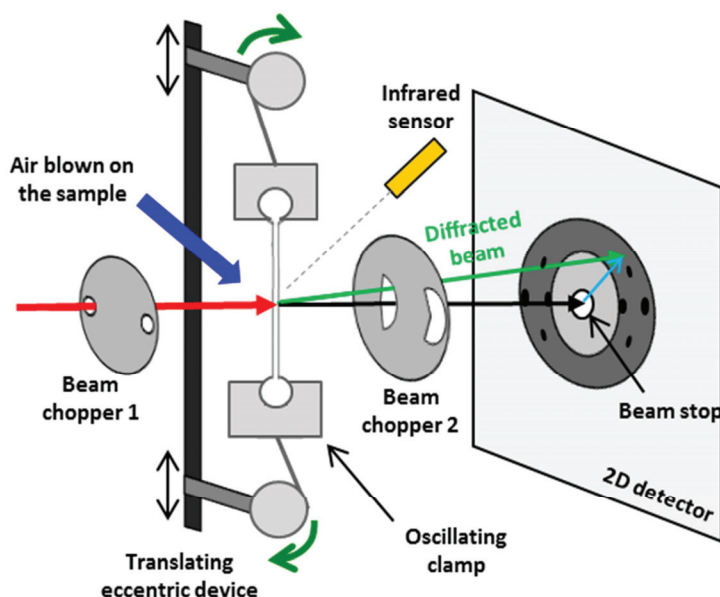


**Figure 144 : Scheme of the oscillations and traction device with the beam choppers for the stroboscopic acquisition of X-ray patterns.**

The oscillating amplitude is also adjustable enabling low and high elongation amplitude experiments. In the first case it is possible to follow the crystallization and melting retardation close to a given elongation and therefore analyze the effect of elongation ratio on the kinetics.

In large amplitude experiments, the crystallization retardation corresponds to a wide range of elongations and the effect of elongation ratio is not taken into account. These second type of experiments can be used to reproduce the condition of fatigue experiments<sup>146</sup>.

All the machine characteristics as well as the chosen values for our experiments are reported in Table 9.

Characteristics	Device capabilities	Applied Values in our study
Static displacement (mm)	0 to 100	25 ; 35 ; 45 ; 55 ; 65 ; 75
Oscillating displacement (mm)	0 to 38	10 ; 38
Measured frequencies (Hz)	0.01 to 50	0.5 ; 1 ; 3 ; 5 ; 10 ; 20
Number of patterns per frequency	unlimited	5
Acquisition time for a pattern (s)	At least 30s to have a sufficient intensity	60

**Table 9 : Device characteristics and selected parameters for the present study.**

We chose to address the heat build-up issue by continuously blowing air on the sample. The Infrared sensor was used to check that the temperature at the surface of the sample was not increasing significantly. In the worst cases i.e. when the oscillation frequency was 20Hz and the sample was highly stretched, we recorded an increase of temperature at the surface of less than 5°C.

The traction phase is known to be an out-of-equilibrium phase whereas the recovery phase is much closer to the crystalline content that the sample would contain in condition of pure equilibrium<sup>90</sup>.

For this reason it is interesting to compare the crystallization obtained in dynamic condition to a quasi-static experiment retraction curve.

The complete deformation (i.e. applied displacement) evolution to which the samples are submitted prior to oscillation cycles is detailed in Figure 145, 2 complete cycles of precycling were applied to obtained stabilized samples in the sense of the Mullins effect. The sequences of oscillations were applied upon the recovery curve of a third cycle starting from the highest average deformation sequence to the lowest.

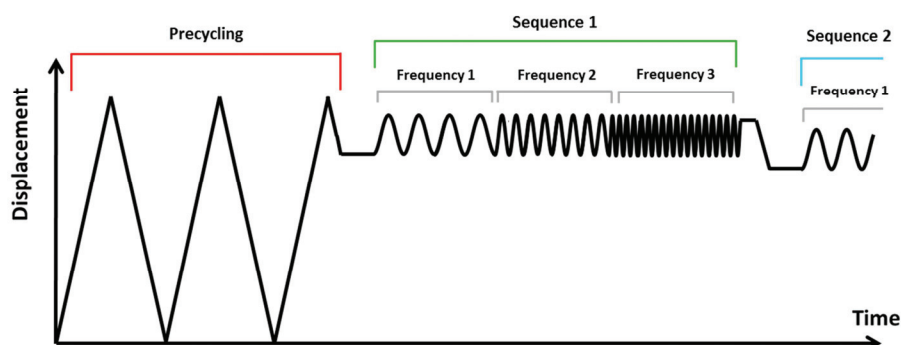


**Figure 145: Testing procedure detail : precycling, stabilization and oscillating sequences of decreasing average amplitude.**

The results presented here were obtained on unfilled NR samples of two different crosslink densities (0.5 and 1.5phr of sulfur) and reinforced NR either during my PhD or by P-A. Albouy<sup>108</sup>.

In all further discussed results, each average elongation was performed for all frequencies, the sample is submitted to a given frequency for approximately 4 minutes which corresponds to the time necessary to record 5 diffraction patterns plus some extra time for the CCD data transfer at each pattern. The collected patterns were analyzed separately and the crystalline content at maximum or minimum for a given frequency is the average value of the five corresponding half patterns.

#### *V.4.b. Interpretation of the results*

The general principle of the kinetics measurements is to carry out oscillating deformation sequences of increasing frequency with stroboscopic acquisition. By monitoring the frequency, we should observe at very long periods complete crystallization and fusion on a cycle whereas very short periods the crystals would neither have time to form or melt and a stationary state is to be reached spotlighting the characteristic time for crystallization and melting. Obviously the lower frequency for reaching the complete equilibrium is not to be found in those experiments of low characteristic time ( $dl/dt$  between 1 and 40s<sup>-1</sup> in our case). Of more interest for us is the characteristic time for the appearance of strain-induced crystallites and the influence of average strain on this factor.

Several scenarios can be envisaged depending on the kinetics of crystallization and fusion of the samples as compared to the solicitation characteristic time (Figure 146)

In the case of very fast crystallization and fusion kinetics, the sample's crystalline content would simply oscillate between the crystallinity at low strain  $X_{\min}$  and high strain  $X_{\max}$  following the same sinusoidal curve as the strain with no phase difference.

For the second case we consider that one phenomenon is slow and the second one is fast (for example the fusion is fast and the crystallization is slow). Then the sample does not have time to crystallize completely during the traction phase but melts down to the crystallinity at low strain.

A third scenario would correspond to a slow fusion and an even slower crystallization process. There is not enough time for the crystallites to form and neither to melt but depending on the

kinetics interval, the stationary regime would give crystalline contents closer to an extrema of the “equilibrium” cycle (in the case presented here, the crystallization being slower, the crystalline contents are closer to the lower point).

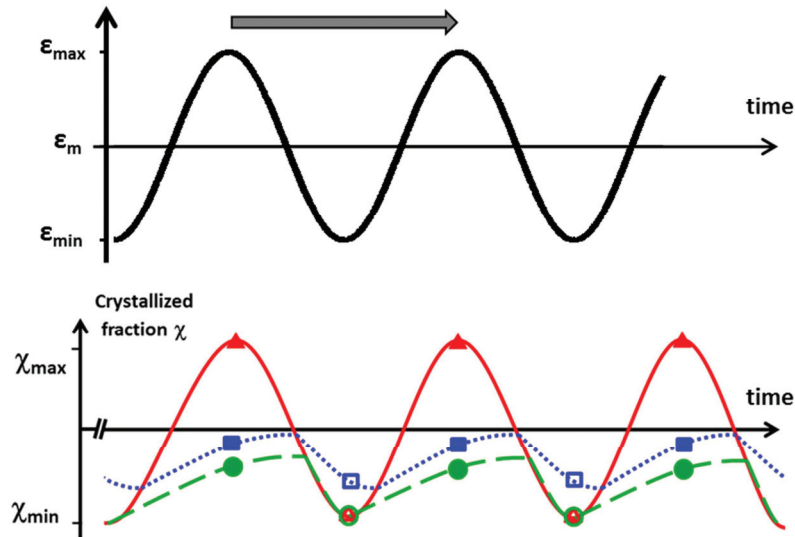


**Figure 146 : a) Applied strain sollicitation and associated period (grey arrow). b) Expected crystallized fraction (denoted  $\chi$ ) evolution according to different kinetics configurations: both fast fusion and crystallization (red line); fast fusion and slow crystallization (green dashes); slow fusion and very slow crystallization (blue dots).**

It is then interesting to report the crystallization fraction at the maximum and minimum of the cycle on the crystallized fraction – strain graph in order to compare the results of dynamic sequences to the “equilibrium” retraction curve.

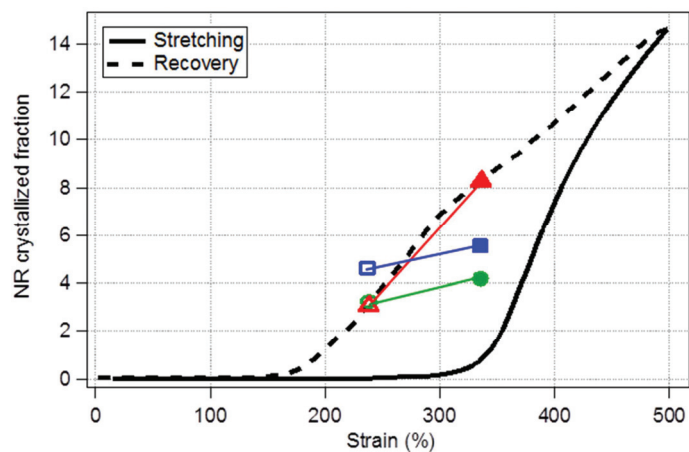


**Figure 147: Comparison of quasi-static retraction curve and oscillations data.**

### V.4.c. Results for Unfilled NR

The investigated range of frequencies in the experiments was limited to 0.5Hz to 20Hz whereas the lowest frequency data obtained by P.A. Albouy were done at 0.05Hz. It appears that there are no differences in crystalline content obtained in the range 0.5-20Hz (Figure 148). At least it confirms that the cooling down of the sample is effective since no crystallization decrease is observed with rising frequencies. The effect of frequency will be further discussed in paragraph V.4.c.ii.

#### V.4.c.i. Effect of average deformation

Figure 149 compares the obtained crystallized fraction at a given elongation averaged over all frequencies to gain accuracy. The results obtained in dynamic tests are compared to the retraction curve of a quasi-static experiment performed on the same sample after the dynamic tests sequences. The quasi-static stress-strain curve was performed on the sample after the oscillations sequences in order to avoid any shift between dynamic and quasi-static data due to a higher residual strain after the dynamic sequences.

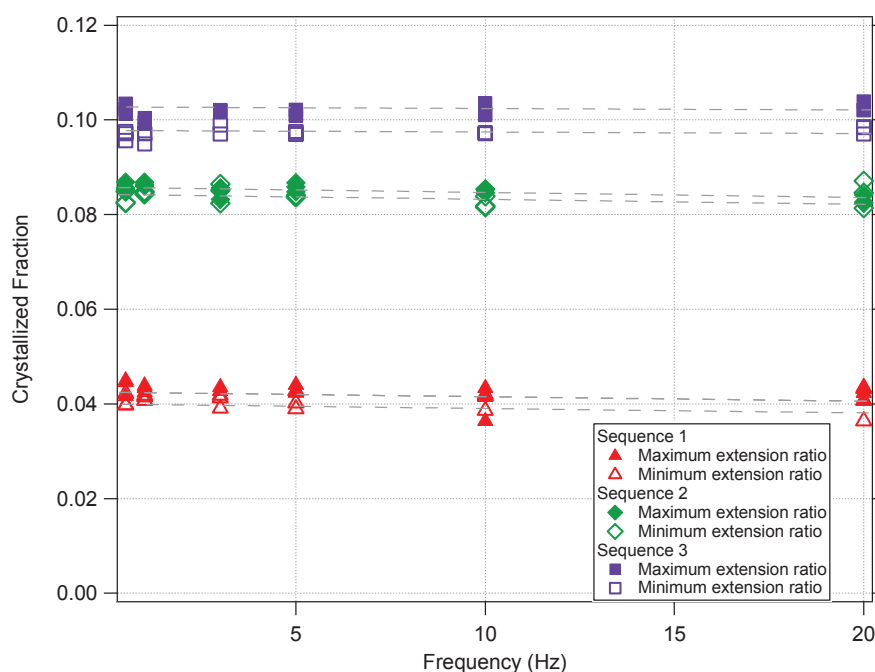


**Figure 148: Crystallized fraction at maximum (filled symbols) and minimum (empty symbols) extensions for three oscillation sequences as a function of frequency.**

In all cases, maximum and minimum points present a shift from the equilibrated curve which confirms that the solicitation time of two to three orders of magnitude shorter than in quasi-static tests has a strong influence on the crystalline content.

More precisely the upper point of the cycle is shifted down to lower crystallites content due to limited time to crystallize and conversely the lower point of the cycle exhibits a higher crystallites content due to melting retardation.

The difference between the upper and lower mechanical points from the same sequence are quite low stemming from rather small kinetics as described in Figure 146 but becomes more important as the average deformation applied increases.

The gap between the crystalline content at the maximum of the cycles and the equilibrated retraction becomes smaller as deformation increases. This is also true for the measurement at the minimum but in a low proportion. The crystallization kinetics is thus promoted by the applied deformation.

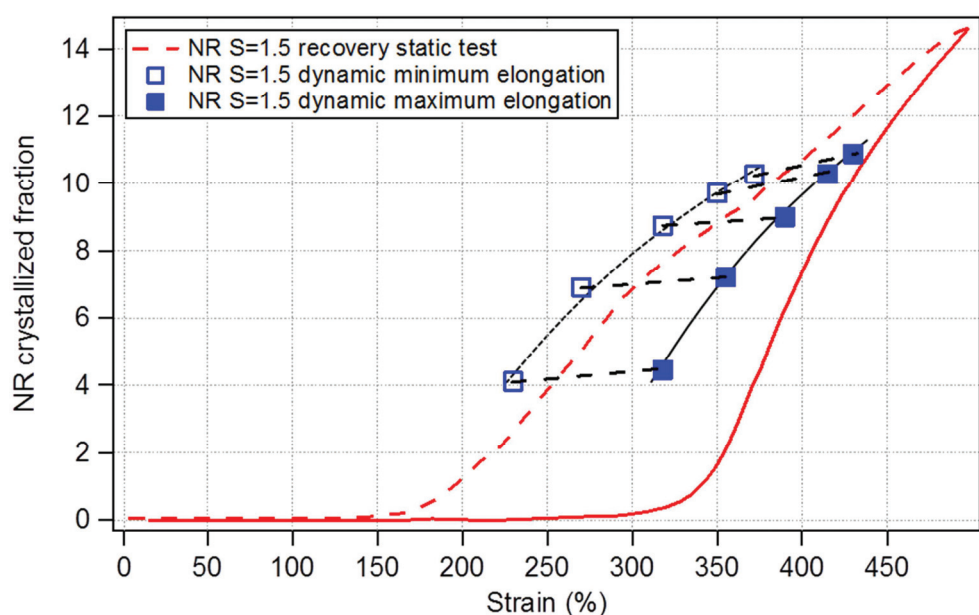


**Figure 149: Quasi static traction recovery curve and results of oscillating sequences for standard crosslinked sample (S=1.5phr): empty and full squares respectively represent the minimum and maximum deformation on the cycles.**

In the case of the weakly crosslinked NR (Figure 150), only the sequences done at large deformations are relevant since the inverse striction phenomenon occurs at lower deformations and does not disappear when performing the periodic cycling.

Fusion seems to be always fast as compared to the applied stretching time since the lower point of the cycle falls on the retraction equilibrated curve. As regards the upper point, it is found to be closer to the equilibrium when the average deformation rises. For the two crosslink density tested, it is shown that the higher the average deformation and the faster the crystallization

The crystallization and melting retardation i.e. the difference between the dynamic and quasi-static measurements at a given strain are plotted as a function of the average deformation applied in an oscillations sequence (Figure 151).

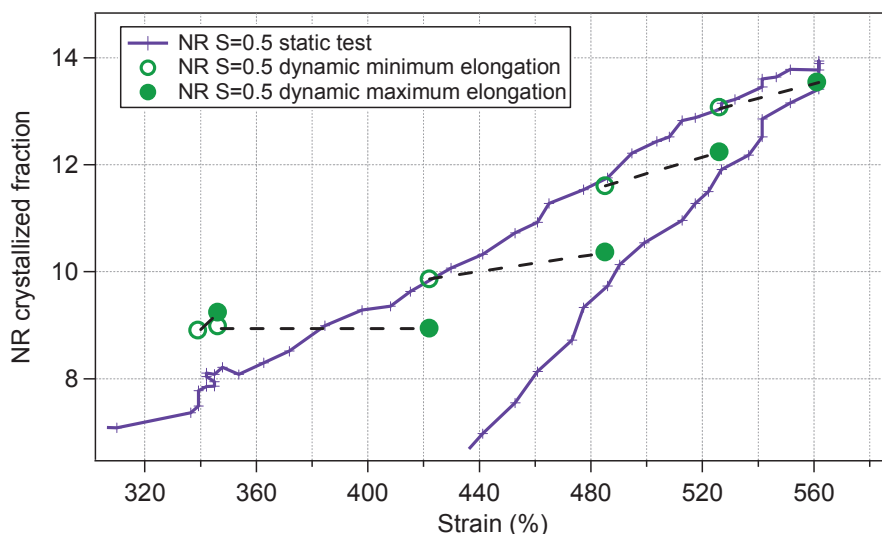


**Figure 150 : Quasi static traction recovery curve and results of oscillating sequences for weakly crosslinked sample (S=0.5phr): empty and full squares respectively represent the minimum and maximum deformation on the cycles.**

Note that the average oscillation strain is taken as the bottom axis and not the actual strain at which the upper or lower point is measured since the crystalline fraction recorded depends on the kinetics of all swept deformations on a cycle.

The values of crystalline fraction shift from equilibrium that is the retardation effect are positive in the case of the minimum elongation and negative for the maximum.

The acceleration of strain crystallization is displayed for both samples. It seems particularly important in the strain of the order of 300% for the standard cured NR (S=1.5phr).

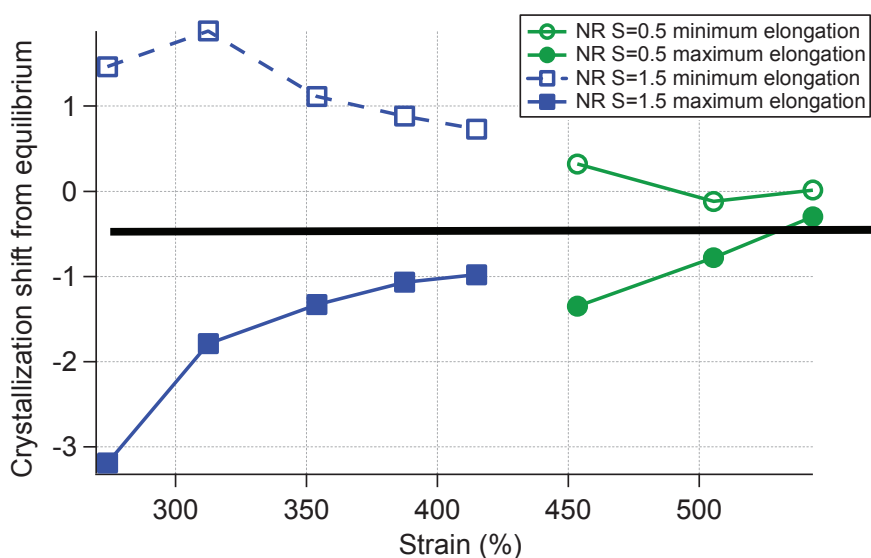


**Figure 151 : Retardation from equilibrium (thick line at zero crystalline fraction shift) at lower (empty symbols) and upper deformation of oscillations cycles for the two tested NR.**

V.4.c.ii. Effect of oscillations frequency

As observed in Figure 148 there is no significant effect of the oscillation frequency up to 20 Hz in our experiments.

Candau et al<sup>158</sup> reported experiments performed on an similar device with the possibility to reach very high frequencies of 70Hz. Their results show a decrease of crystallized fraction at high strain in the same frequency range (1 to 20 Hz) as ours but they did notice a strong heat build-up than can partly account for this decrease.

The fact that the crystallization is not strongly modified in the frequency range we applied indicates that the investigated time range is not of the same order as the crystallization characteristic times. One should recall here that the frequency regions were the crystalline content changes between maximum and minimum elongation found by Kawai<sup>160</sup> were close to 0.01 and 10Hz. Furthermore Albouy's results on the same samples indicate that above 0.5Hz (i.e. a half period time of 1s referred as the stretching time), the crystalline fraction of rubber is constant with frequency at a given maximal or minimal elongation. Those results<sup>108</sup> highlight two distinct strain regimes (Figure 152) in agreement with our previous observations and the lower frequencies applied (longer half period) evidence some crystallization processes of characteristic time of the order of 1 to 10s.

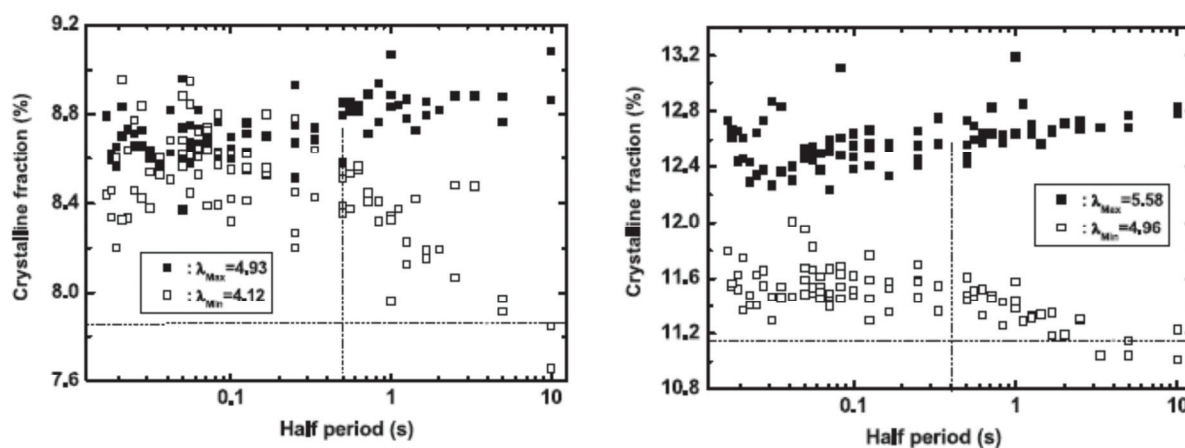


**Figure 152 : Effect of frequency on the crystalline content in large strain regimes at two minima and maximum extension ratios a)  $\lambda_{\min}=4.12$  b)  $\lambda_{\min}=4.96$ . Reproduced from Albouy et al<sup>108</sup>.**

Figure 153 represents the crystallization and melting retardation computed as the dynamic measurement at lower and upper point minus the equilibrium value at an equivalent strain.

The retardation obtained from a half period of 1s is fairly comparable to the results presented in section II.3.c.i demonstrating the reproducibility of the measurements. The other two sets of points corresponding to half periods of 2.5 and 10s follow the expected trend: the crystallization and melting is closer to the equilibrium for longer periods of solicitation.

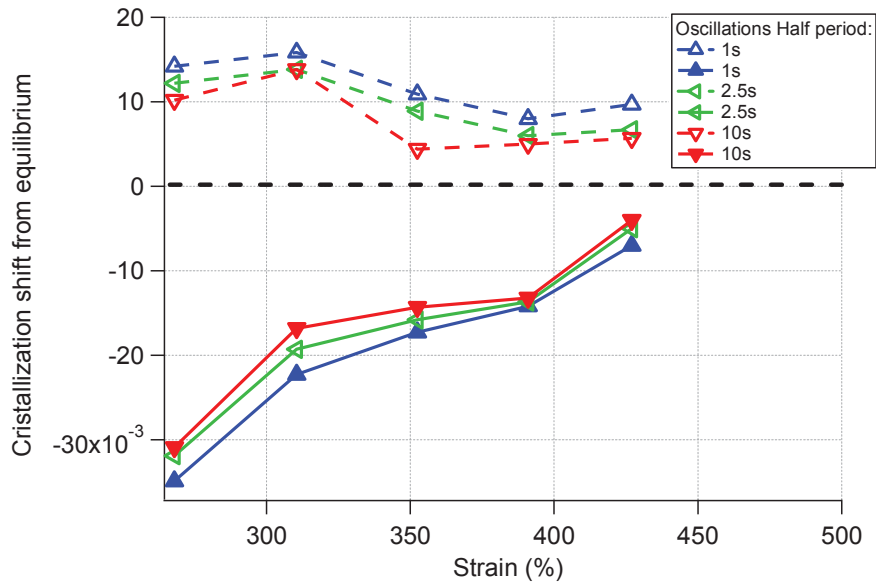


**Figure 153 : Retardation from equilibrium (thick line at zero crystalline fraction shift) at lower (empty symbols) and upper deformation of oscillations cycles for three solicitation periods. Data retreated from Albouy et al<sup>108</sup>.**

Thanks to a specific sample shape, it was possible to apply higher strain amplitude oscillation with our device. Those high amplitude experiments enable to oscillate between an extension ratio ( $\lambda_{\min}=2.4$ ) lower than the melting ratio and a high extension ratio of 5.3. The frequency was found to have much more effect with such high amplitude oscillations (Figure 154) and the evolution of crystallized fraction with solicitation time follows a logarithmic trend. This observation is in agreement with impact tensile measurements performed by Brüning and coworkers<sup>159</sup>. By extrapolating the data, stretching times of the order of the millisecond to the tenth of millisecond could be estimated as characteristic time to suppress SIC at the tested extension ratio.

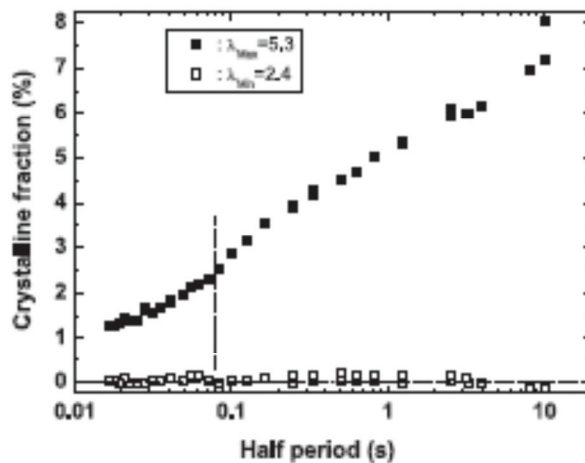


**Figure 154: Effect of frequency on the crystalline content for large amplitude oscillations with a minimum extension ratio  $\lambda_{\min}=2.4$ . Reproduced from Albouy et al<sup>108</sup>.**

*V.4.d. Results for Filled NR*

In the case of filled samples, the width measurements were quite noisy due to a poor contrast in particular with Carbon black thus the measurements of crystallite contents in quasi-static cycle and dynamic oscillations are reported as a function of the applied displacements. Nevertheless, the displacement/strain relationship being very similar for the two analyzed filled rubbers, the comparison is still relevant.

The first remark to be made is the lower crystalline fraction found at the lower point of cycles compared to the quasi-static curve. This may stem from the non-negligible heat build-up in the reinforced NR. Infra-red measurements at the surface of the samples show that the temperature rises of several degrees for frequencies above 3Hz (it is to be reminded that the average crystallized fraction over all frequencies is plotted in Figure 155). The weak crystallized fractions of the lower points (and consequently upper points) can be explained by taking into account the probably higher temperature at the core of the sample. Note that the shift from the quasi-static curve is more pronounced for carbon black in agreement with temperature measurements.

As regards the gap between lower and upper points for each cycle, the main observation is that it is higher for Carbon Black as compared to Silica suggesting higher crystallization kinetics for all the elongation range investigated. Indeed no clear effect of the applied strain level can be highlighted here for Silica neither for Carbon Black.

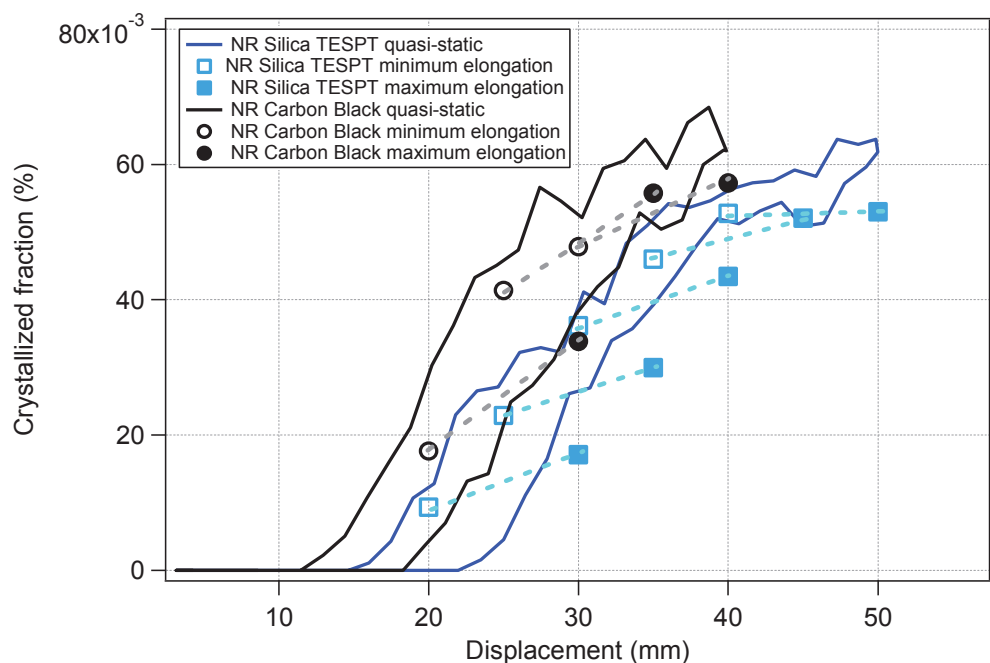


**Figure 155: Quasi static traction-retraction curve and results of oscillating sequences for Silica TESPT and Carbon Black filled NR samples: empty and full squares respectively represent the minimum and maximum displacement on the cycles.**

## V.5. Conclusions

Strain-Induced Crystallization and Amorphous Orientation have been analysed in unfilled and filled NR samples stretched in-situ. The crystallized fraction has been related to the strain measured independently. Crystallite size and orientation were also measured.

In unfilled NR, the SIC onset does not depend significantly on the crosslink density. Above the onset, the crystallite fraction slightly depends on the crosslink density and the steep increase of the true stress is attributed to limited chains extensibility and to the reinforcement effect of crystallites ('self-reinforcement').

In reinforced NR, the crystallization behaviour is strongly modified by the introduction of fillers and the interface plays a key role on the crystallization onsets and the slope of the crystallinity curves. These changes may be interpreted as a broad distribution of local strains in the reinforced samples. The effect of precycling on the SIC behaviour was also interpreted in terms of the modification of the local strain distribution. Precycling would reduce the contribution from higher locally strained parts of the rubber. Some restriction on the formation and growth of crystallites may also explain the lower slope of the crystallization curves and the lower crystalline content at break.

As regards Strain-induced Crystallization kinetics, a new device has been developed. We have shown that Strain induced Crystallization and Melting kinetics could be evaluated both in unfilled and filled rubbers.

The SIC kinetics increases with applied deformation. Melting kinetics is less sensitive to the applied deformation. Increasing the crosslink density lowers the kinetics of melting and enhances the crystallization kinetics at a given strain.

A logarithmic dependence of crystallization on solicitation time has been found in the case of high amplitude cycles.



## VI. Reinforcement

VI.1.	Unfilled NR .....	170
VI.1.a.	Proton DQ-NMR experiments .....	170
VI.1.b.	Equilibrium swelling experiments .....	171
VI.1.c.	Mechanical modulus .....	171
VI.1.d.	Amorphous chain orientation.....	173
VI.1.e.	Correlation of mechanical, amorphous orientation, equilibrium swelling and NMR measurements.....	175
VI.2.	Filled NR .....	179
VI.2.a.	Proton DQ-NMR experiments .....	179
VI.2.b.	Equilibrium swelling experiments .....	180
VI.2.a.	Modulus in the large strain regime.....	181
VI.2.b.	Modulus in the small strain regime.....	182
VI.2.c.	Amorphous chain orientation.....	183
VI.2.c.i.	Amorphous chain orientation vs Strain.....	183
VI.2.c.ii.	Amorphous chain orientation versus true stress .....	185
VI.2.c.iii.	Effect of precycling on the amorphous orientation.....	187
VI.3.	Correlations between the various measurements.....	187
VI.3.a.	Correlations between large amplitude mechanical behaviour, amorphous orientation, swelling and NMR measurements.....	188
VI.3.a.i.	Case of the NSC coupling agent.....	191
VI.3.b.	Mechanical Reinforcement in the linear regime .....	192
VI.3.c.	Strain Amplification discussion .....	195
VI.3.c.i.	Distribution of local strains .....	195
VI.3.c.ii.	Effect of fillers.....	197
VI.3.c.iii.	Effect of precycling on reinforced samples .....	198
VI.3.c.iv.	Effect of the interface type .....	199
VI.4.	Conclusion.....	200

This chapter presents a systematic comparison of the unfilled and filled Natural Rubber behavior under stretching investigated with various techniques and correlated to the crosslink density measured by Roberto Pérez-Aparicio (LPMA) by low field proton NMR. The local chain stretching is investigated by equilibrium swelling, amorphous phase orientation determined by X-ray scattering and mechanical measurements.

Such an approach was first applied to unfilled NR in order to highlight the differences between the techniques that all provide pieces of information on the chain segmental orientation and thus on the crosslink density.

Taking the unfilled rubbers as reference, the effect of fillers and in particular of the filler/polymer interface was highlighted for each testing method by referring to the actual value of crosslinks given by NMR. The correlations of the different techniques provide interesting insights on the mechanisms of reinforcement both in the large and small strain regimes.

## VI.1. Unfilled NR

### VI.1.a. Proton DQ-NMR experiments

The average crosslink density deduced from the residual dipolar couplings is reported as a function of the sulfur content in Figure 156. The fact that the line intercepts the left axis at non-zero values indicates that a significant part of the chain orientation restrictions is not due to sulfur bridges, i.e. to chemical crosslinks. This has already been observed and has been interpreted as due to the presence of entanglements<sup>103,161</sup>. The value at the y-intercept gives an estimate of the density of entanglements (or equivalently the molecular weight between entanglements).

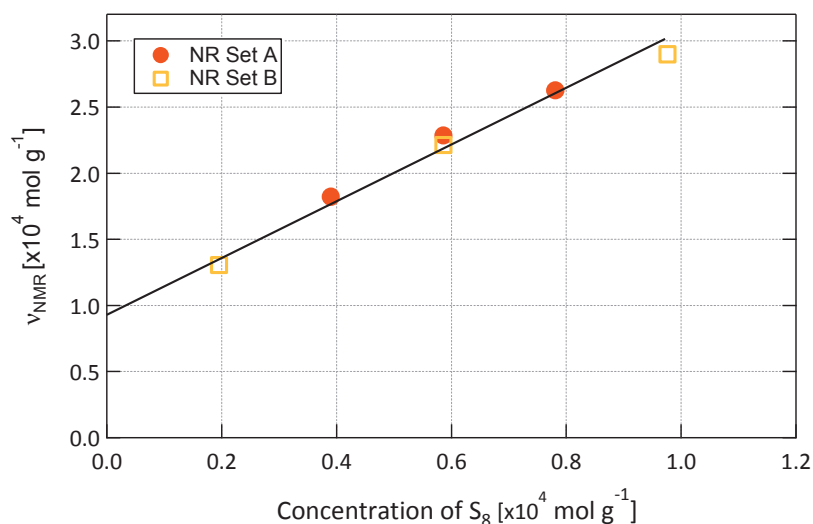


**Figure 156: Crosslink density deduced from proton DQ-NMR experiments as a function of the sulfur amount for samples series 046-11 (set A) and 119-11 (set B).**

### VI.1.b. Equilibrium swelling experiments

The equilibrium degrees of swelling  $Q$  (mass of swollen material divided by unswollen rubber mass, see chapter III) are shown as a function of the sulfur content in Figure 157 for unfilled NR samples, showing the decrease of the swelling ability with increasing content of sulfur. This representation of the data would be interesting when comparing different sample series with various accelerator/sulfur ratios showing the efficiency of the vulcanization (the higher the accelerator content and the higher the crosslink density with the same quantity of sulfur).

The degree of swelling should theoretically tend to 1 for very large amounts of sulfur, i.e. a rubber sample of infinite crosslink density should not swell, since no solvent molecules would be able to penetrate an infinitely tight network.

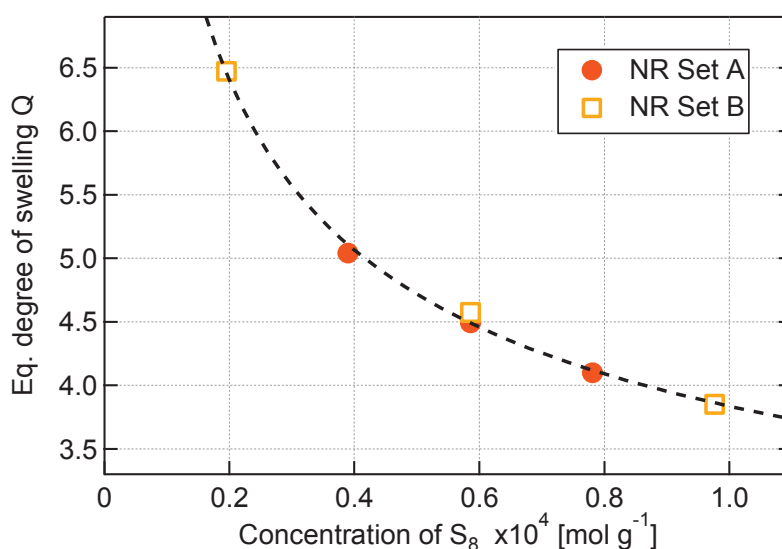


**Figure 157 : Equilibrium degree of swelling (swollen rubber mass/initial mass) versus sulfur content for unfilled NR samples from series 046-11 (set A) and 119-11 (set B). The curve is a guide for the eyes.**

### VI.1.c. Mechanical modulus

The stress-strain curves obtained in traction experiments were fitted with the semi-empirical law proposed by Mooney and Rivlin<sup>23</sup>, in the regime below the stress upturn (Figure 158).

In the Mooney-Rivlin expression (see chapter II), the modulus is decomposed into a contribution  $C_1$ , which is directly related to the elastic contribution of the crosslink density, and a term  $C_2$  that accounts for the small modulus decrease at small deformations. For an extension ratio  $\lambda=1$  the modulus is equal to  $C_1 + C_2$  and tends towards  $C_1$  at higher extensions. The fits were done in the linear regime, i.e., below the stress upturn, which occurs at roughly 2.5 MPa. The fitting parameters  $C_1$  and  $C_2$  (expressed in MPa) are reported in Table 10.

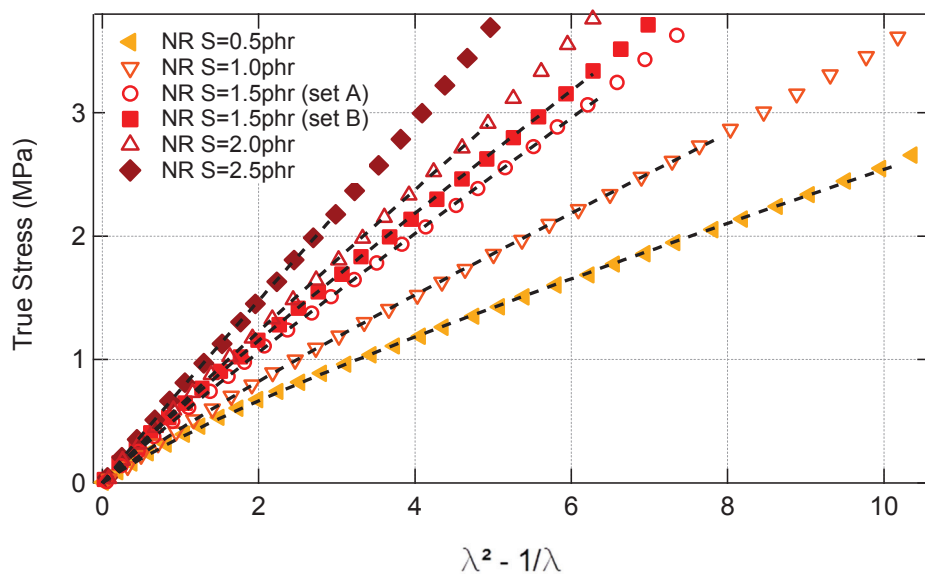


**Figure 158: Mooney-Rivlin fits of the true stress versus the elongation factor ( $\lambda^2 - 1/\lambda$ ). Samples series 046-11 (set A) and 119-11 (set B).**

Compounds			Mooney Rivlin parameters	
Set	Sulfur (phr)	CBS (phr)	$C_1$	$C_2$
B	0.5	0.66	0.087	0.129
A	1.0	1.33	0.141	0.106
A	1.5	2	0.214	0.083
B	1.5	2	0.223	0.106
A	2.0	2.66	0.265	0.069
B	2.5	3.33	0.332	0.062

**Table 10: Mooney-Rivlin parameters (in MPa) deduced from mechanical experiments.**

Some authors have related  $C_2$  to the entanglements effect<sup>21,24</sup> noting that the ratio  $C_2/C_1$  is higher for weakly crosslinked samples and tends to zero in the case of experiments on swollen rubbers or gels<sup>24</sup>. Our measurements are in agreement with this observation: the ratio  $C_2/C_1$  decreases as the crosslink density increases, as shown in Figure 159. This decrease can be interpreted as the decrease of the relative contribution of entanglements to the network. The ratio  $C_2/C_1$  is particularly high for the weakly crosslinked sample suggesting a strong contribution of entanglements to the network in this case.

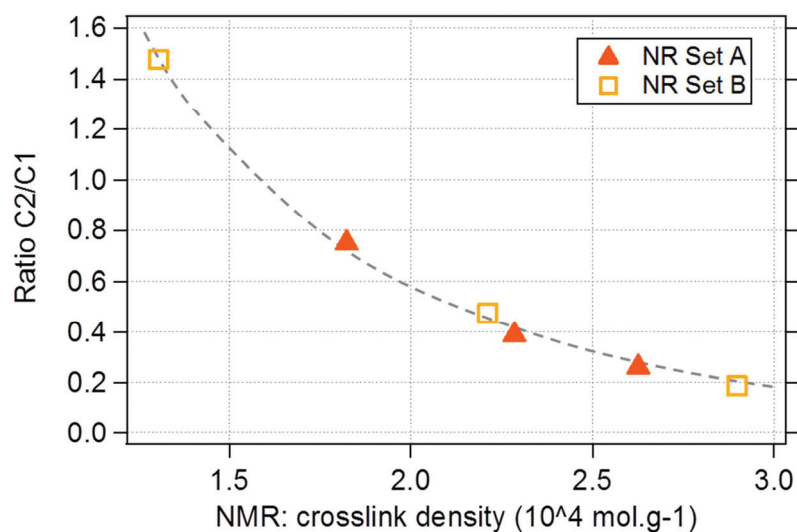


**Figure 159: Ratio  $C_2/C_1$  for unfilled NR samples from series 046-11 (set A) and 119-11 (set B).**

The apparent crosslink density  $\nu_{mecha}$  associated to the mechanical measurement was then computed from the following equation (see chapter II):

$$\nu_{mecha} = \frac{2C_1}{RT\rho_r\psi(\lambda^2 - \frac{1}{\lambda})} \quad (71)$$

The parameter  $\psi$  accounts for the chosen microscopic deformation model (see chapter II):

$\psi=1$  for the affine model.

$\psi=1/2$  for the phantom model assuming tetra-functional crosslinks.

#### *VI.1.d. Amorphous chain orientation.*

The evolution of the stress and amorphous orientation under stretching for all crosslink densities is reported in Figure 160 and has been described in chapter V (as well as the crystallized fraction recorded simultaneously but not plotted here): The amorphous orientation parameter  $\langle P_2 \rangle$  is first linearly related with the deformation function  $(\lambda^2 - \lambda^{-1})$  as predicted by the rubber elasticity theory and once the applied deformation exceeds the SIC strain onset (represented by the arrows in Figure 160b), the amorphous orientation is more or less constant during the crystallization of part of the rubber network.

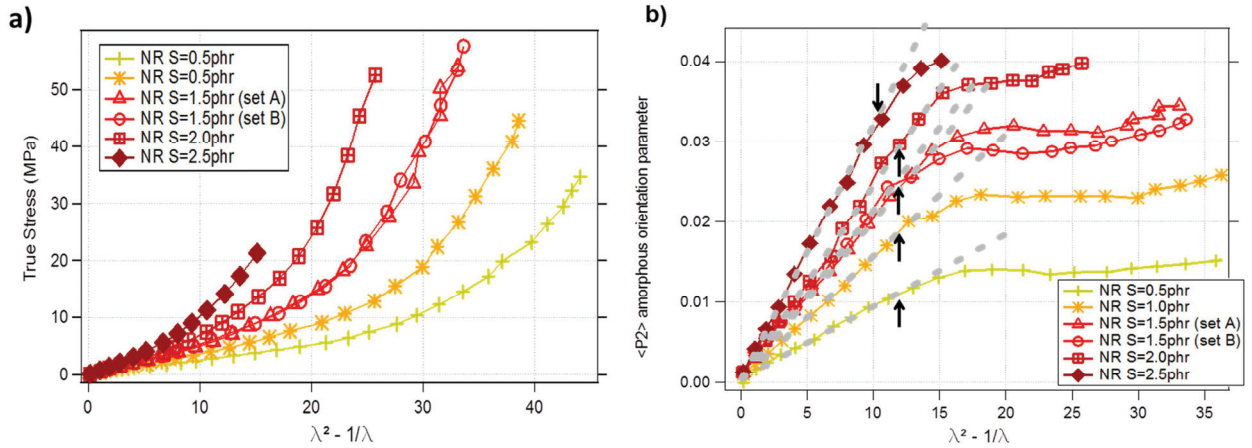


**Figure 160: In-situ tensile test up to failure: a) True stress and b) Amorphous orientation parameter versus rubber strain for unfilled NR of sample series 46-11 (set A) and 119-11 (set B). The arrows indicate the SIC onset as determined in chapter V and the dashed lines represent the prediction of the rubber elasticity.**

The amorphous orientation parameter can also be plotted as a function of the true stress measured in-situ (Figure 161). The above-mentioned first two regimes are still clearly visible: first the stress and amorphous orientation parameter follow a master curve for all samples and once their strain-induced crystallization onset is reached, the stress continuously increases while the amorphous orientation parameter  $\langle P_2 \rangle$  stabilizes at a constant value.

The first regime (enlarged in Figure 161) is rather interesting since it shows that our experimental data are in full agreement with the rubber elasticity prediction (equation 2) up to true stresses of 5 MPa. The true stress is directly related to the orientation of the Gaussian-like chains which network deforms in an affine manner.

Above 5 MPa (or a parameter  $\langle P_2 \rangle$  superior to 0.02) the true stress increases more rapidly than the  $\langle P_2 \rangle$ . In the case of lowly crosslinked samples this is due to the strain-induced crystallization which stabilizes the orientation of the amorphous. In the case of highly crosslinked samples (sulfur content 2.0 and 2.5 phr) the deviation from the linear trend happens before the strain-induced crystallization onset which implies that another phenomenon has to be taken into account to explain the shift from the rubber elasticity prediction (limited chain extensibility, non-affine deformations, network defects). It is also interesting to remark that the phenomenon(s) causing this behaviour is of the same amplitude in all samples i.e. it does not depend to a large extent on crosslink density.

Unlike what was done for mechanical tests, it is not possible to estimate an absolute crosslink density from amorphous orientation measurements since we do not have access to the factor  $K$  which depends on the scattering factor of the isoprene unit. The parameter  $Kv_\chi$  ( $\langle P_2 \rangle$  versus rubber strain slope in Figure 160b) proportional to crosslink density was used to compare the results.

$$Kv_\chi = \frac{\langle P_2 \rangle}{\left(\lambda^2 - \frac{1}{\lambda}\right)} \quad (72)$$

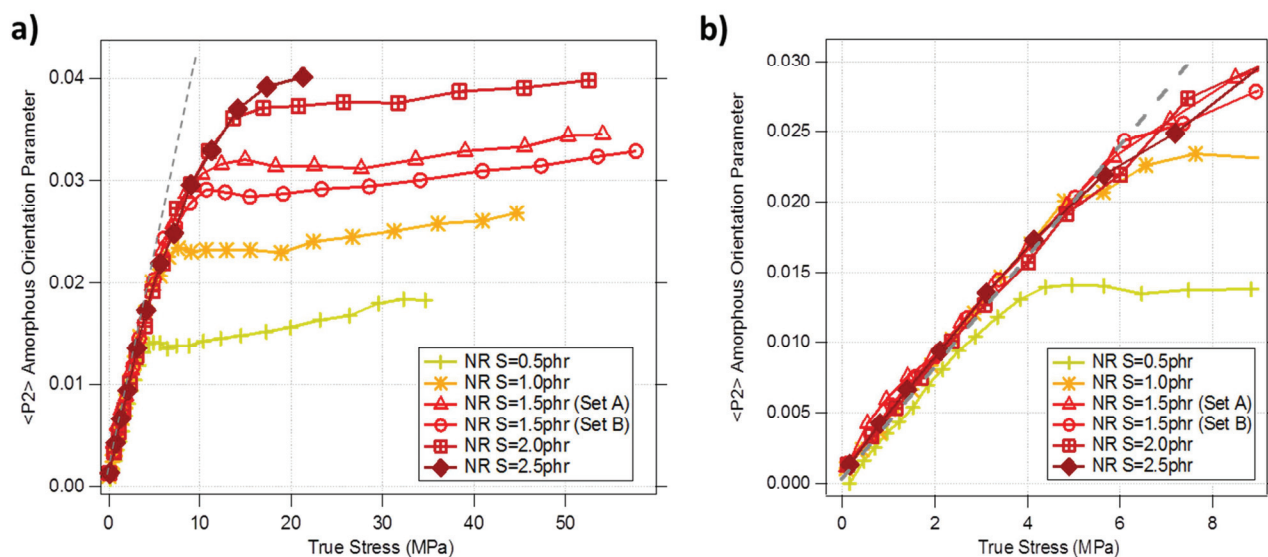


**Figure 161: a) Amorphous orientation parameter versus true stress and b) enlargement on the first regime for samples of series 046-11 (set A) and 119-11 (Set B).**

#### *VI.1.e. Correlation of mechanical, amorphous orientation, equilibrium swelling and NMR measurements*

Figure 162 and Figure 163 plot the crosslink density obtained from true stress and amorphous orientation parameter fits (see Figure 158 and Figure 160b) as a function of crosslink density as determined by DQ-NMR experiments.

In both cases, the points of the two different sets of samples fall on an almost linear curve confirming the very good agreement with the theory and the robustness of our measurements carried out on several samples from two independent series. The amorphous orientation parameter appears as an accurate measurement of the rubber network density in relative, not absolute values.

The slope does not cross the bottom axis at zero crosslinks: this highlights the different frequencies at which the independent measurements are done and consequently the different response of the overall polymer network. The NMR signal probes more contributions of short life-time entanglements at high frequency as compared to the low speed mechanical solicitation applied during X-ray diffraction experiments. Mechanical and X-ray measurements, which are both low frequency measurements, give roughly the same values at x-intercept meaning that the same entanglements are detected in both experiments.

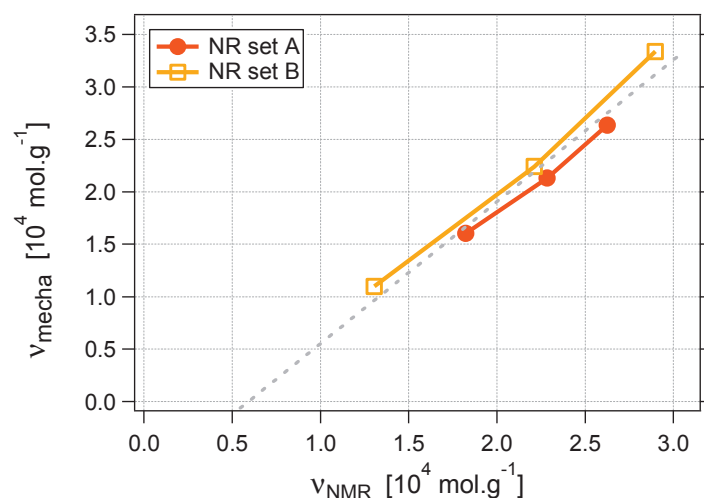


**Figure 162: Crosslink density  $v_{mecha}$  determined from true stress versus crosslink density  $v_{NMR}$  determined from NMR for unfilled NR samples. Series 046-11 (Set A) and 119-11 (Set B).**

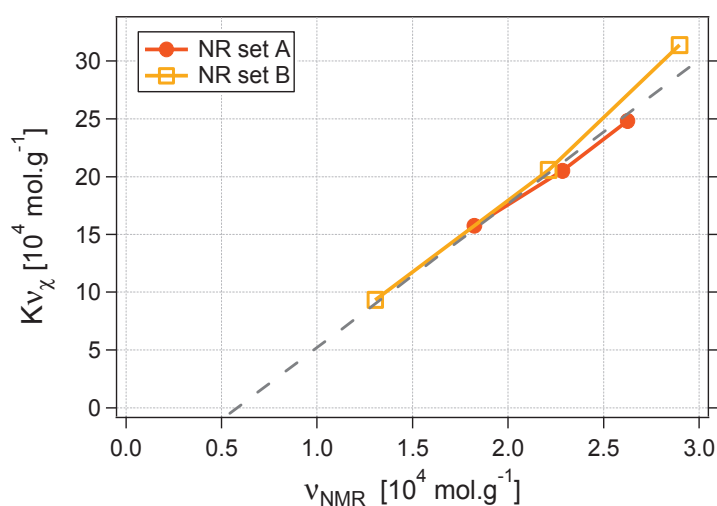


**Figure 163: Crosslink density  $Kv_\chi$  determined from  $\langle P_2 \rangle$  versus crosslink density  $v_{NMR}$  determined from NMR for unfilled NR samples. Series 046-11 (Set A) and 119-11 (Set B).**

The crosslink densities determined by equilibrium swelling measurements are reported as a function of crosslink densities deduced from NMR measurements in Figure 164 for the two sets of studied samples. It was decided to use the relationship based on the phantom model for the calculation of the rubber fraction  $\phi_r$  (see chapters II and III). As a matter of fact, it has been proposed in the literature<sup>81</sup> that this model is more appropriate to describe the deformation behavior during swelling experiments.

All unfilled samples fall on a linear curve confirming the accuracy of the network density estimation from the two methods<sup>81,103</sup>. However, the line has a non-zero x-intercept. Similarly to the observations made for Figure 162 and Figure 163, this is related to the different time scales which are probed in each experiment<sup>81</sup>. In NMR, the response is determined by chain segment

dynamics on a frequency scale of order 10 kHz, whereas equilibrium swelling experiments are static. Thus, some topological constraints (entanglements) are active on a relatively short time scale (NMR) and have time to relax in a static experiment (swelling), leading to effectively higher crosslink density values observed in NMR, which corresponds to the observed non-zero x-intercept in Figure 164.

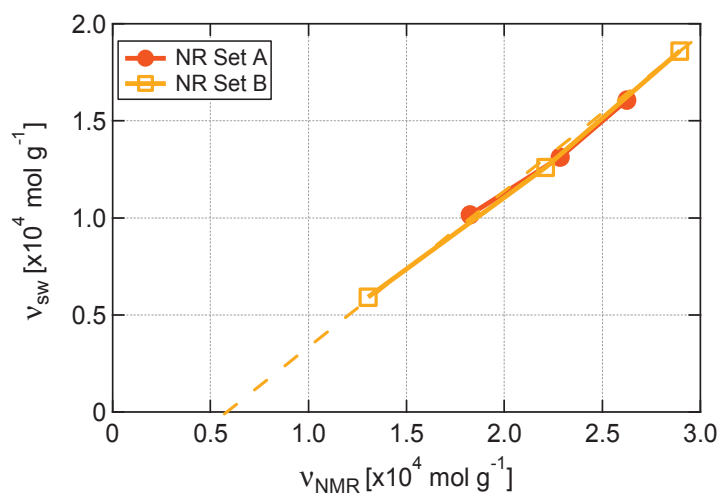


**Figure 164: Crosslink density  $v_{\text{sw}}$  determined from equilibrium swelling versus crosslink density  $v_{\text{NMR}}$  determined from NMR for unfilled NR samples. Series 046-11 (Set A) and 119-11 (Set B).**

In Figure 165 the crosslink density measured from the true stress is plotted versus the parameter  $Kv_\chi$  deduced from the amorphous orientation parameter.

The strong correlation simply illustrates the fact that the modulus was measured in the range where the true stress and the amorphous orientation parameter follow a master curve (Figure 161).

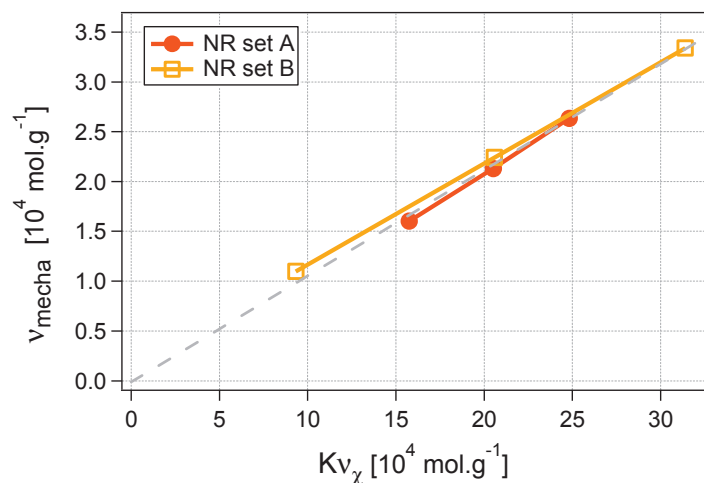


**Figure 165: Crosslink density  $v_{mecha}$  determined from true stress versus crosslink density  $Kv_\chi$  determined from  $\langle P_2 \rangle$  for unfilled NR samples. Series 046-11 (Set A) and 119-11 (Set B).**

To illustrate further the very good concordance between the independent measurements, the crosslink density  $v_{mecha}$  from true stress measurements and the parameter  $Kv_\chi$  deduced from the amorphous orientation parameter are plotted as a function of  $v_{sw}$  (assuming phantom model) in Figure 166 and Figure 167 respectively. Both curves have a zero intercept at origin, suggesting that

the same amount of entanglements are effective in all low frequency or static experiments. More precisely, it suggests that the truly trapped entanglement contribution in swollen state corresponds exactly to the entanglement contribution that is still active in the long-time limit in mechanical and X-ray measurements.

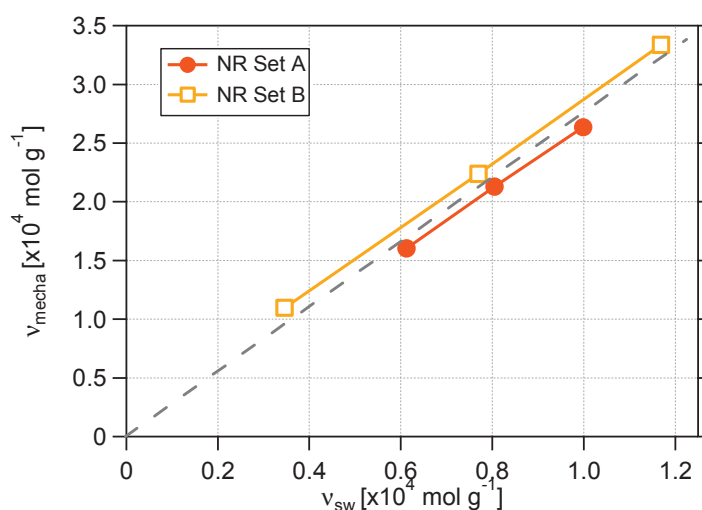


**Figure 166 : Crosslink density  $v_{mecha}$  determined from true stress versus crosslink density  $v_{sw}$  determined from equilibrium swelling for unfilled NR samples. Series 046-11 (Set A) and 119-11 (Set B).**

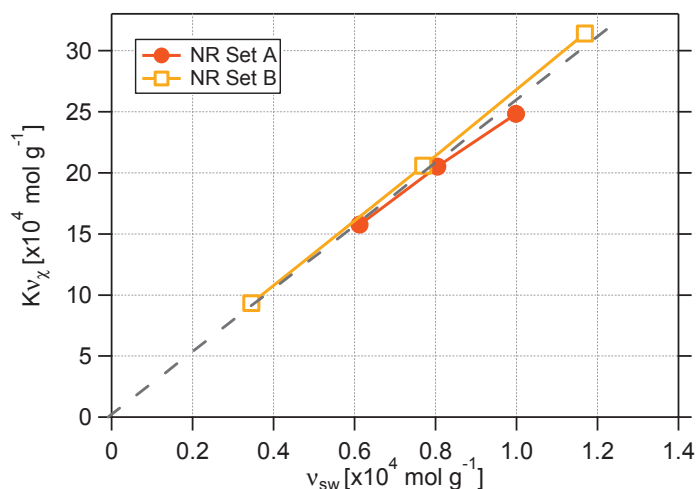


**Figure 167 : Crosslink density  $Kv_x$  determined from  $\langle P_2 \rangle$  versus crosslink density  $v_{sw}$  determined from equilibrium swelling for unfilled NR samples. Series 046-11 (Set A) and 119-11 (Set B).**

## VI.2. Filled NR

### VI.2.a. Proton DQ-NMR experiments

The crosslink densities measured by NMR for the different systems of the series 030-11, 046-11 and 119-11 as a function of the sulfur amount are presented in Figure 168. These sample series include non-reinforced and reinforced systems, both with different sulfur and accelerator amounts (see chapter III). For each type of samples, a nice linear relationship is obtained between the crosslink density (number of crosslinks per unit volume) and the sulfur amount.

Comparing the crosslink densities of the silica reinforced compounds with the corresponding unfilled NR matrices evidences an important aspect of sulfur vulcanization in silica reinforced rubbers: part of the acceleration agents used in sulfur crosslinking are adsorbed on the silica surface<sup>60</sup>. In our case, the CBS accelerator is partly adsorbed, yielding a lower crosslink density at a given sulfur amount. As regards compounds filled with Carbon black, the amount of CBS has been reduced compared to that introduced in the presence of silica, so as to precisely compensate the adsorption on silica and to obtain compounds of similar matrix crosslink densities, which seems quite true from our measurements.

Finally, there are slight differences between samples reinforced with silica and different interface agents as well as with carbon black (making it difficult to determine the real CBS correction necessary to obtain equivalent crosslink densities). This effect of the type of interface can either be due to the influence of the coupling agent on the CBS adsorption or the additional restriction points (new effective crosslinks) brought by the covalent bonds established between the silica surface and the rubber chains.

It may be assumed that, having the same reactive function towards silica surface (the triethoxy group) and similar carbon chain lengths, the TESPT, NSC and OCTEO interface agents induce no significant difference in terms of CBS adsorption. The silica dispersion state seems to be

relatively similar in the three cases (according to Dispergrader measurements, see appendices), which means that the overall available silica surface should be equivalent.

The higher crosslinking of NSC and TESPT samples compared to OCTEO samples may be thus attributed to the interface interactions and a supplementary effect of sulfur release in the case of TESPT.

The numbers of moles of sulfur atoms introduced during mixing and contained in TESPT molecules can be compared. A sulfur amount of 1.5phr corresponds to  $2.9 \times 10^{-4} \text{ mol.g}^{-1}$  whereas the sulfur contained in 4phr of TESPT is of  $1.8 \times 10^{-4} \text{ mol.g}^{-1}$ . In the hypothesis of a complete release of all their sulfur atoms by TESPT molecules, we could expect a strong increase in crosslink density compared to the non-sulfurous coupling agent NSC or to the covering agent OCTEO. As this is not observed, we may conclude that only a small fraction of the crosslink density is brought by an over-crosslinking due to TESPT.

Finally, the comparatively low crosslink density found for the Silica sample with no Silane agent is attributed to a stronger adsorption of CBS, since no Silane molecule covers the silica surface to prevent this phenomenon.

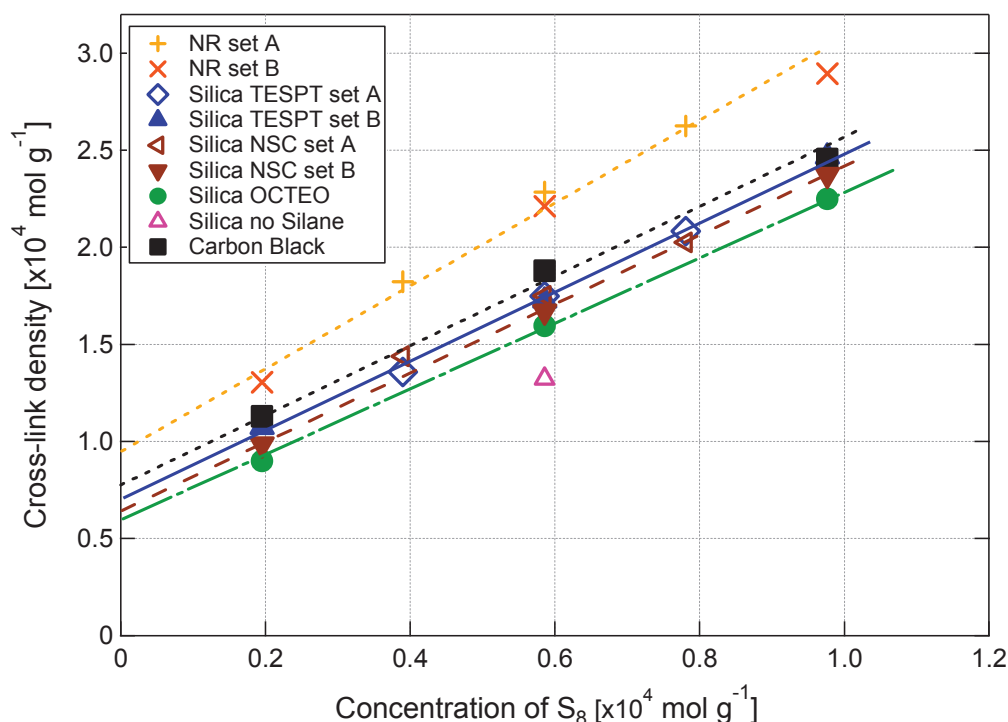


**Figure 168:** Crosslink density deduced from proton DQ-NMR experiments as a function of the sulfur amount for samples series 030-11 (filled set A), 046-11 (unfilled set A) and 119-11 (Set B). The sulfur/accelerator ratio is kept constant in all samples.

### VI.2.b. Equilibrium swelling experiments

The equilibrium degrees of swelling  $Q$  (mass of swollen material divided by unswollen rubber mass) are shown as a function of the sulfur content in Figure 169 for filled and unfilled NR

samples. A direct comparison of the degrees of swelling of the unfilled and filled samples is insufficient since the NMR results have shown that the crosslink densities are different for a given sulfur amount. The correlation of both measurements (VI.3) is thus necessary to check the effect of non-covalently coupled silica on equilibrium swelling. Nevertheless one can already observe that the solvent intake is reduced when using carbon black or Silica with a covalent coupling agent as expected from previous studies<sup>84</sup>.

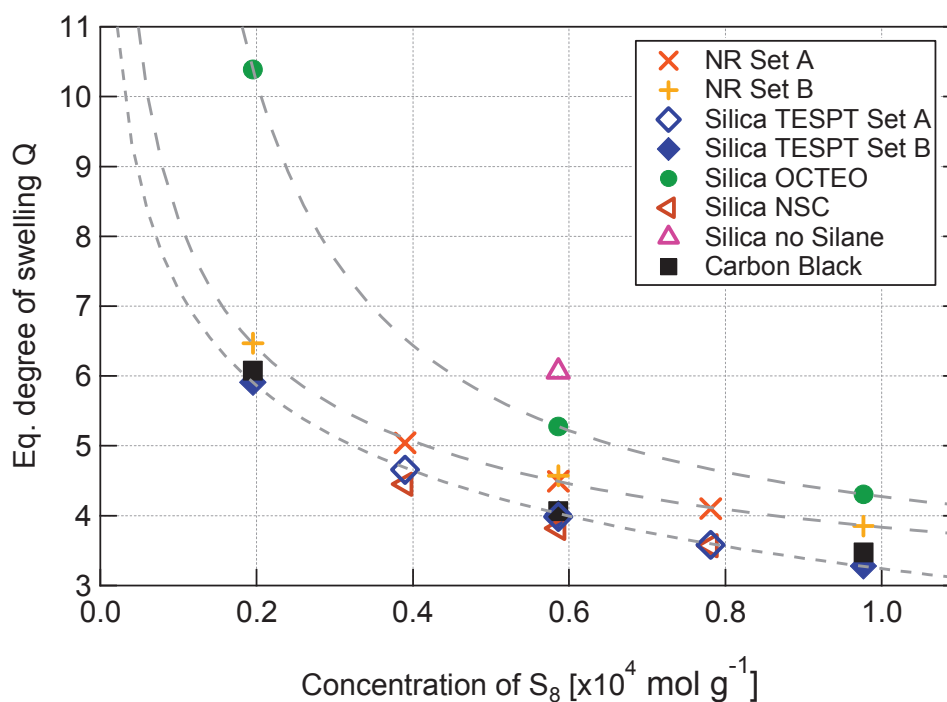


**Figure 169: Equilibrium degree of swelling (swollen rubber mass/initial mass) versus sulfur content for filled NR samples from series 030-11, 046-11 (set A) and 119-11 (set B). The curves are guides for the eyes.**

### VI.2.c. Modulus in the large strain regime.

In reinforced NR, the true stress-rubber strain curves were approximated by linear curves, which defines an effective modulus  $\tilde{E}$ . The linear approximation was carried out in the large strains regime before the stress upturn roughly defined by the inflexion point of the true stress versus rubber strain curve. Examples of linear approximation for Carbon Black-filled NR samples are given in Figure 170. An ‘apparent crosslink density’  $\nu_{mecha}$  is then defined from  $\tilde{E}$  by a relationship analogous to the one used to calculate the crosslink density from mechanical measurements in unfilled samples (equation (71)):

$$v_{mecha} = \frac{\bar{E}}{RT\rho_r\psi(\lambda^2 - \frac{1}{\lambda})}$$

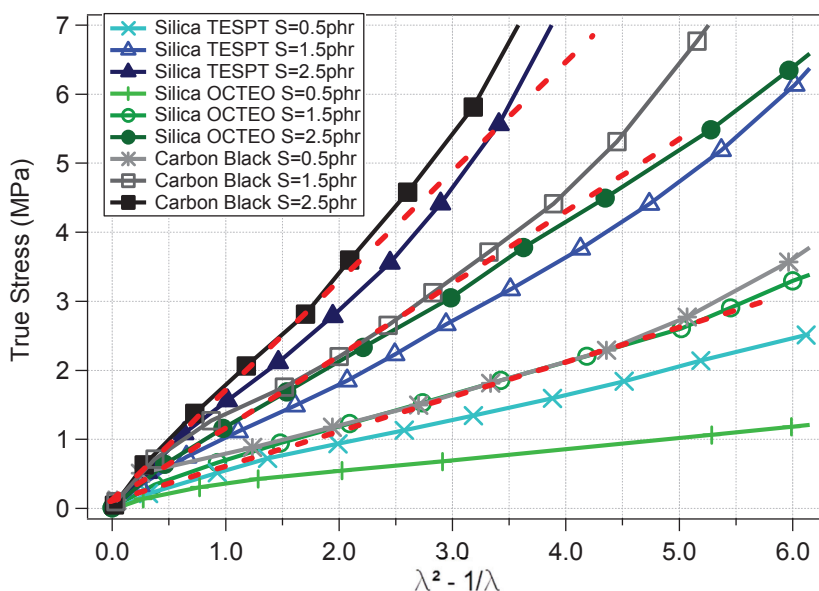


**Figure 170: Enlargement of true stress versus rubber strain curves for reinforced samples of series 119-11). Examples of linear fits are given for the 3 carbon black filled NR.**

*VI.2.d. Modulus in the small strain regime*

Figure 171 shows the modulus drop in the small strain regime (Payne effect) as measured by DMA experiments. The effect of crosslink density is shown here for both Silica-*TESPT*-filled and silica-*OCTEO*-filled NR, in comparison to unfilled NR.

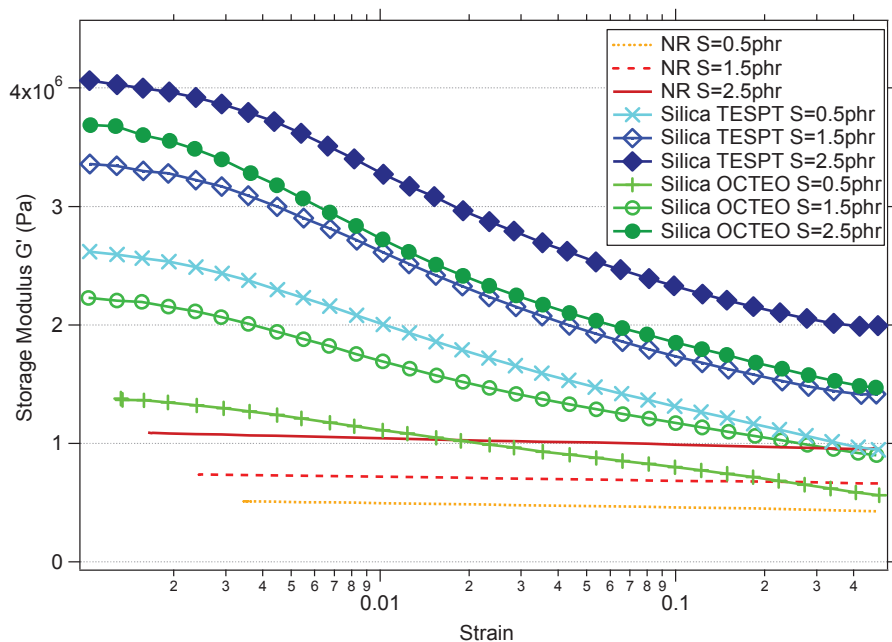


**Figure 171: Storage modulus as a function of strain from DMA experiments on unfilled and filled NR (sample series 119-11).**

From the maximum and minimum values measured in these strain sweep measurements, the moduli  $G'_0$  (at strain amplitude 0.001),  $G'_{50}$  (at strain amplitude 0.5) and modulus drop  $\Delta G' = G'_{50} - G'_0$  can be defined (see also chapter IV).

### VI.2.e. Amorphous chain orientation

#### VI.2.e.i. Amorphous chain orientation versus Strain.

The amorphous orientation parameter as a function of rubber strain is reported on Figure 172 for one unfilled rubber sample with a sulfur amount of 1 phr and for three NR reinforced with Carbon Black, Silica TESPT and Silica OCTEO, all at the standard sulfur level of 1.5 phr which was found to yield quite similar crosslink densities in NMR.

It is clear that, below the SIC onset, the amorphous orientation is amplified by the addition of fillers and that the interface is a key parameter. The covering agent OCTEO induces less local chain orientation than the coupling agent TESPT at a given macroscopic strain. The phenomenon of strain amplification may account for these differences: the more effective the stress transfers at the interface the higher the orientation of the elastomer chains. The Carbon black filled NR material shows an intermediate amorphous orientation parameter between TESPT and OCTEO.

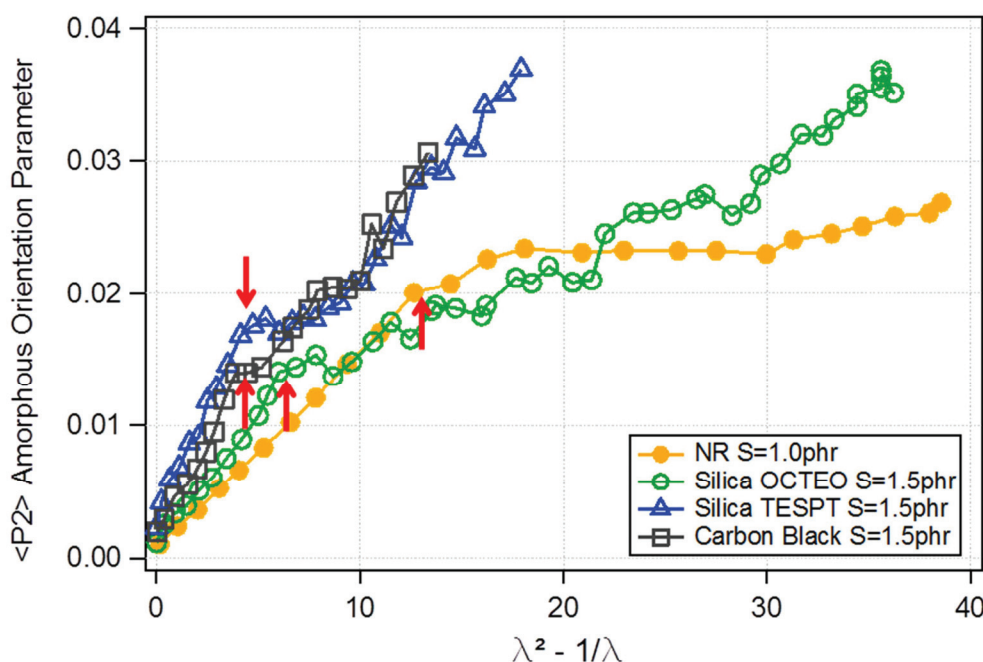


**Figure 172: Influence of the interface on the amorphous orientation parameter  $\langle P_2 \rangle$  as a function of rubber strain for unfilled (series 046-11) and filled samples at equivalent crosslink densities (sample series 119-11). The red arrows indicate the SIC onset (see chapter V).**

The other main feature is that the  $\langle P_2 \rangle$  evolution with rubber strain for filled NR is comparable to what has been described for pure NR (Figure 160). The main discrepancy being that the third regime at high extensions, in which the amorphous orientation parameter increases again, is far more pronounced in reinforced samples. Once the onset has been reached, a small plateau appears in the amorphous orientation parameter curves, corresponding to some relaxation of the amorphous part of the chains. However, this plateau is rather tiny for filled NR. In the third regime, the amorphous orientation increases with strain and the slope depends on the type of interface. This behaviour suggests an heterogeneity in the state of extension at the microscopic scale. Parts of the rubber may be submitted to a high local strain and may crystallize at a low macroscopic strain, whereas some parts may remain amorphous and continue to orient even above the overall SIC onset. Conversely, in an unfilled NR, the local strain is quite homogenous and in average equivalent to the macroscopic strain. Hence, once the SIC has been reached, a well-defined orientation plateau is reached.

Figure 173 shows a zoom on the first regime in which  $\langle P_2 \rangle$  depends linearly on the rubber strain. The results from three levels of crosslink densities are shown here for each interface agent and the curve of the unfilled NR samples with a sulphur amount of 1 phr is kept as reference. Although the number of recorded points before SIC onset is lower than for pure NR and the measurements are somehow less precise (due to adsorption of the incident X-ray beam by Silica), the slopes obtained in samples with TESPT and OCTEO are clearly different for a given sulphur content. This effect will be further discussed in the next section where the slopes of  $\langle P_2 \rangle$  as a function of “rubber strain” ( $\lambda^2 - 1/\lambda$ ) are plotted against the crosslink densities measured by NMR. It can be noted that the orientation in reinforced samples is generally slightly higher for

the very first values at low strains. This effect could be attributed to residual orientation after precycling in filled samples.

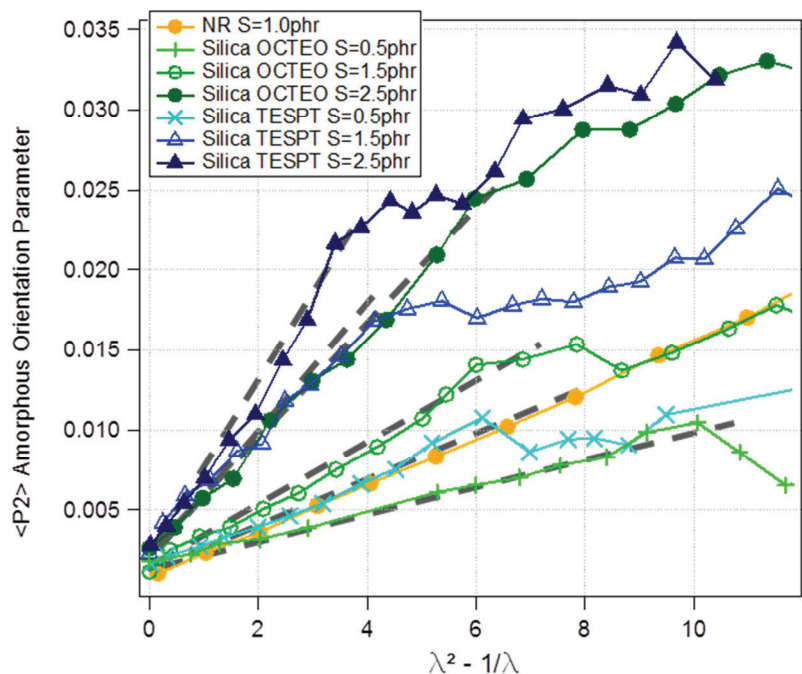


**Figure 173: Influence of the interface and crosslink density on the amorphous orientation parameter  $\langle P_2 \rangle$  as a function of rubber strain for unfilled (series 046-11) and filled samples with several sulfur amounts (sample series 119-11)**

#### VI.2.e.ii. Amorphous chain orientation versus true stress

The very good agreement between stress and amorphous phase orientation in unfilled NR samples has been highlighted in paragraph VI.1.e. Under a true stress of about 5MPa, the network behaves like predicted in the rubber elasticity theory. Above this threshold some deviation from the theory occurs but the correspondence between chains orientation and stress is still valid. In other words, whatever the crosslink density of the network, a given macroscopic stress corresponds to a given chain average orientation between crosslinks.

The variation of the amorphous orientation parameter as a function of true stress (Figure 174a) is very similar for silica-filled samples before the SIC onset. Conversely, in carbon black filled NR samples (Figure 174b), the slope  $\langle P_2 \rangle$  versus true stress in the linear regime decreases as the crosslink density increases and drops below the master curve obtained for unfilled NR samples and Silica-filled NR samples. The interpretation for this lower orientation and decrease of the slope with crosslink density is not clearly understood at the moment.

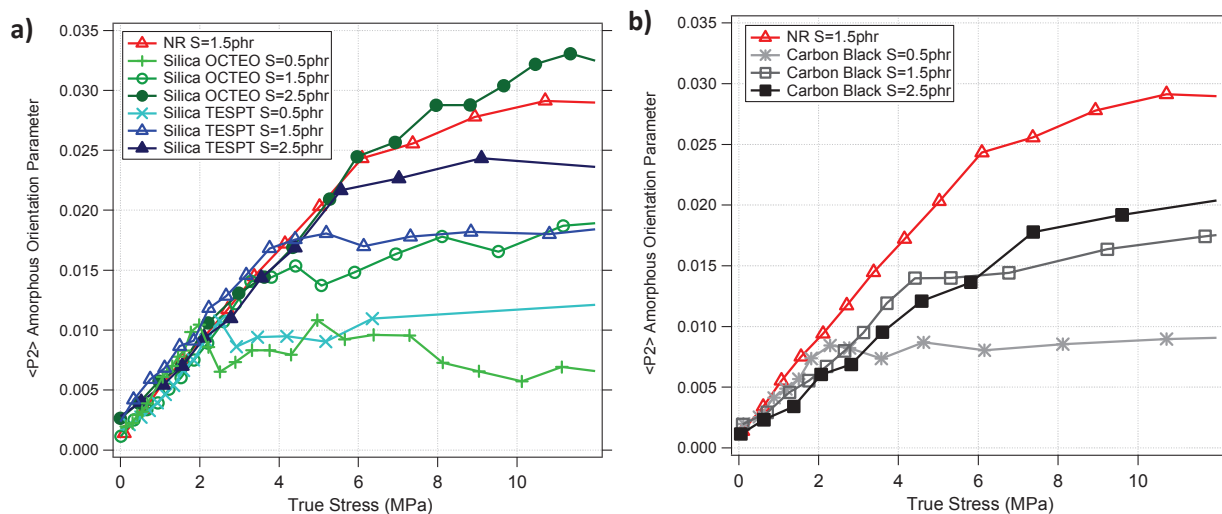


**Figure 174: Influence of a) Silica and interface agent and b) Carbon Black on the amorphous orientation parameter  $\langle P_2 \rangle$  as a function of true stress.**

After reaching the SIC onset, the orientation of the amorphous phase still increases in reinforced samples (as seen in Figure 172) with similar slopes in all samples, as shown in Figure 175. However, the curves are shifted upwards as the sulfur content increases (since orientation at SIC depends on the crosslink density of the matrix). It is also interesting to note that, for a given crosslink density, the orientations at break are of the same order whatever the interface type.

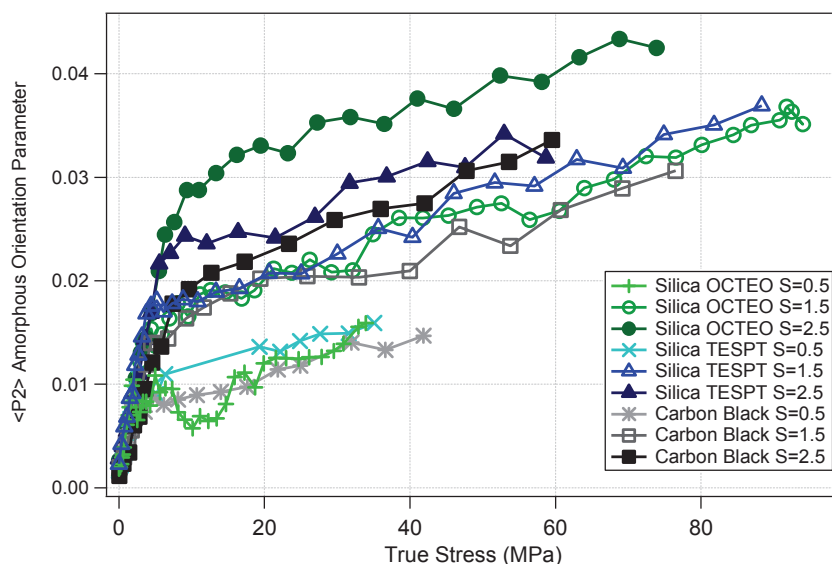


**Figure 175: Influence of interface type on the amorphous orientation parameter  $\langle P_2 \rangle$  as a function of true stress.**

VI.2.e.iii. Effect of precycling on the amorphous orientation

The effect of precycling at large strain amplitudes on the crystalline fraction has been described in chapter V. The lower SIC onset and crystallized fraction versus strain were interpreted as a modification of the local strain distribution, the head of the distribution being reduced by chain slippage and breakage in the highly strain amplified regions.

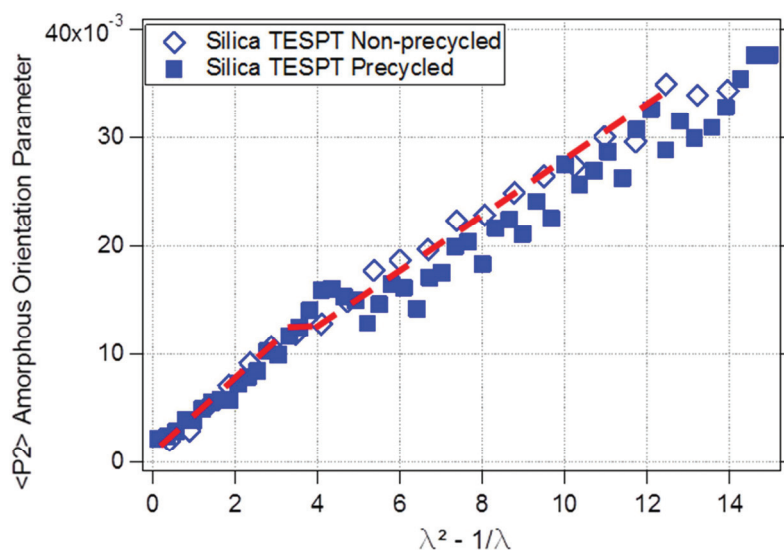


**Figure 176 : Influence of precycling on amorphous orientation parameter  $\langle P_2 \rangle$  (NR Silica TESPT sample of series 030-11). The red dashed line corresponds to the behavior of the non-precycled sample (empty diamonds).**

As regards the orientation of the amorphous phase, a small modification of the  $\langle P_2 \rangle$  parameter is recorded when using an as-prepared (non-precycled) sample (Figure 176). The orientation plateau occurs at lower strain and is less pronounced, which indicates a lower relaxation of amorphous chains, in agreement with the lower slope of the crystallized fraction vs strain. Once both samples have started to crystallize, the overall orientation of the amorphous phase is slightly higher in the case of the non-precycled samples, which confirms the presumed higher average strain amplification in as-prepared samples.

### VI.3. Correlations between the various measurements

We shall analyze the correlations between the results of NMR, amorphous phase orientation and equilibrium swelling measurements (which are all related to the crosslink density) and mechanical measurements. This is done first in the large strain regime, then the modulus in the linear regime is also correlated to the crosslink density measured by NMR and to the amorphous orientation parameter. In this way, we will see that specific reinforcement mechanisms in the linear regime can be distinguished from reinforcement at high strain amplitude.

### VI.3.a. Correlations between large amplitude mechanical behaviour, amorphous orientation, swelling and NMR measurements

First the amorphous phase orientation measured by in-situ X-ray diffraction, described by the apparent (not quantitative) crosslink density  $Kv_\chi$ , and the apparent crosslink density  $v_{mecha}$  are correlated to the crosslink density obtained by NMR. For each type of samples,  $Kv_\chi$  approximately varies linearly with the crosslink density  $v_{NMR}$  (Figure 177). The shift towards higher orientations as compared to unfilled NR corresponds to the local strain amplification.

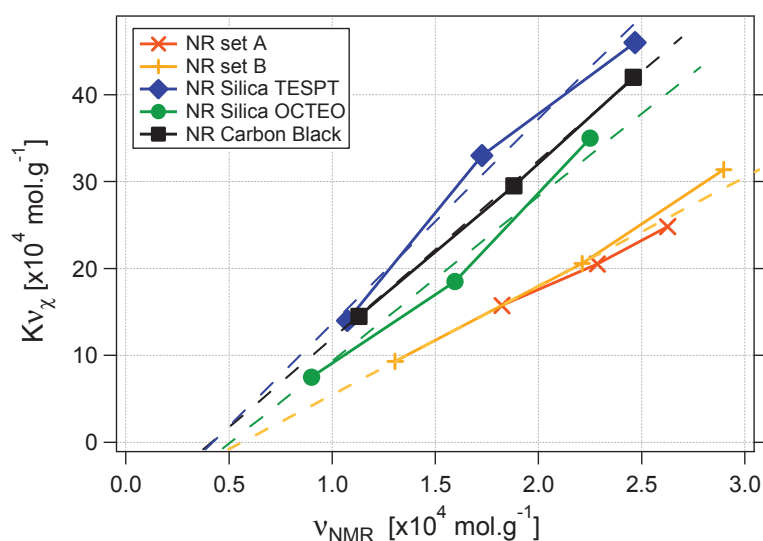


**Figure 177 : ‘apparent crosslink density’  $Kv_\chi$  (measured from amorphous phase orientation) versus crosslink density  $v_{NMR}$  (measured from NMR) for unfilled and filled NR samples from series 046-11 (Set A) and 119-11 (Set B).**

A similar correlation is obtained for the apparent crosslink density  $v_{mecha}$  deduced from traction curves and the crosslink density  $v_{NMR}$  (Figure 178). In both Figures Figure 177 and Figure 178, Carbon Black-filled NR and Silica-TESPT-filled NR show a larger strain amplification than Silica-OCTEO-filled NR. All correlation lines cross the bottom axis at roughly the same point. The corresponding value has been attributed to a higher entanglement contribution in NMR measurements, which have a shorter characteristic time scale.

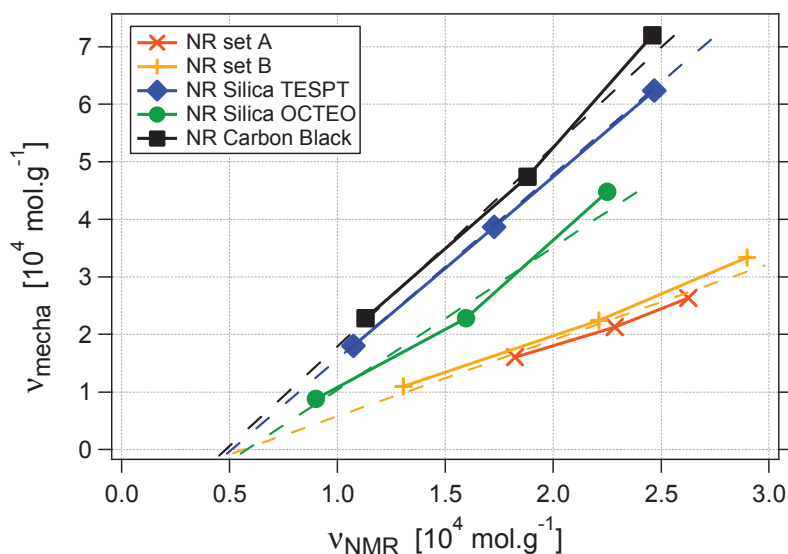


**Figure 178 :** ‘apparent crosslink density’  $v_{mecha}$  (measured from true stress) versus crosslink density  $v_{NMR}$  for unfilled and filled NR from series 046-11 (Set A) and 119-11 (Set B).

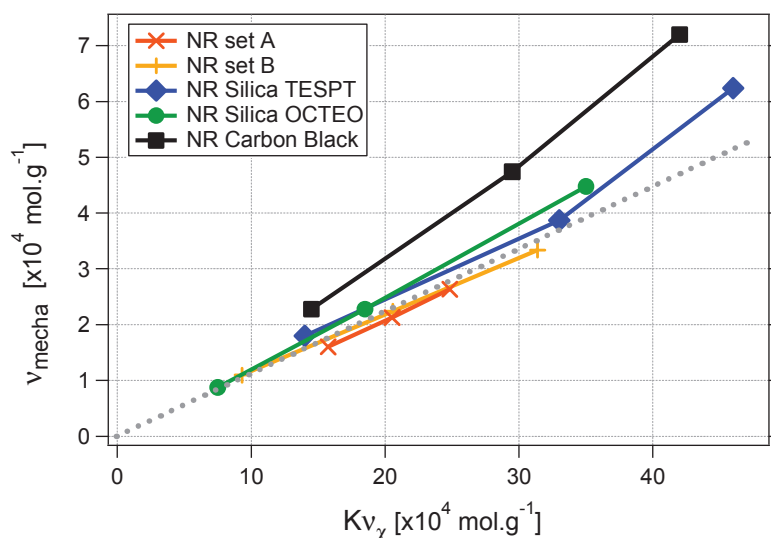


**Figure 179:** ‘apparent crosslink density’  $v_{mecha}$  (measured from true stress) versus ‘apparent crosslink density’  $Kv_{\chi}$  (measured from amorphous phase orientation) for unfilled and filled NR from series 046-11 (Set A) and 119-11 (Set B).

The differences of strain amplification recorded by the two techniques can be pointed out by directly comparing  $v_{mecha}$  and  $Kv_{\chi}$  (Figure 179).

This representation emphasizes the relatively good concordance of the ‘average local strain’ measurements. However, a deviation is obtained for carbon black samples, with a comparatively higher stress at a given segmental orientation.

The correlation between the apparent crosslink density obtained from equilibrium swelling  $v_{sw}$  and NMR measurements is shown in Figure 180 for unfilled and filled NR. As described earlier for the unfilled NR samples, the obtained line for the filled samples crosses the x axis at a non-zero value, reflecting the effect of entanglements and other topological constraints that are removed during the swelling process.

The apparent crosslink densities  $v_{sw}$  for samples with Carbon Black and Silica TESPT were calculated thanks to equation (55) (see chapter II) assuming that no debonding occurs at the interface. All reinforced samples show a more or less pronounced deviation from the unfilled sample line due to the impact of the fillers on swelling: the higher the restriction of solvent intake, the higher the slope of the corresponding line.

One may conclude that the interface restriction is of the same order for those two reinforcing systems with a more important effect for the covalently coupled Silica. In the case of Silica without covalent bonds (Silica OCTEO), we first applied the equation (55) as well, assuming no debonding at the interface (represented by filled symbols).

In this case almost no deviation from the unfilled NR curve is found, meaning that the matrix is allowed to swell freely and that almost no restrictions stem from the high filler content.

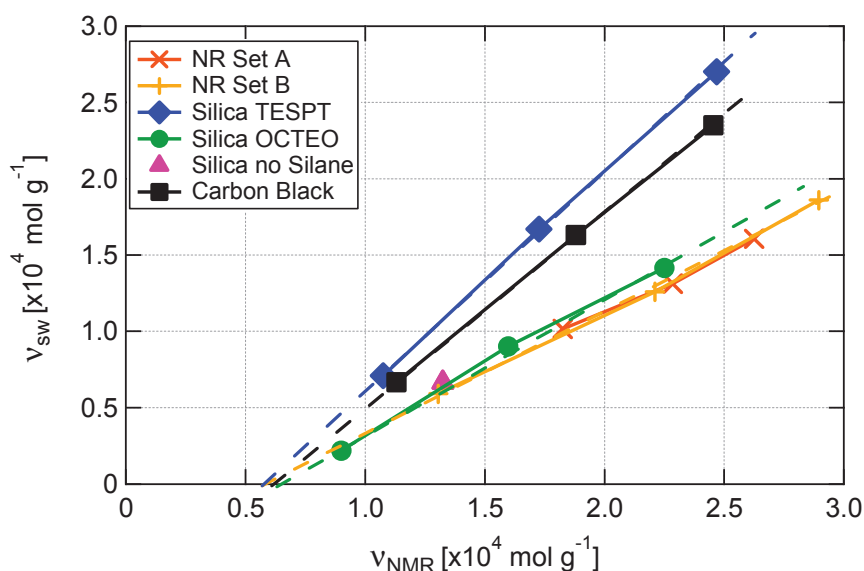


**Figure 180: ‘apparent crosslink density’  $v_{sw}$  (measured by equilibrium swelling) versus crosslink density  $v_{NMR}$  (measured from NMR) for unfilled NR and filled NR (sample series 030-11, 046-11 and 119-11).**

The second case considered (empty symbols in Figure 181) taking into account the vacuoles correction (equation (59) (see chapter II)) leads to an important deviation from the unfilled NR curve. It can be seen as a system where vacuoles form at the interface but the matrix solvent intake is limited by long chains wrapped and entangled around fillers. It can also be presumed that the swelling behavior is modified in presence of silica aggregates even without active bonding to the rubber chains due to filler volume effect.

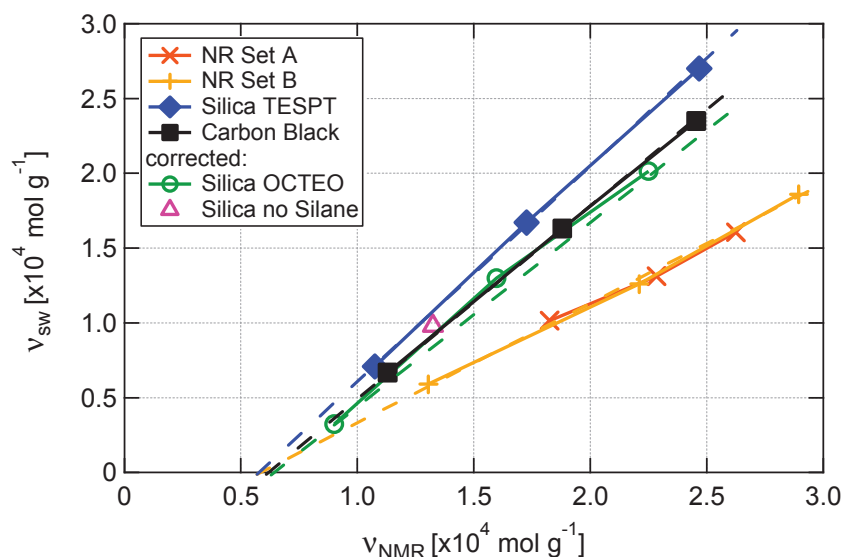


**Figure 181 :** ‘apparent crosslink density’  $v_{sw}$  (measured by equilibrium swelling versus crosslink density  $v_{NMR}$  (measured from NMR) for unfilled NR and filled NR (sample series 030-11, 046-11 and 119-11) with the vacuoles correction for Silica-OCTEO and Silica-no Silane samples.

Finally we propose that the restrictions of swelling in the presence of fillers provide also a direct measurement of local strain amplification, explaining the similarity of the correlations with the other measurements presented in the previous paragraph. Here the local chain stretching is imposed by thermodynamic equilibrium (through the Flory-Rehner theory, see chapter II.1.d) and the resulting macroscopic strain (related to volume increase by solvent intake) is measured.

Note that the phantom model has been chosen for the calculation of the crosslink density from equilibrium swelling, whereas for other experiments (NMR, mechanics and amorphous orientation) the affine model was assumed. This may modify all the graphs (by changing the slopes) but not the conclusions on strain amplification. Indeed, the strain amplification is always deduced from the comparison of filled and unfilled NR responses, thus the relative increase of apparent crosslink density would be identical if the affine model had been used for swelling as well.

### VI.3.a.i. Case of the NSC coupling agent

As regards the NR-Silica samples with NSC as the coupling agent, not all the measurements were performed. In particular the X-ray diffraction experiments were not carried out for the series 119-11 but the swelling behavior of series 030-11 has been analyzed (Figure 182). It is observed that the strain amplification is slightly higher in the case of silica-NSC filled samples compared to silica-TESPT.

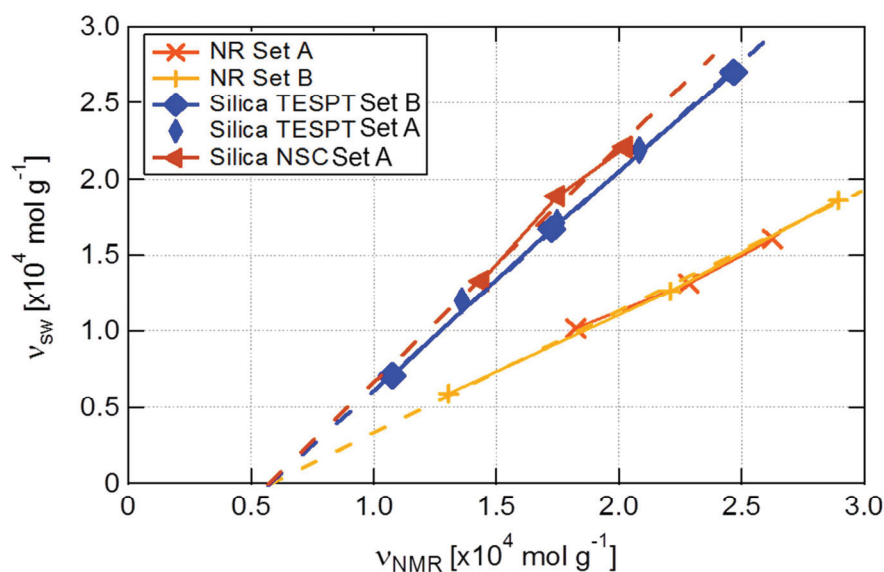


**Figure 182 :** ‘apparent crosslink density’  $v_{sw}$  (measured by equilibrium swelling versus crosslink density  $v_{NMR}$  (measured from NMR) for unfilled NR (series 046-11 (set A) and 119-11(set B)) and filled NR sample (series 030-11 (set A) and 119-11 (set B)).

### VI.3.b. Mechanical Reinforcement in the linear regime

We have seen that in the large strain regime (up to SIC onset), stress measurements are in good agreement with the average local deformation deduced from segmental orientation measurements, provided that strain amplification in filled samples is taken into account. It is now interesting to compare the modulus measured in small strain regimes with the same average local deformation and with the crosslink density. The moduli  $G'_0$ ,  $G'_{50}$  and modulus drop  $\Delta G'$  plotted in this section correspond to the maximum and minimum values measured in strain sweep measurements of the Payne effect (see chapter IV).

Firstly the relationship between the shear modulus at 50% strain and the crosslink density is discussed (Figure 183). The higher slope of the modulus versus crosslink density for reinforced samples highlights the strain amplification described in the previous paragraphs, with a similar classification of interface types. Nevertheless the reinforced samples were not submitted to any precycling before the Payne effect characterization which results in higher modulus compared to the precycled samples investigated in in-situ experiments. Accordingly the amplification factors (ratio of the slope in reinforced NR to that of unfilled NR in Figure 183) are higher in this case.

The behavior of the modulus  $G'_0$  in the linear regime does not follow the same behavior. This is a key result of this analysis. It indicates that the modulus  $G'_0$  does not only depend on the crosslink density, especially for strongly reinforced samples such as Carbon Black-filled and Silica-TESPT-filled samples. A second, non-rubbery contribution has to be taken into account. The relative contribution can be given by the y-intercept in the modulus versus crosslinks plot (see Figure 183).

This result is in contradiction with the Payne effect models based only on filler/rubber interactions (see chapter II). Several interpretations indeed relate the Payne effect to adsorption/desorption mechanisms in which the magnitude of the reinforcement is proportional to the number of anchored chains at the interface. In this picture, the modulus should be proportional to the crosslink density since the rubber phase bears the entire load through stress transfer at the interface.

It is also interesting to note that the Silica-OCTEO and Silica-NSC-filled samples have quite a different behavior much closer to a high strain amplification scheme (or to a scheme based on filler/rubber interactions).

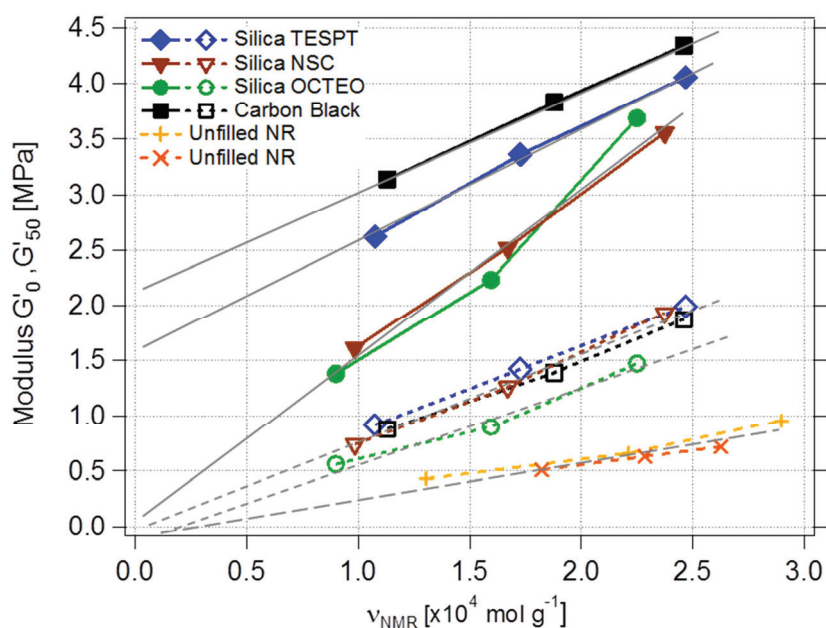


**Figure 183: Shear Modulus for strains of 0.1% ( $G'_{0}$ ) and 50% ( $G'_{50}$ ) versus crosslink density  $\nu_{\text{NMR}}$  for unfilled NR (series 046-11 and 119-11) and filled NR samples (series 119-11).**

In Figure 184, the shear modulus  $G'_{0}$  and  $G'_{50}$  are correlated to the apparent crosslink density  $K\nu_{\chi}$  measured by X-ray scattering. The main difference from Figure 183 is that  $K\nu_{\chi}$  is related to the average local state of chain extension. Thus, this parameter incorporates the local strain amplification at large strains described earlier. This explains why the  $G'_{50}$  values fall on a common curve for reinforced samples. This common line should in fact also be close to the unfilled NR  $G'_{50}$  data line as it was the case in Figure 179 but the different mechanical history may explain the discrepancy here. The shear modulus is indeed measured on as-prepared samples whereas the amorphous orientation parameter was measured by X-ray scattering on pre-stretched samples. Despite this restriction, we suggest that most of the strain amplification involved in the large strain regime is taken into account in the apparent crosslink density  $K\nu_{\chi}$ . The difference between the continuous lines ( $G'_{0}$ ) and dashed lines ( $G'_{50}$ ) in Figure 184 would thus combine the rubbery and non-rubbery part of the modulus increase at very low strain.

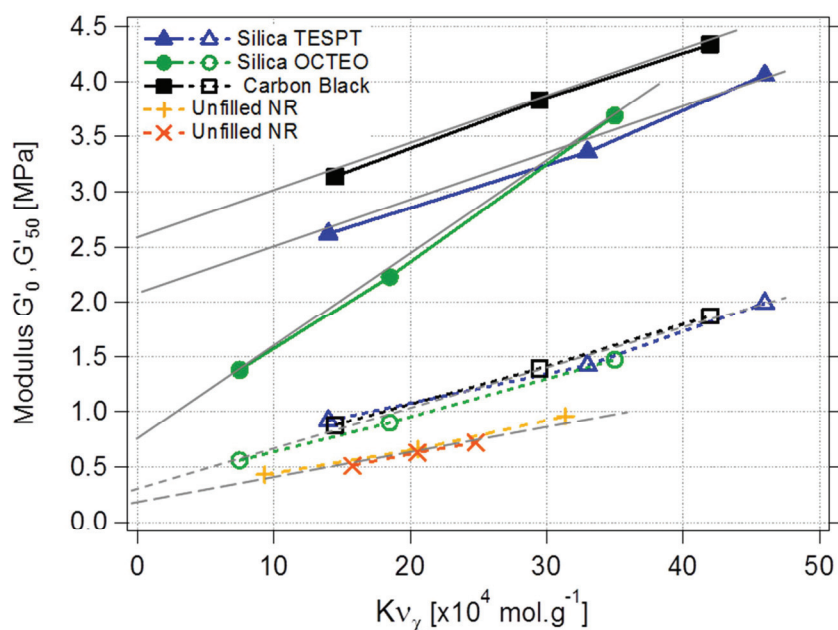


**Figure 184 : Shear Modulus for strains of 0.1% ( $G'_0$ ) and 50% ( $G'_{50}$ ) versus ‘apparent crosslink density’  $Kv_{\chi}$  (measured from amorphous phase orientation) for unfilled NR (series 046-11 and 119-11) and filled NR samples (series 119-11).**

The modulus drop ( $\Delta G' = G'_0 - G'_{50}$ ) is reported as a function of crosslink density determined by NMR (Figure 185a) and apparent crosslink density  $Kv_{\chi}$  (Figure 185b). As discussed above, the strain amplification phenomenon at large strain is at the origin of the discrepancy between the two graphs.

The highest contribution of the non-rubbery phase to the modulus is found for the carbon black-filled samples. Silica-TESPT-filled samples follow a similar behavior but this contribution is lower. This result tends to support the idea that the lower Payne effect for Silica reinforced NR compared to Carbon Black reinforced NR comes from a lower contribution of glassy bridges. Either a better distribution of silica aggregates or a lower interface strength could account for this results.

However, for Silica-OCTEO and Silica-NSC NR samples the modulus drop  $\Delta G'$  depends significantly on the crosslink density and the contribution that is not related to crosslink density is lower or close to zero. In chapter IV, we proposed that the lower Payne effect for Silica-NSC NR samples could be attributed to an improved distribution of fillers. In the scheme of interpretation of the glassy layers, this could account for the quite lower contribution of the non-rubbery phase to the Payne effect at the tested temperature (60°C). Regarding the Silica-OCTEO-filled samples, the lower contribution of a non-rubbery phase would rather be due to the weak interactions between the filler and the rubber chains leading to a low contribution of glassy bridges.

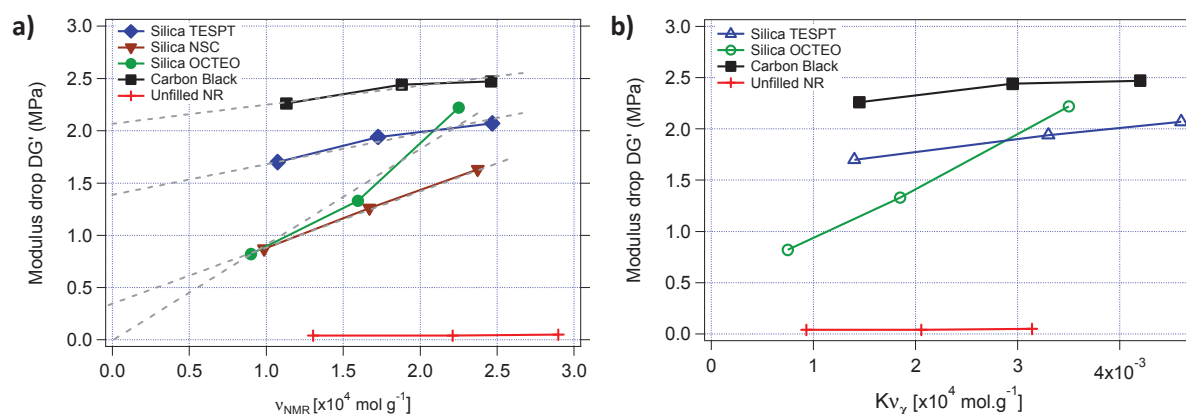


**Figure 185: Modulus drop ( $\Delta G' = G'_0 - G'_{50}$ ) in the Payne effect regime as a function of a) crosslink density  $\nu_{\text{NMR}}$  and b) versus 'apparent crosslink density'  $K\nu_\chi$  (measured from amorphous phase orientation) for unfilled and filled NR samples of series 119-11.**

### VI.3.c. Strain Amplification discussion

#### VI.3.c.i. Distribution of local strains

It is of interest to remind here the results obtained by Dupres et al<sup>72</sup> who have compared mechanical measurements, Deuterium NMR experiments to investigate chains orientation and SIC onset measurements by X-ray diffraction on unfilled and Carbon black filled Polyisoprene with various grades of Carbon black.

Among the differences between our study and the work of Dupres, one should note that we used precycled samples and we have shown that the Mullins effect is associated with an overall reorganization and homogenization of filled rubber structure that involve shortest chains breakage and slippage and filler reorganization. Secondly the way we measured chain orientation is less probe-dependent as the dynamics of the dodecane molecule may be affected by the presence of fillers and lead to underestimated values of chain orientation.

Their results have shown a fairly good agreement between mechanical and SIC onset measurements whereas NMR splitting which characterize chain orientation gives lower amplification factor than the two other measurements. These differences are expected to come from a broad distribution of local strain, the deuterium NMR probes the entire network (and so does our amorphous orientation parameter extracted from X-ray scattering) whereas the stress and crystallization onset may only account for a highly stretched portion of the polymer. It indicates that the higher the discrepancy between measurements and the higher the heterogeneity of strain amplification. Their comparison of two carbon black grades having equivalent specific surfaces but different structures has shown that the heterogeneity increases with the structuration of the filler. This increased heterogeneity of the local strain distribution can be understood in terms of a higher occluded rubber fraction for a filler with a higher structure.

The equilibrium swelling behaviour should probe the local chain response of the complete rubber network even if we may imagine that highly crosslinked regions might not be swollen, nevertheless such sulfur bridges clusters have not been reported in our sample in particular by DQ-NMR which is an efficient tool to analyse the heterogeneity of crosslinks.

Figure 186 illustrates this hypothesis that each technique is sensitive to a certain portion of the local strain distribution function. Dupres et al. have proposed that the overall average local strain was probed by the orientation of chains measured by deuterium NMR (corresponding to amorphous orientation before the SIC onset in our experiments). They have also attributed the crystallization onset to the upper part of the distribution (highly strain amplified zones). We adopt an identical scheme and propose that the equilibrium swelling is also sensitive to the entire local strain distribution. The relevant range of the strain distribution for stress measurement was also added. Considering that part of the rubber chains are not submitted to a high strain amplification and elastically inactive, we propose that the stress mainly depends on the regions that are highly stretched chains, the concerned range being nevertheless larger than for the SIC onset since only a weak number of chains are concerned by the beginning of the crystallization process (typically 1% that is roughly the detection limit of crystallized content in our measurements).

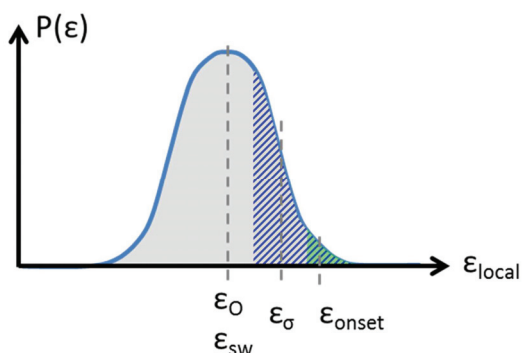


**Figure 186 : Schematic representation of the supposed local strain ranges probed by: the equilibrium swelling and amorphous phase orientation (all the strain distribution of average probed strain  $\epsilon_{sw}$  and  $\epsilon_0$ ), true stress (blue hatched area of average probed strain  $\epsilon_\sigma$ ) and onset of SIC (green area of average probed strain  $\epsilon_{onset}$ ).**

This approach of different relevant ranges of local strain for each measurement can be used to account for the differences highlighted in VI.3.a.

Strain amplification factors have thus been determined as the ratio of the reinforced NR response versus pure NR response. The amplification factors  $A_{sw}$ ,  $A_0$  and  $A_\sigma$  are computed as the ratio of the reinforced NR samples slopes versus pure NR slopes in the plots of  $v_{sw}$  versus  $v_{NMR}$ ,  $Kv_\chi$  versus  $v_{NMR}$  and  $v_{mecha}$  versus  $v_{NMR}$  (respectively in Figure 181 or Figure 182, Figure 177 and Figure 178). In the case of equilibrium swelling for Silica OCTEO both non-corrected and vacuoles corrected data are presented.

The amplification factor  $A_{onset}$  is obtained as the ratio of the crystallization strain onset for an unfilled natural rubber and a filled NR of equivalent crosslink density according to NMR measurements. Conversely to the three other amplification factors defined above, the crystallization onset amplification factor slightly depends on crosslink density since the strain onset was found to slightly depend on the crosslink density in certain ranges but this would not change the relative position of the interface types in terms of amplification.

In the case of a very homogenous network only a slight discrepancy would be found for the amplification factors  $A_{sw}$  and  $A_O$  on the one hand and  $A_\sigma$  and  $A_{onset}$  on the other hand. On the opposite a sample with a strong strain distribution would show strong differences between the different amplification factors.

The strain amplification factors evaluated from the four independent measurements (equilibrium swelling, orientation of amorphous, stress and crystallization strain onset) are reported in Figure 187. In the adopted interpretation scheme, our measurements indicate that Silica-OCTEO NR samples have a more homogeneous strain distribution than Silica-TESPT NR samples. The distribution of local strains appears even more heterogeneous for Carbon black NR samples.

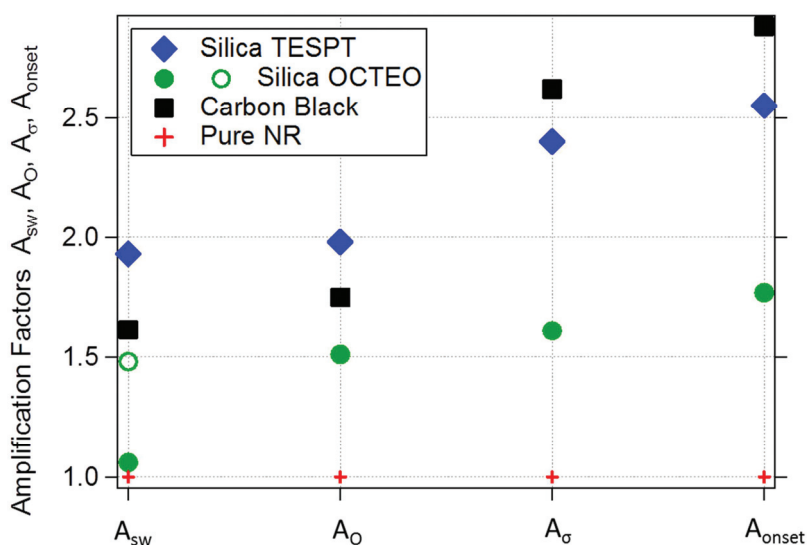


**Figure 187 : Amplification factor calculated from the measurements of swelling ( $A_{sw}$ ), amorphous phase orientation ( $A_O$ ), stress ( $A_\sigma$ ) and SIC onset ( $A_{onset}$ )**

In order to go further in the description of our reinforced NR materials, we propose to represent the distribution of local strains in unfilled and filled NR samples for several macroscopic strains. These schematic plots are presented in the following paragraphs and summarize qualitatively some results of the strain induced crystallization study (slope and onset of the crystalline content with strain) presented in chapter V and the results of the correlation of techniques (equilibrium swelling, true stress and amorphous orientation measurements) presented in the present chapter.

### VI.3.c.ii. Effect of fillers

The SIC strain onset for a perfect network is assumed to be 400% of strain. The kinetics effects on strain-induced crystallization are considered as negligible in these quasi-static experiments therefore once some fraction of the rubber chains reach the SIC onset the crystallization begins. The higher the fraction of rubber extended above the onset and the higher the crystalline content.

- In the case of the pure Natural rubber, the distribution of local strain is quite homogeneously spread around the macroscopic strain. A small broadening of the distribution of local strains with the macroscopic strain is assumed here. For macroscopic strains between 300 and 400%, some crystallites begin to form since the extremity of the distribution reaches the local crystallization strain onset of 400%.

- In a reinforced NR, the local state of extension is expected to be far more heterogeneous and on average higher than in the unfilled counterpart. At a macroscopic strain of the order of 100%, the highest strain amplified regions are close to the SIC onset (400% of local strain). It is also believed that a large part of the rubber chains stay in a weakly deformed state even under the application of large macroscopic strains broadening the distribution of local strains. The lower slope of crystallized fraction versus strain is understood as the effect of the wide distribution of local strains even if some restrictions on the crystallites formation may also be invoked here.

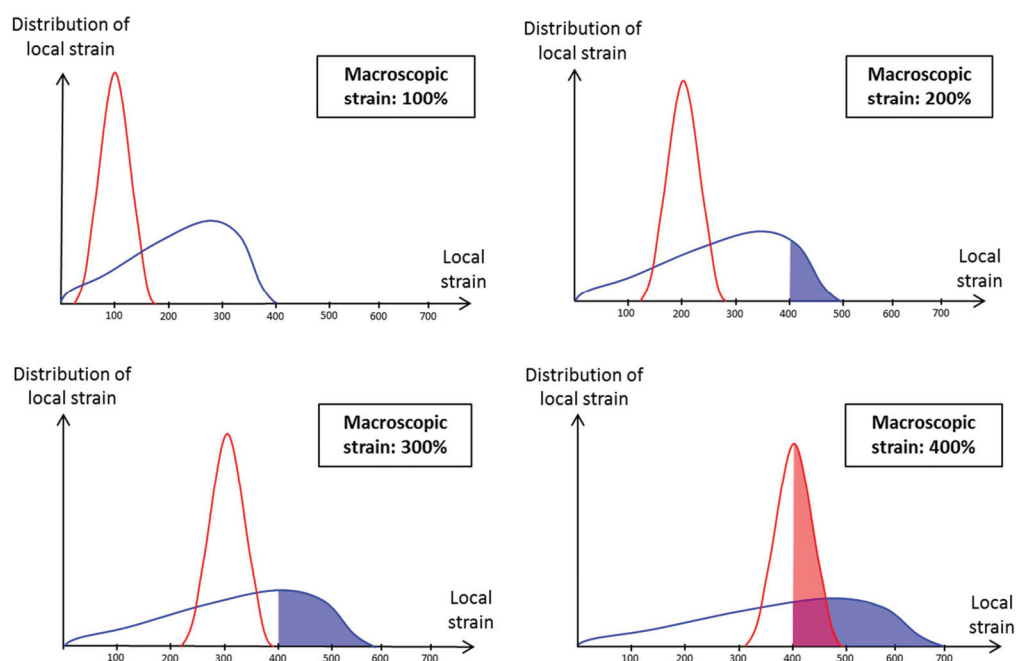


**Figure 188: Schematic distribution of local strain at fixed values of the imposed macroscopic strain (100%, 200%, 300% and 400%) for unfilled NR (red) and reinforced NR (blue). The hatched area under the curves for local strains higher than 400% represents the rubber fraction that may crystallize.**

### VI.3.c.iii. Effect of precycling on reinforced samples

The influence of precycling at high deformation has been discussed in terms of crystalline content in chapter V and amorphous orientation parameter in VI.2.e.iii. Applying high strain levels to filled NR leads to an increase of both the SIC strain onset and the slope of crystalline fraction versus strain. This behavior can be explained by a narrower distribution of local strain due to the breakage and slippage of the shortest chains (or part of chains) that reach their maximum extensibility during the precycling phase.

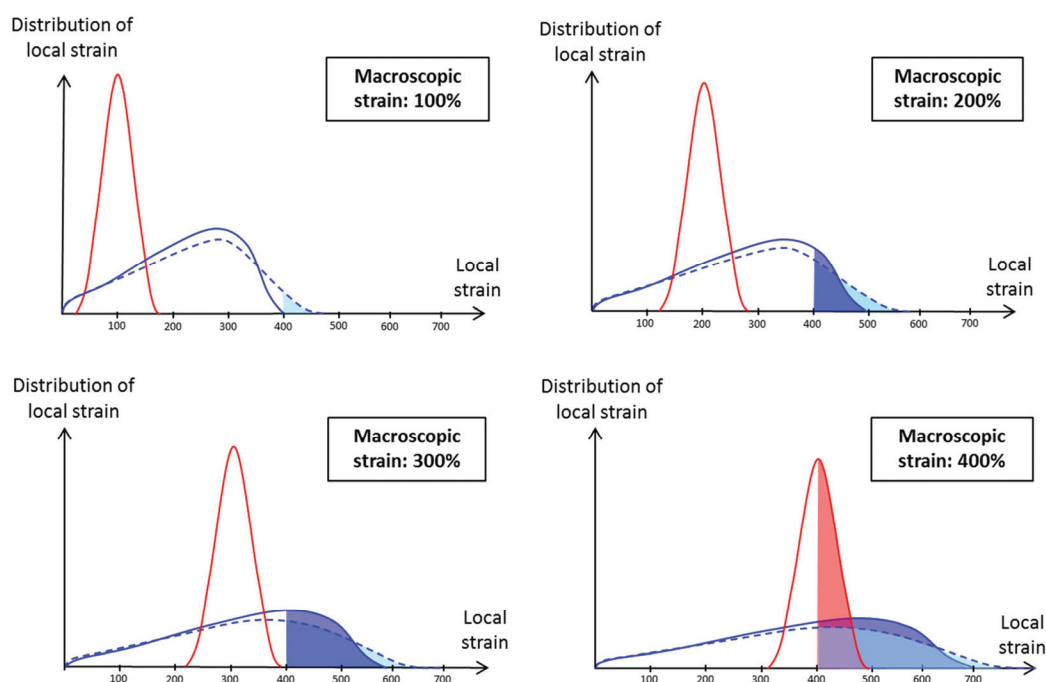


**Figure 189 : Schematic distribution of local strain at fixed values of the imposed macroscopic strain (100%, 200%, 300% and 400%) for unfilled NR (red), filled NR (blue continuous line) and filled NR without precycling (blue dashed line). The hatched area under the curves for local strains higher than 400% represents the rubber fraction that may crystallize.**

Medalia<sup>39</sup> has reported that the electrical conductivity increases after applying cycles of large amplitude to rubber carbon black composites suggesting a reorganization of the fillers under the effect of strain. The local strain distribution modification could thus result of the reorganization of fillers themselves, the particles being more homogeneously distributed after applying the strain.

#### VI.3.c.iv. Effect of the interface type

As regards the comparison of Silica TESPT and Carbon black, our results indicate that the amplification factor is on average lower for Carbon Black but the distribution is broader since the SIC strain onset is lower and the stress higher. The strain distribution of Carbon black was thus represented with a higher fraction of weakly strained regions (similar to the so-called occluded rubber) compared to Silica TESPT (Figure 190).

The amplification factors obtained for the Silica OCTEO system stress out lower average strain amplification and maximum strain amplification levels. The distribution is in consequence narrower for Silica-OCTEO. The fact that the crystallized fraction of an unfilled NR eventually becomes larger than for a Silica OCTEO filled NR can be explained by the poorly stretched regions remaining in the case of the filled compound whereas the average local strain in unfilled rubber is expected to increase quite linearly with the macroscopic strain in our representation. As a result, the amount of rubber chains stretched above the local SIC onset in the case of the

unfilled rubber becomes larger than in the Silica OCTEO sample at a macroscopic strain of approximately 400%.

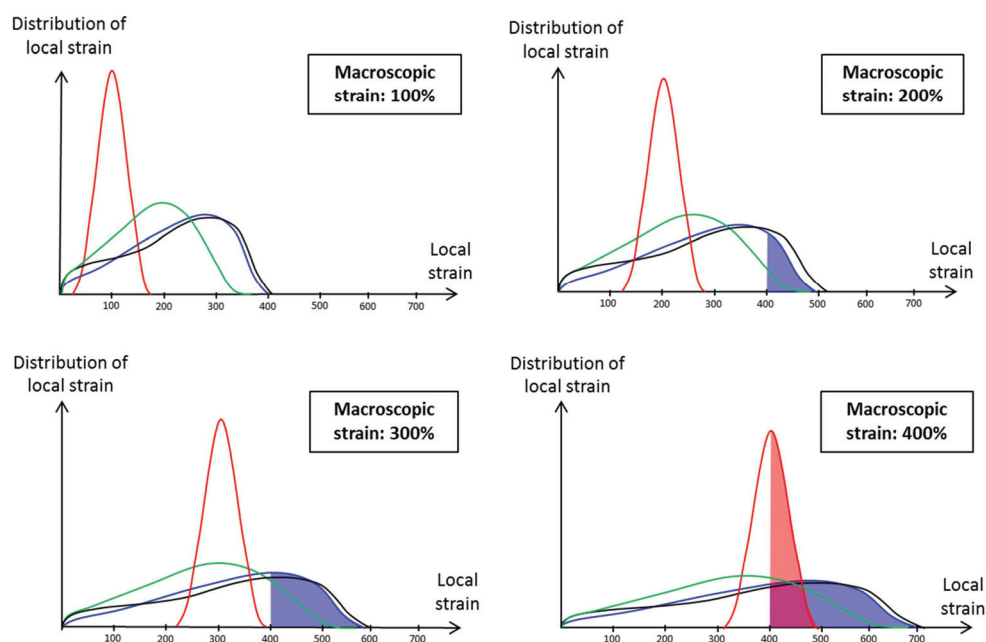


**Figure 190: Schematic distribution of local strain at fixed values of the imposed macroscopic strain (100%, 200%, 300% and 400%) for unfilled NR (red), NR Silica TESPT (blue), NR Silica OCTEO (green) and NR Carbon Black (black). The hatched area under the curves for local strains higher than 400% represents the rubber fraction that may crystallize.**

As regards the Silica NSC system, the higher amplification factor than Silica TESPT can be deduced from Figure 182 meaning that on average the strain amplification imposed to the chains is higher than TESPT. On the other hand the mechanical measurements would lead to equivalent strain amplification factor as the very close stress-strain behavior suggests it (see chapter IV). Those results might indicate that the local strain distribution is slightly more homogeneous for a NSC system compared to TESPT but further measurements in particular amorphous orientation measurements would be necessary to confirm this trend.

## VI.4. Conclusion

This chapter proposes a combination of various techniques to investigate the local chains stretching modification by the addition of fillers in order to evidence the reinforcement mechanisms in our Natural Rubber samples.

Equilibrium solvent intake, Elongation modulus, amorphous orientation parameter were reported to the crosslink density measured in the unstrained state by DQ-NMR in order to highlight strain amplification effects and SIC onset was also considered in this respect. The influence of the

coupling agent for silica could be highlighted and local strain distribution scenarios were proposed showing the highly heterogeneous strain distribution in the case of carbon black.

Finally we suggested that the reinforcement in the small strain regime results from the combination of a strain amplification contribution and a contribution that does not depend on the crosslink density of the rubber matrix. We understand this second term as the modulus increase brought by low mobility polymer layers that overlap creating a strong filler-polymer-filler network.

This non-rubbery contribution was rather important for NR samples filled with carbon black, and for NR Silica TESPT system whereas the Silica coupled with the non-sulfurized agent (NSC) exhibits a weaker non-rubbery reinforcement effect that could be attributed to a better distribution of silica aggregates (chapter IV). The lower contribution of a non-rubbery phase for Silica-OCTEO NR samples would rather be due to weak filler-polymer interactions.

---

## VII. Dissipation at large strain and Ultimate properties

VII.1.	Dissipation at high strain.....	204
VII.1.a.	Mullins effect .....	204
VII.1.b.	Dissipation on « stabilized » samples .....	206
VII.1.c.	Dissipation on « non-stabilized » samples.....	209
VII.1.d.	Relationship between dissipation and tangent modulus.....	211
VII.2.	Cavitation.....	213
VII.2.a.	Introduction.....	213
VII.2.b.	Measurements principle.....	213
VII.2.a.	Effect of fillers and interface on cavities formation.....	215
VII.3.	Microscopic observations.....	217
VII.4.	Resistance to failure for un-notched sample.....	218
VII.5.	Conclusions.....	220

This chapter is dedicated to the properties of reinforced NR at high strains. The description of the stress-strain curves for as prepared samples has been given in chapter IV. In this chapter the dissipation properties measured during mechanical cycles and cavitation that may occur at high strains are presented.

The relative dissipation is measured as the hysteresis energy versus the brought energy during the traction phase. It has been measured first on the first mechanical cycle and then as a function of strain by two different methods.

In-situ tensile measurements of X-ray absorption and thickness reduction were used to estimate the decrease of the absorption coefficient of rubber samples during stretching, which may be interpreted as the formation of cavities in the material at large strain.

The ultimate properties obtained for unfilled and filled NR with different interface types and several crosslink densities are also reported at the end of this chapter. These measurements were performed by Benoit Moreaux (Rhodia Silica).

## VII.1. Dissipation at high strain

In the following we shall distinguish the dissipation measured during the first mechanical cycle, which corresponds to the Mullins effect, and the dissipation measured after previous cycling. Two methods were used to measure the dissipation properties as a function of strain after previous cycling. In the first method, the samples have been precycled up to large strain amplitude (“stabilized” samples) whereas in the second the samples (“non-stabilized” samples) have only been submitted to strain up to the maximum strain applied for measuring the hysteresis (see chapter III).

### VII.1.a. Mullins effect

When submitted to a series of extension cycles of high strain amplitude, reinforced elastomers exhibit a stress-softening effect known as Mullins effect. This effect is particularly pronounced after the first extension cycle: the stress is much reduced during the second cycle compared to the response of the as-prepared sample (Figure 191).

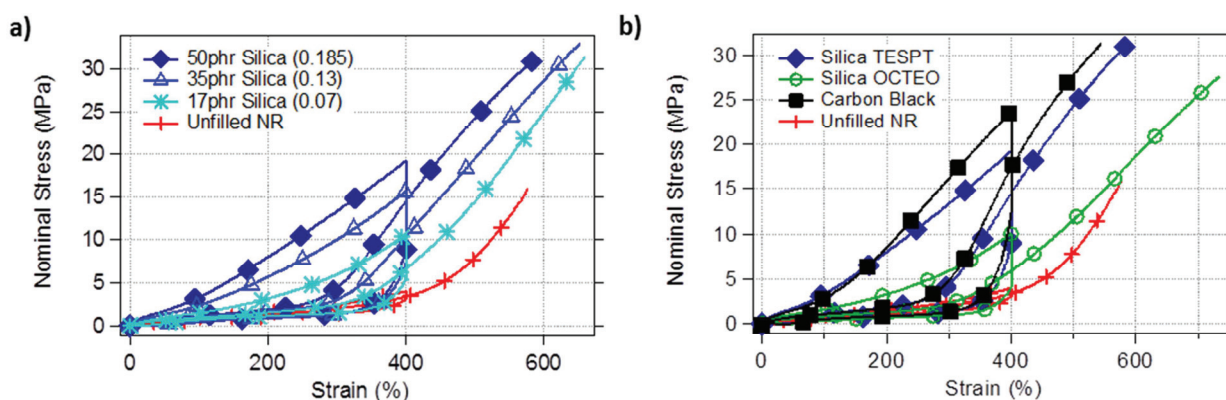


**Figure 191: Stress softening after one extension cycle of maximum strain 400% a) influence of the Silica volume fraction and b) influence of the interface type (sample series 115-10).**

The stress-softening effect then decreases as the number of cycles increases and it is generally admitted that no additional softening is observed after five cycles. In our case, we have considered that no important softening was observed further than three cycles.

The amplitude of stress softening depends on the filler amount and the interface type as shown in Figure 191. It can be noticed that the dissipation on the first cycle rises with the stress at the maximum cycling strain.

In order to quantify the stress softening which occurs during the 1<sup>st</sup> cycle, the relative dissipated energy was calculated as the ratio of the dissipated energy (area between the traction and retraction curves) to the energy input to the sample during traction (area under the traction curve). The obtained relative dissipated energies are reported as a function of the filler volume fraction in Figure 192, for several NR samples filled with Silica or Carbon Black. The effects of the filler fraction and interface type on the stress softening during the 1<sup>st</sup> cycle may be discriminated in this graph. Indeed, the data show that the relative dissipated energy increases with the filler fraction but does not seem to depend on the filler/ rubber interactions.

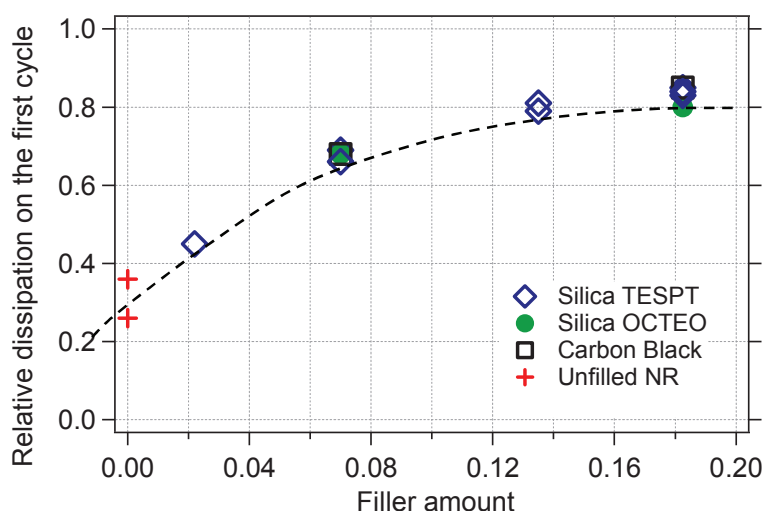


**Figure 192: Relative dissipated energy during the first cycle versus the filler volume fraction. (sample series 115-10 and older series from Gabrielle<sup>74</sup>). The curve is a guide for the eyes.**

It is also important to stress out that a weak stress softening effect can be observed in unfilled rubber matrices at large enough strain values as shown in Figure 193. This observation can be made for maximum strain values lower than the strain-induced crystallization onset, ruling out here a contribution of SIC to the stress softening effect in this regime.

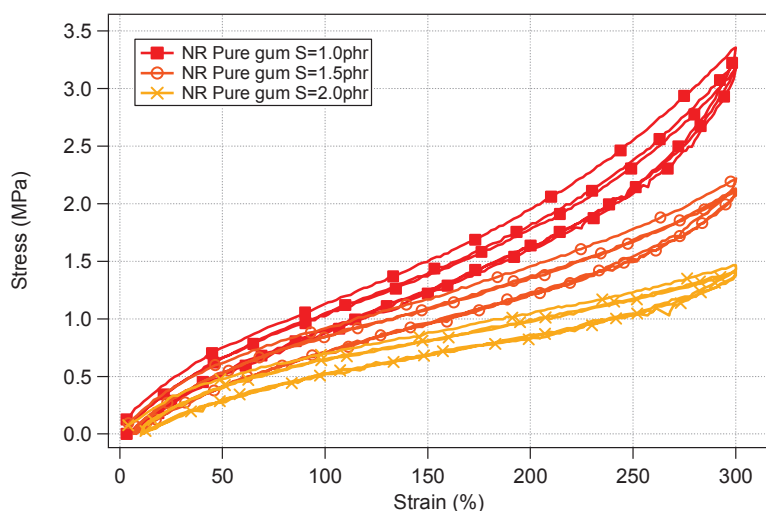


**Figure 193: Slight stress-softening effect for unfilled NR (series 046-11) submitted to large strain (below the SIC onset however).**

#### Discussion:

The observed hysteresis at high strain or dissipated energy is believed to result from numerous phenomena from chains friction, cavitation, strain-induced crystallites formation and melting, chains adsorption and desorption on the filler surface, reorganizations in the matrix involving chains slippage and breakage, yielding/reformation of glassy bridges.

The silica surface treatments induce different local strain amplification and as a consequence different stresses and hysteresis energies during the first cycle. Nevertheless for a given brought mechanical energy, the dissipation is equivalent showing that the stress softening processes are of similar amplitude whatever the interface. This would indicate that the Mullins effect is mainly due to reorganizations occurring in the matrix as chains slippage and breakage in high amplification zones between fillers<sup>68,76</sup> and not at the interface itself.

The slight stress-softening effect observed in unfilled NR shows that some reorganization also occurs in the unfilled material during the first traction.

#### *VII.1.b. Dissipation on « stabilized » samples*

Strain-induced crystallization (SIC) which occurs in Natural Rubber induces dissipation in the material during oscillating deformation as in the case of fatigue solicitations. This effect on the dissipation properties can be evidenced with simple traction-retraction cycles below and above the SIC onset, as shown in Figure 194.

In order to illustrate this effect, it is interesting to plot the relative dissipation during the cycle, which corresponds to the hysteresis (cycle) area divided by the mechanical energy input (area below the traction curve).

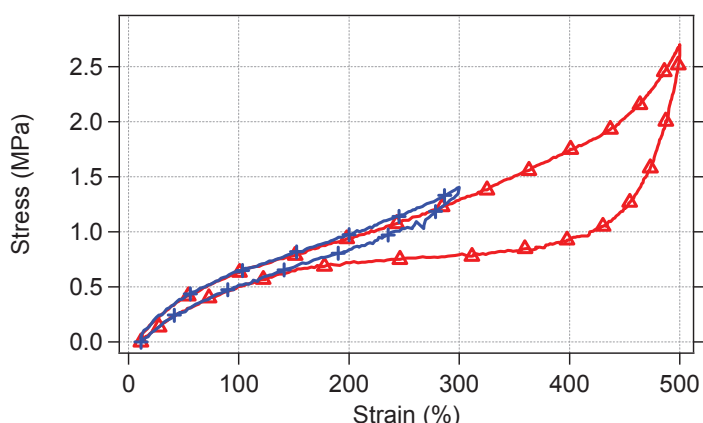


Figure 194 : Hysteresis increase above SIC onset for unfilled NR (series 046-11).

A study of the dissipation properties over a wide range of maximum cycle strains was performed by B. Gabrielle in his thesis<sup>74</sup>. He has shown that in a non-crystallizing rubber like SBR, the relative dissipation decreases with increasing maximum strain (Figure 195). In the case of Natural Rubber, the same behavior is observed up to the SIC crystallization onset, above which the relative dissipation increases. This effect is due to the hysteresis in the crystallization and melting processes: on the traction phase, a large over-stretching is required to form the crystallites (because crystallization has a relatively low kinetics), crystallites then melt at a lower strain during the retraction phase, leading to a lower modulus during retraction compared to stretching<sup>71,108</sup>.

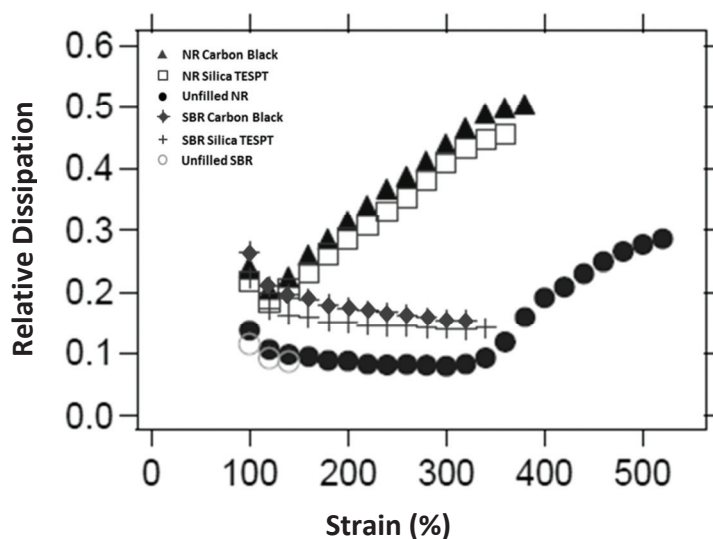
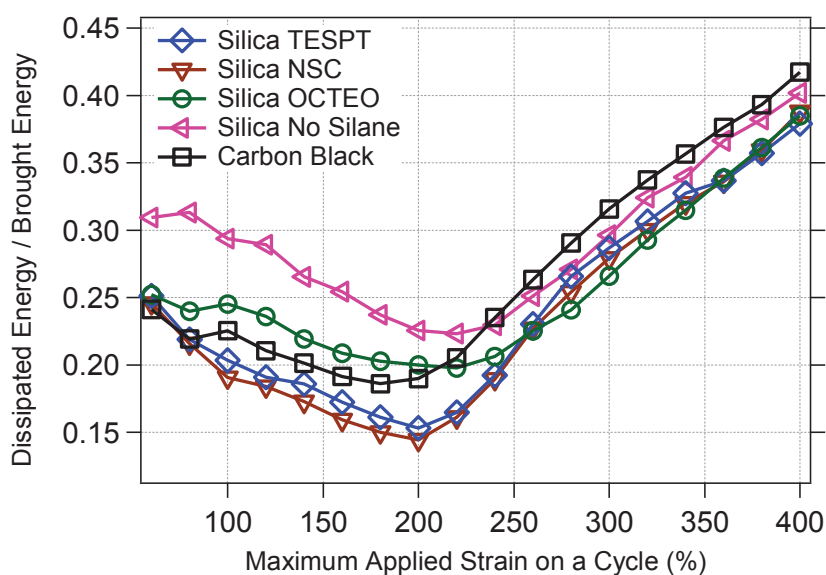


Figure 195 : Comparison of relative dissipation versus strain for both unfilled and filled SBR and NR from Gabrielle<sup>74</sup>. The length of the samples after 3 cycles was taken as the reference for calculation of the strain.

In a similar approach, the dissipation properties have been studied on stabilized samples by means of mechanical cycling tests carried out straight after 3 stabilization cycles. In Gabrielle's experiments the length after precycling was taken as zero strain whereas in our procedure the plotted deformation is computed from the sample's initial length explaining why the dissipation minimum is shifted from roughly 100 to 200%.

Figure 196 represents the dissipated energy for several systems changing the interface type, the dissipation differences are sharp before the dissipation minimum: it is first noticed that the non-treated silica induces a high level of relative dissipation maybe due to numerous weak interactions at stake here. On the opposite the samples with Silica and a coupling agent (NSC and TESPT) show the lowest dissipation values, OCTEO and Carbon Black displaying an intermediate behavior.



**Figure 196: Relative dissipated energy during cycles of increasing amplitude on stabilized samples from series 095-10 and 030-11. Crosshead speed of 100mm/min ( $\dot{\lambda}=2 \times 10^{-2} \text{ s}^{-1}$ ).**

The data from Figure 196 were normalized to a common relative dissipation of 0.15 at the strain level for which the dissipation minimum was observed (Figure 197). This minimum position can be associated to the SIC strain onset and the slope of relative dissipation versus strain gives indications on the crystallization behavior.

As regards the dissipation inflexion, it suggests that Carbon black undergoes crystallization at the lowest strain around 180%, followed by Silica-TESPT and Silica-NSC at 200% and Silica samples with no covalent coupling beginning crystallizing at larger strain (i.e. 220%). These results prove to compare fairly well to the X-ray diffraction results presented in chapter V.

The slope of the relative dissipation as a function of strain is lower for Silica samples with no coupling agent up to a strain of 300%. Then the slopes are very similar for all samples.

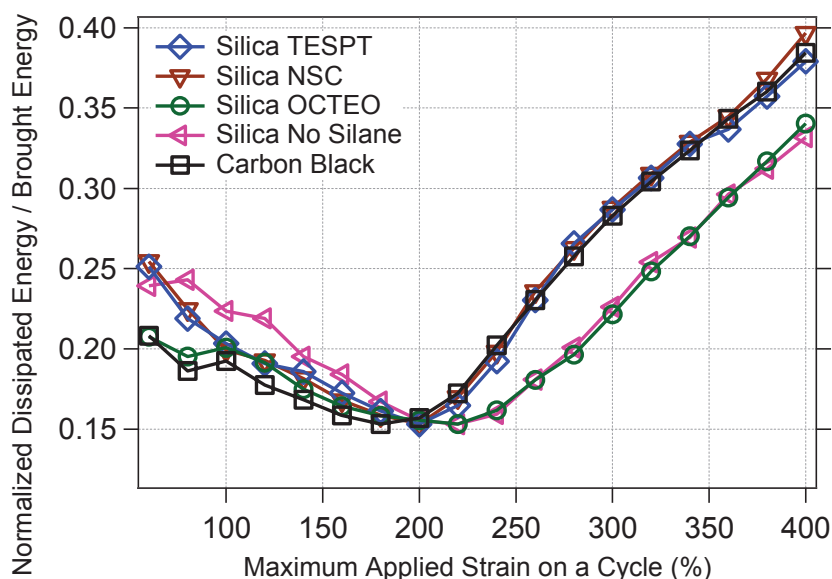


**Figure 197: Normalization of the relative dissipated energy at a common minimum representing SIC onset. Samples from series 095-10 and 030-11. Crosshead speed of 100mm/min ( $\dot{\lambda}=2 \times 10^{-2} \text{ s}^{-1}$ ).**

### VII.1.c. Dissipation on « non-stabilized » samples

Some formulations were tested according to a slightly different procedure that consisted into directly apply the cycles of increasing amplitude but in order to remove the Mullins effect at the considered strain, three cycles were performed at each maximum strain level. The third one was considered as stabilized in terms of Mullins effect but conversely to the previous dissipation procedure the sample had not been previously stretched at very large amplitude. In other words, the main difference between the two tests is the maximum deformation submitted to the sample.

The relative dissipated energy for the two coupling agents (TESPT and NSC) and the non-treated silica is reported in Figure 198a. The relative dissipation strongly increases at strains of 100% for the coupled Silica NR material and 150% for the non-treated Silica NR material. This significant increase can be attributed to the SIC phenomenon. The lower dissipation increase onset compared to stabilized samples is due to the fact that no high strain cycles have been applied here and consequently there is almost no permanent set at these levels of maximum strain.

The slope of the relative dissipation versus strain is also in agreement with the stabilized samples method results: the Silica treated with a covalent coupling agent induces a higher dissipation increase as a function of strain compared to the non-treated Silica. In addition, the onset of the relative dissipation increase is shifted towards higher strains for the non-treated silica (Figure 198b).

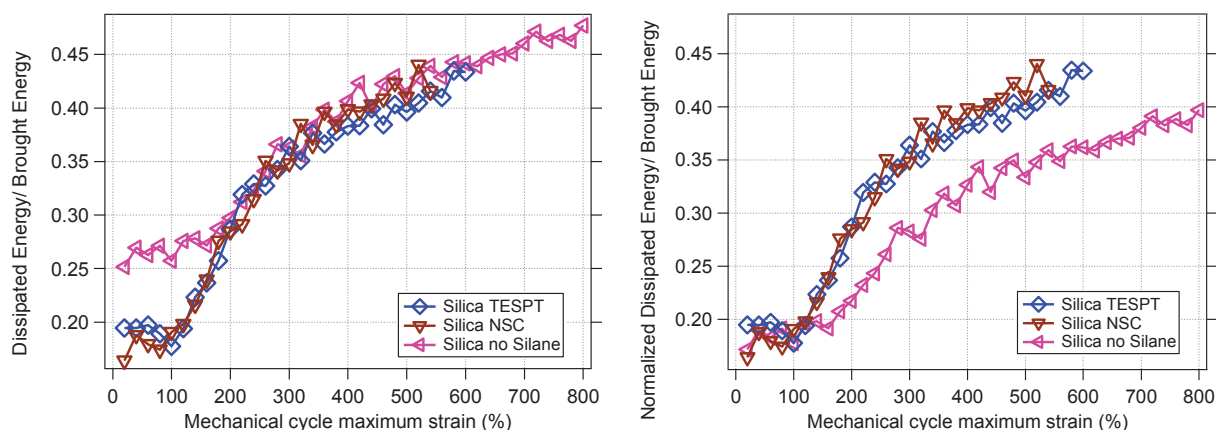


**Figure 198: a) Relative dissipated energy and b) Normalized Relative Dissipated energy during cycles of increasing amplitude for non-stabilized samples from series 030-11. Crosshead speed of 100mm/min ( $\dot{\lambda}=2 \times 10^{-2} \text{ s}^{-1}$ ).**

The discrepancy between the two dissipation methods is shown in Figure 199: the curves of relative dissipation versus strain obtained with both methods are plotted for NR Silica-TESPT. The strain is calculated with the initial sample length for the stabilized sample method but once the sample has been cycled three times at 400% a residual strain of around 40% is detected when unloading the sample to zero stress. In order to compare the relative dissipation of this sample precycled at 400% to the relative dissipation without previous precycling (non-stabilized samples), a strain correction taking into account the permanent set was used and yields the corrected strains curve presented in Figure 199 (dashed line). The corrected maximum strains applied on a cycle are thus computed from the length after precycling which is why they are lower.

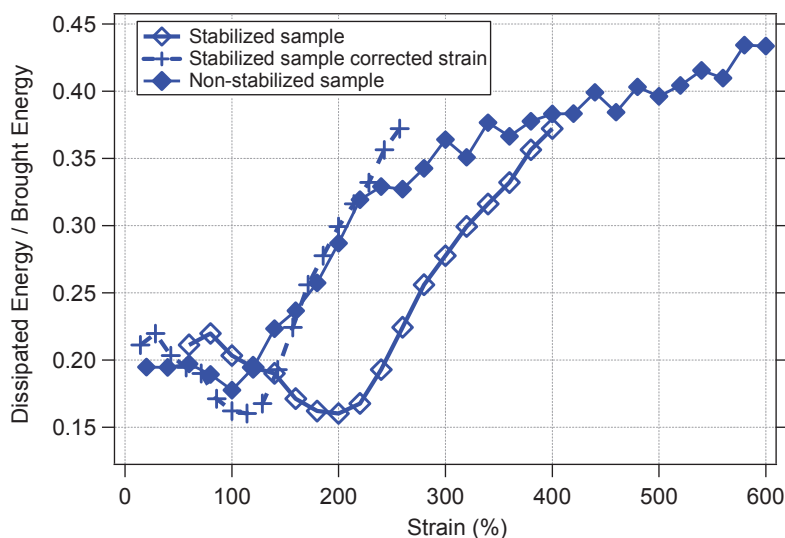


**Figure 199 : Comparison of the two relative dissipation results i.e. on stabilized (precycled up to 400%) and non-stabilized samples (series 030-11). The corrected stabilized sample strain was obtained after taking into account the permanent strain due to the high strain cycles.**

Thanks to this correction, the discrepancy between the two methods appears more clearly. This can be attributed to the modification of the composite behavior by stretching it to a very large extent with the stabilized samples method. This result is in full agreement with strain-induced crystallization measurements for precycled and as-prepared samples described in chapter V. It confirms that the SIC phenomenon occurs at lower strain for the non-stabilized samples sample since the heterogeneity in local strain is broader.

The non-stabilized samples method also allows us to compare the residual strain as a function of the applied maximum strain on a cycle for the different coupling agents (see Figure 200). The non-treated Silica sample shows a higher permanent set than the covalently coupled Silica samples that can be interpreted as the effect of rubber chains slippage at the interface. The Silica TESPT sample reaches higher residual strain levels than Silica NSC for large strains cycles (above 300%) which could also be understood as higher number of failures of the interface bonds.

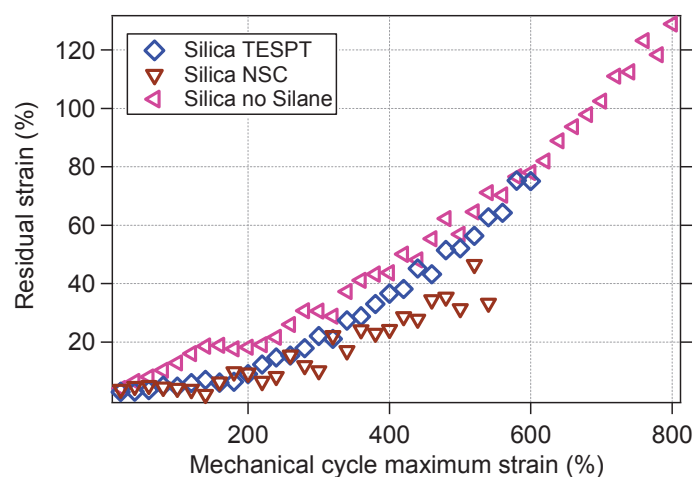


**Figure 200 : Permanent set or residual strain increase with maximum strain applied on a cycle for the samples of series 030-11 tested with the non-stabilized samples method.**

#### *VII.1.d. Relationship between dissipation and tangent modulus*

The tangent modulus (presented in chapter IV) and dissipation on as-prepared samples are compared for Silica-TESPT and non-treated Silica NR materials in Figure 201. The similarity of the dissipation and tangent modulus curves for a given system suggests that the same mechanisms are at the origin of both properties. In the strain range from 100 to 200%, the modulus increase and strong dissipation increase for Silica TESPT can be attributed to the beginning of the crystallites formation. Above 300%, the relative dissipation increases more slowly maybe due to a lower dissipating effect of newly created crystallites.

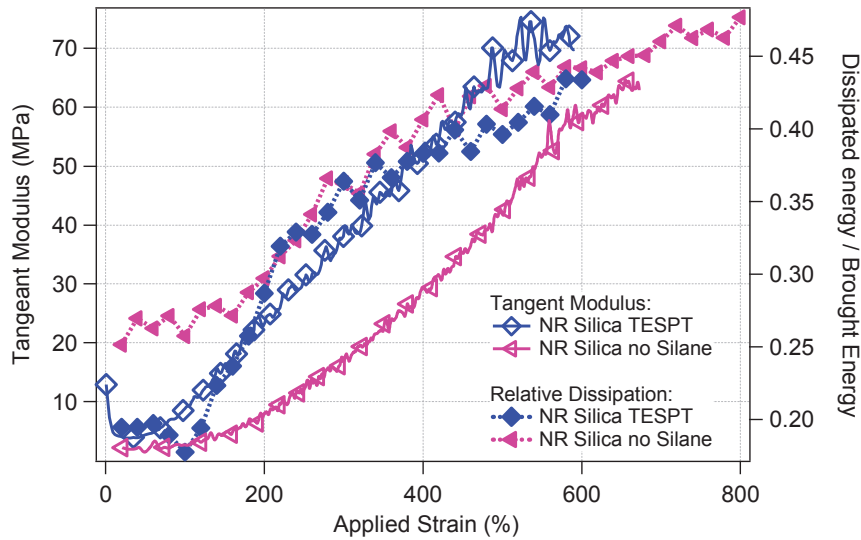


**Figure 201: Similar evolution of tangent modulus and relative dissipated energy for Silica-TESPT and Silica with no silane coupling NR materials (samples series 030-11).**

The relationship between the dissipated energy and tangent modulus does not seem to depend on the Silica rubber interface as shown in Figure 202b. Two regimes can be distinguished in Figure 202b: first the dissipation increases strongly with modulus as the first crystallites form during the cycle. Then the dissipation increase slower with modulus maybe due to the fact that dissipation mainly originates from SIC whereas the modulus increase is due to SIC and to limited chain extensibility. The relative dissipation for a given value of tangent modulus is higher for the non-treated Silica NR samples compared to Silica-TESPT NR samples.

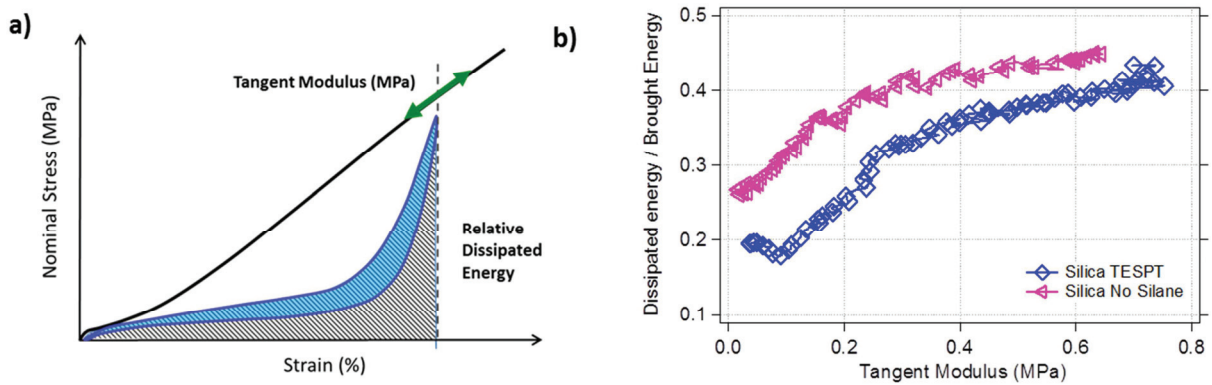


**Figure 202: a) Representation of tangent modulus and relative dissipated energy on a non-precycled reinforced samples Stress-strain curve. b) Correlation between both measurements for Silica-TESPT and Silica with no silane coupling NR materials (series 030-11).**

## VII.2. Cavitation

### VII.2.a. Introduction

Although the key role that may play cavities forming at large extension in rubbers, the cavitation phenomenon remains poorly studied and the different characterization works during tensile tests did not enable to have a clear picture of cavitation. Dilatometry<sup>139,162,163</sup> has been the most often used technique. Volume variations during large amplitude extension are monitored by placing the sample in water or in a closed vessel in which the gas pressure is monitored very accurately. Precise measurements of volume variations can also be obtained by digital image correlation. Le Cam et al.<sup>164,165</sup> have measured volume variations with simultaneous vertical and horizontal measurements of the strain. Their data show a small volume increase of approximately 5% in unfilled rubber (SBR and NR) samples, whereas in filled NR the volume increase reaches 20%. Note that the decrease of volume due to SIC (because crystallites are more dense than the amorphous phase), must be carefully taken into account when assessing volume variations due to cavitation quantitatively. De Crevoisier et al.<sup>80</sup> have performed 3D measurements of the deformations in Carbon black filled styrene-butadiene rubbers (SBR). They have shown that the contractions in thickness and width are not equivalent and reveal a volume increase above a given strain threshold. The same materials were also analyzed by Small Angle X-ray Scattering<sup>79</sup> and it was found that the overall scattering intensity increases above a similar strain threshold, confirming the onset of cavitation in these samples.

### VII.2.b. Measurements principle

The principle of our cavitation measurement is based on the reduction of the X-ray absorption coefficient of the sample when air-containing cavities are formed. While the X-ray absorption coefficient is a signature of the volume of rubber encountered, the simultaneous and independent optical measurement of sample width is characteristic of the system rubber + voids.

The cavitation data were obtained from the in-situ tensile experiments under X-ray illumination meant to analyze the SIC phenomenon (see chapters III & V). Here we compare the width reduction measured by the optical camera (and which has been used to compute the strain) and the X-ray beam absorption coefficient of the sample. This latter measurement was made possible thanks to a photodiode placed in the beamstop in front of the X-ray detector.

Let us consider an incompressible stripe of rubber of initial length  $l_0$ , width  $w_0$  and thickness  $t_0$  (Figure 203). The photodiode measures a direct beam  $I_0$ :

$$I_0 = B e^{-\mu_0 t_0} \quad (74)$$

With  $B$  the incident X-ray beam reaching the sample and  $\mu_0$  the absorption coefficient of the rubber or filled rubber.

The rubber piece is now stretched in a uniaxial manner, meaning that the width and thickness reduction are both related to the applied extension ratio  $\lambda$  according to the following relationships:

$$w_M = \frac{w_0}{\sqrt{\lambda}} \quad (75)$$

$$t_M = \frac{t_0}{\sqrt{\lambda}} \quad (76)$$

In this conditions some air cavities are formed thus the volume of the sample (system rubber + air) increases in an isotropic fashion (note that the rubber volume is conserved). The volume fraction of rubber is denoted  $\phi$  (the rubber+voids volume is  $V=V_r.\phi^{-1}$  with  $V_r$  the rubber volume) and the width  $w_M$  of this sample containing cavities is measured by the optical camera.

The beam absorption measures the thickness of rubber effectively encountered which is lower than  $t_M$ :

$$t_{rubber} = t_M \phi^{\frac{1}{3}} \quad (77)$$

The thickness measured by absorption of the X-ray beam is the one of a hypothetical stretched sample without any voids (third sample in Figure 203). The measured intensity during stretching can be written:

$$I = B e^{-\mu_0 t_M \phi^{\frac{1}{3}}} \quad (78)$$

One obtains the fraction of rubber  $\phi$  by combining equations (74) and (78):

$$\ln\left(\frac{I_0}{B}\right) = -\mu_0 t_0 \quad (79)$$

$$\ln\left(\frac{I}{B}\right) = -\mu_0 t_0 \frac{t_M}{t_0} \Phi^{\frac{1}{3}} \quad (80)$$

$$\Phi^{\frac{1}{3}} = \frac{t_0 \ln\left(\frac{I_M}{B}\right)}{t_M \ln\left(\frac{I_0}{B}\right)} \quad (81)$$

According to equations (75) and (76) the ration of widths is identical to the ratio of thicknesses, the fraction of rubber is thus calculated thanks to this equation where all parameters are measured:

$$\Phi^{\frac{1}{3}} = \frac{w_0 \ln\left(\frac{I_M}{B}\right)}{w_M \ln\left(\frac{I_0}{B}\right)} \quad (82)$$

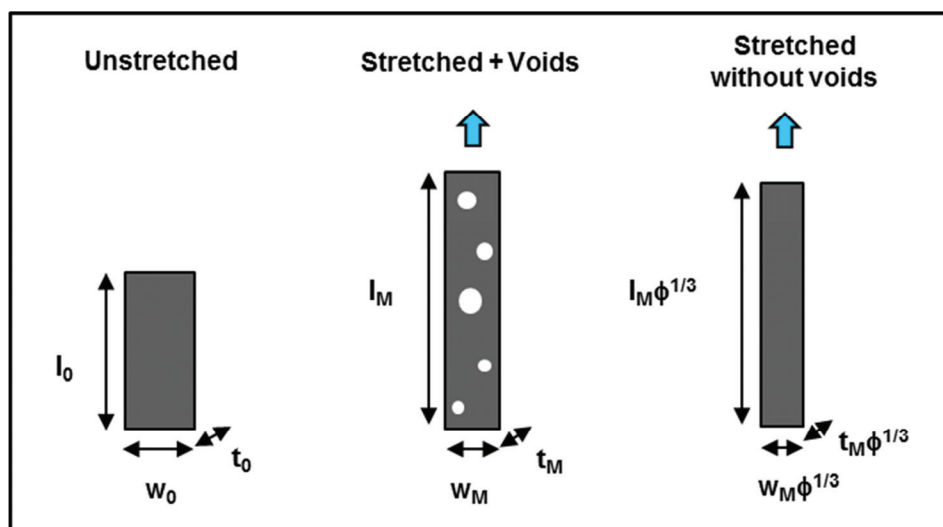


**Figure 203: Schemes of the different states: Unstretched, Stretched with voids (as measured by the optical camera) and Stretched without voids (as measured by the beam absorption).**

This analysis was applied to the tensile tests carried out on precycled samples of unfilled NR and filled NR with different interface agent and crosslink densities. The results are pretty noisy due to fluctuating shutter opening durations that impact the absorption measurements.

### VII.2.c. *Effect of fillers and interface on cavities formation*

The obtained cavities fractions ( $\phi_{\text{cavities}}=1-\phi$ ) are of the same order for all unfilled samples whatever the crosslink density. Cavitation already occurs in the first recorded tens of percent of strain and increases up to deformations of approximately 250% which is very close to the SIC onset for these samples (Figure 204). The second part of the curve follows a decreasing trend which can be related with the contraction effect of crystallization: the rubber chains reorganization in crystallites reduces the occupied volume of NR<sup>28</sup> and consequently lowers the overall volume of partly crystallized rubber. These results are in agreement with the work of Le Cam et al.<sup>165</sup> who reported a positive volume variation up to the SIC onset above which the volume started to decrease due to a crystallites formation effect.

In Figure 204 are compared three types of rubber/filler interface: Silica with TESPT, Silica with OCTEO and Carbon Black, each graph representing one common sulfur amount for filled NR. Interestingly the fraction of cavities is highly enhanced by the addition of fillers. Le Cam et al.<sup>164</sup> also observed a sharp increase in the fraction of cavities from unfilled NR to Carbon black filled samples due to stress intensification brought by the reinforcing fillers.

The cavitation phenomenon appears more important in strongly reinforced samples (TESPT and Carbon Black). This result is in contradiction with the measurement of Ramier and coworkers<sup>139</sup> on SBR with different interface agents. By means of volume variation measurements, these authors evidenced a higher cavitation in the case of a non-covalent coupling of the SBR rubber on the silica as compared to covalently coupled silica. The interpretation of those results is that more debonding occurs at the weak rubber/silica interface. In our case, the higher voids formation for strongly interacting interface suggests that most of the vacuoles are formed in the

rubber matrix and not at the interface. The reinforcement being higher for TESPT and Carbon Black, the high local stress in the rubber phase seems to trigger more cavitation for a given macroscopic strain.

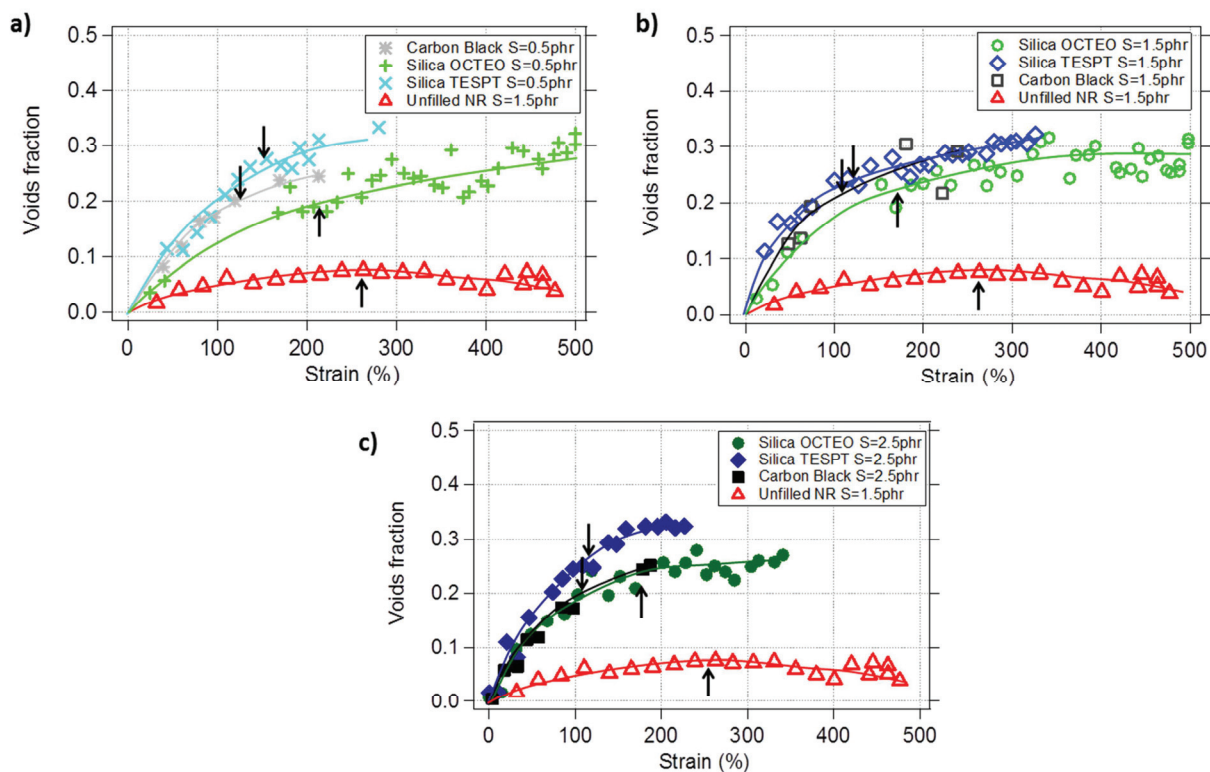


**Figure 204: Fraction of cavities versus strain for Reinforced samples with Carbon black and Silica. Comparison of a unfilled NR with Reinforced samples with several sulfur amounts: a) 0.5 phr, b) 1.5 phr and c) 2.5 phr (sample series 119-11). The arrows indicate the SIC strain onsets.**

The main drawback of our technique is that we compare the optical measurement in the width direction and absorption measurement in the thickness direction. The result will be exactly the same if the deformation state is identical in the two directions of a plane transverse to stretching direction. Nevertheless de Crevoisier and coworkers have shown by DIC that the elongation ratio  $\lambda_2$  in the width direction is higher than expected when supposing a uniaxial situation (Figure 205). They attributed this effect to a possible anisotropy of the filled rubber induced by the processing step of calendaring.

This remark is all the more true in our sample whose holding cylindrical part may lower the width reduction (keep the width less deformed than in a classical uniaxial test) and on the opposite enhance the reduction of the thickness. A precise estimation of this effect requires additional optical measurements of the thickness reduction. Taking this effect into consideration, our cavities fraction may have been strongly over-estimated as may be the values found by Le Cam and co-workers.

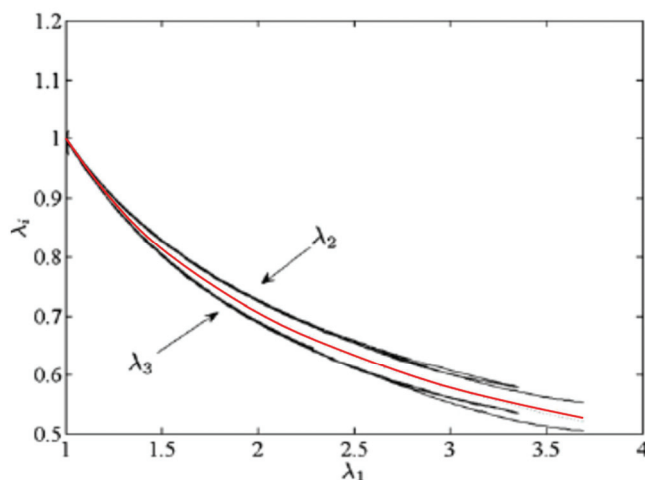


**Figure 205: Elongation ratios in width ( $\lambda_2$ ) and thickness directions ( $\lambda_3$ ) as a function of elongation ratio  $\lambda_1$  in stretching directions according to De Crevoisier<sup>80</sup>. The red line represents the uniaxial prediction  $(\lambda_1)^{-1/2}$**

Nevertheless, it appears from the results of Le Cam et al.<sup>165</sup> that the fraction of cavities is lower for filled SBR rubber than filled NR (10% for filled SBR against 25% for filled NR at  $\lambda=3$ ) even if they found volume changes two times more important than other authors<sup>80,139</sup> (volume change of less than 5% at  $\lambda=3$ ). This can be explained by an actual influence of the polymer type on cavitation. As a matter of fact the high resistance and dissipation properties of reinforced NR may be partly due to an important ability to form fibrils and cavities<sup>74,166</sup> (in addition to the effect of SIC).

In addition, comparing our results with the ones of Ramier and coworkers, it can be observed that the covering agent does not lead to a stronger cavitation in our NR samples as if the local state of extension and stress governs the formation of cavities in the rubber matrix whereas the SBR silica interface would be more subjected to loss of cohesion.

A complete DIC analysis of the strain in the three directions coupled with X-ray absorption measurements and SIC evaluation would provide more insights in the volume changes during deformation and the competition between cavitation and SIC in the case of Natural rubber.

### VII.3. Microscopic observations

SEM observations were performed on Silica and Carbon Black filled NR samples in the unstretched and stretched states in view to follow the evolution of the microstructure. Three pictures are presented in Figure 206, one in the unstretched state and two stretched up to 200%.

It was found that this strain level is a threshold for the formation of fibrils. This apparition of a mesoscopic orientated structure goes with the formation of elliptical voids. Large aggregates of several hundred of nanometers may to be at the origin of local stress amplification leading to those voids.

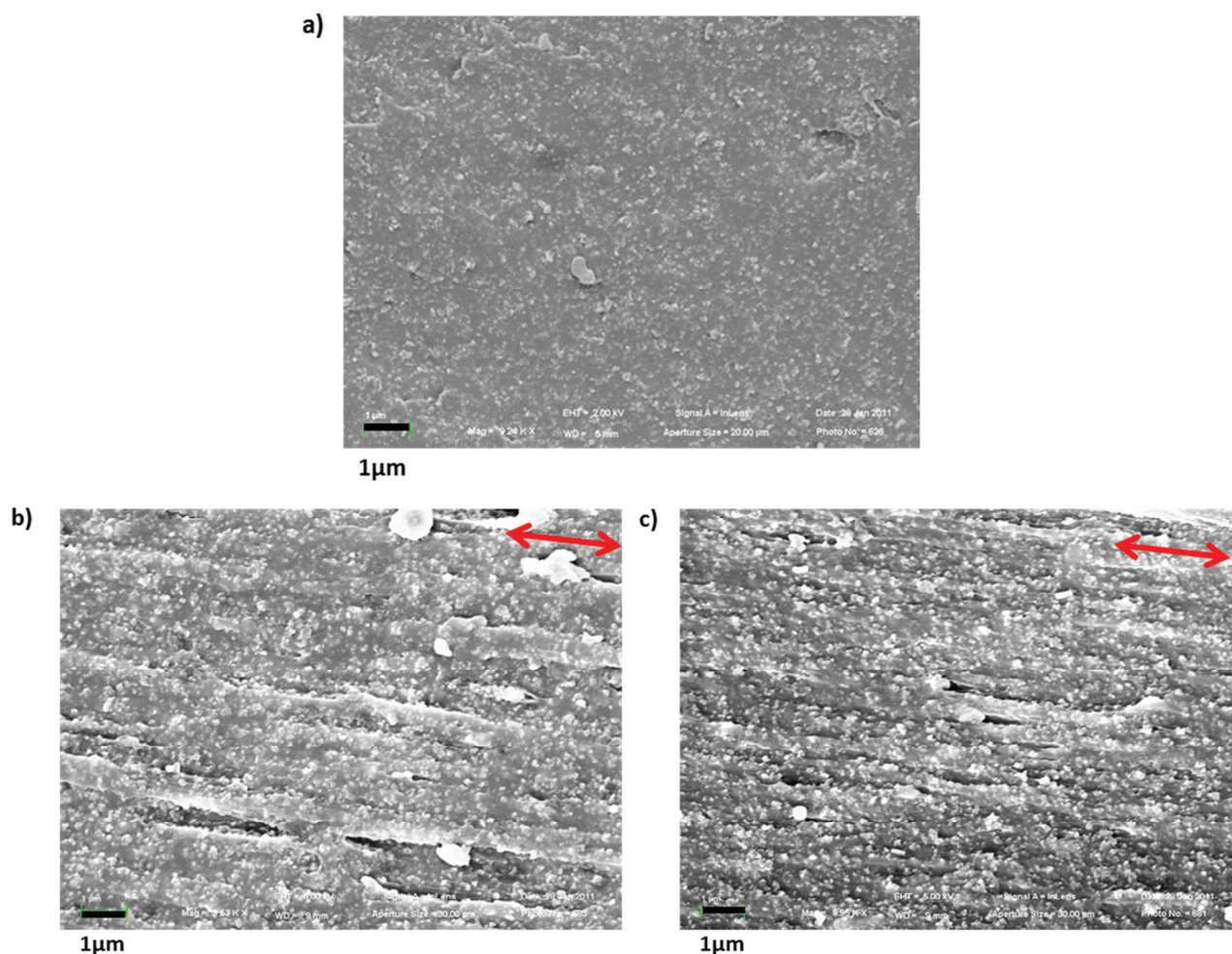


**Figure 206 : SEM pictures: a) Silica TESPT sample in the unstretched state, b) Silica TESPT and c) Carbon Black samples stretched at an elongation ratio  $\lambda=3$  in the direction of the red arrows (sample series 095-10).**

The second main conclusion from these observations is that the local state of extension is quite heterogeneous with some regions that do not seem much deformed and highly strained rubber in fibrils and ligaments.

It can also be remarked that the fibrils formation occurs in the strain range of the strain-induced crystallization onset but the latter phenomenon is not necessary to obtain fibrils since similar structures were observed in non-crystallizing SBR sample. One may think that the crystallites will preferably form from the highly strained natural rubber chains contained in the fibrils.

#### **VII.4. Resistance to failure for un-notched sample.**

The ultimate properties of our un-notched reinforced NR compounds are presented here, the comparison with tear resistance results presented in the next chapter may be of interest.

Ultimate properties can refer to the strain at break, stress at break and energy at break, the three of them are addressed here but if no precision is given we associate the ultimate properties to the energy at break since it combines the stress and strain at break to give the amount of energy necessary to break the sample. In order to draw clear trends, we use to compare three or more crosslink density for each interface type.

The influence of filler/rubber interface and crosslink density has already been partly discussed in chapter IV. The results of stress and strain at break are summarized in Figure 207. In general the stress and strain at break can be related to the reinforcement effect of each filler/coupling agent system: a highly reinforcing system has a rather low strain at break and high stress at break. This is particularly true for Carbon Black and on the opposite a Silica OCTEO system shows a high strain at break and low stress at break. It is to be noticed that if the true stress was considered here, the Silica OCTEO sample would exhibit a higher true stress at break. In the case of the Silica NSC compounds, both strain and stress at break are rather low compared to the other coupled Silica system being Silica TESPT.

The relationship between crosslink density and ultimate properties is similar whatever the interface type: the stress at break reaches a maximum for crosslink densities of roughly  $1.8 \times 10^4 \text{ mol.g}^{-1}$  (according to NMR measurements) and the strain at break decreases with crosslink density. The stress at break maximum for unfilled NR samples is slightly higher (roughly  $2.0 \times 10^4 \text{ mol.g}^{-1}$ ).

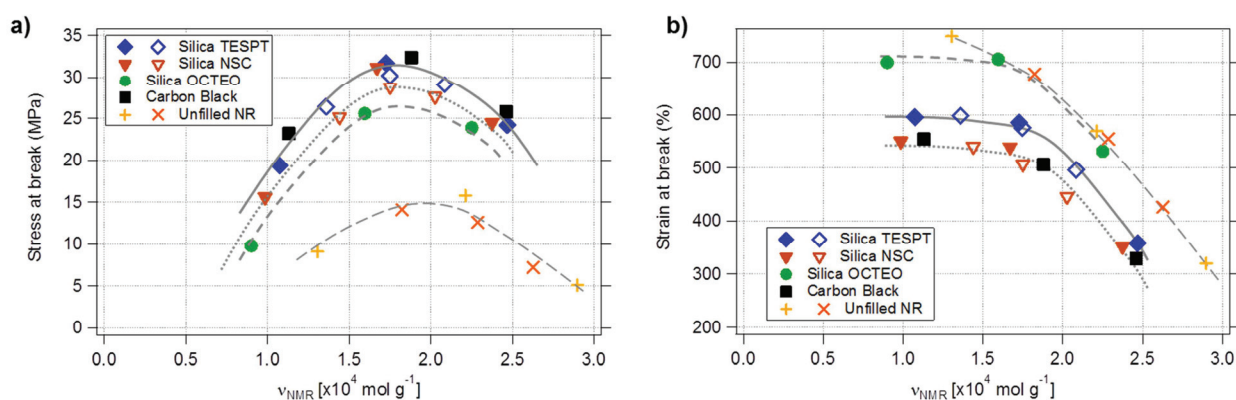


**Figure 207: a) Stress and b) Nominal Strain at break in tensile tests for un-notched unfilled NR samples (series 046-11 and 119-11) and filled NR samples of series 30-11 (empty symbols) and 119-11 (filled symbols). Curves are guides for the eyes.**

The energy at break is computed as the area under the stress-strain curve up to failure. Since the shape of the curves is quite similar for all studied samples, the energy at break is related to the product of stress and strain at break and therefore shows a maximum for crosslink densities (roughly at  $1.7 \times 10^4 \text{ mol.g}^{-1}$  according to NMR measurements for filled samples and slightly higher for unfilled samples). The energy at break is somehow lower for Silica NSC compared to Carbon Black and Silica TESPT. Silica OCTEO samples also shows a lower energy at break mainly due to a low modulus in the large strains regime.

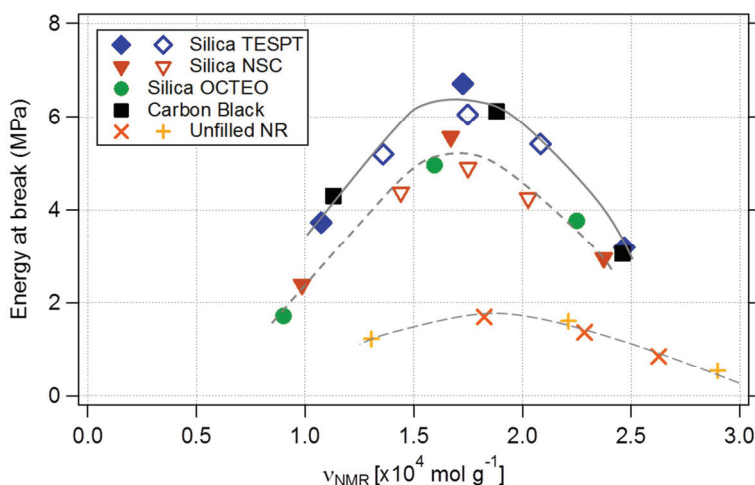


**Figure 208: Energy at break in tensile tests for un-notched unfilled NR samples (series 046-11 and 119-11) and filled NR samples of series 30-11 (empty symbols) and 119-11 (filled symbols). Curves are guides for the eyes.**

### Discussion

One may try to relate the ultimate properties and in particular the energy at break to the dissipation properties. A hypothesis that can be made is that a system that dissipates a lot of energy during traction may break at a higher total brought energy. For all tested reinforced NR, the values of the relative dissipation in the large strain regime are quite similar (see Figure 196 and Figure 198) as well as the energy at break. Only the lower energy at break for unfilled NR (Figure 208) could be related to a lower relative dissipation (see Figure 195).

## VII.5. Conclusions

This chapter presented several investigations meant to better understand the properties of reinforced Natural rubber at large strains. The dissipation properties were investigated by means of mechanical cycling experiments and the cavities formation were estimated thanks to absorption measurements.

The relative dissipation (i.e. ratio of dissipated on brought energy) of filled rubbers during the first cycle was found to depend on the filler fraction and only slightly on the interface type. This would mean that for a given energy input, the dissipated energy mainly results from the matrix softening through breakage and slippage of chains.

The relative dissipation measurements performed on samples precycled up to 400% (first testing method) and samples precycled up to the tested strain in terms of dissipation (second testing method) have shown that above the SIC strain onset, the crystallization and melting of crystallites has a predominant effect on the relative dissipation. The decrease of the SIC strain onset with the filler interface strength observed in chapter V was confirmed by relative dissipation measurements. Also in agreement with the observations made in chapter V, the effect

of precycling on filled samples was found to increase the SIC onset as revealed by a comparison of the two dissipation methods.

The formation of cavities seems to be fairly enhanced when fillers are added to NR and may depend on the filler-rubber interface type. The formation of elliptical voids was confirmed by electronic microscopy observations.

The last part of this chapter dedicated to the ultimate properties of un-notched reinforced Natural Rubber samples has shown that the interface type has a slight effect on the energy at break. The optimum of crosslink density in terms of energy at break has also been determined and lies close to  $1.7 \times 10^4 \text{ mol.g}^{-1}$  according to NMR measurements. At very large strain, the dissipation levels and cavities contents were quite similar for all tested reinforced NR samples thus no correlations with energy at break were established.

---

## VIII. Tear Resistance in Reinforced Natural Rubber

VIII.1.	Tear resistance in unfilled NR .....	224
VIII.1.a.	Stress-strain curves.....	224
VIII.1.b.	Evaluation of the tear energy in the pure shear geometry.....	226
VIII.1.c.	Effect of crosslink density on tear resistance .....	229
VIII.2.	Tear resistance in reinforced Rubbers.....	229
VIII.2.a.	Tear behavior for reinforced Synthetic and Natural Rubbers .....	229
VIII.2.b.	Effect of filler/rubber interface on tear resistance.....	232
VIII.2.c.	Effect of crosslink density on tear resistance .....	234
VIII.2.d.	Effect of test speed .....	236
VIII.3.	Study of the crack tip .....	236
VIII.3.a.	State of the crack tip.....	237
VIII.3.b.	Strain amplification at the crack tip .....	239
VIII.3.c.	Local stress estimation at crack tip .....	243
VIII.3.d.	Crystallized zone at crack tip .....	244
VIII.3.a.	Crystallized fraction measurement at crack tip .....	245
VIII.4.	Conclusion .....	248

Resistance to the crack propagation has been investigated in our unfilled and reinforced Natural Rubber compounds by means of tensile tests on pre-notched pure shear samples. The results obtained in unfilled NR are presented first, then the effect of fillers is analyzed. The effects of the filler/polymer interface and crosslink density are discussed.

Finally the state of the filled rubber at the crack tip is analyzed on different scales, first at the reinforcing aggregates scale by SEM observation and then at the mesoscopic scale by means of non-optical local strain measurements by digital image correlation. The strain-induced crystallization at the crack tip has been characterized by means of specific X-ray diffraction experiments. The criterion for failure at the crack tip is discussed as well as the role of the crystallized zone at the crack tip.

## **VIII.1. Tear resistance in unfilled NR**

### *VIII.1.a. Stress-strain curves*

The tear propagation in unfilled NR in Pure Shear geometry was found to be instable. The cracks do propagate at such high speeds that they appear to be instantaneous to the eye (crack speeds of the order of 1m/s were measured in filled NR). The crack propagations were either catastrophic meaning that the sample was entirely broken after a single fast propagation event or sometimes non catastrophic leaving some part of the sample in a stretched configuration. This behavior may be interpreted as the combination of a crack propagation and a crack arrest properties.

The stress at break reached during Pure Shear tear tests are quite small compared to the values in simple un-notched tensile tests (Figure 209). As regards the strain at break, highly crosslinked samples break at quite low maximum strains whereas the weakly crosslinked samples (sulfur amounts of 0.5 phr and 1.0 phr) present significantly higher strains at break.

It was also noticed that non-catastrophic propagations of the crack were more frequent with those weakly crosslinked samples (see Figure 209). This result can be interpreted as a better crack propagation arrest property in the case of weakly crosslinked samples. This could be attributed to a higher degree of dangling free chains segments that are expected to increase the dissipation of the material and thus may impart better crack arrest properties. Additional experiments using trousers samples may help to go further in the characterization of this crack arrest property.

Although the crack propagation could present instabilities, the crack path was rather straight conversely to filled NR as shown in the next section. Some crack tip blunting may play a role in improving the strength compared to unfilled SBR most probably in relationship with the formation of crystallites at the crack tip as demonstrated by Trabelsi and coworkers in natural rubber notched stripes<sup>115</sup>.

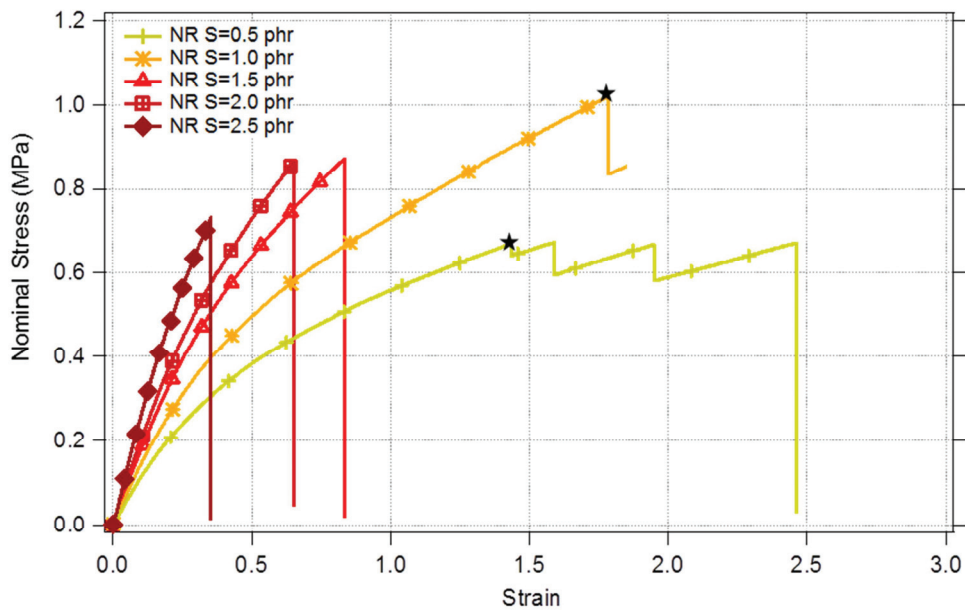


**Figure 209: Typical Nominal Stress versus Strain curves for pure shear pre-notched unfilled NR samples (series 046-11 and 119-11). Non-catastrophic propagation events occur in samples with sulfur contents of 0.5 and 1.0 phr (the black stars mark the propagation). Note that once the propagation started the values of the calculated nominal stress are not correct due to the reduction of the cross-section.**

The dispersion of tear energies was important with sometimes input energies to propagate the crack that could be the double depending on the sample. This is illustrated in Figure 210 with six unfilled samples curves (sulfur content S=1.0phr).

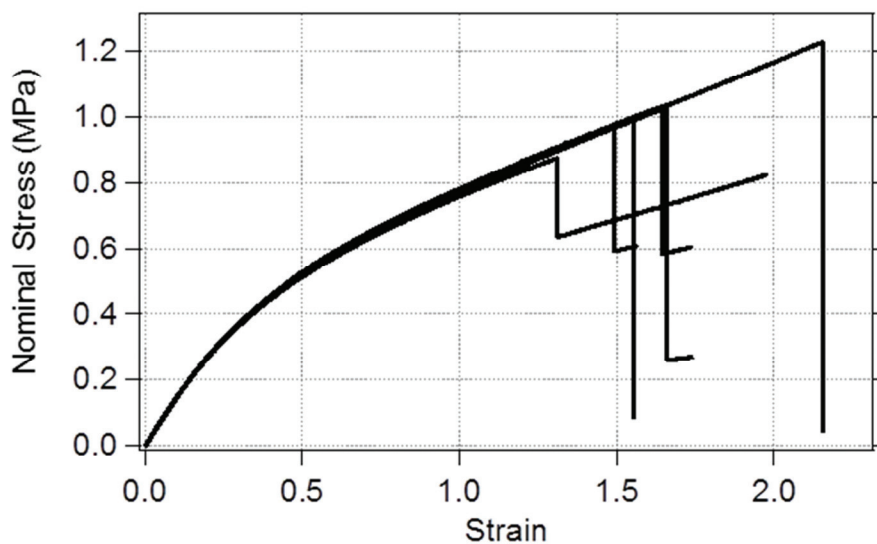


**Figure 210: Examples of stress-strain curves obtained for six samples of a given unfilled NR formulation (S=1.0phr, series 046-11).**

*VIII.1.b. Evaluation of the tear energy in the pure shear geometry*

The non-catastrophic crack propagations observed in pure NR enable us to relate a given amount of released energy to a given length of propagated crack. This relationship between the energy released by the propagation of the crack and the propagated crack length  $c$  (Figure 211) was compared to the classical relationship between energy released at break and the full length of the sample in order to check the agreement with the crack propagation description in Pure Shear geometry given by Rivlin and Thomas<sup>119</sup>.

The elastic energy stored in the sample right before the propagation is denoted  $E_1$  and the density of elastic energy  $W_1$  is obtained from the integration of the stress-strain curve up to the propagation onset :

$$E_1 = W_1 L e h \quad (83)$$

The total energy stored in the sample decreases from  $E_1$  to  $E_2$  since a large part of the sample has been transferred from stretched to unstretched state. The remaining elastic energy stored in the sample is denoted  $E_2$  and can be computed from  $E_1$  and the ratio of forces  $F_2$  and  $F_1$  (Figure 211):

$$E_2 = E_1 \frac{F_2}{F_1} \quad (84)$$

Once the crack propagation stops the energy density in the pure shear region is considered exactly the same ( $W_1$ ) since the time for the crack to propagate is very small compared to the stretching rate so no additional energy is brought to the sample between the beginning and the end of the propagation.

In Pure Shear geometry, the stored energy in the sample after the crack propagation  $E_2$  is assumed to be only stored in the unbroken region and can thus be expressed as a function of the propagated crack length  $c$  and the energy density before propagation  $W_1$ :

$$E_2 = W_1 (L - c) e h \quad (85)$$

$\Delta E$  can thus be written as following:

$$\Delta E = (E_1 - E_2) = W_1 c e h \quad (86)$$

The tear energy is defined as the ratio of the energy necessary to propagate the crack and the crack area. It can be expressed as a function of the energy released by the crack  $\Delta E$  or as a function of the total brought energy  $E_1$ :

$$T = \frac{\Delta E}{\Delta A} = \frac{\Delta E}{c e} \quad (87)$$

$$T = \frac{\Delta E}{\Delta A} = \frac{E_1}{L e} = W_1 h \quad (88)$$

It is thus equivalent to compute the tear energy by measuring the energy released by the crack  $\Delta E$  and the length  $c$  or by measuring the energy  $E_1$  considering that it corresponds to a propagation of length  $L$ .

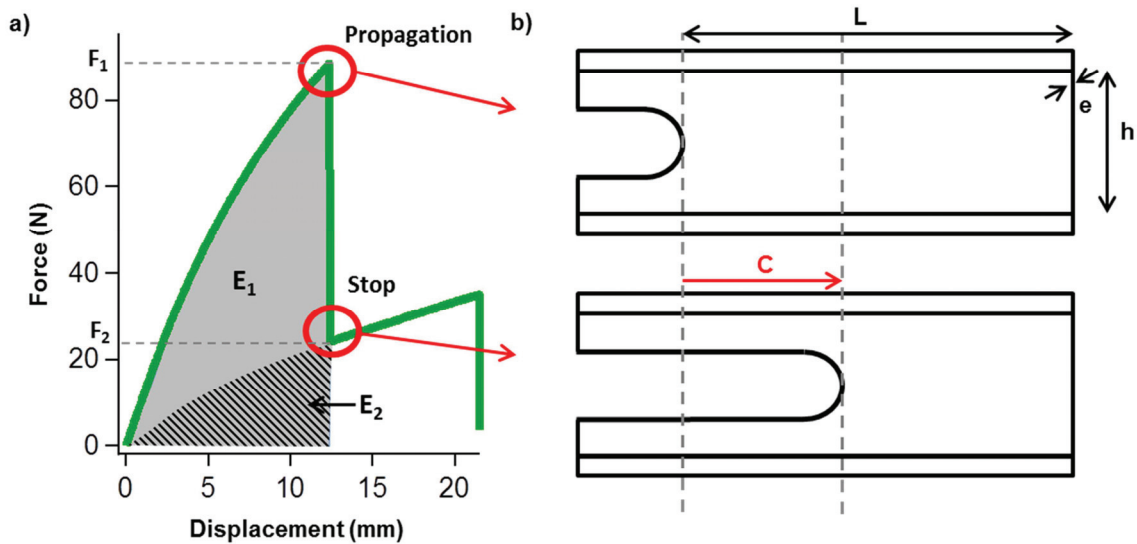


**Figure 211 : a) Force-displacement curve showing an apparent stress decrease due to forward propagation of the crack in unfilled NR (Pure Shear pre-notched sample). The energy stored in the sample before and after the crack propagation are respectively denoted  $E_1$  (grey area) and  $E_2$  (hatched area). b) Schematic view of the same sample right before and after propagation of a crack of length  $c$ .**

Figure 212 presents for each sample (represented by a given symbol) the quantities  $\Delta E$  plotted versus  $c$  and the quantity  $E_1$  plotted against  $L$  (87.5 mm for all samples).

The slope  $\Delta E/c$  and  $E_1/L$  correlate fairly well for each sample which confirms that the pure shear treatment is valid for the samples with no catastrophic failure. The tear energy can be directly computed from the energy at the crack propagation initiation considering this energy is fully released in the creation of a crack of length  $L$ .

The torn surface was found to be smooth in most cases although some rough parts were also to be observed on several analyzed samples. In those cases the amount of created surface may be underestimated accounting for the deviations between the measurements.

The dispersion of tear energies from one sample to the other corresponds to the different slopes.

Samples where the first crack led to a complete failure of the sample are represented in filled squares in Figure 213: the propagated crack distance is taken as the initial length of the pre-notched sample i.e. 87.5mm. Nevertheless the obtained energy levels seem quite high compared to the samples with a non-catastrophic propagation (diamonds, triangles and circles)

This suggests that the elastic energy stored in these samples when the crack starts to propagate is not completely converted in the creation of the crack surface and that some residual energy is available at the end of the fracture (in other words the crack speed is not zero at the end of the propagation). It can be assumed that if the samples were longer, such energies would lead to higher crack lengths (empty square) as presented in Figure 213.

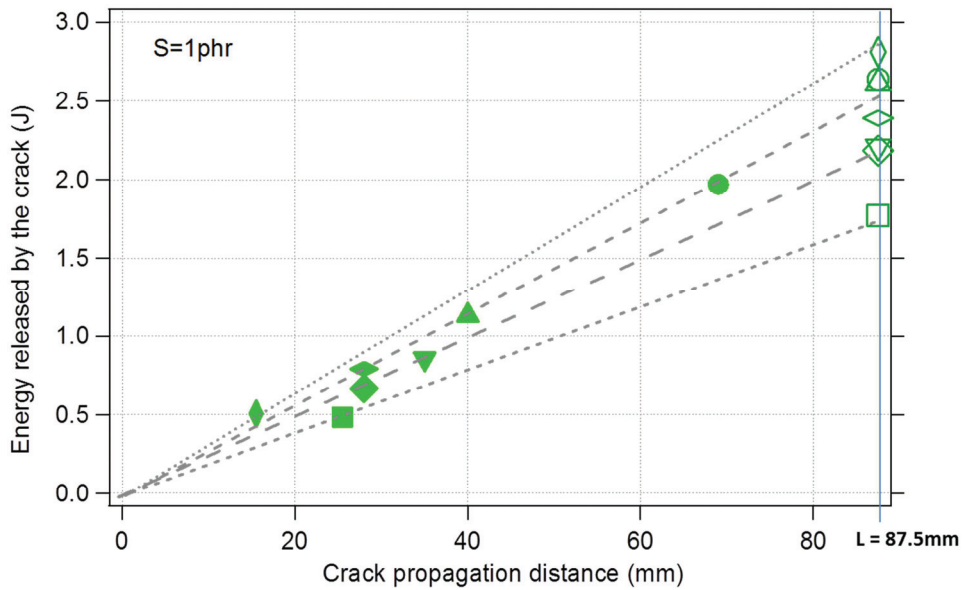


Figure 212 : Energy released by the crack propagation  $\Delta E$  versus the crack propagated distance  $c$  (filled symbols) and brought energy at  $E_1$  versus  $L$  (empty symbols) for unfilled NR samples with 1phr of sulfur (series 046-11) showing a non-catastrophic failure.

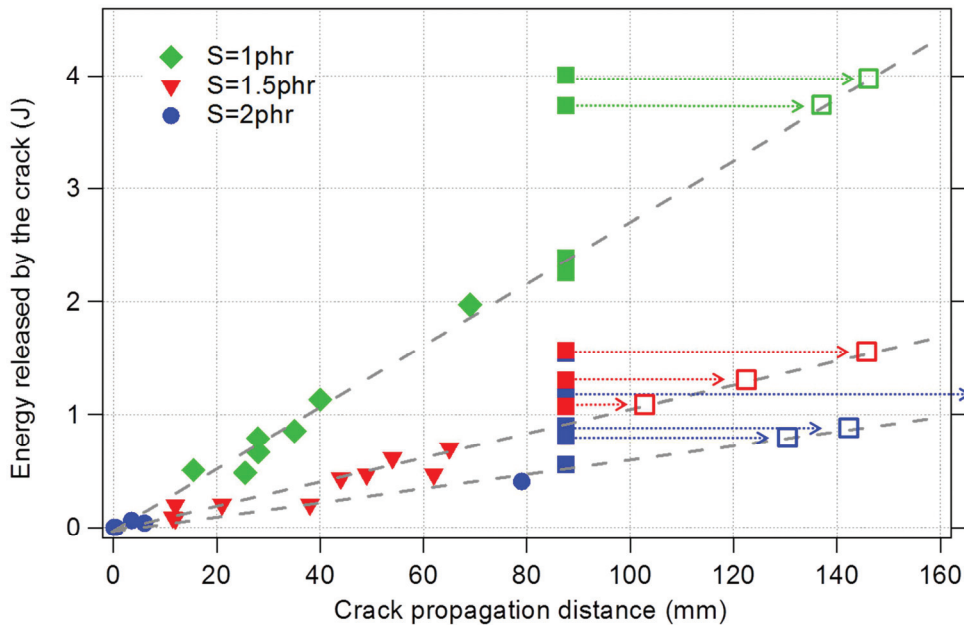
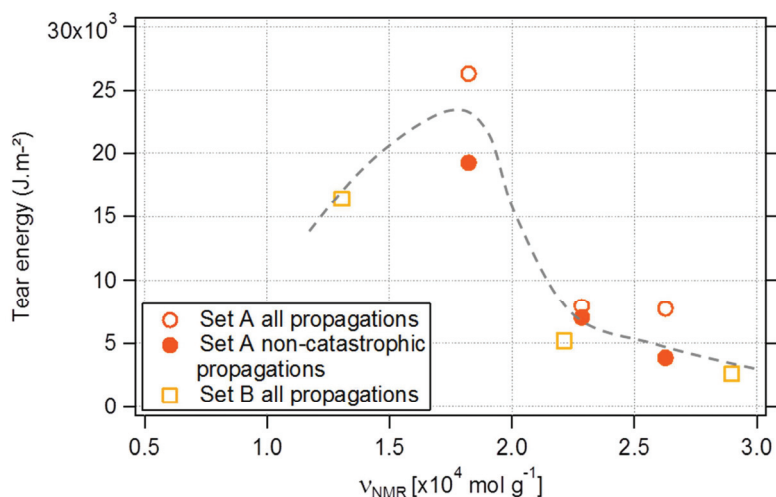


Figure 213: Energy density released  $\Delta W$  during the crack propagation versus the propagated distance  $c$ . Three unfilled NR samples of series 046-11 were tested (sulfur amount 1.0, 1.5 and 2.0). The energy density released for samples where a complete propagation of the crack was observed are reported at the maximum propagation length  $L$  of 87.5mm.

### VIII.1.c. Effect of crosslink density on tear resistance

The tear energies obtained for different crosslink densities first highlight the presence of an optimum of crosslink density in terms of tear resistance (Figure 214). According to the literature<sup>11,167,168</sup>, the optimum crosslink density in terms of tensile strength is higher than the optimum crosslink density in terms of tear strength but this is not the case for our unfilled samples (see energies at break in chapter VII).



**Figure 214:** Tear energy as a function of the crosslink density determined by NMR for unfilled NR samples (series 046-11 (set A) and 119-11 (set B)). For Set A we distinguished the Tear energy evaluated for all samples (empty circles) and only for sample with a non-catastrophic propagation (full circles).

## VIII.2. Tear resistance in reinforced Rubbers.

### VIII.2.a. Tear behavior for reinforced Synthetic and Natural Rubbers

In the range of extension rates accessible with standard electromechanical machines, the comparison of a reinforced Natural Rubber to a synthetic reinforced rubber such as Styrene-Butadiene Rubber (SBR) in terms of Pure Shear Tear tests highlights two distinct crack propagation behaviors. In the case of the filled SBR, the crack propagation is stable and observable to the eye whereas it is unstable for NR and the crack propagates at very high speeds making the propagation appear instantaneous to the eye (Figure 215). Some measurements of the catastrophic crack propagation speed in reinforced NR were carried out thanks to a high speed camera at a frame rate of 235 000 frames per seconds (fps). The crack speed was found to be of the order of several meters per seconds in this case.

Another important feature of the crack propagation in filled NR is that a crack bifurcation phenomenon occurs. This consists in a modification of the crack direction (often associated with

a change in crack speed) from the perpendicular to the parallel direction with respect to the stretching direction.

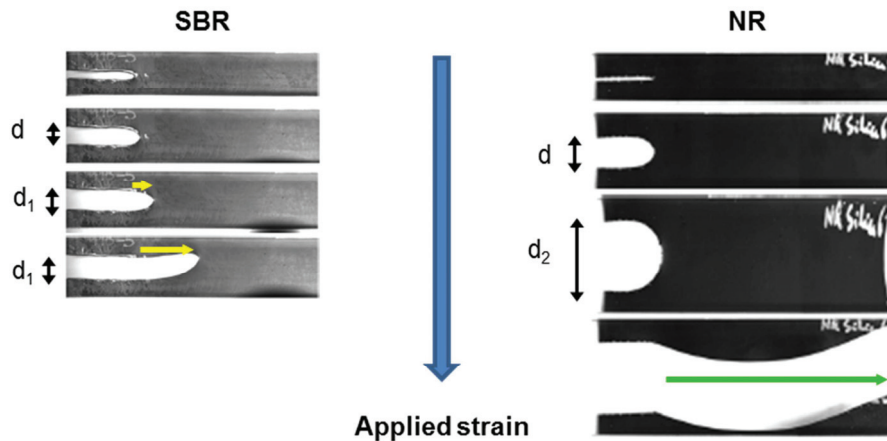


**Figure 215: Stable crack growth in filled Styrene-Butadiene Rubber (images on the left) and unstable crack growth in Natural Rubber (images on the right).**

The effect of the tear rotation on the energy at break has been studied by means of single edge notched tensile (SENT) tests by Gabrielle in his PhD and the length of propagated crack parallel to the stretching direction (or rotations total length) was found to be directly proportional to the energy at break<sup>129</sup>. In other words, the tear rotation is a crack tip blunting mechanism that strongly increases the crack tip radius.

According to Gabrielle et al<sup>74,129</sup> the energy at break for the filled SBR sample is far lower than the obtained values for filled NR illustrating the superior crack propagation resistance of NR. The dispersion of the results is small in the case of filled SBR samples whereas filled NR samples can yield energies at break varying from the simple to the double for a given formulation. This high dispersion of the results in filled NR has been confirmed in Pure Shear geometry and is attributed to the random character of the tear bifurcation phenomenon.

The tear bifurcations can also be described as transitions between two propagation paths in the material: a forward propagation path and a sideways propagation path (bifurcated crack). This way of interpreting the phenomenon was in particular adopted by Marano and coworkers<sup>132</sup>.

In Pure Shear geometry, the tear energy can be easily computed from the amount of mechanical energy brought to the sample up to the propagation of the crack (area under the nominal stress-strain curve) multiplied by the initial sample's height<sup>169,170</sup>. This relation relies on the fact that the input energy brought up to the propagation onset transfers part of the material from the pure shear region in extension to the relaxed state after propagation.

Nevertheless, we observed in several cases that the crack stops before the complete failure of the sample similarly to what was observed for unfilled NR. The occurrence of such a large but non-catastrophic propagation in the forward direction could be related with visible accidents on the stress-strain curve (Figure 216). The actual cross section bearing the load being reduced, the stress applied to the remaining part of the samples is in fact equivalent right before and after the propagation event. The apparent stress decrease can be used to indirectly measure the crack area created during the propagation.

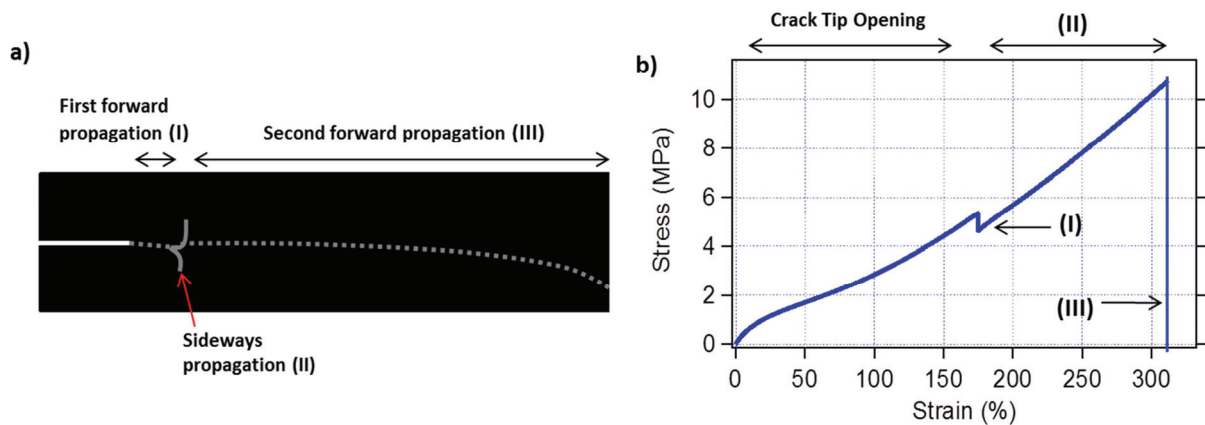


**Figure 216: Forward and sideways propagation of a crack in Pure Shear pre-notched Reinforced NR. a) Schematic representation of forward and sideways crack growth by respectively dotted and continuous lines. b) Stress-strain behavior in relationship with the propagation direction.**

The estimation of the energy density released by small forward propagations in reinforced NR could not be performed similarly to unfilled NR since the distinction between sideways and forward propagation is not always clear in reinforced samples: the forward propagation events often deviate sideways and the length associated to load drops is a combination of forward and sideways crack area. Moreover the tear rotations occurring during the first part of the tear tests correspond to advances of the crack of only a few hundred of micrometers which is not sufficient to plot an energy release rate profile.

The onset of the incomplete crack propagation was considered as the tear onset even if the test had to be continued to completely break the sample. The approach applied here is thus similar to stick-slip crack propagation in trouser tests samples: the unstable propagation is described as a series of crack initiation and arrest. The tear energy being the energy release rate at the onset of propagation, it does not include the property of crack arrest.

Only incomplete propagations leading to a visible accident on the stress-strain curve were taken into account, an example of such a small stress decrease is given in Figure 217 for a Silica OCTEO sample. In this case, the density of elastic energy up to a strain of 236% was used to calculate the tear energy (first accident on the curve: zoom in the left upper diagram).

The load measurements precision can be considered precise down to 0.5% according to the machine specifications. According to the theory described by Thomas<sup>119</sup> and reminded in chapter 2, the propagation of the crack transfers some part of the material from the pure shear stretched region to the un-stretched region but the main part of the sample section bears a uniform stress. Thus one may consider that a decrease of 0.5% of the stress is the consequence of the failure of a similar percentage (0.5%) of the total sample length. This would correspond in our samples to a length of propagated crack of the order of 500  $\mu\text{m}$  which is in agreement with inter-rotations distances that were observed by optical microscopy (see Gabrielle<sup>74</sup>).

In consequence, it has to be noted that the distinction that we made upon visible and non-visible crack advances with respect to the mechanical curves is equivalent to distinguishing between crack advances lower and higher than 500 $\mu\text{m}$ , only the latter being considered as tear initiation.

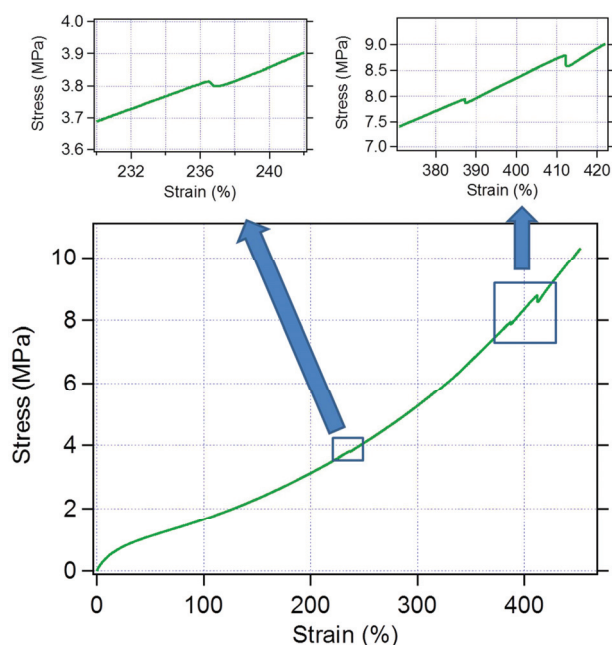


**Figure 217 : Slight load decrease due to forward crack advances for a Pure Shear pre-notched Silica OCTEO sample.**

### *VIII.2.b. Effect of filler/rubber interface on tear resistance*

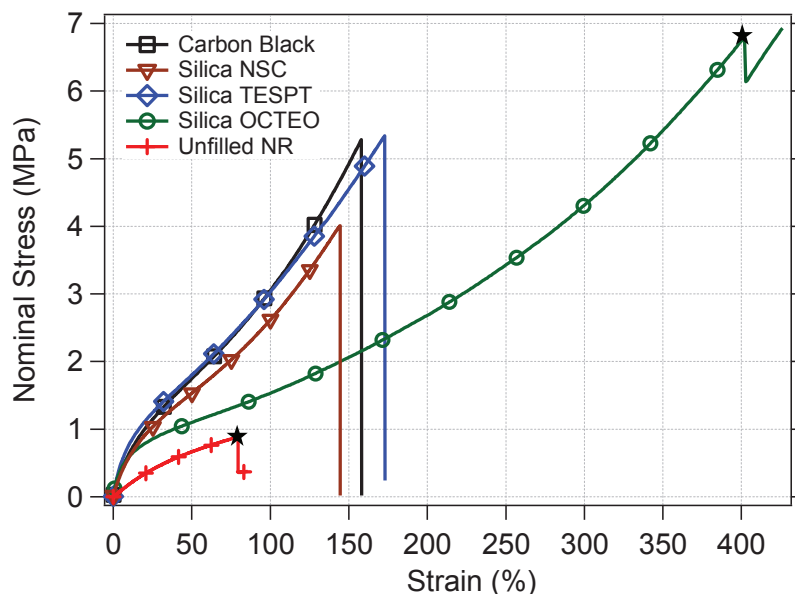
Firstly, the introduction of fillers leads to a very important increase of the critical energy release rate. The stress at break is far higher for reinforced samples versus unfilled rubber and conversely to un-notched samples, the strain at break is greatly improved as well by the introduction of fillers (Figure 218). Among the reasons that can be proposed to explain this result, filled samples have superior dissipation properties and better ability of the heterogeneously stretched network to reorganize. In addition for Natural rubber, the SIC strain onset being lower for reinforced samples, the amount of crystallites for a given strain at the crack tip is also improved when introducing fillers which explains why the tear resistance is so strongly increased.

Figure 218 shows a representative curve for each of the reinforced NR systems studied in series 095-10 and an unfilled NR form series 046-11. As the results were highly dispersed due to the unstable propagation and tear bifurcations, a total of 8 samples were tested for each sample type and the average tear energies obtained are shown in Figure 222 for three types of samples.

The Carbon Black filled NR samples show close but slightly lower tear energies than the Silica TESPT system. In the case of Silica NSC, the tear energy is significantly reduced compared to Silica TESPT which can be related to the lower energy at break in un-notched samples.

On the contrary the tear energy is greatly increased with the covering agent OCTEO with far higher strains at break and equivalent or higher stress at break. This result is quite unexpected due to the lower energy at break for un-notched samples (see chapter VII) and the weakness of the interface supposed to lead to debonding and lower crystallites amount. One of the possible

explanations for this result is the higher number of tear rotations observed for the Silica OCTEO tear samples.



**Figure 218: Stress-Strain curves for Pure Shear pre-notched unfilled (series 046-11) and reinforced NR samples (series 095-10). Crosshead speed  $1 \text{ mm}\cdot\text{min}^{-1}$ .**

In addition to the tear energy, the crack propagation velocity was measured for some samples with a very high frame rate camera. At very high frame rates, the recording duration is strongly limited by the quantity of generated data (the maximum recording duration was close to 2 seconds), the camera was therefore operated in a specific recording mode that erases progressively the previous images as new images are recorded. A trigger function enables to stop the recording as soon as the crack had propagated so that only the images taken in the last 2 seconds are kept.

In those experiments, crosshead speeds of 100 mm/min and 1000 mm/min were chosen. The few points recorded for each formulation seem to fall on a common tear energy versus crack speed curve (Figure 219). It can be noticed that the Silica TESPT samples show slightly higher tear energies for a fixed crack speed compared to the Silica NSC agent and Carbon black compounds.

#### Discussion:

The higher propagation resistance of filled rubber as compared to unfilled rubber is often attributed to higher dissipation properties stemming from the chains slippage at the interface and reorganizations on the micro-scale in general. We suggest that the high local strain heterogeneity as described in chapters V and VI may contribute to this ability of the reinforced rubber composites to reorganize under strain and thus increase the crack propagation resistance. The exceptional tear resistance is also to be related with the SIC phenomenon. The introduction of fillers decreases the strain onset for the crystallites formation leading to a further anisotropy of properties at crack tip that may promote the tear bifurcation phenomenon.

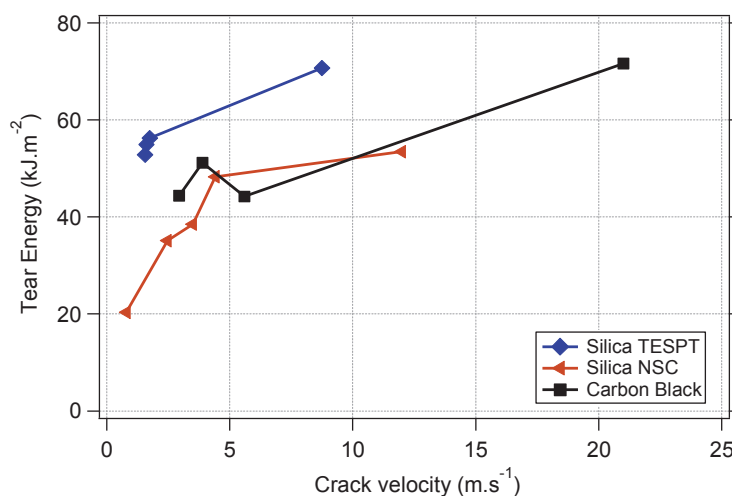


**Figure 219: Tear energy as a function of crack speed for catastrophic propagation of the crack in reinforced NR samples (series 095-10).**

### VIII.2.c. Effect of crosslink density on tear resistance

The effect of crosslink density on tear resistance has also been investigated for sets of samples with different interface types. A representative stress-strain curve for each tested formulation is presented in Figure 220 and the average value obtained for several samples of each formulation are plotted versus the crosslink density obtained by NMR in Figure 221.

The previously described differences for the three main interface types are still true for this series of samples: similar tear energy for coupled Silica (TESPT) and Carbon Black whereas the energy input required to propagate a crack is higher with Silica OCTEO even if the gap is smaller in this case. The crosslink density has a strong effect on the strain and stress at break. Increasing crosslink density (sulfur amount of 2.5 phr) leads to lower stress and strain at break in agreement with the deterioration of simple tensile ultimate properties.

A particular behavior is reported for reinforced NR with a low crosslink density (sulfur amounts of 0.5 phr). Once the crack tip has reached a maximum diameter, the crack propagates in a stable way at a low speed similarly to the propagation behavior observed for filled SBR. It can be noted that the carbon black and Silica TESPT samples show a somehow intermediate behavior since some samples exhibit a slow stable propagation whereas in some others the crack propagation is faster and unstable. The slightly higher crosslink density measured by NMR for those samples compared to Silica OCTEO suggest that there is a critical crosslink density under which the propagation becomes stable at the test speed considered ( $\dot{\lambda}=8 \times 10^{-4} \text{ s}^{-1}$ ). The singularity in the crack propagation observed at this crosslink density can be compared to the high SIC strain onset compared to higher crosslink densities described in chapter V. A lower crystallites fraction at the crack tip may explain why the crack propagation is stable with no deviations. It would be interesting to test an unfilled NR sample having a similar crosslink density in order to check this hypothesis.

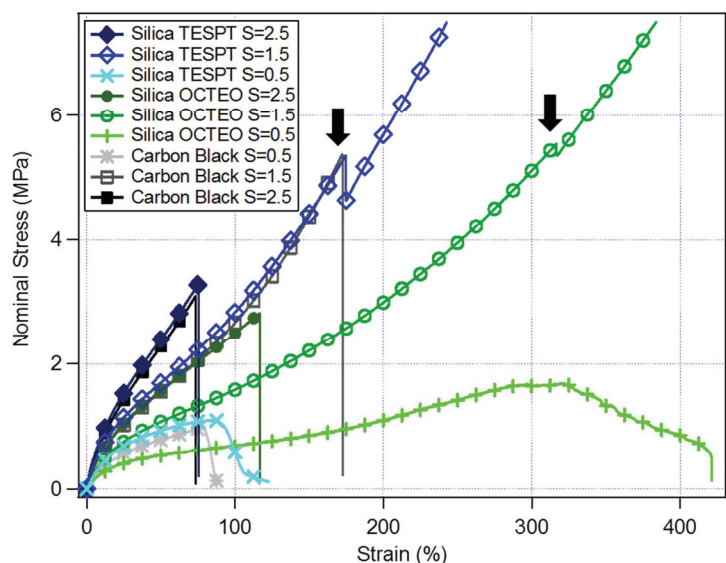


**Figure 220: Nominal Stress versus Strain during Tear tests on Silica and Carbon Black reinforced NR samples of series 119-11. The samples with a sulfur amount of 0.5phr show a slow propagation (visible by the slow stress decrease). Crosshead speed 1 mm.min<sup>-1</sup>.**

The tear energies obtained for reinforced NR samples reported in Figure 221 show that whatever the interface type, there is an optimum of crosslink density. This optimum of crosslink density is similar to the one obtained in chapter VII in terms of resistance to failure for un-notched samples. It is also interesting to note that this optimum is very similar to the one obtained for unfilled samples (see Figure 214) except for the Silica-OCTEO NR samples for which the optimum seems to be slightly shifted.

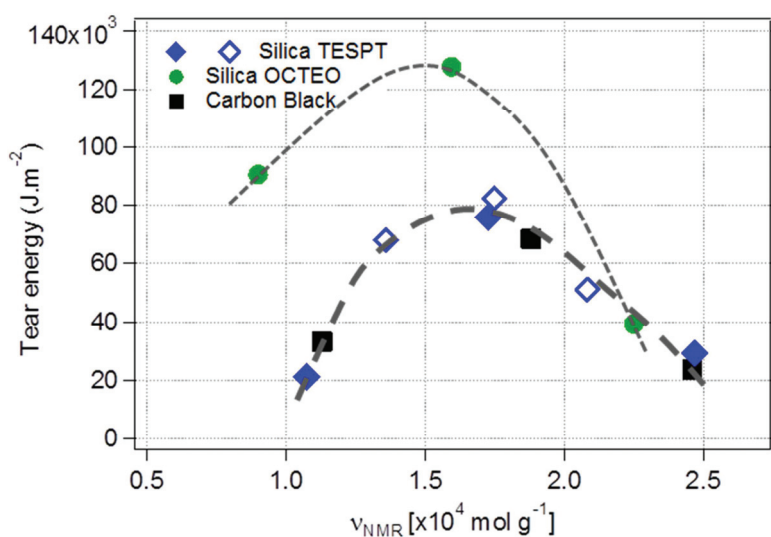


**Figure 221: Tear energy in tensile tests for un-notched reinforced samples of series 30-11 (empty symbols) and 119-11 (filled symbols). Crosshead speed 1 mm.min<sup>-1</sup>.**

### VIII.2.d. Effect of test speed

In addition to tear energy measurements made with a very low crosshead speed of  $1\text{mm}\cdot\text{min}^{-1}$ , crosshead displacement speeds of  $100$  and  $1000\text{mm}\cdot\text{min}^{-1}$  were applied to pre-notched pure shear samples. It was found that increasing the strain rate in this range leads to lower tear energies for all studied samples (Figure 222). The decrease with strain rate is of the same order whatever the interface type.

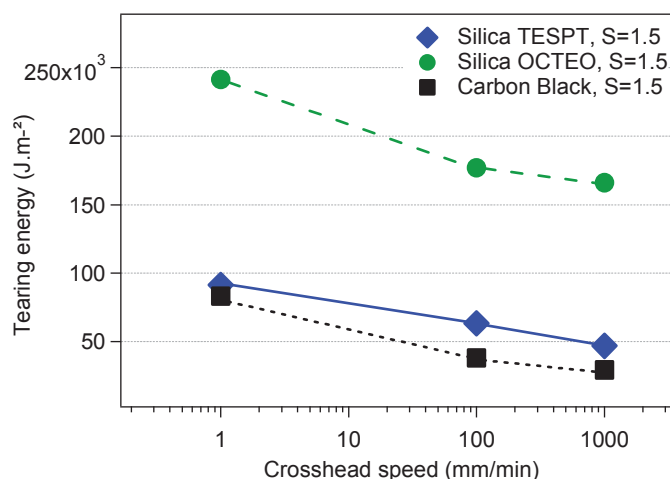


**Figure 222: Influence of strain rate (crosshead speed) on tearing energy for Reinforced NR samples (series 095-10).**

Sakulkaew et al<sup>123,124</sup> have studied the effect of strain rate on tear energy of NR and other rubbers thanks to very fast stretching experimental set-ups. In those studies, the tear energy is plotted against the rate of change of the energy release rate which is directly related to the strain rate for a given mechanical stress-strain response. In the case of Natural Rubber filled with 50phr of Carbon Black, they reported a similar decrease of the tear energy up to rates of change of the energy release rate of the order of  $100\text{kJ}\cdot\text{m}^{-2}\cdot\text{s}^{-1}$  to  $1000\text{kJ}\cdot\text{m}^{-2}\cdot\text{s}^{-1}$  depending on the crosslink density. Above those values, the tearing energy increases with strain rate due to suppression of strain-induced crystals.

In our experiments the highest crosshead speed applied ( $1000\text{mm}\cdot\text{min}^{-1}$ ) yields rates of change of approximately  $40\text{kJ}\cdot\text{m}^{-2}\cdot\text{s}^{-1}$ . The decreasing tear energy observed is thus in agreement with the tear energy regimes described by Sakulkaew et al.

### VIII.3. Study of the crack tip

Several characterization experiments were carried out to better understand the evolution of the crack tip during tear resistance. Firstly stretched filled NR was observed by electronic microscopy. Then Digital image correlation was carried out during tear test on Pure Shear samples in order to analyze the strain field at the crack tip and its evolution. The strain profiles are presented for several filled NR materials. Finally such DIC experiments are used to computed stress profiles at the crack tip (from strain profile and stress-strain curves obtained in

chapter IV). The size of crystallized zone at the crack tip could also be estimated based on SIC strain onset determined in chapter V.

*VIII.3.a. State of the crack tip*

Observations of the crack tip of a single edged notched tensile samples stretched to a macroscopic strain of approximately 50% were carried out by SEM. The crack tip shows an almost flat crack tip characteristic of the crack tip blunting in filled NR (Figure 223).

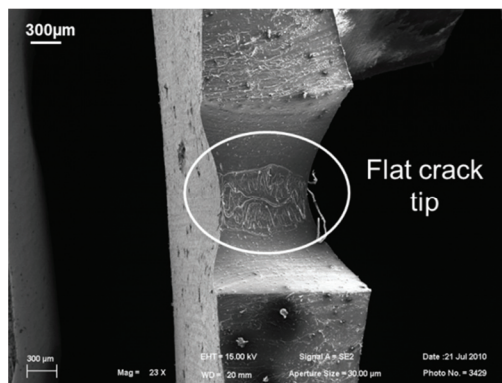


**Figure 223: Observation zone at the crack tip of a single edge notched tensile (SENT) sample stretched up to a macroscopic strain close to 50%.**

The crack tip blunting zone is the consequence of a first tear rotation whose edges are clearly visible on both samples observed in Figure 224. Then the propagation occurs in the sideways direction with the development of a highly stretched crack tip where strained regions organized in elliptical zone as reported by Le Cam et al<sup>171,172</sup>. The left image also enable us to observe the relaxed zone corresponding to a second tear rotation stressing out the fact that the forward and sideways propagation can occur at the same time.

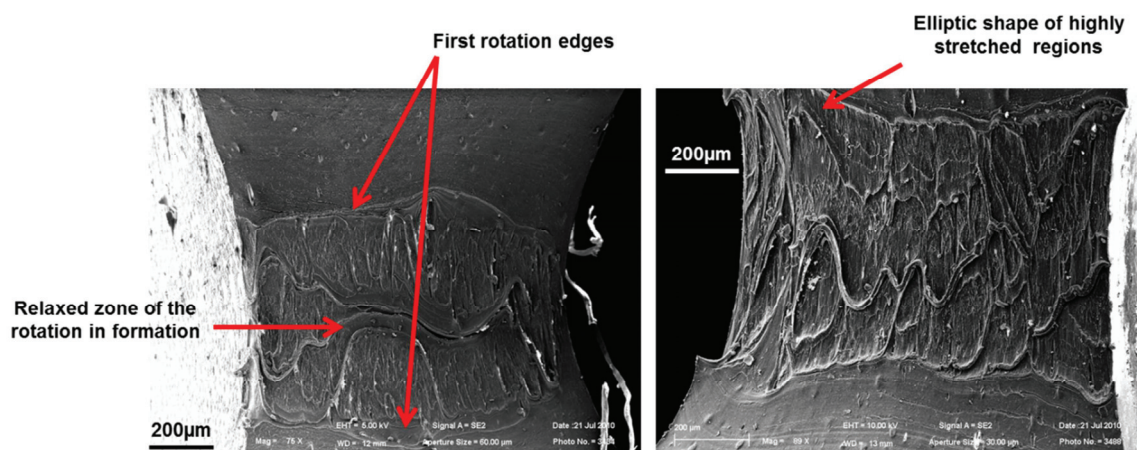


**Figure 224: Crack tip blunting in the case of two reinforced NR samples stretched at a macroscopic strain of the order of 50%.**

The state of the material in the relaxed zone due to the forward propagation (Figure 225 c)) is compared to the locally highly stretched state in the sideways propagation region (Figure 225 f)) where the crack tip continues to open. As the crack propagates forward, the fibrils observed in image f) are broken and lead to an un-stretched pattern as shown in image c).

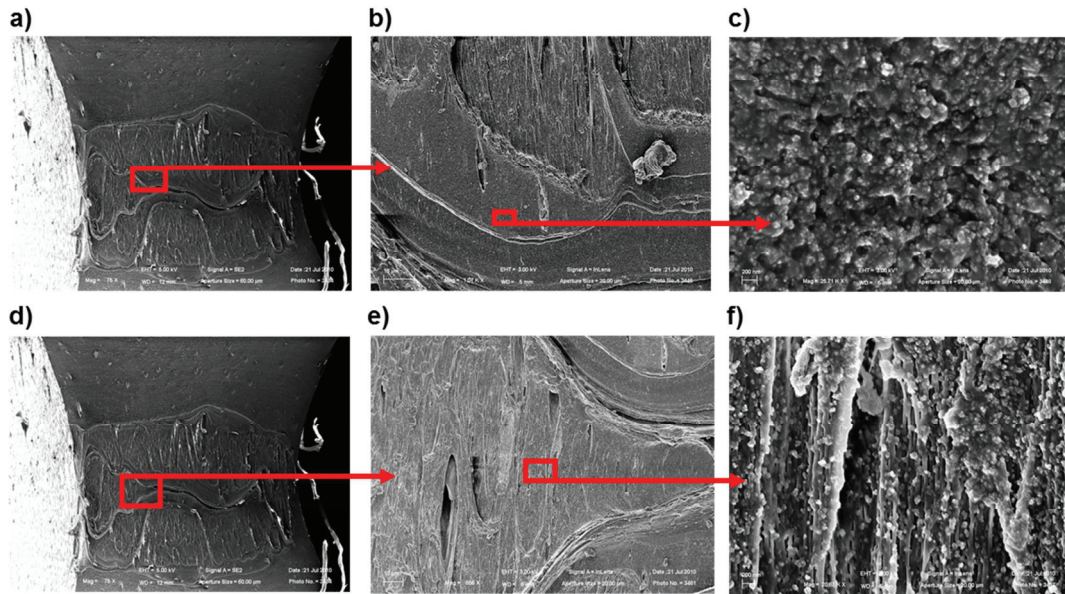


**Figure 225: SEM micrographs of the crack tip of a stretched single edge notched tensile sample. Images b) and c) show a region where the local strain is low due to the forward propagation of the crack (second rotation edge). Images e) and f) show a highly stretched region.**

The local state of extension is very heterogeneous at the crack tip in highly stretched zones (Figure 226). The filled rubber tends to organize in fibrils of a few hundred of nanometers containing the fillers with some regions that appear poorly stretched whereas in others the rubber matrix is submitted to very large strains between silica aggregates.

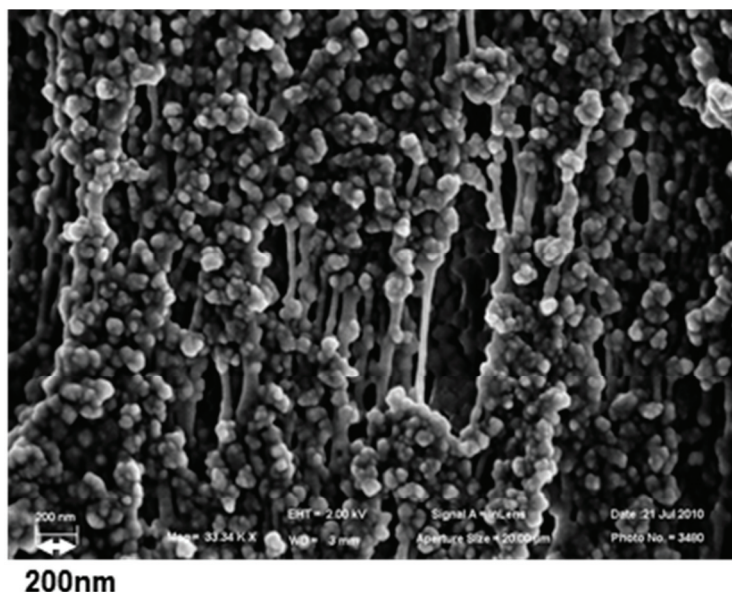


**Figure 226: Highly stretched zone as observed by SEM at the crack tip of a pre-notched Silica filled NR sample. (Magnification x33000).**

### *VIII.3.b. Strain amplification at the crack tip*

Note that the term “strain amplification” refers here to the intensification of the strain on the mesoscopic scale due to the stress concentration at the crack tip and is therefore completely different from the strain amplification on the microscopic scale (i.e. between fillers) described in chapter 5.

The strain amplification profiles are computed from digital image correlation applied to images recorded during tear tests in the Pure Shear geometry. In order to calculate the actual distance to the crack tip for each analyzed zone, a specific analysis zone is defined at the crack tip by the grey level pattern and its coordinates are obtained in all images. The coordinates of the analyzed zones are then simply subtracted to the crack tip coordinates in all recorded images up to failure. The strain field obtained for a Carbon Black NR sample under strain is shown in Figure 227: the strain field obtained is superposed to the image in b). The black line represents a section for which the strain profile is presented in a) as a function of the distance to the crack tip. The grey dashed lines mark out the beginning and end of the section in the strain field. Note that the maximal distance to crack tip recorded in this image is lower than the initial width of the sample (87.5 mm for this sample) due to the fact that the edge of the sample cannot be analyzed and also for some width reduction occurs showing that the sollicitation is not completely of a pure shear type but remains close to this case. The uniform local strain (except for the crack tip) is another indication that the theory of crack propagation in a sample in a pure shear sollicitation mode can be applied in our case (see chapter 2).

The strain amplification at the crack tip is quite important with a local strain that reaches 300% for the first point of the strain profile close to the crack tip. A local strain amplification factor of 3 is thus obtained in this sample at this macroscopic strain level. The size of the zone affected by

the crack tip is of the order of 5mm which is in agreement with the measurements of Mzabi<sup>173</sup> of an influence zone (ZI) in filled SBR having a similar geometry.

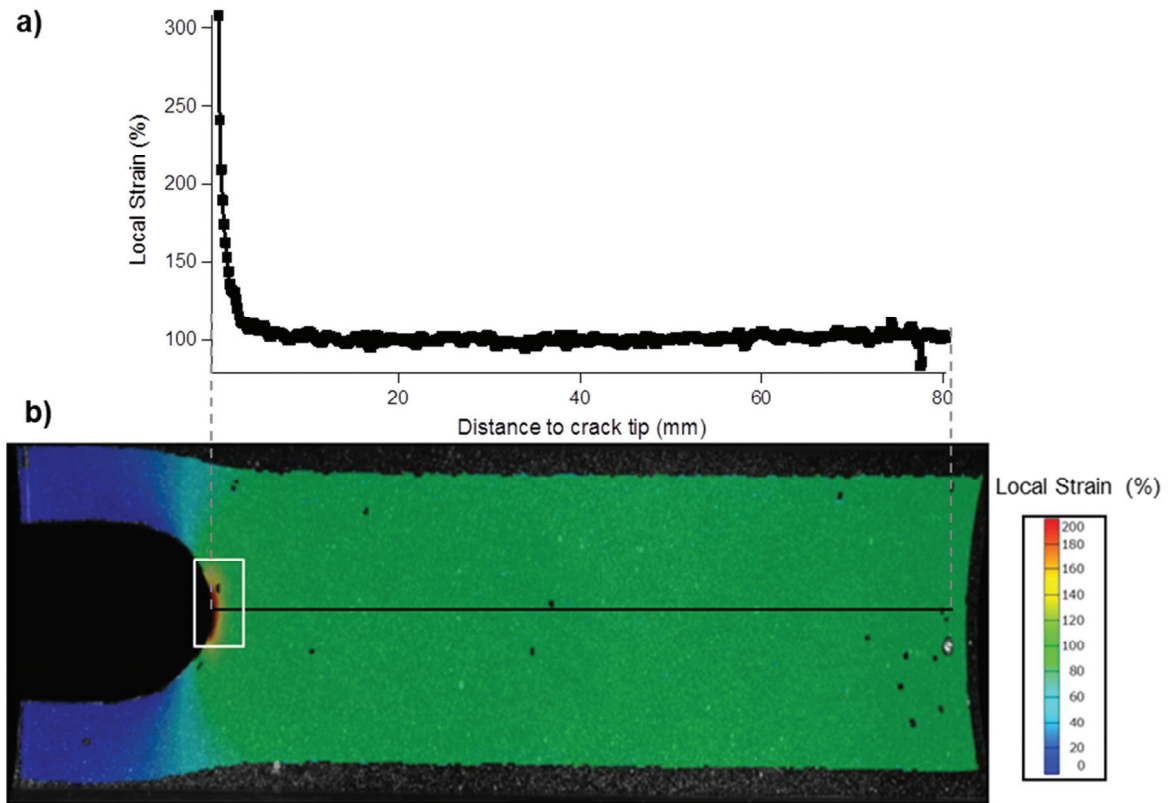


**Figure 227: a) Mesoscopic strain amplification profile (local strain versus distance to crack tip) for the complete Pure Shear sample (NR Carbon black) stretched up to a macroscopic strain of approximately 100%. b) Local strain distribution in the sample (strain fields), the black line shows the section of local strain plotted in a) and the white rectangle corresponds to the crack tip zone displayed in Figure 228.**

The strain profile in the near crack tip region is shown for four increasing macroscopic strains in Figure 228b. The size of the non-analyzed regions at the crack tip is of the order of 150  $\mu\text{m}$  in this case but can be higher in other cases. This zone is due to the fact that the facets cannot overlap the crack tip since no grey contrasts are to be found beyond the sample. The minimum size of this zone is thus equivalent to the overlapping of the facets and may be higher when a loss of contrast occurs in this highly stretched zone.

The four amplification profiles show that the size of the zone affected by the crack tip tend to increase with applied strain.

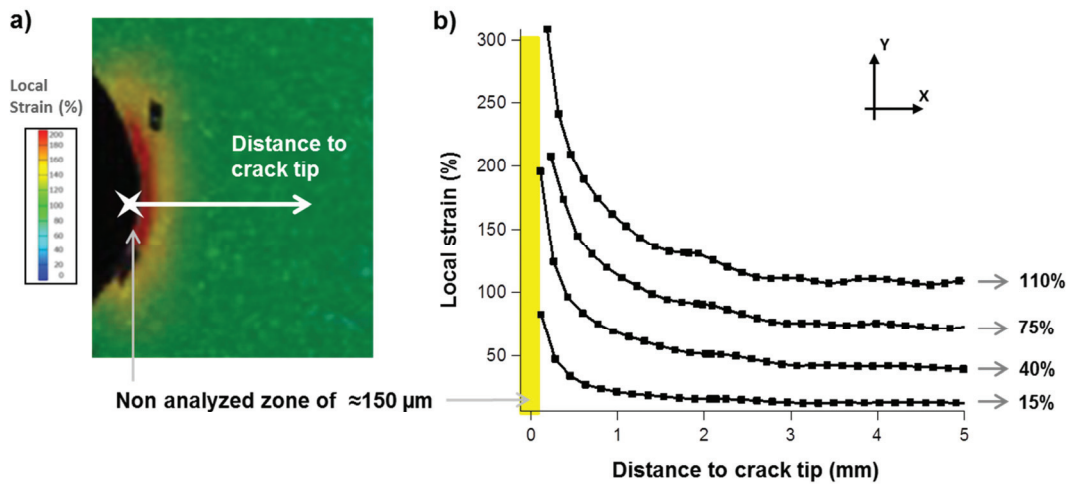


**Figure 228: a) Strain field as obtained from DIC during tear testing. b) Strain amplification profiles for four macroscopic strains (15; 40; 75 and 110%)**

The strain amplification profiles have been compared for three interfaces types and several macroscopic strains. Only three of them are plotted in Figure 229 for clarity reasons. The strain profile is in general easier to compute with Carbon Black filled sample since no whitening of the composite occurs at high deformation due to the strong light absorption provided by the carbon black. This explains why the strain profile can be determined closer to the crack tip in this case. The main observation that can be made from this comparison is that a steeper local strain profile is obtained for the highly reinforced samples (Carbon Black and Silica TESPT) compared to a Silica OCTEO NR sample.

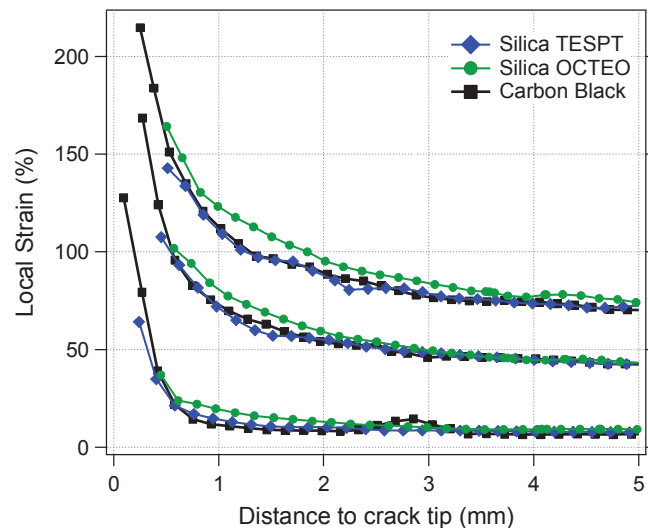


**Figure 229: Local strain profiles comparison for three macroscopic strains and three interfaces types (Silica TESPT, Silica OCTEO and Carbon Black of the sample series 095-10).**

The strain profiles have been fitted by a power law for each interface types and at different macroscopic strains. Examples of the fits are given for TESPT in Figure 230a, it can be noted that the singularity of the strain profile decreases with the applied strain. This is confirmed by the evolution of the exponent of the power law detailed in Figure 230b for the three tested interfaces. One remarks as well that the steeper strain profile is confirmed for the Carbon Black and Silica TESPT samples whatever the applied strain in this range.

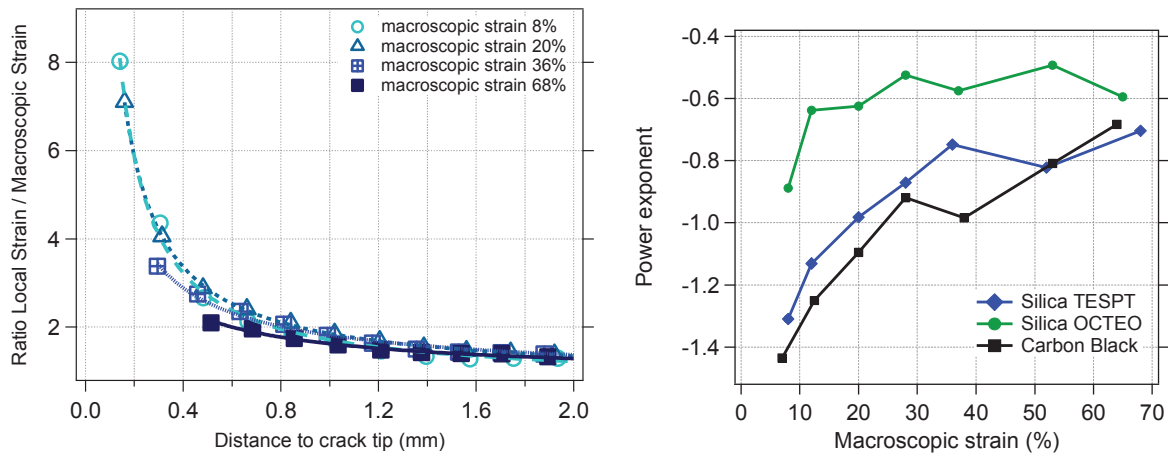


**Figure 230: Power law fits of the relative local strains at four different macroscopic strains for a Silica TESPT NR sample on a range of distances to crack tip from 0 to 5mm (sample series 095-10)**

The strain profiles were recorded up to the catastrophic propagation of the crack in another series of tests using another Silica TESPT sample series. The local strain obtained for the OCTEO and TESPT systems for several macroscopic strains are reported in Figure 231.

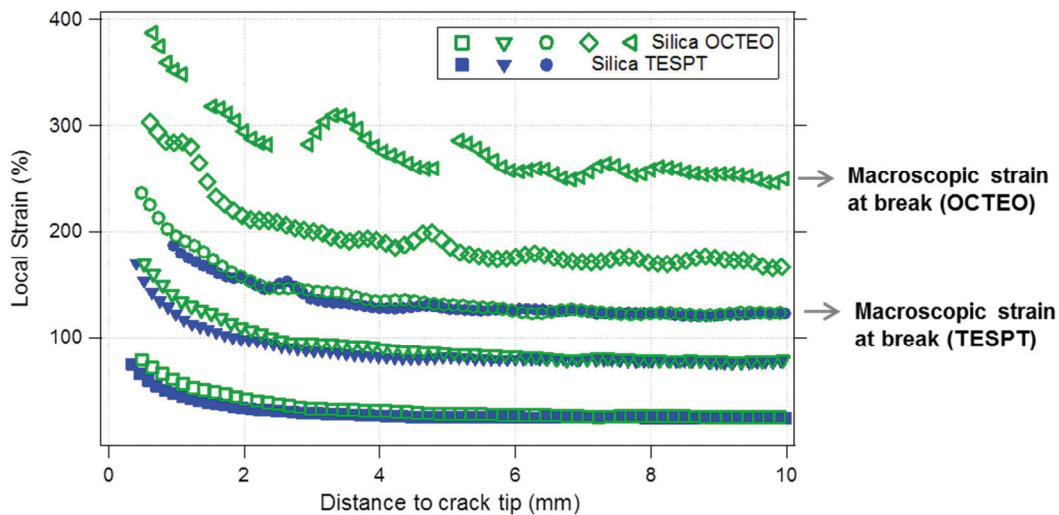


**Figure 231: Comparison local strain profiles for Silica OCTEO and Silica TESPT (respectively from sample series 095-10 and 030-11). Each maximum macroscopic strain presented corresponds to the last image taken before fracture.**

The macroscopic strain for the occurrence of the catastrophic crack propagation is almost twice higher for the NR Silica OCTEO sample and though some data lack in the strain profile, one can assume that the maximum local strain at the crack tip is also higher compared to TESPT.

### VIII.3.c. Local stress estimation at crack tip

The local stress has been computed from the strain profile and the simple un-notched tensile test curves relating stress and strain for each formulation. By using the un-notched uniaxial stress-strain curve, we make the assumption that the mechanical response of the filled rubber at the crack tip is similar to a uniaxially stretched stripe of rubber. Therefore we assume that the vicinity of the crack tip enables the rubber to deform in the X direction (conversely to the complete sample which behavior is assumed to follow the pure shear hypothesis: no reduction of the sample width).

Due to the higher modulus of samples with TESPT as interface agent, it is not surprising to find a higher local stress when compared to a Silica OCTEO sample at a fixed macroscopic strain (Figure 232). This plot shows that a strong interface leading to a higher reinforcement (higher modulus) induces a higher local stress at the crack tip for a given applied strain.

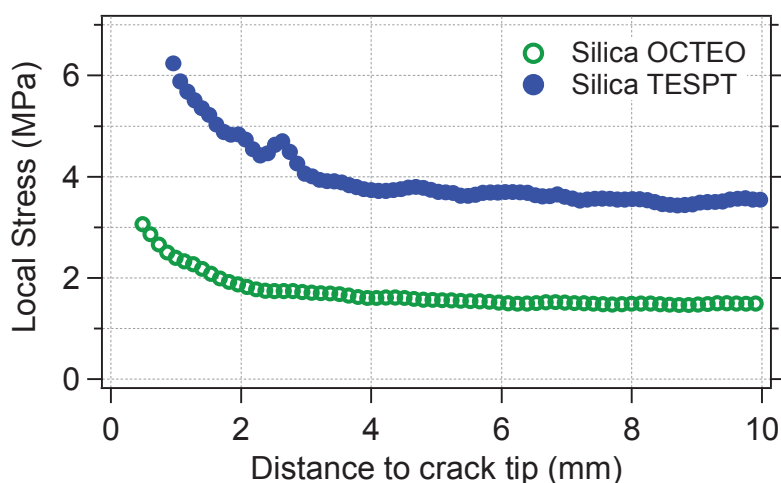


**Figure 232: Local stress profiles for a macroscopic strain of 125% based on strain profile and simple tensile stress-strain relationship for Silica OCTEO and Silica TESPT (respectively from sample series 095-10 and 030-11).**

Three stress profiles are now compared in Figure 233 and the highest local stresses curve was calculated from the last recorded strain profile before the crack propagation. In other words, the upper stress profiles correspond to the strain profiles at a macroscopic strain of respectively 125% and 250% for TESPT and OCTEO.

The strain profiles corresponding to the macroscopic strain at break in Figure 231 yield identical macroscopic stress which is in agreement with the tear stress-strain results presented in VIII.2.b. The stress profiles for a given macroscopic stress are very similar for the two silica systems suggesting that the stress profile is related to the geometry of the notched samples and the strain

profiles differ due to each stress-strain behavior. It can be proposed that the local stress at break is similar for TESPT and OCTEO samples.

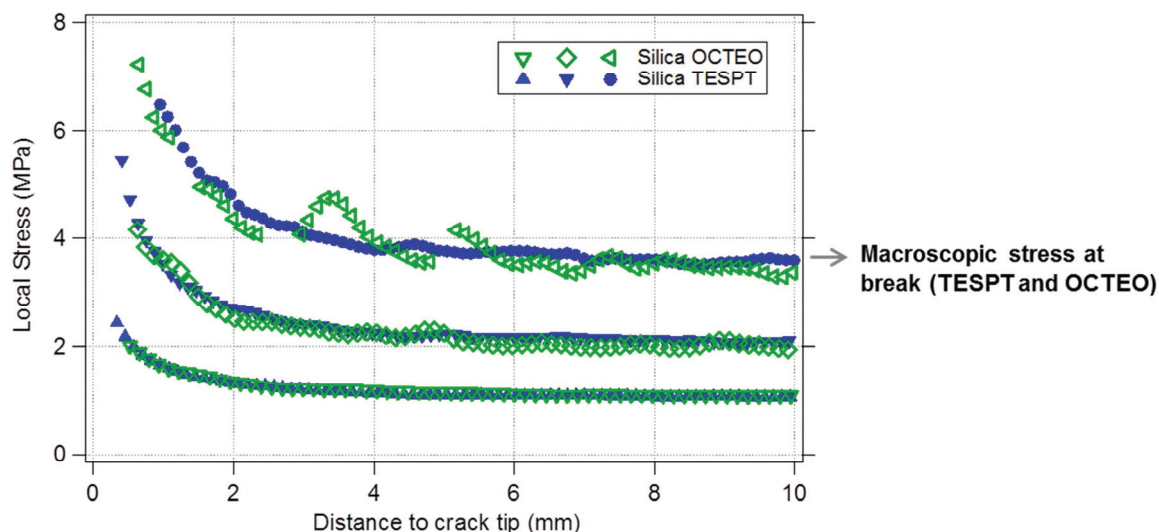


**Figure 233: Comparison local stress profiles based on strain profile and simple tensile stress-strain relationship for Silica OCTEO and Silica TESPT (respectively from sample series 095-10 and 030-11). Each maximum macroscopic stress presented corresponds to the last image taken before fracture.**

#### *VIII.3.d. Crystallized zone at crack tip*

Based on the SIC onset data presented in chapter V, it is possible to estimate the size of the crystallized zone at the crack tip during tear experiments by making the assumption that the SIC behavior of the near crack tip region is similar to a un-notched stripe of rubber under strain. The size of the crystallized zone ahead of the crack tip in the direction perpendicular to the strain was estimated by assuming a local SIC onset at 80% of strain (Figure 234). As a matter of fact, the filled rubber has not been precycled in the case of Pure-Shear tests thus the onset of crystallization is assumed to be around 80% (see chapter V). Note that for a given macroscopic strain, the crystallized zone depth would be smaller if considering the SIC onset after precycling. Some crystallites start to appear at a macroscopic strain of the order of 20% which seems to correspond to the beginning of the crack tip blunting and it can be proposed that the sideways propagation may occur above this macroscopic strain onset.

Once the macroscopic strain has reached 80%, some crystallites may appear far from the crack tip as well and the crystallized zone covers almost all the sample even if the highest crystallized fractions are located at the crack tip.

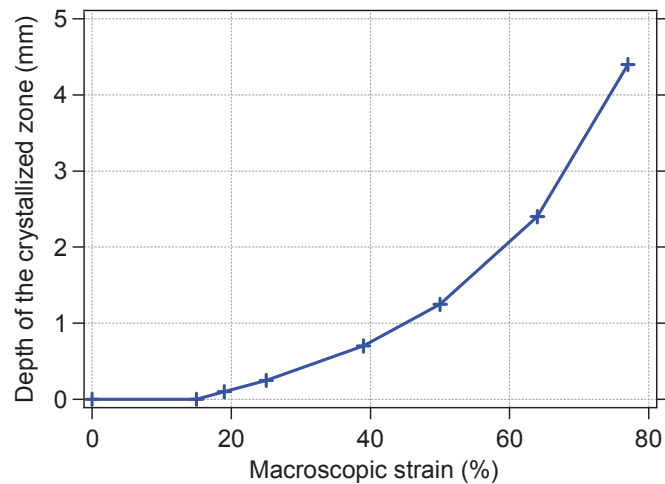


**Figure 234: Estimation of the crystallized zone depth in a non-precycled NR Silica TESPT sample as a function of applied macroscopic strain.**

### VIII.3.e. Crystallized fraction measurement at crack tip

The Crystallized fraction around the crack tip has been directly measured on pre-notch stripes of Silica filled NR but the stretching device did not allow us to test Pure Shear samples. Therefore direct comparisons of the crystallized zone cannot be carried out for the very different strain fields applied in the two cases.

The reinforced NR stripe is stretched up to a fixed macroscopic strain in a specific stretching device (Figure 235). The macroscopic strain is measured thanks to distance between white marks made on the sample.

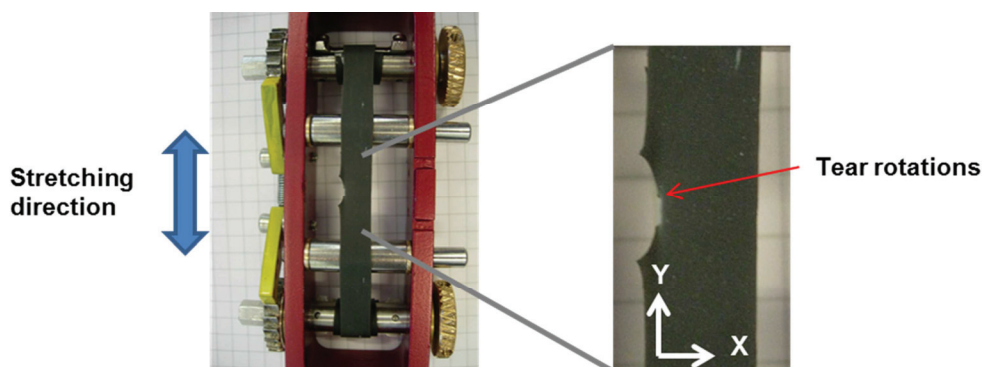


**Figure 235: Pre-notched filled NR stripe stretched in the extension device. The device is then mounted on a translation stage moving in the X and Y direction.**

Once the sample has been stretched up to the fixed strain, the device is mounted on the translation stage in order to map the crystallized fraction in directions X and Y (Figure 236). The diameter of the X-ray beam is 50 $\mu$ m enabling to plot crystallized fraction with an important

precision. A mapping of the absorption of the direct X-ray beam is also carried out and used to check precisely the position of the crack tip in the X-Y plane.

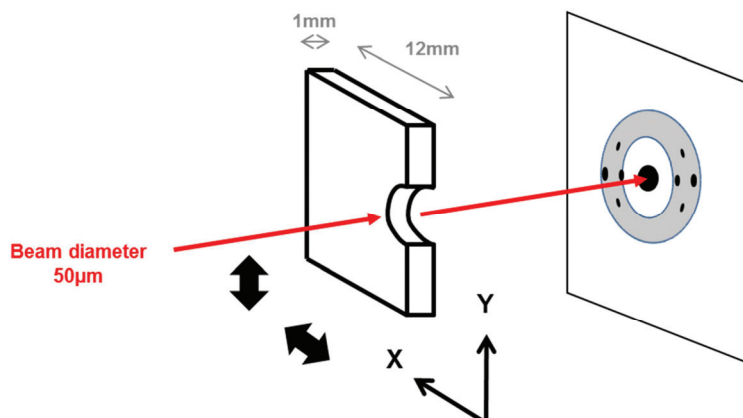


**Figure 236: Crystallized fraction mapping around the crack tip. The initial notch made on the sample is 2.5 mm long.**

The beam absorption mapping at a given applied strain (200%) and the crystallized fraction measurements along the X direction for four macroscopic strains are shown in Figure 237.

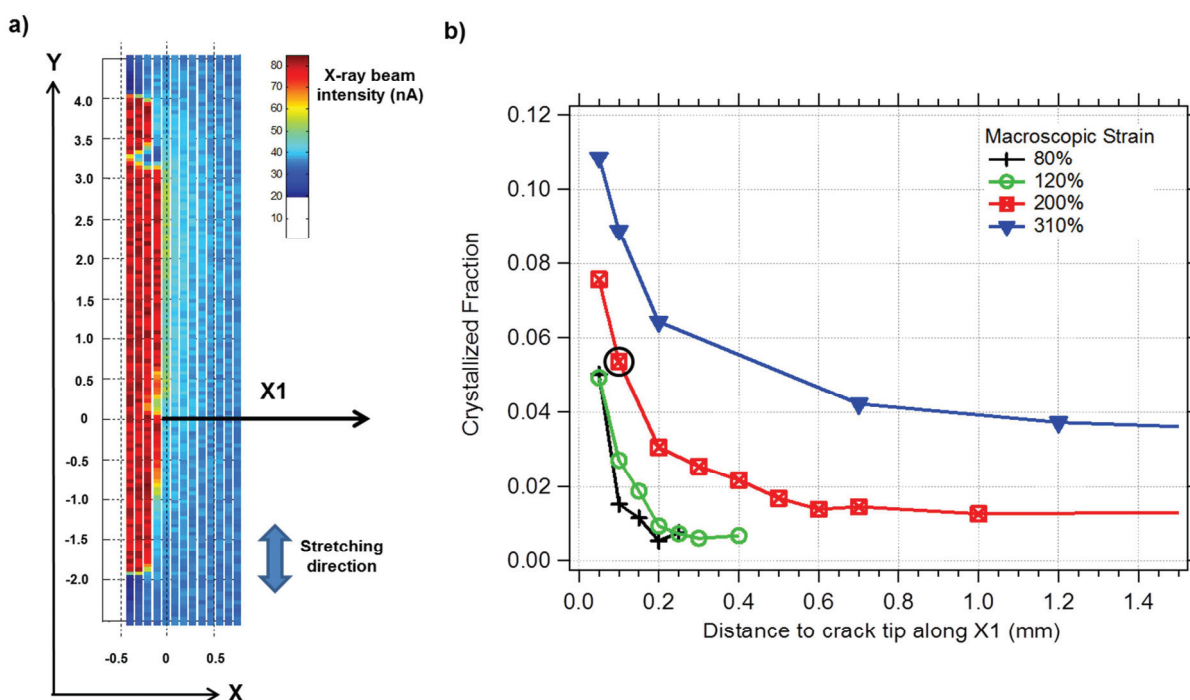


**Figure 237: a) Beam absorption mapping for a macroscopic strain of 200%. b) Crystallized fraction as a function of distance to crack tip (X1) for a pre-notched Silica TESPT NR stripe (series 021-10) stretched at four macroscopic strains. The circle identifies a common measurement in Figure 238 b).**

The absorption measurements indirectly show the shape of the crack tip and the local strain state. As a matter of fact, the thicker the rubber and the lower the transmitted beam (blue spots). Some tear rotation edges (as shown in Figure 224 and Figure 225) can be identified (at Y values being -0.8;0.2 and 3.3 mm). The strong increase of the crystallized fraction close to the crack tip is in agreement with the strain amplification at the crack tip. Conversely to the crystallites content profiles performed on notched unfilled NR by Trabelsi et al<sup>115</sup>, there is no evidence of a zone of maximum crystallinity in our reinforced samples. Our results compare fairly well with the previous works of Lee and Donovan<sup>114</sup> on Carbon Black filled NR even if the crystalline content at the crack tip is lower in our case.

The crystallized fraction of rubber and the deviation of the crystallites orientation from the stretching direction denoted  $\Delta\phi$  are reported as a function of the distance Y1 (Figure 238). Note that due to the slightly curved shape of the crack tip, the sweep in Y direction was performed at value X1 100 $\mu$ m (see circle in Figure 237).

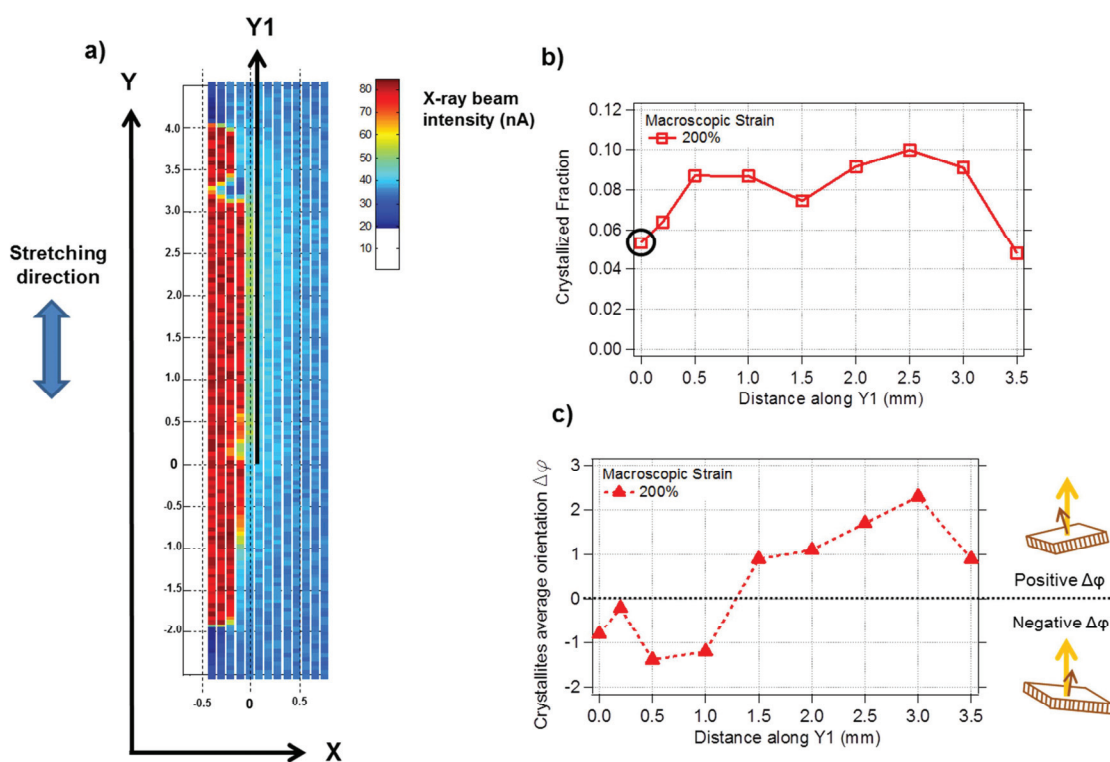


**Figure 238 : Macroscopic strain of 200%: a) Beam absorption mapping. b) Crystallized fraction as a function of distance Y1 for a pre-notch Silica TESPT NR stripe (series 021-10). The circle identifies a common measurement in Figure 237. c) Deviation of crystallites average orientation  $\Delta\phi$  from the loading direction as a function of distance Y1.**

Together with the absorption mapping in a), the plot of the crystallized fraction highlights the relationship between local extension state and crystallized fraction. The crystallized fraction is the highest in the regions where the filled rubber thickness is the lowest (green/yellow dots) and the lower crystallinity at Y=1.5mm may mark the presence of a forward crack developing (further leading to a tear rotation).

This observation is confirmed by the change in the average crystallites orientation  $\Delta\phi$ . As a matter of fact, the sign of  $\Delta\phi$  change at roughly  $Y1=1.3\text{mm}$  indicating a local strain direction change. This position may thus mark as the center of the crack tip where the crack propagation is likely to occur.

#### **VIII.4. Conclusion**

The study of tear resistance in unfilled and filled NR has shown that crack propagation is unstable in this material.

Strong differences between tear energies for samples with and without catastrophic propagation in pure NR highlighted that the unstable propagation can lead to some difficulties in the measurement of the tear energy. An optimum of crosslink density in terms of tear energy was found in pure NR. The effect of crosslink density in pure NR was found to be more important on tear resistance than it was on resistance to failure in un-notched pure NR samples (chapter VII).

As far as reinforced Natural Rubber is concerned, the tear energy is dramatically increased as compared to unfilled NR. The tear energy for the Silica-OCTEO system is strongly higher than for the other filled NR samples due to a similar stress at break but a higher strain at break. The tear energy measurements for different crosslink densities show that there is an optimum of crosslink density and that similarly to unfilled NR this optimum is in agreement with un-notched ultimate properties. The influence of the strain rate on tear resistance was also investigated. Whatever the rubber-filler interface, the tear energy was found to decrease with strain rate. This could be understood as an effect of SIC kinetics retardation at the crack tip.

The mesoscopic strain amplification profiles as a function of distance to crack tip were analyzed by means of digital image correlation during the tear tests. The corresponding stress profiles were estimated from stress-strain curves and the stress at the crack tip was found to be similar for Silica-TESPT and Silica-OCTEO samples.

The strain profiles were also used to estimate the size of the crystallized zone at crack tip as a function of the macroscopic strain. X-ray diffraction experiments at the crack tip were also performed to measure the crystalline content at the crack tip in filled NR stripes.

---

## IX. General Conclusion

After introducing the general context of this study and the background in the field of rubber reinforcement, the compounding procedures were detailed in order to highlight the effect of the processing steps on the obtained properties.

Several strain regimes can be defined on the basis of the mechanical behavior of filled and unfilled rubber. The influence of different material variables such as crosslink density, filler fraction, filler specific area and interface type on the mechanical properties is studied in these strain regimes.

In the linear regime, a strong increase of the modulus is associated to the filler fraction and the specific surface suggesting the important role played by the distances between aggregates.

The magnitude of the Payne effect was found to be the highest for Carbon Black as compared to Silica. The use of a coupling agent such as NSC with Silica was found to decrease the Payne effect which could be related to a better distribution of the silica aggregates. The higher strain at the loss modulus peak for this system compared to Silica-TESPT may confirm that the distribution process of the fillers is affected by the coupling agent.

The modulus in the large strain regime has been studied. The modification of the stress-strain curve shape with increasing filler volume fraction was understood in terms of an heterogeneous local strain amplification. The influence of the interface strength on the modulus at high strain has been evidenced, the Silica-OCTEO system showing a weak but not inexistent reinforcement effect.

Regarding the Strain-induced Crystallization behavior, series of unfilled and filled rubber samples have been studied by in-situ X-ray diffraction on a tensile device recording stress and strain up to failure. Thanks to a thorough analysis of the diffraction and scattering patterns, we measured the crystallized fraction, crystallite orientation and orientation of the chain segments in the amorphous phase through the associated anisotropic scattering halo.

The crystalline content versus strain does not strongly depend on the crosslink density in unfilled NR conversely to the orientation of the amorphous phase that follows the prediction of the rubber elasticity theory before the SIC onset and then stabilizes as the formation of crystallites proceeds.

As far as the reinforced NR samples are concerned, the presence of fillers was proved to strongly modify the formation of crystallites and the role of the interface was stressed out. Firstly, the strain onset decreases with fillers and the shift was found to be more pronounced for stronger interfaces (Carbon Black and Silica-TESPT). The slope of crystalline content versus strain and the crystalline content at break are reduced for filled samples. This could be understood as the combination of two phenomena being first a restriction of the rubber chains ability to crystallize in presence of filler due to higher constraints on their mobility. This assumption was supported by measurements of the decrease of crystallite size and orientation along the stretching direction when adding fillers. Secondly the strain amplification between fillers is thought to be strongly heterogeneous thus accounting for the lower slope of crystalline content versus strain.

In another part of this work, the kinetics of Strain-Induced Crystallization and Melting have been studied by a newly developed in-situ oscillating X ray scattering device equipped with a stroboscopic acquisition system. After detailing the principle of the tests and the practical set up, the results obtained on NR with two crosslink densities were presented. We highlight the fact

that the average strain promotes the crystallization and to a lower extent the melting kinetics. According to our measurements on a sample with a low crosslink density, decreasing the crosslink density increases the melting kinetics. A logarithmic dependence of crystallization on solicitation time has been found in the case of high amplitude cycles.

We further investigated the relationships between the segmental orientation, the true stress, the equilibrium swelling degree and crosslink density as determined respectively by X-ray scattering, mechanics, equilibrium swelling experiments and Double-Quantum NMR. Those measurements being all related to the local chains orientation, they were found to only differ due to different entanglements contributions at different characteristic probing frequencies.

A similar comparison was carried out with reinforced samples. Whatever the measurement technique, a higher apparent crosslink density (thus a higher local chain stretching) was found for filled NR samples compared to unfilled NR samples at an equivalent crosslink density. This was interpreted in terms of strain amplification.

Strain amplification factors have thus been determined as the ratio of the reinforced NR response versus pure NR response. A fourth amplification factor based on the shift on the crystallization onset was added. In order to account for the discrepancies observed between the different amplification factors, it has been proposed that the portion of the strain distribution relevant for each technique is different. The equilibrium swelling and amorphous orientation would probe the entire chains whereas the true stress and the crystallization onset could only account for the highly stretched regions of the rubber. In this interpretation scheme, a strongly heterogeneous strain distribution was pointed out for Carbon Black compared to Silica-TESPT, Silica-OCTEO presenting the most homogeneous distribution of local strains.

Furthermore, the shear modulus in linear and small strains regimes was reported to the crosslink density estimated by NMR and with segmental orientation determined by X-ray scattering. This suggested that the reinforcement in the small strain regime results from the combination of a strain amplification contribution and a contribution that does not depend on the crosslink density of the rubber matrix. We understand this second term as the modulus increase brought by low non-rubbery (glassy) bridges between fillers.

In traction-retraction cycles, the hysteresis normalized by the energy brought to the sample during traction was found to depend on the interface type. Before the SIC strain onset, Silica-OCTEO lead to a strong dissipation compared to coupled silica. The steep dissipation increase in the large strains regime above the SIC onset is in agreement with the crystallized fraction measured with X-ray diffraction experiments.

Finally in situ tensile measurements of the X-ray beam absorption and thickness reduction were used to calculate the decrease of the absorption coefficient of rubber samples during stretching which was interpreted as a cavities formation phenomenon. Higher fractions of cavities were detected thanks to this technique in reinforced samples as compared to pure rubber.

Tear experiments have been performed on Pure Shear pre-notched samples at various test speeds. A strong increase in the tearing energy was obtained for reinforced NR samples as compared to pure NR samples. As regards the effect of the filler/polymer interface, Carbon black and Silica-TESPT exhibit similar strength whereas Silica-OCTEO requires a higher energy to propagate the crack. The tear energy measurements for different crosslink densities show that there is an

optimum of crosslink density and that similarly to unfilled NR this optimum is in agreement with un-notched ultimate properties.

The strain amplification profiles as a function of distance to crack tip were obtained by means of digital image correlation applied to images recorded during the tear tests. Assuming a stress-strain relationship locally equivalent to the bulk, the stress profiles could be estimated. The obtained results for different rubber/filler interface types tend to show that the tear propagation occurs for an equivalent stress level at the crack tip. The strain profiles were also used to estimate the size of the crystallized zone at crack tip. Additional X-ray diffraction mapping were carried out showing the relationship between the local state of extension and the crystallites content and orientation.

---

## X. Bibliography

- (1) *The Pneumatic Tire*; Gent, A. N.; Walter, J. D., Eds.; National Highway and Traffic Safety Administration, **2006**.
- (2) Pike, E. *Opportunities to Improve Tire Energy Efficiency*; **2011**.
- (3) Daniel, M. In *Multi-scale dynamics of structured polymeric materials*; **2010**.
- (4) Wolff, S. *Kautschuk Gummi Kunststoffe* **1981**, *34*, 280–284.
- (5) Rauline, R. Rubber compounds and tires made on such compounds **1991**.
- (6) Wang, M. *Kautschuk Gummi Kunststoffe* **2007**, *60*, 438–443.
- (7) Klüppel, M.; Heinrich, G. *Rubber Chemistry and Technology* **2000**, *73*, 578–606.
- (8) Persson, B. N. J. *Journal of Chemical Physics* **2001**, *115*, 3840–3861.
- (9) Wang, M. *Rubber Chemistry and Technology* **1998**, *71*, 520–589.
- (10) *EU Tire Label Tire Performance Label : A Global Trend*; **2011**.
- (11) *Science and Technology of Rubber: Third Edition*; Mark, J. E.; Erman, B.; Eirich, F. E., Eds.; **2005**.
- (12) Saalwächter, K. *Rubber Chemistry and Technology* **2012**, *85*, 350–386.
- (13) Klüppel, M.; Menge, H.; Schmidt, H.; Schneider, H.; Schuster, R. H. *Macromolecules* **2001**, *34*, 8107–8116.
- (14) Halary, J. L.; Laupêtre, F.; Monnerie, L. *Mecanique des matériaux polymères*; Belin.; **2008**.
- (15) Flory, P. J. *Principle of Polymer Chemistry*; Press, C. U., Ed.; **1953**.
- (16) Kuhn, W. *Journal of Polymer Science* **1946**, *1*, 380–388.
- (17) Flory, P. J. *Journal of Chemical Physics* **1951**, *19*, 1435–1439.
- (18) James, H. M.; Guth, E. J. *Journal of Chemical Physics* **1943**, *11*, 455–481.
- (19) Edwards, S. F. *Proceedings of the Physical Society* **1967**, *92*, 9–16.

- (20) Treloar, L. R. G. *The Physics of Rubber Elasticity*; Clarendon Press: Oxford, U., Ed.; 3rd ed.; Clarendon Press: Oxford, UK: Oxford, **1975**; Vol. 8.
- (21) Erman, B.; Flory, P. J. *Macromolecules* **1982**, *15*, 806–811.
- (22) Rubinstein, M.; Panyukov, S. *Macromolecules* **2002**, *35*, 6670–6686.
- (23) Mooney, J. *Journal of Applied Physics* **1940**, *11*, 582–592.
- (24) Mark, J. E. *Rubber Chemistry and Technology* **1975**, *48*, 495–512.
- (25) Erman, B.; Wagner, W.; Flory, P. J. *Macromolecules* **1980**, *13*, 1554–1558.
- (26) Kloczkowski, A.; Mark, J. E.; Erman, B. *Macromolecules* **1995**, *28*, 5089–5096.
- (27) Boyce, M. C.; Arruda, E. M. *Rubber Chemistry and Technology* **2000**, *73*, 504–523.
- (28) Flory, P. J.; Rehner, J. *Journal of Chemical Physics* **1943**, 512–520.
- (29) Smallwood, H. M. *Journal of Applied Physics* **1944**, *15*, 758–766.
- (30) Guth, E. J.; Gold, O. *Physical Review* **1938**, *53*, 322–322.
- (31) Medalia, A. I. *Rubber Chemistry and Technology* **1987**, *60*, 45–61.
- (32) Maier, P. G.; Göritz, D. *Kautschuk Gummi Kunststoffe* **1996**, *49*, 18–21.
- (33) Chabert, E. Propriétés mécaniques de nanocomposites à matrice polymère: Approche expérimentale et modélisation (thesis), INSA de Lyon, **2002**.
- (34) Heinrich, G.; Klüppel, M. *Kautschuk Gummi Kunststoffe* **2004**, *57*, 452–454.
- (35) Merabia, S.; Sotta, P.; Long, D. R. *Macromolecules* **2008**, *41*, 8252–8266.
- (36) Payne, A. R. *Reinforcement of elastomers*; G Kraus Edition, Ed.; Interscien.; New-York, **1965**.
- (37) Kraus, G. *Journal of Applied Polymer Science* **1984**, *39*, 75–92.
- (38) Payne, A. R.; Whittaker, R. E. *Rubber Chemistry and Technology* **1971**, *44*, 440–478.
- (39) Medalia, A. I. *Rubber Chemistry and Technology* **1986**, *59*, 432–454.
- (40) Funt, J. M. *Rubber Chemistry and Technology* **1988**, *61*, 842–865.
- (41) Luginsland, H.-D. *Rubber Chemistry and Technology* **2002**, *75*, 563–580.

- (42) Wagner, M. P. *Rubber Chemistry and Technology* **1976**, *49*, 703–774.
- (43) O'Brien, J.; Cashell, E.; Wardell, G. E.; McBrierty, V. J. *Macromolecules* **1976**, *9*, 653–660.
- (44) Coran, A. Y.; Donnet, J.-B. *Rubber Chemistry and Technology* **1992**, *65*, 1016–1041.
- (45) Freund, B.; Niedermeier, W. *Kautschuk Gummi Kunststoffe* **1998**, *51*, 444–449.
- (46) Wolff, S.; Wang, M. *Rubber Chemistry and Technology* **1991**, *65*, 329–342.
- (47) Wolff, S.; Wang, M. *Kautschuk Gummi Kunststoffe* **1994**, *47*, 102–107.
- (48) Klüppel, M.; Schuster, R. H.; Heinrich, G. *Rubber Chemistry and Technology* **1997**, *70*, 243–255.
- (49) Sternstein, S. S.; Zhu, A.-J. *Macromolecules* **2002**, *35*, 7262–7273.
- (50) Leblanc, J. L. *Progress in Rubber and Plastics Technology* **1994**, *10*, 112–129.
- (51) Marceau, S.; Brown, D.; De Puydt, Y.; Albérola, N. D. *Polymer* **2002**, *43*, 5577–5586.
- (52) Gauthier, C.; Reynaud, E.; Vassoile, R.; Ladouce-Stelandre, L. *Polymer* **2004**, *45*, 2761–2771.
- (53) Guy, L.; Bomal, Y.; Ladouce-Stelandre, L.; Cochet, P. *Kautschuk Gummi Kunststoffe* **2005**, *58*, 43–49.
- (54) Berriot, J.; Montes, H.; Lequeux, F.; Long, D. R.; Sotta, P. *Macromolecules* **2002**, *35*, 9756–9762.
- (55) Berriot, J.; Montes, H.; Lequeux, F.; Long, D. R.; Sotta, P. *Europhysics Letters* **2003**, *64*, 50–56.
- (56) Berriot, J.; Lequeux, F.; Montes, H.; Pernot, H. *Polymer* **2002**, *43*, 6131–6138.
- (57) Gusev, A. A. *Macromolecules* **2006**, *39*, 5960–5962.
- (58) Merabia, S.; Long, D. R. *The European physical journal. E, Soft matter* **2002**, *9*, 195–206.
- (59) Dequidt, A.; Long, D. R.; Sotta, P.; Sanseau, O. *The European physical journal. E, Soft matter* **2012**, *35*, 1–22.
- (60) Mujtaba, A.; Keller, M.; Ilisch, S.; Radusch, H.-J.; Thurn-Albrecht, T.; Saalwächter, K.; Beiner, M. *Macromolecules* **2012**, *45*, 6504–6515.

- (61) Guy, L.; Daudey, S.; Cochet, P.; Bomal, Y. *Kautschuk Gummi Kunststoffe* **2009**, 383–391.
- (62) Montes, H.; Chaussée, T.; Papon, A.; Lequeux, F.; Guy, L. *The European physical journal. E, Soft matter* **2010**, 31, 263–268.
- (63) Papon, A.; Montes, H.; Lequeux, F.; Oberdisse, J.; Saalwächter, K.; Guy, L. *Soft Matter* **2012**, 8, 4090–4096.
- (64) Frohlich, J.; Niedermeier, W.; Luginsland, H.-D. *Composites Part A: Applied Science and Manufacturing* **2005**, 36, 449–460.
- (65) Ramier, J.; Gauthier, C.; Chazeau, L.; Stelandre, L.; Guy, L. *Journal of Polymer Science: Part B: Polymer Physics* **2007**, 45, 286–298.
- (66) Mihara, S. Reactive processing of silica-reinforced rubber tire (thesis), University of Twente, **2009**.
- (67) Mullins, L. *Rubber Chemistry and Technology* **1948**, 21, 281–300.
- (68) Bueche, F. *Journal of Applied Polymer Science* **1960**, 4, 107–114.
- (69) Godin, N.; Chaki, S.; Courbon, J.; Deschanel, S.; Gillet, S.; Gautier, B. *Polymer Testing* **2009**, 28, 103–105.
- (70) Dannenberg, E. M. *Rubber Chemistry and Technology* **1975**, 48, 410–444.
- (71) Trabelsi, S.; Albouy, P.-A.; Rault, J. *Macromolecules* **2003**, 36, 9093–9099.
- (72) Dupres, S.; Long, D. R.; Albouy, P.-A.; Sotta, P. *Macromolecules* **2009**, 42, 2634–2644.
- (73) Chenal, J.-M.; Gauthier, C.; Chazeau, L.; Guy, L.; Bomal, Y. *Polymer* **2007**, 48, 6893–6901.
- (74) Gabrielle, B. Etude du renforcement et de la résistance à la propagation d’entaille dans les élastomères renforcés (thesis), Université Lyon I, **2010**.
- (75) Clément, F.; Bokobza, L.; Monnerie, L. *Rubber Chemistry and Technology* **2001**, 74, 847–870.
- (76) Lapra, A.; Clément, F.; Bokobza, L.; Monnerie, L. *Rubber Chemistry and Technology* **2003**, 76, 60–81.
- (77) Medalia, A. I.; Kraus, G. In *Science and Technology of Rubber*; Mark, J. E.; Erman, B.; Eirich, F. R., Eds.; **1994**.

- (78) Ramier, J. Comportement mécanique d'élastomères chargés, influence de l'adhésion charge-polymère, influence de la morphologie (thesis), Université Lyon 1, **2004**.
- (79) Zhang, H.; Scholz, A. K.; Crevoisier, J.; Vion-loisel, F.; Besnard, G.; Hexemer, A.; Brown, H. R.; Kramer, E. J.; Creton, C. *Macromolecules* **2012**, *45*, 1529–1543.
- (80) De Crevoisier, J.; Besnard, G.; Merckel, Y.; Zhang, H.; Vion-Loisel, F.; Caillard, J.; Berghezan, D.; Creton, C.; Diani, J.; Brieu, M.; Hild, F.; Roux, S. *Polymer Testing* **2012**, *31*, 663–670.
- (81) Valentín, J. L.; Carretero-González, J.; Mora-Barrantes, I.; Chassé, W.; Saalwächter, K. *Macromolecules* **2008**, *41*, 4717–4729.
- (82) Chassé, W.; Lang, M.; Sommer, J.-U.; Saalwächter, K. *Macromolecules* **2012**, *45*, 899–912.
- (83) Kraus, G. *Journal of Applied Polymer Science* **1963**, *7*, 861–971.
- (84) Valentín, J. L.; Mora-Barrantes, I.; Carretero-González, J.; Lopez-Manchado, M. A.; Sotta, P.; Long, D. R.; Saalwächter, K. *Macromolecules* **2010**, *43*, 334–346.
- (85) Mora-Barrantes, I.; Ibarra, L.; Rodriguez, A.; González, L.; Valentín, J. L. *Journal of Materials Chemistry* **2011**, *21*, 17526–17533.
- (86) Mora-Barrantes, I.; Rodriguez, A.; Ibarra, L.; González, L.; Valentín, J. L. *Journal of Materials Chemistry* **2011**, *21*, 7381–7392.
- (87) Huneau, B. *Rubber Chemistry and Technology* **2011**, *84*, 425–452.
- (88) Persson, B. N. J.; Albohr, O.; Heinrich, G.; Ueba, H. *Journal of Physics: Condensed Matter* **2005**, *17*, 1071–1142.
- (89) Toki, S.; Sics, I.; Ran, S.; Liu, L.; Hsiao, B. S.; Murakami, S.; Senoo, K.; Kohjiya, S. *Macromolecules* **2002**, *35*, 6578–6584.
- (90) Trabelsi, S.; Albouy, P.-A.; Rault, J. *Macromolecules* **2003**, *36*, 7624–7639.
- (91) Bekkedhal, N.; Wood, L. A. *Industrial & Engineering Chemistry* **1941**, *33*, 381–384.
- (92) Chenal, J.-M.; Chazeau, L.; Bomal, Y.; Gauthier, C. *Journal of Polymer Science Part B: Polymer Physics* **2006**, *45*, 955–962.
- (93) Miyamoto, Y.; Yamao, H.; Sekimoto, K. *Macromolecules* **2003**, *36*, 6462–6471.
- (94) Tosaka, M.; Murakami, S.; Poompradub, S.; Kohjiya, S.; Ikeda, Y.; Toki, S.; Sics, I.; Hsiao, B. S. *Macromolecules* **2004**, *37*, 3299–3309.

- (95) Toki, S.; Hsiao, B. S.; Amnuaypornsi, S.; Sakdapipanich, J. *Polymer* **2009**, *50*, 2142–2148.
- (96) Tanaka, Y. *Rubber Chemistry and Technology* **2001**, *74*, 355–375.
- (97) Andrews, E. H.; Owen, P. J.; Singh, A. *Rubber Chemistry and Technology* **1972**, *45*, 1315–1333.
- (98) Shimizu, T.; Tosaka, M.; Tsuji, M.; Kohjiya, S. *Rubber Chemistry and Technology* **2000**, *73*, 926–936.
- (99) Marchal, J. Cristallisation des caoutchoucs chargés et non chargés sous contrainte : Effet sur les chaînes amorphes (thesis), Université Paris XI, **2006**.
- (100) Flory, P. J. *Journal of Chemical Physics* **1947**, *15*, 397–408.
- (101) Ikeda, Y.; Yasuda, Y.; Hijikata, K.; Tosaka, M.; Kohjiya, S. *Macromolecules* **2008**, 5876–5884.
- (102) Suzuki, T.; Osaka, N.; Endo, H.; Shibayama, M.; Ikeda, Y.; Asai, H.; Higashitani, N.; Kokubo, Y.; Kohjiya, S. *Macromolecules* **2010**, *43*, 1556–1563.
- (103) Valentín, J. L.; Posadas, P.; Fernández-Torres, A.; Malmierca, M. A.; González, L.; Chassé, W.; Saalwächter, K. *Macromolecules* **2010**, *43*, 4210–4222.
- (104) Poompradub, S.; Tosaka, M.; Kohjiya, S.; Ikeda, Y.; Toki, S.; Sics, I.; Hsiao, B. S. *Journal of Applied Physics* **2005**, *97*, 1–9.
- (105) Rault, J.; Marchal, J.; Judeinstein, P.; Albouy, P.-A. *Macromolecules* **2006**, *39*, 8356–8368.
- (106) Brüning, K.; Schneider, K.; Heinrich, G. *Journal of Polymer Science Part B: Polymer Physics* **2012**, *50*, 1728–1732.
- (107) Mitchell, G. R. *Polymer* **1984**, *25*, 1562–1572.
- (108) Albouy, P.-A.; Guillier, G.; Petermann, D.; Vieyres, A.; Sanseau, O.; Sotta, P. *Polymer* **2012**, *53*, 3313–3324.
- (109) Jarry, J.; Monnerie, L. *Journal of Polymer Science: Part B: Polymer physics* **1980**, *18*, 1879–1890.
- (110) Amram, B.; Bokobza, L.; Queslel, J. P.; Monnerie, L. *Polymer* **1986**, *27*, 877–882.
- (111) Sotta, P.; Deloche, B.; Herz, J.; Durand, D.; Rabadeux, J. C. *Macromolecules* **1987**, *20*, 2769–2774.

- (112) Toki, S.; Sics, I.; Ran, S.; Liu, L.; Hsiao, B. S. *Polymer* **2003**, *44*, 6003–6011.
- (113) Rault, J.; Marchal, J.; Judeinstein, P.; Albouy, P.-A. *The European physical journal. E, Soft matter* **2006**, *21*, 243–261.
- (114) Lee D, J.; Donovan J, A. *Macromolecules* **1987**, *60*, 910–923.
- (115) Trabelsi, S.; Albouy, P.-A.; Rault, J. *Macromolecules* **2002**, *35*, 10054–10061.
- (116) Huneau, B.; Beurrot, S.; Rublon, P.; Verron, E.; Leygue, A.; Saintier, N.; Mocuta, C.; Thiaudière, D. In *Proceedings Depos 24*; **2012**; pp. 31–32.
- (117) Irwin, G. R. *Journal of Applied Mechanics* **1957**, *24*, 361–364.
- (118) Griffith, A. A. *Philosophical Transactions of the Royal Society A* **1920**, *221*, 163–198.
- (119) Rivlin, R. S.; Thomas, A. G. *Journal of Polymer Science* **1953**, *10*, 291–318.
- (120) Tsunoda, K.; Busfield, J. J. C.; Davies, C. K. L.; Thomas, A. G. *Journal of Materials Science* **2000**, *5*, 5187–5198.
- (121) Thomas, A. G. *Journal of Polymer Science* **1955**, *18*, 177–188.
- (122) Thomas, A. G. *Rubber Chemistry and Technology* **1994**, *67*, 50–60.
- (123) Sakulkaew, K.; Thomas, A. G.; Busfield, J. J. C. *Polymer Testing* **2011**, *30*, 163–172.
- (124) Sakulkaew, K.; Thomas, A. G.; Busfield, J. J. C. *Polymer Testing* **2013**, *32*, 86–93.
- (125) Busse, W. F. *Industrial & Engineering Chemistry* **1934**, 1194–1199.
- (126) Glucklich, J.; Landel, R. F. J. *Journal of Applied Polymer Science* **1976**, *20*, 121–137.
- (127) Hamed, G. R.; Kim, H. J.; Gent, A. N. *Rubber Chemistry and Technology* **1996**, *69*, 807–818.
- (128) Greensmith, H. W. *Journal of Polymer Science* **1956**, *21*, 175–187.
- (129) Gabrielle, B.; Guy, L.; Albouy, P.-A.; Vanel, L.; Long, D. R.; Sotta, P. *Macromolecules* **2011**, *44*, 7006–7015.
- (130) Kendall, K. *Proceedings of the Royal Society A: Mathematical, Physical and Engineering Sciences* **1975**, *344*, 287–302.
- (131) Gent, A. N.; Razzaghi-Kashani, M.; Hamed, G. R. *Rubber Chemistry and Technology* **2003**, *76*, 122–131.

- (132) Marano, C.; Calabro, R.; Rink, M. *Journal of Polymer Science: Part B: Polymer physics* **2010**, *48*, 1509–1515.
- (133) Hamed, G. R.; Rattanasom, N. *Rubber Chemistry and Technology* **2002**, *75*, 935–941.
- (134) Gherib, S.; Chazeau, L.; Pelletier, J. M.; Satha, H. *Polymer* **2010**, *118*, 435–445.
- (135) Donnet, J.-B.; Custodero, E.; Wang, T. K. *Kautschuk Gummi Kunststoffe* **1996**, *49*, 274–279.
- (136) Guy, L. Elastomer reinforcement by precipitated silicas -DIK Seminar **2009**.
- (137) Luginsland, H.-D. *Kautschuk Gummi Kunststoffe* **2000**, *53*, 10–23.
- (138) Goerl, U.; Hunsche, A.; Mueller, A.; Koban, H. G. *Rubber Chemistry and Technology* **1997**, *70*, 608–623.
- (139) Ramier, J.; Chazeau, L.; Gauthier, C.; Stelandre, L.; Guy, L.; Peuvrel-Disdier, E. *Journal of Materials Science* **2007**, *42*, 8130–8138.
- (140) Bomo, F. *Macromolecular Chemistry, Macromolecular Symposia* **1989**, *23*, 321–328.
- (141) Dierkes, W. K. Economic mixing of silica-rubber compounds (thesis), University of Twente, **2005**.
- (142) Wang, M. *Kautschuk Gummi Kunststoffe* **2005**, *58*, 626–637.
- (143) Le, H. H.; Oßwald, K.; Ilisch, S.; Pham, T.; Stöckelhuber, K. W.; Heinrich, G.; Radusch, H.-J. *Macromolecular Materials and Engineering* **2012**, *297*, 464–473.
- (144) Reuvekamp, L. A. E. M.; Ten Brinke, J. W.; Van Swaaij, P. J.; Noordermeer, J. W. M. *Kautschuk Gummi Kunststoffe* **2002**, *55*, 41–47.
- (145) Sarkawi, S. S.; Dierkes, W. K.; Noordermeer, J. W. M. In *International Rubber Conference Proceedings*; **2012**.
- (146) Muñoz, L. Etude expérimentale des mécanismes d'endommagement par fatigue dans les élastomères renforcés (thesis), Université Lyon I, **2011**.
- (147) *ASTM Standard D1646 - Viscosity, Stress Relaxation, and Pre-Vulcanization Characteristics (Mooney Viscometer)*; **2004**.
- (148) Saalwächter, K.; Herrero, B.; López-Manchado, M. A. *Macromolecules* **2005**, *38*, 9650–9660.
- (149) Saalwächter, K. *Progress in Nuclear Magnetic Resonance Spectroscopy* **2007**, *51*, 1–35.

- (150) Trabelsi, S.; Albouy, P.-A.; Rault, J. *Rubber Chemistry and Technology* **2004**, *77*, 303–316.
- (151) Kucherskii, A. M. *Polymer Testing* **2003**, *22*, 503–507.
- (152) Albouy, P.-A.; Marchal, J.; Rault, J. *The European physical journal. E, Soft matter* **2005**, *17*, 247–259.
- (153) Chenal, J.-M.; Chazeau, L.; Guy, L.; Bomal, Y.; Gauthier, C. *Polymer* **2007**, *48*, 1042–1046.
- (154) Le Saux, V.; Marco, Y.; Calloch, S.; Doudard, C.; Charrier, P. *International Journal of Fatigue* **2010**, *32*, 1582–1590.
- (155) Kim, H. G.; Mandelkern, L. *Journal of Polymer Science Part A2* **1968**, *6*, 181–196.
- (156) Tosaka, M.; Senoo, K.; Sato, K.; Noda, M.; Ohta, N. *Polymer* **2012**, *53*, 864–872.
- (157) Beurrot, S.; Huneau, B.; Verron, E.; Rublon, P.; Thiaudière, D.; Mocuta, C.; Zozulya, A. In *Constitutive Models for Rubber VII*; **2012**; pp. 353–358.
- (158) Candau, N.; Chazeau, L.; Chenal, J.-M.; Gauthier, C.; Munch, E.; Rochas, C.; Ferreira, J. *Polymer* **2012**, *53*, 2540–2543.
- (159) Brüning, K.; Schneider, K.; Roth, S. V; Heinrich, G. *Macromolecules* **2012**, *45*, 7914–7919.
- (160) Hiroaki, H.; Hashiyama, M.; Tomita, S.; Kawai, H. *Journal of Macromolecular Science, Part B: Physics* **1973**, *8*, 101–126.
- (161) Sotta, P.; Fülber, C.; Demco, D. E.; Blümich, B.; Spiess, H. W. *Macromolecules* **1996**, *29*, 6222–6230.
- (162) Mullins, L.; Tobin, N. R. *Rubber Chemistry and Technology* **1958**, 505–512.
- (163) Shinomura, T.; Takahashi, M. *Rubber Chemistry and Technology* **1970**, *43*, 1025–1035.
- (164) Le Cam, J.-B.; Toussaint, E. *Macromolecules* **2008**, *41*, 7579–7583.
- (165) Le Cam, J.-B.; Toussaint, E. *Mechanics of Materials* **2009**, *41*, 898–901.
- (166) Beurrot, S.; Huneau, B.; Verron, E. *Journal of Applied Polymer Science* **2010**, *117*, 1260–1269.
- (167) Grobler, J. H. A.; McGill, W. J. *Journal of Polymer Science: Part B: Polymer Physics* **1994**, *32*, 287–295.

- (168) González, L.; Rodríguez, A.; Valentín, J. L.; Marcos-Fernandez, A.; Posadas, P. *Kautschuk Gummi Kunststoffe* **2005**, 638–643.
- (169) Rivlin, R. S.; Thomas, A. G. *Journal of Polymer Science* **1953**, 10, 291–318.
- (170) Thomas, A. G. *Journal of Applied Polymer Science* **1960**, 3, 168–174.
- (171) Le Cam, J.-B.; Huneau, B.; Verron, E.; Gornet, L. *Macromolecules* **2004**, 37, 5011–5017.
- (172) Le Cam, J.-B.; Toussaint, E. *Macromolecules* **2010**, 43, 4708–4714.
- (173) Mzabi, S. Caractérisation et analyse des mécanismes de fracture en fatigue des élastomères chargés (thesis), Université Paris VI, **2010**.



## XI. Appendices

### X.1. Sample series recipes

The recipes used for the compounding of the samples are detailed in the following tables. Note that the amounts in phr denoted for the sulfur, CBS and TBzTD are the exact amounts introduced for 100 grams of rubber. The EPDM rubber mass on which the chemicals are supported at the time of introduction has been taken into account (the EPDM rubber + chemical mass is superior to the mass written in the tables). For instance a sulfur amount of 1.5phr corresponds to a sulfur+EPDM mass of 1.88phr since the mass fraction of sulfur in the sulfur+EPDM granule is 80%.

#### *X.1.a. Series 021-10*

Formulation	1	2	3	4	5	6	7	8	9
NR CV 60 peptisé	100	100	100	100	100	100	100	100	100
Z 1165 MP	50				50	50	50	50	
Z 1115 MP		50							
Z 200 MP			50						50
Coral Silcea 2				50					
TESPT (Z6940)	4	2,8	5	4		2,8	1,2		
OCTEO (Z 6341)					4,1	1,25	2,9		
Phenyl SILANE								3,6	4,5
6PPD	1,9	1,9	1,9	1,9	1,9	1,9	1,9	1,9	1,9
Acide stéarique	4	4	4	4	4	4	4	4	4
ZnCO3	4,6	4,6	4,6	4,6	4,6	4,6	4,6	4,6	4,6
SOUFRE	1,5	1,5	1,5	1,5	1,5	1,5	1,5	1,5	1,5
CBS	1,7	1,7	1,7	1,7	1,7	1,7	1,7	1,7	1,7
TBzTD	0,2	0,2	0,2	0,2	0,2	0,2	0,2	0,2	0,2

#### *X.1.b. Series 054-10*

XI: APPENDICES

Formulation	1	2	3	4	5	6	7
NR SMR 5L	100	100	100	100	100		
NR CV 60 (np)						100	100
Z 1165 MP	50	55		50		50	
N234			50		45		45
N330						4	4
TESPT (Z6940)	4	4,4		4		4	
6PPD	1,9	1,9	1,9	1,9	1,9	1,9	1,9
Acide stéarique	4	4	4	4	4	4	4
ZnO	4	4	4	4	4		
ZnCO3						4,6	4,6
SOUFRE	1,5	1,5	1,5	1,5	1,5	1,5	1,5
CBS	2	2,2	1,5	2	1,5	1,7	1
TBzTD	0,2	0,2	0,2	0,2	0,2	0,2	0,2

*X.1.c. Series 095-10*

Formulation	1	2	3	4	5	6	7	8
SMR 5L	100	100	100	100	100	100	100	100
Z 1165 MP	50	50	50	50			50	
CS 2					50			45
N234						45		
TESPT	4		2,9		4		4	
OCTEO		4,1						
Azosilane			1,5					
NSC				4,5				
6PPD	1,9	1,9	1,9	1,9	1,9	1,9	1,9	1,9
Acide stéarique	2	2	2	2	2	2	2	2
ZnO	4	4	4	4	4	4	4	4
SOUFRE	1,5	1,5	1,5	1,5	1,5	1,5	1,5	1,5
CBS	2	2	2	2	2	1,5	1,5	2
TbZTD	0,2	0,2	0,2	0,2	0,2	0,2	0,2	0,2

*X.1.d. Series 115-10*

XI: APPENDICES

Formulation	1	2	3	4	5	6	7	8	9
NR (CV60) peptisé	100	100	100	100	100	100	100	100	100
Z 1165 MP		50	35	17	50	17			
Z 1115 MP							50		
N234								45	15
TESPT		4	2,8	1,4			2,8		
OCTEO					4,1	1,4			
6PPD	1,9	1,9	1,9	1,9	1,9	1,9	1,9	1,9	1,9
Acide stéarique	4	4	4	4	4	4	4	4	4
ZnCO3	4,6	4,6	4,6	4,6	4,6	4,6	4,6	4,6	4,6
SOUFRE	1,5	1,5	1,5	1,5	1,5	1,5	1,5	1,5	1,5
CBS	1,7	1,7	1,7	1,7	1,7	1,7	1,7	1	1
TbZTD	0,2	0,2	0,2	0,2	0,2	0,2	0,2	0,2	0,2

*X.1.e. Series 030-11*

Formulation	1	2	3	4	5	6	7	8	9
SMR 5L	100	100	100	100	100	100	100	100	100
Z 1165 MP	50	50	50	50	50	50	50	50	
N234									45
TESPT		4	4	4				4	
NSC					4,5	4,5	4,5		
6PPD	1,9	1,9	1,9	1,9	1,9	1,9	1,9	1,9	1,9
Acide stéarique	2	2	2	2	2	2	2	2	2
ZnO	4	4	4	4	4	4	4	4	4
SOUFRE	1,5	1	1,5	2	1	1,5	2	1,5	1,5
CBS	2	1,3	2	2,6	1,3	2	2,6	2	1,5
TbZTD	0,2	0,2	0,2	0,2	0,2	0,2	0,2	0,2	0,2

*X.1.f. Series 046-11*

XI: APPENDICES

Formulation	1	2	3	4	5	6	7	8
NR (SMR 5L)	100	100	100	100	100		100	100
Z 1165 MP							60	
Z 1085 Gr				50				
HRS 1200 MP					50			
HRS 1200 MP						50		
TESPT				2	5		4,8	
NSC						5,6		
6PPD	1,9	1,9	1,9	1,9	1,9	1,9	1,9	1,9
Acide stéarique	2	2	2	2	2	2	2	2
ZnO	4	4	4	4	4	4	4	4
SOUFRE	1	1,5	2	1,5	1,5	1,5	1,5	1,5
CBS	1,3	2	2,6	2	2	2	2	2
TBzTD	0,2	0,2	0,2	0,2	0,2	0,2	0,2	0,2

*X.1.g. Series 119-11*

Formulation	1	2	3	4	5	6	7	8	9	10	11	12	13	14	15
SMR 5L	100	100	100	100	100	100	100	100	100	100	100	100	100	100	100
Z 1165 MP	50	50	50	50	50	50	50	50	50						
N234													45	45	45
TESPT	4	4	4												
OCTEO				4,1	4,1	4,1									
NSC							4,5	4,5	4,5						
6PPD	1,9	1,9	1,9	1,9	1,9	1,9	1,9	1,9	1,9	1,9	1,9	1,9	1,9	1,9	1,9
Stearic Acid	2	2	2	2	2	2	2	2	2	2	2	2	2	2	2
ZnO	4	4	4	4	4	4	4	4	4	4	4	4	4	4	4
Sulfur	0,5	1,5	2,5	0,5	1,5	2,5	0,5	1,5	2,5	0,5	1,5	2,5	0,5	1,5	2,5
CBS	0,66	2	3,33	0,66	2	3,33	0,66	2	3,33	0,66	2	3,33	0,5	1,5	2,5
TbZTD	0,2	0,2	0,2	0,2	0,2	0,2	0,2	0,2	0,2	0,2	0,2	0,2	0,2	0,2	0,2

*X.1.h. Series 038-12*

Formulation	1	2	3	4	5	6	7	8	9	10	11	12
SBR BUNA VSL 2525-0	100	100	100	100	100	100						
SBR BUNA VSL 5025-0							100	100	100	100	100	100
Z 1165 MP (S025-12)		30	30	50	50			30	30	50	50	
N234 Columbian							45					45
TESPT			2,46		4				2,46		4	
OCTEO (Z 6341)		2,4		4,1				2,4		4,1		
6PPD	1,9	1,9	1,9	1,9	1,9	1,9	1,9	1,9	1,9	1,9	1,9	1,9
Acide stéarique	4	4	4	4	4	4	4	4	4	4	4	4
ZnO	2,5	2,5	2,5	2,5	2,5	2,5	2,5	2,5	2,5	2,5	2,5	2,5
SOUFRE	1,2	1,2	1,2	1,2	1,2	1,2	1,2	1,2	1,2	1,2	1,2	1,2
CBS	1,9	1,9	1,9	1,9	1,9	1,4	1,9	1,9	1,9	1,9	1,9	1,4
TbZTD	0,2	0,2	0,2	0,2	0,2	0,2	0,2	0,2	0,2	0,2	0,2	0,2

The Carbon Black grade used for the sample n°6 and 12 came from a different supplier (Columbian) as the usual one (Cabot) and was found to be particularly pulverulent making its incorporation in the rubber more difficult than as usual.

*X.1.i. Series 051-12*

Formulation	1	2	3	4	5	6	7	8
NATSYN Z200 (PI)	100	100	100	100				
NR SMR 5L					100	100	100	100
Z 1165 MP		50	50	50		50	50	
N234								45
TESPT			4	4		4	4	
OCTEO		4,1						
6PPD	1,9	1,9	1,9	1,9	1,9	1,9	1,9	1,9
Acide stéarique	4	4	4	4	4	4	4	4
ZnO	2,5	2,5	2,5	2,5	2,5	2,5	2,5	2,5
SOUFRE	1,5	1,5	1,5	1,5	1,5	1,5	1,5	1,5
CBS	2,5	2,5	2,5	2,5	2,5	2,5	2,5	2,5

**X.2. Dispergrader**

*X.2.a. Measurements*

The Dispergrader is an apparatus designed to quantify the dispersibility of the fillers in the rubber matrix on the microns scale. The accessible scale range is thus limited to agglomerates that have not been broken and dispersed during the mixing step. As the measurement relies on the light reflectivity contrast of the matrix and the fillers, silica and carbon black compounds can difficultly be compared since the contrast is lower between silica and rubber than for the carbon black-rubber couple.

The closer to 1 the value of Z is and the better the dispersion of the filler.

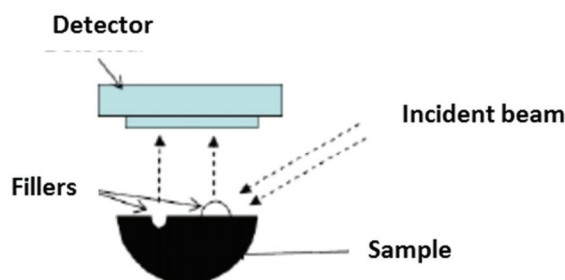


**Figure 239 : Light reflectivity of clean-cut compounds as used with the Dispergrader apparatus to analyze remaining agglomerates of fillers**

*X.2.b. Results for series 030-11*

Formulation	1	2	3	4	5	6	7	8	9
Z	97	98	99	99	99	93	99	92	92



## I. Résumé en français

Les caoutchoucs chargés présentent une microstructure complexe composée d'une matrice élastomère dans laquelle sont dispersés des agrégats de quelques centaines de nanomètres. L'introduction de telles charges conduit à une forte augmentation des propriétés mécaniques. L'augmentation du module est désignée par le terme de renforcement. Les propriétés ultimes telles que la résistance à la rupture et la résistance à la propagation d'entaille sont également améliorées.

Une meilleure compréhension des mécanismes de renforcement et des propriétés ultimes est nécessaire pour d'améliorer les compromis de propriétés des caoutchoucs renforcés. Le renforcement dans le régime des faibles déformations (auquel l'effet Payne est associé) est particulièrement important pour les propriétés de résistance au roulement et d'adhérence sur sol humide. L'étude de la résistance à la propagation de fissure (déchirure) est motivée par le lien entre la résistance à l'usure et à la résistance à la propagation de fissure. Une identification plus précise des mécanismes à l'origine des propriétés observés doit conduire à proposer des voies d'amélioration des matériaux.

Un bref descriptif du contexte applicatif dans lequel s'inscrit ce travail de thèse est donné en première partie. On identifie trois critères de performances clés pour les pneumatiques: la résistance au roulement, l'adhérence sur sol humide et la résistance à l'usure. Notre étude vise à mieux comprendre les mécanismes physiques à l'origine de ces propriétés. Le chapitre II est consacré à la revue de la littérature pertinente pour notre étude. Les bases de l'élasticité caoutchoutique sont rappelées. L'effet de charges renforçantes sur les propriétés mécaniques dans le régime des faibles et moyennes déformations (effet Payne) puis des grandes déformations (effet Mullins) est décrit. Le phénomène de cristallisation induite sous étirement est présenté. Enfin la résistance à la propagation de fissure dans les caoutchoucs renforcés est introduite. Les formulations utilisées et les procédures suivies pour la réalisation des échantillons sont détaillées dans le chapitre III. Les propriétés mécaniques de nos matériaux dans le domaine des faibles (effet Payne) et des grandes déformations sont décrites au chapitre IV. Le phénomène de cristallisation sous étirement fait l'objet du chapitre V. Une première partie concerne l'évolution de la cristallisation avec la déformation lors de mesures d'étirement quasi-statique. La seconde partie présente des mesures dynamiques visant à estimer les cinétiques de cristallisation et de fusion. Le chapitre VI rassemble les résultats de différentes techniques permettant d'évaluer l'étirement local des chaînes du caoutchouc. Des mesures de contrainte, d'orientation de la phase amorphe, de gonflement à l'équilibre et de RMN à bas champ sont ainsi corrélés sur les matériaux purs et chargés afin de préciser les mécanismes de renforcement aux grandes et aux faibles déformations. Les propriétés de dissipation et de cavitation aux grandes déformations ainsi que les propriétés ultimes sont abordées dans le chapitre VII. Les résultats d'essais de résistance à la déchirure sont reportés dans le chapitre VIII. Des mesures de champ de déformation durant certains essais de déchirure ont été réalisées et l'importance de la zone cristallisée en fond d'entaille est discutée à l'appui de mesures de diffraction des rayons X en fond d'entaille.

## Chapitre I : Contexte

Le Caoutchouc Naturel produit à partir de l'hévéa est largement utilisé pour la production de pneumatiques en raison de ses excellentes propriétés mécaniques. Il est ainsi majoritairement employé pour la confection de pneumatiques pour poids lourds et véhicules de chantier ou ses propriétés de résistance à l'usure et à la déchirure ainsi que son faible auto-échauffement en font un élastomère de choix.

L'Union Européenne a adopté une réglementation sur les performances des pneumatiques qui s'est traduite en 2012 par un étiquetage de tous les pneumatiques de véhicules de tourisme vendus dans l'UE. Ce dispositif vise à inciter les consommateurs à privilégier les meilleurs pneumatiques en termes de résistance au roulement (donc de consommation de carburant), d'adhérence sur sol humide et de volume sonore.

Au cours des années 1990, la commercialisation de pneumatiques dit « vert » par Michelin a marqué une avancée technique avec l'amélioration des performances en termes de résistance au roulement et d'adhérence sur sol humide. Cette avancée est le résultat de l'utilisation de la silice de précipitation comme charge renforçante combinée à une formulation adaptée comprenant un agent de couplage silice-caoutchouc. Nous cherchons à mieux comprendre l'effet de la silice sur les propriétés des caoutchoucs renforcés et en particulier dans le cas du caoutchouc naturel.

## Chapitre II : Revue bibliographique

### Propriétés mécaniques des élastomères:

Les propriétés des polymères dépendent de leur température d'utilisation. Les élastomères sont caractérisés par la flexibilité des chaînes qui les composent et la création d'un réseau tridimensionnel (vulcanisation dans le caoutchouc). La flexibilité des chaînes se traduit par une température de transition vitreuse  $T_g$  basse (inférieure à  $0^\circ\text{C}$ ). Les caoutchoucs sont généralement constitués de chaînes insaturées ce qui permet de conserver des sites réactionnels pour la création de ponts entre ces chaînes. Ces nœuds du réseau assurent une grande élasticité aux caoutchoucs réticulés qui présentent ainsi une très faible déformation plastique lors de chargements de plusieurs centaines de pourcents de déformation.

Il est à noter que le réseau vulcanisé peut être fortement hétérogène au niveau microscopique cependant un réseau parfait est considéré dans le cadre des théories de l'élasticité. La théorie de l'élasticité caoutchoutique est dite entropique car elle repose sur le grand nombre de conformations accessibles aux segments de chaînes entre deux nœuds distants du réseau. Une description Gaussienne de la distribution de conformations est généralement adoptée. Pour cette description, on rappelle l'expression de la contrainte vraie en fonction du taux d'extension  $\lambda$ , de la température et de la densité de chaînes qui est proportionnelle à la densité de réticulation. Les deux principaux modèles moléculaires de déformation d'un réseau sont le modèle affine et le modèle fantôme. Le premier considère que les nœuds du réseau sont fixes et que les déformations appliquées aux chaînes au niveau microscopique sont équivalentes à la déformation macroscopique appliqué. Dans le modèle fantôme, les nœuds du réseau ont la possibilité de fluctuer autour de leur position d'équilibre. Ces modèles rendent plutôt bien compte des comportements observés même si le modèle semi-empirique de Mooney-Rivlin décrit de façon plus quantitative la relation entre contrainte et déformation.

Le Renforcement par les charges:

L'incorporation de charges renforçantes dans les mélanges caoutchouc modifie profondément les propriétés mécaniques dans le domaine des faibles déformations. Le régime où le module dépend linéairement de la déformation est restreint aux très faibles déformations (au maximum 0,1% de déformation typiquement). Dans le domaine caoutchoutique ( $T > T_g$ ), le module est largement supérieur au module de la matrice non chargée en particulier pour des températures proches de  $T_g$ . Une décroissance du module avec la déformation qualifiée d'effet Payne est également observée. Les mécanismes qui régissent le niveau du module dans le domaine linéaire et par conséquent l'adoucissement avec la déformation (effet Payne) ont fait l'objet de nombreuses études. Historiquement, les premiers modèles établis s'appuyaient sur la présence d'un réseau de charges connectées entre elles par des interactions de type Van der Waals. On peut également citer par opposition les modèles considérant une hausse de la densité de réticulation ou d'enchevêtrements induite par les charges qui font donc intervenir une interaction charge-polymère mais pas les interactions charges-charges.

Plus récemment, un modèle basé sur la percolation de zones de polymère dans l'état vitreux entre les charges a été développé. La dépendance en température du module dans le domaine linéaire est donnée par la fusion des ponts vitreux avec l'augmentation de la température alors que la plastification de ces ponts sous l'effet de la contrainte a été avancée pour expliquer l'effet Payne. Les deux paramètres clés identifiés dans cette vision du renforcement sont la force des interactions à l'interface charge-polymère et la distance entre particules voisines.

Finalement, l'effet Payne peut être décomposé en une composante liée à la matrice dépendante notamment de la densité de réticulation, une composante hydrodynamique, une composante indépendante de la déformation liée à la fraction d'élastomère que ne participe pas à la déformation du réseau (souvent qualifié de polymère occlus) et enfin une composante qui diminue avec la déformation relié au réseau charge-polymère-charge.

Le comportement mécanique aux grandes déformations est également fortement impacté par la fraction de charge introduite. Le module de première traction augmente fortement comparé à la matrice et un phénomène prononcé d'adoucissement de contrainte (effet Mullins) est constaté après un cycle de charge-décharge. Le haut niveau de contrainte lors de la première traction par rapport à la contrainte à appliquer sur un échantillon précyclé correspond donc aux contributions irréversibles de l'effet Mullins. À l'inverse la contribution répétable de la contrainte peut être recouverte après un temps assez long. La contribution incompressible correspond à la contrainte obtenue à la rétraction d'un cycle mécanique. Le haut niveau de module durant la première traction peut s'expliquer de la manière suivante : la déformation locale entre les charges est fortement amplifiée du fait que ces dernières sont indéformables. La contrainte à appliquer pour déformer le matériau augmente fortement lorsque les chaînes les plus courtes atteignent des niveaux de déformations élevés proche de leur extensibilité limite. L'effet Mullins peut être attribué à certaines chaînes soumises à de grandes déformations locales qui cassent lors d'un cycle de déformation macroscopique maximale donnée et ne sont alors plus actives au cycle suivant. En revanche, pour une déformation supérieure à la déformation maximale du cycle, le module est à nouveau élevé car d'autres chaînes atteignent un état d'extension proche de leur extensibilité limite. D'autres auteurs ont considéré des phénomènes de glissement, et d'adsorption/désorption de chaînes à la surface de la charge pour décrire l'adoucissement de contrainte. En plus des effets de la densité de réticulation de la matrice et de la fraction de charge, l'interface peut jouer un rôle important sur le renforcement aux grandes déformations. En

présence de faibles interactions entre la charge et la matrice, le niveau de renforcement est faible. L'effet de l'interface peut également être mis en évidence par des essais de gonflement à l'équilibre dans un bon solvant.

#### La cristallisation induite sous étirement :

Le phénomène de cristallisation induite sous étirement dans le caoutchouc naturel a fait l'objet de nombreuses études. La très grande stéréorégularité des chaînes de caoutchouc naturel est à l'origine de sa faculté de cristalliser sous étirement et à froid. La présence d'impuretés agissant comme nuclei pour la formation des cristallites a également été avancée par certains auteurs. Lors d'un cycle mécanique, un caoutchouc non chargé cristallise à partir d'une déformation seuil d'environ 300%. La formation des premiers cristallites s'accompagne d'une relaxation des portions de chaînes amorphes et donc d'un court plateau de contrainte. Les cristallites jouent ensuite le rôle de renfort ou de nœuds du réseau ce qui provoque un durcissement de l'échantillon. La densité du réseau a une influence sur la courbe cristallisation-déformation.

L'introduction de charges décale le seuil de cristallisation vers des déformations plus faibles et ce d'autant plus que la fraction volumique est élevée. En revanche la pente de la courbe cristallisation-déformation est inférieure pour un caoutchouc naturel chargé. Afin de mieux comprendre le rôle de la cristallisation sur la résistance à la propagation de fissure, des mesures de cristallinité en fond d'entaille ont été réalisées. Elles indiquent une forte décroissance de la cristallinité avec la distance au fond d'entaille en accord avec l'intensification de déformation.

#### Résistance à la déchirure :

La théorie de Griffith établit que l'énergie nécessaire pour créer une quantité de surface (énergie de déchirure) est équivalente au taux de restitution d'énergie qui est la quantité d'énergie libérée lors de la propagation d'une fissure d'aire  $A$ .

Un certain nombre d'éprouvettes sont utilisées pour l'évaluation de la résistance à la déchirure dans les élastomères. Chaque géométrie permet de faire des hypothèses simplificatrices qui facilitent le calcul de l'énergie de déchirure à partir des données de l'essai. L'énergie de déchirure augmente avec la vitesse de propagation de la fissure pour des caoutchoucs qui ne cristallisent pas sous étirement. La propagation dans le caoutchouc naturel s'avère plus complexe car il apparaît des instabilités de propagation, l'énergie à fournir pour propager la fissure étant plus importante du fait de ces instabilités.

Il a été montré que le phénomène de rotation d'entaille ou bifurcation de déchirure est relié à l'anisotropie du matériau. Ceci explique que les rotations d'entaille soient plus nombreuses lorsque le taux de charge augmente (anisotropie supplémentaire de la déformation locale) et pour un caoutchouc qui cristallise sous étirement.

## **Chapitre III : Matériaux, Mise en œuvre et Méthodes**

Les matériaux utilisés sont constitués de caoutchouc Naturel renforcé avec du Noir de Carbone ou de la Silice de précipitation. Les Silices de précipitation Rhodia qui ont été utilisées ont toutes la même structure et une surface spécifique qui varie de 80 à 200m<sup>2</sup>/g. La surface spécifique de la Silice la plus employée est de 160m<sup>2</sup>/g ce qui est supérieur au 120m<sup>2</sup>/g du Noir de Carbone N234 mais les deux charges donnent des propriétés mécaniques comparables une fois incorporées. Différents agents de surface sont utilisés durant le mélangeage pour traiter la surface de la silice. Deux agents de couplage, l'un contenant du Soufre (TESPT) et l'autre non (NSC)

ont été utilisés pour établir des liaisons covalentes avec le caoutchouc et à l'inverse un agent de recouvrement (OCTEO) qui ne réagit pas avec le caoutchouc a été employé. Un échantillon NR Silice sans agent de surface a également été utilisé. Le mélangeage est réalisé en une ou deux étapes avec incorporation de la charge durant la première. Après détermination du temps de vulcanisation au rhéomètre, la vulcanisation est réalisée sous presse.

Le module à faibles déformations et l'effet Payne sont déterminés par Analyse Mécanique Dynamique et les courbes contrainte-déformation sont mesurées en traction uni-axiale. La dissipation aux grandes déformations est mesurée en appliquant des cycles d'amplitude croissante avec ou sans précyclage initial. Pour chaque cycle, l'hystérèse est rapportée à l'aire sous la courbe contrainte-déformation à l'aller pour obtenir la dissipation relative en fonction de la déformation maximale appliquée sur le cycle.

L'énergie de déchirure est mesurée sur des éprouvettes de type cisaillement pur pré-entaillées. Certains échantillons sont recouverts d'un mouchetis et filmés durant l'essai afin de calculer les champs de déformations par corrélation d'images numériques.

Des mesures de gonflement à l'équilibre ont été faites dans le toluène dans le but d'estimer la densité de réticulation du caoutchouc naturel non chargé et l'effet des charges sur le gonflement pour les échantillons renforcés.

La diffraction des rayons X permet d'étudier la cristallisation sous étirement en traction simple et en mode oscillant pour estimer les cinétiques. L'intégration azimutale des clichés de diffraction fournit la fraction cristallisée et la désorientation des cristallites par rapport à l'axe de traction. Cette analyse permet également de quantifier l'anisotropie du halo amorphe qui est associé à l'orientation préférentielle des chaînes de caoutchouc naturel selon l'axe de traction. Le paramètre d'orientation de la phase amorphe nous renseigne ainsi sur l'état d'orientation des chaînes d'un essai mécanique. Une intégration radiale donne accès à la largeur des pics de diffraction qui est reliée à la taille des cristallites dans une direction donnée.

## **Chapitre IV : Présentation des Propriétés Mécaniques**

Le comportement mécanique du caoutchouc naturel non renforcé peut être décomposé en un régime linéaire jusqu'à des déformations de l'ordre de 300% selon la densité de réticulation et un régime de grandes déformation ou l'extensibilité limite des chaînes et la cristallisation provoquent une forte hausse du module. Pour les échantillons chargés, le régime linéaire est restreint à environ 0.1% de déformation, le régime des faibles déformations ou se produit une chute du module est défini jusqu'à 50%, viennent ensuite les grandes déformations jusqu'à environ 200% et les très grandes déformations qui marquent le domaine où le caoutchouc naturel est cristallisé.

### Faibles et moyennes déformations:

Le renforcement dans le domaine linéaire pour des températures proches de la  $T_g$  augmente fortement et de façon non-linéaire avec la fraction de charge. Le renforcement atteint des valeurs importantes (jusqu'à 30 fois le module du caoutchouc naturel (NR) pur) pour les échantillons NR chargés à 18% en volume. Ce renforcement est plus important pour le Noir de Carbone et l'écart avec les autres systèmes est plus marqué pour une grande fraction volumique.

La chute du module avec la déformation (c'est-à-dire l'amplitude de l'effet Payne) augmente fortement avec la fraction de charge et la surface spécifique engagée ce qui suggère une contribution importante du réseau formé par les charges connectées par du polymère à l'état

vitreux ou à faible mobilité. La chute de module est non négligeable pour une faible fraction volumique ce qui semble indiquer qu'il n'y a pas de seuil net de percolation dans ces matériaux.

A la température mesurée, l'effet Payne est plus important pour le Noir de Carbone comparé à Silice-*TESPT* en accord avec les mesures de renforcement dans le domaine linéaire. On note également que l'effet Payne diminue pour l'échantillon avec un couplage covalent non soufré *NSC* comparé à l'agent de couplage *TESPT*. On peut rapprocher ce résultat de la position du pic de dissipation. En effet la déformation pour laquelle le module de perte est maximal dépend de l'agent de couplage et on constate qu'elle est la plus élevée pour les échantillons Silice-*NSC*. Ce résultat peut s'interpréter comme l'effet de plus grandes distances entre charges c'est-à-dire une meilleure distribution de la charge ce qui expliquerait également l'amplitude plus faible du module à cette température.

#### Grandes déformations :

Le module aux grandes déformations est étudié dans le caoutchouc naturel pur et chargé. Dans les deux cas, le module augmente avec la densité de réticulation et l'énergie à la rupture passe par un maximum. Augmenter la fraction volumique de silice augmente le module aux grandes déformations mais modifie également la forme de la courbe. Le renforcement peut être relié à l'amplification de déformation : les chaînes atteignent leur limite d'extensibilité ou cristallisent plus tôt dans les zones de forte amplification. On avance que l'hétérogénéité de l'amplification locale augmente avec la fraction de charge ce qui expliquerait l'augmentation plus progressive de la contrainte avec la déformation pour des taux de charge élevés.

Le renforcement est plus faible pour la Silice recouverte (*OC<sub>TEO</sub>*) que pour une Silice couplée (*TESPT* ou *NSC*) due au nombre limité d'interactions avec les chaînes de caoutchouc. Cependant, on remarque que le module est tout de même significativement supérieur à celui de la matrice pure ce qui traduit un certain niveau de transfert de contrainte. Le noir de carbone présente le plus fort renforcement aux grandes déformations malgré une plus faible surface engagée comparé à la silice ce qui souligne la force et/ou la densité des interactions mises en jeu avec l'élastomère.

## **Chapitre V : Cristallisation induite sous étirement**

L'étude de la cristallisation induite par diffraction des rayons X porte en premier lieu sur la cristallisation au cours d'essais en traction quasi-statique. L'effet de la densité de réticulation dans le NR non chargé est discuté. La cristallisation induite dans le NR chargé est ensuite abordé (sur des échantillons précyclés) et l'effet de l'interface est particulièrement souligné. La seconde partie est consacrée aux cinétiques de cristallisation et de fusion étudiées au moyen d'un dispositif de sollicitation dynamique récemment développé.

#### **Essais quasi-statiques :**

##### NR non chargé :

La fraction cristallisée, le paramètre d'orientation de la phase amorphe et la contrainte sont mesurées simultanément au cours de cycles de traction-rétraction.

L'orientation de la phase amorphe augmente avec la déformation jusqu'à se stabiliser au seuil de cristallisation. Le paramètre d'orientation reste alors constant ce qui montre la relaxation des chaînes amorphes lors de la formation des premiers cristallites. Une légère remontée de l'orientation de l'amorphe accompagne le durcissement aux grandes déformations. On en déduit

que l'effet renforçant des cristallites prédomine alors sur la relaxation des chaînes environnantes à partir d'une certaine fraction de cristallites. Au cours de la rétraction, après une phase de diminution de la contrainte et de l'orientation de l'amorphe, les deux grandeurs se stabilisent lorsque l'orientation de la phase amorphe (et par conséquent son état de déformation) est identique à l'orientation à la fusion. Les phases cristallines et amorphes sont alors en équilibre. Des mesures sur des échantillons de différentes densités de réticulation montrent que le seuil de cristallisation ne dépend pas de ce paramètre. En revanche la cristallisation augmente légèrement plus vite avec la déformation lorsque la densité de réticulation augmente. En dessous du seuil de cristallisation, l'orientation de la phase augmente d'autant plus vite que la densité de réticulation est grande ce qui est en accord avec la théorie de l'élasticité caoutchoutique. L'orientation des cristallites selon l'axe de traction et la taille des cristallites diminuent avec la densité de nœuds du réseau.

### NR chargé (après précyclage) :

Le seuil de cristallisation est fortement abaissé pour le NR renforcé et cela d'autant plus que l'interface est forte. Le Noir de Carbone est ainsi le système qui présente le plus faible seuil de cristallisation devant Silice-TESPT alors que Silice-OCTEO présente un seuil plus élevé mais encore significativement inférieur à la matrice NR.

Au-delà du seuil, la cristallisation augmente moins rapidement avec la déformation pour un échantillon renforcé comparé au non renforcé. L'hétérogénéité de la déformation locale discutée au chapitre IV peut expliquer la hausse plus progressive de la cristallisation.

On remarque que la fraction cristallisée à la rupture est plus faible pour les échantillons chargés ce qui pourrait traduire une restriction de la formation et/ou de la croissance des cristallites induite par les charges. Ce scénario semble confirmé par la plus grande désorientation des cristallites et la diminution de leur taille pour le NR chargé quelque que soit le type d'interface.

La comparaison avec un échantillon non-précyclé montre que le seuil augmente avec le précyclage en accord avec l'idée que l'application de cycles de grande amplitude induit une réorganisation qui diminue la portion de zone de forte amplification de déformation.

### **Essais dynamiques :**

#### Principe des mesures :

Le principe des mesures de cinétique est d'appliquer une sollicitation périodique à l'échantillon de caoutchouc et de comparer la cristallinité obtenue en dynamique à la cristallinité obtenue au retour pour un cycle quasi-statique (considérée comme la cristallinité à l'équilibre). On enregistre les clichés de diffraction uniquement aux points haut et bas des cycles. Pour cela deux obturateurs sont mis en rotation synchrones lors de ces mesures : le premier, fixé en amont de l'échantillon, ne laisse passer le faisceau incident qu'en positions d'extension minimale et maximale, l'autre est placé en aval de l'échantillon, juste devant la caméra X obture alternativement le côté gauche et le côté droit de celle-ci. Les oscillations peuvent se faire dans une gamme de fréquence de 0.05Hz à 50Hz ce qui permet d'accéder à des périodes de sollicitations de l'ordre d'une dizaine de millisecondes au minimum. L'amplitude du déplacement imposé lors des oscillations peut être significativement modifiée avec une amplitude maximale de 38mm.

La procédure d'essai débute systématiquement par l'application de trois cycles de traction quasi-statiques de grande amplitude puis plusieurs séquences d'oscillations sont réalisées chacune autour d'une déformation moyenne donnée. On débute par la séquence autour de la déformation moyenne la plus élevée en allant vers les séquences de déformation moyenne les plus basses ce qui évite des effets de fluage trop importants d'une séquence à l'autre.

Les valeurs de cristallinité aux points haut et bas des cycles obtenues pour toutes les déformations moyennes sont reportées sur un graphique cristallinité-déformation ou elles sont comparées aux valeurs « à l'équilibre » obtenue sur un cycle quasi-statique effectué sur le même échantillon après les séquences d'oscillations (là aussi pour éviter les effets du fluage sur la mesure de déformation). L'écart entre les points acquis en dynamique et ceux en statique correspond au retard à la fusion ou à la cristallisation.

#### Résultats obtenus:

Pour des oscillations périodiques d'amplitude modérée, on montre que l'écart entre les mesures dynamiques et quasi-statiques diminue avec la déformation moyenne d'oscillations. Cela traduit une accélération de la cinétique de cristallisation et dans une moindre mesure de la cinétique de fusion avec la déformation. Pour un échantillon de faible réticulation, la cinétique de cristallisation semble également augmenter avec la déformation alors que l'écart à la fusion reste faible ce qui tend à montrer que la fusion des cristallites est rapide lorsque la densité de réticulation est faible. L'effet de la fréquence d'oscillation reste limité dans la gamme étudiée pour des oscillations de faible amplitude.

L'application de cycles périodiques de plus grande amplitude confirme que des temps de quelques millisecondes sont suffisants pour l'apparition de la cristallinité sous étirement et met en évidence une dépendance logarithmique de la quantité de cristallites avec la période du cycle (c'est-à-dire avec le temps d'élongation).

Des oscillations d'amplitude modérée réalisés sur des échantillons NR renforcé semblent indiquer que l'introduction de charges augmente les cinétiques de fusion et de cristallisation.

## **Chapitre VI : Renforcement**

Dans cette partie sont présentés les résultats de différentes techniques visant à caractériser l'état d'étirement local des chaînes de caoutchouc dans des échantillons purs et renforcés. Des mesures de gonflement à l'équilibre, de contrainte et d'orientation de la phase amorphe telle qu'introduite précédemment sont ainsi réalisés. Ces mesures sont corrélées à une évaluation précise de la densité de réticulation réalisée en RMN bas champ par Roberto Pérez-Aparicio (LPMA). L'objectif final est de clarifier les mécanismes de renforcement.

#### **NR non-chargés :**

##### Différentes mesures de la densité de réticulation :

Les mesures de densité de réticulation par RMN montrent l'augmentation de la densité de réticulation avec la quantité de soufre introduite dans le mélange. On met également en évidence une contribution à la densité de réticulation qui ne dépend pas de la quantité de soufre : il s'agit des enchevêtrements. Le gonflement à l'équilibre et le module dans le domaine linéaire sont également directement reliés à la quantité de Soufre utilisée. Pour des déformations inférieures au seuil de cristallisation, le paramètre d'orientation de la phase amorphe augmente linéairement

avec le terme de déformation entropique ( $\lambda^2 - \lambda^{-1}$ ) et la pente de la courbe est corrélée à la densité de réticulation en accord avec la théorie classique de l'élasticité. Une courbe maîtresse paramètre d'orientation de l'amorphe/contrainte est mise en évidence pour les différentes densités de réticulation testées.

#### Corrélation des mesures :

La corrélation des mesures mécaniques, de l'orientation de la phase amorphe et du gonflement à l'équilibre avec la densité de réticulation obtenue par RMN est très bonne pour les échantillons non chargés. Une contribution supplémentaire liée à une partie des enchevêtrements est détectée par la mesure de RMN. Cette partie des enchevêtrements est en effet relaxée après des temps caractéristiques faibles et n'est donc détectée qu'avec la RMN dont le temps caractéristique de mesure est de l'ordre de la dixième de milliseconde.

#### **NR chargés (après précyclage) :**

##### Différentes mesures de la densité de réticulation apparente :

De manière analogue aux échantillons NR purs, les mesures par RMN dans le NR renforcé montrent la relation entre la densité de réticulation et le taux de soufre introduit ainsi que la contribution des enchevêtrements. On met également en évidence une diminution de la densité de réticulation par rapport à un NR pur ayant un même taux de soufre. Ce résultat peut être expliqué par l'adsorption de l'accélérateur de vulcanisation CBS à la surface de la Silice qui réduit ainsi l'efficacité du système de vulcanisation. L'agent de surface utilisé pour la silice a un impact relativement faible sur la densité de réticulation. On note néanmoins une légère augmentation de la densité de réticulation pour un agent de couplage comparé à l'agent de recouvrement OCTEO. De plus l'agent de couplage TESPT donne une densité de réticulation légèrement supérieure à l'agent de couplage NSC ce qui peut s'expliquer par une libération d'une partie des atomes de soufre du TESPT. On constate une restriction du gonflement à l'équilibre pour certains matériaux chargés comparés au NR pur à même quantité de soufre. En ce qui concerne les propriétés mécaniques, on distingue le module aux grandes déformations (dans la gamme de 50 à 200% de déformation environ) et le module dans le domaine linéaire (à 0,1% de déformation mesuré par DMA en cisaillement, mesures en partie présentées dans le chapitre IV). L'évolution du paramètre d'orientation de la phase amorphe avec le terme de déformation entropique est linéaire jusqu'au seuil de cristallisation et dépend de la densité de réticulation et de l'interface charge-caoutchouc. On constate que pour une densité de réticulation identique, le paramètre d'orientation de la phase amorphe est plus important dans un échantillon NR chargé comparé à un échantillon NR pur. Pour les matériaux chargés silice, le paramètre d'orientation de l'amorphe en fonction de la contrainte suit la courbe maîtresse mise en évidence pour les matériaux non renforcés en revanche une déviation de la courbe maîtresse est observée pour les échantillons chargés avec du noir de carbone.

##### Renforcement aux grandes déformations

Les densités de réticulation apparentes déduites de différentes mesures que sont le module aux grandes déformations, le paramètre d'orientation de la phase amorphe et le gonflement à l'équilibre sont rapportées à la densité de réticulation mesurée par RMN. Pour chaque type d'interface charge-matrice, une dépendance linéaire de la densité de réticulation apparente avec la densité de réticulation mesurée par RMN est trouvée. Ces relations montrent une augmentation

de la densité de réticulation apparente dans les matériaux chargés par rapport aux non chargés quelle que soit la mesure effectuée. Cette augmentation est interprétée comme un effet d'amplification locale de la déformation entre les charges.

Pour chaque technique de mesure (contrainte, orientation de l'amorphe et gonflement à l'équilibre) et chaque type d'interface on définit un facteur d'amplification de déformation en utilisant la relation obtenue pour le NR pur comme référence. Un quatrième facteur d'amplification basé sur le décalage de la déformation seuil de cristallisation (mesurée au chapitre V) est calculé. Par analogie à des travaux antérieurs, on émet l'hypothèse que les portions de la distribution de déformation locale qui participent ne sont pas les mêmes selon la mesure considérée. Dans cette interprétation, seule la fraction de caoutchouc soumise à la plus grande déformation locale intervient dans le seuil de cristallisation. La fraction de chaînes les moins déformés est supposée ne pas participer à la contrainte mesurée, on attribue donc la partie haute (fortement déformée) de la distribution de déformation à la contrainte. On considère enfin que la totalité de la distribution de déformation locale est mise en jeu dans la mesure de gonflement (le solvant pénètre dans la totalité du réseau) et dans le paramètre d'orientation de la phase amorphe (toutes les chaînes diffusent). La comparaison des facteurs d'amplification pour les matériaux NR Silice-*TESPT* et NR-Silice-*OC*TEO mettent en évidence une amplification de déformation plus forte et plus hétérogène avec l'agent de couplage *TESPT*. Les facteurs d'amplification de déformation pour le Noir de Carbone comparés à ceux de Silice-*TESPT* sont respectivement inférieurs d'après le gonflement à l'équilibre et l'orientation de la phase amorphe et supérieurs d'après la contrainte et la déformation seuil de cristallisation. On en déduit une plus forte hétérogénéité de la déformation locale comparé à un système Silice sans agent de couplage.

#### Renforcement aux faibles déformations

Les modules à faible (0.1%) et moyenne (50%) déformations mesurés lors des tests d'effet Payne sont rapportés à la densité de réticulation mesurée par RMN. Les modules à moyenne déformations  $G'_{50}$  dépendent de la densité de réticulation de manière similaire au module à grande déformation mesuré in-situ et discuté précédemment. Le module dans le domaine linéaire  $G'_0$  augmente également avec la densité de réticulation mais une contribution importante n'est pas reliée à la densité de réticulation de la matrice. Nous interprétons cette contribution comme celle d'une fraction de caoutchouc à la faible mobilité (ou vitreux), son module est donc supérieur au module de la fraction à l'état caoutchoutique et dépend peu de la densité de réticulation. La comparaison des matériaux renforcés indique que le renforcement issu de ces ponts vitreux est plus important pour le Noir de Carbone et la Silice couplée avec le *TESPT*.

## **Chapitre VII : Dissipation aux grandes déformations et propriétés ultimes**

### Dissipation :

La dissipation relative désigne l'énergie dissipée sur un cycle (hystérèse) rapporté à l'énergie apportée à la traction. La dissipation d'énergie est d'abord étudiée sur un cycle de grande amplitude de déformation sur des échantillons non-précyclés. L'énergie dissipée sur ce premier

cycle dépend de la fraction de charge utilisée mais assez peu de l'interface charge-caoutchouc. Deux types d'essai ont ensuite été réalisés pour mesurer la dissipation. Dans le premier, l'échantillon subit trois cycles de grande amplitude de déformation (400%) puis on applique des cycles d'amplitude croissante de 60 à 400%. Dans le second type d'essai, l'échantillon n'est pas précyclé mais trois cycles sont effectués à chaque amplitude de déformation et seul le troisième cycle est analysé ce qui donne un échantillon précyclé à la déformation considéré. Dans les deux cas, la dissipation augmente fortement au-delà de la déformation seuil de cristallisation. Pour des déformations inférieures à celle-ci, la dissipation dépend de l'interface charge-caoutchouc. Les échantillons NR Silice-agent de couplage montrent une plus faible dissipation relative d'énergie comparée aux échantillons NR Silice-OCTEO, NR Silice sans agent de surface et NR-Noir de Carbone. Au-delà du seuil de cristallisation, la dissipation relative augmente et les écarts dus à l'interface sont moins importants ce qui confirme le résultat obtenu sur le premier cycle précédemment. Une normalisation des courbes de dissipation relative permet de mettre en évidence les écarts d'augmentation de dissipation lorsque les échantillons cristallisent. Plus les interactions à l'interface sont fortes et plus le seuil d'augmentation de la dissipation diminue. Ce résultat est en accord avec les résultats de cristallisation sous étirement présentés au chapitre V. La comparaison des résultats des deux types d'essais montrent que la dissipation augmente plus tardivement et plus fortement pour un échantillon précyclé à grande amplitude de déformation. Cette observation confirme les résultats du chapitre V sur l'effet du précyclage sur la déformation seuil et la pente de la cristallisation.

### Cavitation :

Nous avons utilisés des mesures d'absorption du faisceau X et de réduction de la largeur de l'échantillon réalisés lors des essais de diffraction des rayons X pour estimer la cavitation dans le NR chargé et le NR non-chargé. Le principe étant de mettre en évidence une fraction de cavité par la diminution de l'absorption du faisceau comparé à l'absorption attendue connaissant la réduction de la largeur à chaque mesure. La fraction de cavité obtenue est sensiblement supérieure pour un échantillon chargé comparé à un non chargé et semble dépendre du type d'interface charge-caoutchouc. Cependant une limite de notre mesure semble se trouver dans la géométrie de nos échantillons qui n'assure pas une réduction proportionnelle de la largeur et de l'épaisseur de l'échantillon. Or l'absorption du faisceau X se fait dans le sens de l'épaisseur et la caméra optique mesure la réduction de la largeur. Il est donc vraisemblable que les fractions de cavités mesurées soient surestimées.

Des observations par microscopie électronique à balayage d'échantillons NR chargés soumis à une déformation de l'ordre de 200% ont montré que le caoutchouc s'organise en fibrilles et que des cavités elliptiques se forment. Le caractère hétérogène de la déformation locale a également pu être mis en évidence par ces clichés de microscopie.

### Propriétés ultimes :

Les données de déformation, contrainte nominale et énergie à la rupture sont extraites des tests de traction sur échantillons non précyclés présentés au chapitre IV et sont reportés à la densité de réticulation. On constate que la contrainte nominale à la rupture passe par un optimum de

réticulation (ce qui serait également le cas de la contrainte vraie à la rupture) alors que la déformation à la rupture tend à décroître lorsque la densité de réticulation augmente. L'énergie à la rupture passe par un maximum pour une densité de réticulation d'environ  $1.7 \times 10^4 \text{ mol.g}^{-1}$ . L'énergie à la rupture dépend peu de l'interface charge-caoutchouc.

## Chapitre VIII : Résistance à la déchirure

### NR non chargé :

Les mesures d'énergie de déchirure sont réalisées en traction sur des éprouvettes de type cisaillement pur pré-entaillées. Pour les vitesses de sollicitation testées, la propagation de fissure dans le Caoutchouc Naturel est instable. L'analyse de l'effet de la densité de réticulation dans le NR non chargé montre un optimum de densité de réticulation pour l'énergie de déchirure. L'énergie de déchirure est plus particulièrement élevée pour les échantillons les moins réticulés du fait d'une plus grande déformation à la rupture. D'autre part on remarque que pour ces matériaux un nombre important d'échantillons ne sont pas rompus complètement après la propagation de l'entaille. La corrélation de la longueur d'entaille propagée à l'énergie libérée par la propagation définit l'énergie de déchirure.

### NR chargé :

Les instabilités de propagation (rotations d'entaille) dans le caoutchouc naturel chargé rendent plus difficile la définition de l'énergie de déchirure. Les rotations d'entaille combinent une propagation parallèle à l'axe de traction et une propagation droite (perpendiculaire à l'axe de traction) et la distinction entre ces deux chemins de propagation n'est pas aisée. Cette propagation droite mène parfois à un accident visible sur la courbe si la longueur propagée est suffisamment grande. Le critère fixé pour la prise en compte d'une propagation de fissure pour le calcul de l'énergie de déchirure a donc été d'obtenir une chute de force détectable sur la courbe de charge durant l'essai de déchirure. Comparé à un échantillon non-chargé, la déformation et la contrainte à la rupture augmentent fortement. L'énergie de déchirure augmente donc très fortement lorsque l'on introduit des charges renforçantes. L'énergie de déchirure varie globalement assez peu entre les systèmes Silice-agent de couplage et Noir de Carbone, en revanche les échantillons Silice-OCTEO atteignent des valeurs de déformation à la rupture bien supérieures aux autres échantillons renforcés et ceux avec une contrainte à la rupture proche. A ce stade, nous ne disposons pas d'éléments clairs pour expliquer ce résultat étant donné les valeurs proches de résistance à la rupture en géométrie non entaillée.

L'effet de la densité de réticulation sur l'énergie de déchirure pour les différents types d'interface montre un optimum de densité de réticulation proche de celui mentionné au chapitre VII pour la résistance à la rupture en géométrie non entaillée. L'effet de la vitesse de déformation appliquée (à ne pas confondre avec la vitesse de propagation de fissure) a également été mis en évidence avec des essais à trois différentes vitesses de traction. Pour chaque type d'interface, l'énergie de déchirure diminue avec l'augmentation de la vitesse de déformation. On peut attribuer cet effet à une diminution de la fraction cristallisée en fond d'entaille lorsque le temps de sollicitation diminue (effet de la cinétique de cristallisation).

Etude du fond d'entaille :

Les rotations d'entailles et l'état de déformation du NR chargé en fond d'entaille ont été observés par microscopie électronique. Un état de déformation local fortement hétérogène est mis en évidence en fond d'entaille. Le caoutchouc dans un état fortement déformé s'organise en fibrilles d'une centaine de nanomètres environ.

Les champs de déformation ont été calculés par corrélation d'image numérique pour plusieurs états de déformation macroscopique au cours d'essais de déchirure dans des échantillons NR chargés. Les profils de déformation en fonction de la distance au fond d'entaille sont extraits de cette analyse des champs de déformation. Les profils de déformations obtenus avec NR Silice-OCTEO semblent différer légèrement de ceux obtenus pour NR Silice-TESPT et NR Noir de Carbone. Les profils de contrainte ont été estimés à partir de lois de comportement obtenues en traction simple. On remarque que le profil de contrainte est très proche pour les systèmes NR Silice-TESPT et NR Silice-OCTEO et la contrainte en fond d'entaille semble identique pour ces matériaux.

La taille de zone cristallisée en fond d'entaille a pu être estimée en géométrie cisaillement pur en tenant compte du profil de déformation calculé par corrélation d'image numérique et du seuil de cristallisation déterminé pour un matériau NR Silice-TESPT non précyclé. D'après ces mesures, la cristallisation peut se produire en fond d'entaille pour des déformations macroscopique de l'ordre de 20% seulement.

La cristallinité en fond d'entaille a également été directement mesurée par diffraction d'un faisceau fin de rayons X permettant une cartographie de la cristallinité avec une résolution de 50 $\mu$ m. Ces mesures ayant été faites sur des bandes entaillées, il n'est pas possible de vérifier leur accord avec la profondeur de zone cristallisée estimée par les champs de déformation en géométrie cisaillement pur. On met en évidence une forte décroissance de la fraction cristallisée avec la distance au fond d'entaille qui est qualitativement en accord avec les mesures de profils de déformation.

---

## Résumé de la thèse :

Cette étude vise à mieux comprendre les mécanismes physiques à l'origine des propriétés mécaniques et des propriétés ultimes des caoutchoucs renforcés dans le but d'améliorer les compromis de propriétés de ces matériaux. Des échantillons de caoutchouc naturel dans lequel sont dispersés des agrégats de silice précipitée ou de Noir de Carbone et vulcanisés au Soufre ont été mis en œuvre. Les paramètres étudiés sont la densité de réticulation, la surface spécifique de la charge, la fraction volumique de charge ainsi que l'interface charge-caoutchouc modifiée au moyen de différents traitements de surface de silice.

L'effet des charges et du type d'interface sur le seuil de cristallisation induite par la déformation, la pente de la fraction de cristallites avec la déformation, la fraction de cristallites à rupture et l'orientation moyenne des cristallites est discuté en termes d'amplification locale hétérogène de la déformation. Les résultats obtenus peuvent également être partiellement expliqués par une restriction de la mobilité des chaînes en présence de charges. Les cinétiques de cristallisation et de fusion ont été étudiées au moyen d'un nouvel appareil de diffraction *in-situ* des rayons X équipé d'un système d'acquisition stroboscopique. Les résultats obtenus avec deux densités de réticulation montrent une augmentation de la cinétique de cristallisation et dans une moindre mesure de la cinétique de fusion avec la déformation moyenne pour des oscillations d'amplitude modérée autour d'une extension donnée.

Pour les échantillons non-chargés, le module est bien corrélé à la densité de réticulation mesurée par RMN, au degré de gonflement à l'équilibre et à l'orientation moyenne des segments de chaînes mesurée par diffusion des rayons X et cela en accord avec la théorie de l'élasticité caoutchoutique. Pour le Caoutchouc Naturel renforcé dans le régime des grandes déformations (supérieures à 50%), un phénomène d'amplification locale de déformation explique l'augmentation de la déformation locale des chaînes mesuré par le paramètre d'orientation de la phase amorphe. En ce qui concerne le module dans le domaine linéaire (0.1% de déformation), un effet de renforcement supplémentaire qui n'est pas relié à la densité du réseau est souligné.

Dans le régime des grandes déformations, l'effet de l'interface charge-matrice sur la dissipation est relié à la fraction cristalline. Les propriétés ultimes c'est-à-dire l'énergie à la rupture pour des échantillons non entaillés a également été étudiée. Des essais de déchirure à différentes vitesses de traction ont été réalisées sur des échantillons de type cisaillement pur pré-entaillés. Une forte augmentation de l'énergie de déchirure est observée pour les échantillons chargés par rapport aux échantillons non chargés. Concernant l'effet de l'interface charge-caoutchouc, une forte augmentation de l'énergie à apporter pour propager la fissure est mesurée dans le cas d'échantillons avec une faible interaction silice-caoutchouc. Les profils d'amplification de déformation à l'échelle de la centaine de micromètres en fonction de la distance au fond d'entaille ont été obtenus par corrélation d'image numériques durant les essais de déchirure. Les profils de déformation et la zone cristallisée en fond d'entaille mesurée par diffraction *in-situ* des rayons X sont discutés.

---

## Summary of the thesis:

This study aims at better understanding the physical mechanisms responsible for the mechanical and ultimate properties in reinforced rubber materials in a view to improve the compromise of properties. Sulfur vulcanized samples made of a Natural Rubber matrix in which aggregates of precipitated Silica or Carbon Black are dispersed have been manufactured. Control parameters are the crosslink density, filler specific surface, filler volume fraction and the filler/rubber interactions through different silica surface treatments.

The effect of fillers and interface type on the strain-induced crystallization (SIC) onset, slope of crystalline content with strain, crystalline content at break, crystallites average orientation is discussed in terms of distribution of heterogeneous local strain amplification. A restriction of chain mobility in presence of fillers may also account for the obtained results. The kinetics of Strain-Induced Crystallization and Melting have been studied by a newly developed in-situ oscillating X ray scattering device equipped with a stroboscopic acquisition system. Results obtained on NR samples with two different crosslink densities are presented showing an increase of crystallization kinetics and to a lower extent of melting kinetics with average strain for oscillations of moderate amplitude around a given extension.

Mechanical measurements have proved to correlate fairly well to the crosslink density measured by NMR, to equilibrium swelling degree and to the average chain segment orientation measured by X-ray scattering in unfilled NR in agreement with the rubber elasticity theory. In reinforced NR at large strains (above 50%), a local strain amplification phenomenon accounts for the increase of the local chain stretching measured by the amorphous orientation parameter. As regards the modulus in the linear regime (0.1% of strain), a supplementary reinforcement effect which is not correlated to the matrix crosslink density is highlighted.

In the high strain regime, the effect of the filler-matrix interface on the dissipation has been found to correlate well with the crystalline content. The ultimate properties i.e. energy at break in un-notched samples were also investigated. Tear experiments have been performed on Pure Shear pre-notched samples at various drawing speeds. A strong increase in the tearing energy is obtained for reinforced NR samples as compared to unfilled samples. As regards the rubber/filler interface effect, weakly interacting Silica samples require a higher energy to propagate the crack. Mesoscopic Strain amplification profiles as a function of distance to crack tip were obtained by means of digital image correlation during the tear tests. The local strain profiles and the crystallized zone at tear tip detected by in-situ X-ray diffraction are discussed.